Magnetic Resonance Fingerprinting for Rapid
Quantitative Imaging of the Liver

By

Jason Ostenson

Dissertation

Submitted to the Faculty of the

Graduate School of Vanderbilt University

in partial fulfillment of the requirements

for the degree of

DOCTOR OF PHILOSOPHY

in

Chemical and Physical Biology

February 29, 2020

Nashville, Tennessee

Approved:

John C. Gore, PhD

Sandeep S. Arora, MBBS

Richard D. Dortch, PhD

William A. Grissom, PhD

E. Brian Welch, PhD

To my parents

and

To David and Anne

ACKNOWLEDGMENTS

TABLE OF CONTENTS

LIST OF TABLES

LIST OF FIGURES

Chapter 1

INTRODUCTION

1.1   Purpose

The purpose of this work is to present developments in and applications of quantitative magnetic resonance imaging (qMRI) of the liver. Nonalcoholic fatty liver disease (NAFLD) is a highly prevalent pathology whose pathogenesis and longitudinal behavior is not entirely understood. There is currently no non-invasive diagnostic test sensitive to all the stages of NAFLD progression, but several qMRI metrics such as fat signal fraction, T_1, and T_2 correlate with different liver histopathological states related to NAFLD. The abdomen is a challenging site for qMRI because of its large size, anatomical heterogeneity, and respiratory motion. These challenges affect the practicality of using qMRI in the abdomen to determine their relationship with NALFD histopathology. A recent development in qMRI called magnetic resonance fingerprinting (MRF) permits simultaneous estimation of multiple MRI parameters in scan times $\lesssim$ 20 s. However, the original form of this technique was not sensitive to partial volumes of fat and was generally not tailored for use in the abdomen. The following present developments and applications towards unbiased and repeatable MRF parameter estimation in the liver for NAFLD study.

1.2 Organization and Scope

Chapter 2 provides background on conventional MRI and the recent development of MRF. Historical developments important to MRI relaxometry, conventional methods for estimation of T_1 and T_2, and image reconstruction are briefly discussed. Similarly, the development of MRI fat imaging is presented, including relatively recent work in non-linear fitting of confounding factors like static field deviations (ΔB_0). The initial development of MRF and its commonly used methods are introduced. This includes a primer on extended phase graph (EPG) signal modeling. Applications of MRF beyond relaxometry are also mentioned.

An introduction and background material for NAFLD is given in Chapter 3. This includes a brief review of prevalence, nonalcoholic steatohepatitis, and what is known about the etiology, hepatic histological findings in the disease, and prognosis. The current clinical diagnostic tests available for NAFLD are explored with an emphasis on imaging in general and MRI, including: ultrasound elastography, computed tomography, MRI elastography, MRI of fat fraction, and MRI relaxometry. The advantages and disadvantages of these different modalities are put forth. The discussion of qMRI includes pre-clinical and clinical research on the sensitivity and specificity of different qMRI metrics to different histopathological features of NAFLD/NASH.

Chapter 4 further discusses the motivation for this work and its specific aims. The research and clinical questions from Chapter 3 are tied to the recent MRF advances in Chapter 2 and challenges yet to be addressed in the MRF literature. This union motivates the specific aims of this work. In summary, these aims are: (1) use MRF to separate fat from water with simultaneous water relaxometry; (2) compensate for non-idealities such as static and applied magnetic field perturbations, respiratory motion, and slice-profile effects; and (3) incorporate MRF developments into a small study of intra-subject repeatability of MRF relaxometry metrics and show proof-of-concept that MRF can be employed in NAFLD subjects. This chapter also further elucidates the interweaving of the technical developments in this work with the specific aims.

The MRF technical developments towards accomplishing the specific aims begins in Chapter 5 by addressing blurring in MRF. MRF pulse sequences often employ spiral trajectories in the spatial-frequency (k-space) domain for data readout. Spiral k-space acquisitions are vulnerable to blurring in the spatial domain in the presence of static field off-resonance. This work describes a blurring correction algorithm for use in spiral MRF and demonstrates its effectiveness in phantom and *in vivo* experiments. Results show that image quality of T_1 and T_2 parametric maps is improved by application of this correction. This MRF correction has negligible effect on the concordance correlation coefficient and improves coefficient of variation in regions of off-resonance relative to uncorrected measurements.

An MRF fat-water separation technique is proposed in Chapter 6. This method separates fat and water signals, estimates water T_1 and T_2, and accounts for B_0 effects with spiral blurring correction, in a single sequence. A k-space-based fat-water separation method is further extended to a specific form of MRF with swept echo time. Repeated application of this k-space fat-water separation to demodulated forms of the measured data allows a static field (B_0) map and correction to be approximated. The method is compared with MRF without fat separation across a broad range of fat signal fractions (FSFs), water T_1s and T_2s, and under heterogeneous static fields in simulations, phantoms, and *in vivo*. The proposed method's FSF estimates are shown to be highly concordant with conventional measurements and reduces biases in the T_1 and T_2 estimates due to fat signal relative to other MRF sequences by several hundred milliseconds. The blurring correction improves the FSF, T_1, and T_2 estimation compared to those estimates without correction.

Chapter 7 closely examines the role of slice-profile on the specific MRF sequence used in Chapters 5 and 6. Slice-selective, gradient-crushed, transient-state sequences used for MRF relaxometry in this study are sensitive to slice profile effects. Extensions of the extended phase graph (EPG) formalism are proposed, called slice-selective EPG (ssEPG), that model slice profile effects. The hard-pulse approximation to slice-selective excitation in the spatial domain is reformulated in k-space. Excitation is modeled by standard EPG operators. This ssEPG modeling is validated against spatial domain simulations and phantom slice profile measurements. ssEPG relaxometry accuracy and variability are compared with other EPG methods in an MRI phantom and human leg *in vivo*. The role of off-resonance interactions with slice profile and gradient crushers are investigated. Simulations and slice profile measurements show that ssEPG can model highly dynamic slice profile effects of gradient-crushed sequences. The ssEPG T_2 estimates are shown to be less biased relative to other modeling approaches. Small deviations in B_0 can produce substantial bias in T_2 estimations from a range of MRF sequence types, and these effects are modeled and explained by ssEPG.

Chapter 8 studies MRF fat-water separation application and repeatability in the liver. The previous chapters' technical developments were not immediately available for deployment of MRF abdominal imaging and parameter estimation. To determine the effect

3

of the methodologies developed in Chapters 5-7 and repeatability of the relaxometry parameters in the liver, we image a small cohort of subjects without reported liver pathology using MRF with fat-water separation. The improvements to MRF fat-water separation parameter estimation in the liver are explored. We also show proof-of-concept that we may employ this technique in a NAFLD population by imaging a single biopsy-proven NASH subject. The results of this chapter indicate that an MRF sequence of 20 s duration employed in a single breath hold can be done in non-pathological and NAFLD subjects. The intra-subject repeatability of fat-separated water T_1 and T_2 are calculated, and the NASH subject is successfully imaged. It is proposed that further technical developments or sequence modifications will be required to reduce bias in fat signal fraction and T_2.

General conclusions from the preceding chapters and avenues for future work are explored in Chapter 9. The successes and limitations of the MRF blurring correction, fat-water separation, and slice-profile modeling are discussed. The future directions proposed include: different reconstruction methods to reduce bias intrinsic to the original form of MRF fat-water separation, characterization of fat, application MRF fat-water separation outside the liver, flow compensation, and volumetric MRF imaging.

BACKGROUND ON MAGNETIC RESONANCE IMAGING RELAXOMETRY AND FAT QUANTITATION

2.1. Background on Relaxometry

In the following section, the basic characteristics of longitudinal (T_1) and transverse (T_2) relaxation time constants are discussed. This section includes a theoretical description of magnetization behavior over time, the factors affecting T_1 and T_2, and conventional ways to measure these time constants.

2.1.1 The Bloch equations and the phenomenological role of T_1 and T_2

This section will describe how the change of the nuclear magnetic resonance (NMR) signal over time depends on the relaxation properties of the measured tissue and how these changes can be measured. This will help provide a direct connection between relaxation and the observed signal.

The Bloch equations[1] describe the evolution of the net ensemble magnetization induced by the main static magnetic field (B_0) and other magnetic fields,

$$\frac{d\mathbf{M}}{dt} = \begin{bmatrix} -\dfrac{1}{T_2} & \gamma B_z & -\gamma B_y \\ -\gamma B_z & -\dfrac{1}{T_2} & \gamma B_x \\ \gamma B_y & -\gamma B_x & -\dfrac{1}{T_1} \end{bmatrix} \mathbf{M}(t) + \begin{bmatrix} 0 \\ 0 \\ \dfrac{M_0}{T_1} \end{bmatrix}. \qquad [2.1]$$

Here, $\mathbf{M}$ is the vector of magnetization; B_x, B_y, and B_z are the Cartesian components of the magnetic field; γ is the gyromagnetic constant; T_1 and T_2 are, respectively, the longitudinal and transverse relaxation time constants; and M_0 is the thermal equilibrium magnetization (along z). The magnetic field can be segregated as

$$B_i = \begin{cases} B_i = B_{1+,i} & \text{for} \quad i = x, y \\ B_i = B_0 + B_{1+,z} & \text{for} \quad i = z \end{cases} \qquad [2.2]$$

where $B_{1+,i} = B_{1+,i}(t)$ is the applied radiofrequency field.

In the absence of an applied radiofrequency field Eq. 2.1 shows that the transverse component of the magnetization will be attenuated, and the longitudinal component will recover towards M_0 with time. The transverse magnetization undergoes exponential decay with time:

$$M_{x,y}(t) = M_{x,y}(t = 0)e^{-t/T_2 - it\omega_0}. \qquad [2.3]$$

Here the compact complex notation for transverse notation has been used $M_{x,y} = M_x + iM_y$, where $i = \sqrt{-1}$; ω_0 is the Larmor frequency of the magnetization precession. The longitudinal magnetization exhibits exponential recovery:

$$M_z(t) = M_0\left(1 - e^{-t/T_1}\right) + M_z(t = 0)e^{-t/T_1}. \qquad [2.4]$$

The transverse magnetization, $M_{x,y}$, is sinusoidally oscillating at the Larmor frequency given by $\omega_0 = \gamma B_z$. If $M_{x,y}$ is sufficient in magnitude, the oscillating magnetization can, by Faraday induction, create an oscillating current in an adjacent coil. In this way, the signal $S(t) \propto M_{x,y}$ can be measured. Thus, relaxation effects in the transverse plane can be interrogated since the signal is directly proportional to the component of magnetization experiencing attenuation due to T_2. But, it is also possible to indirectly measure M_z.

By application of short pulses of applied radiofrequency B_{1+} of length τ ($\ll T_1, T_2$), Eq. 2.1 shows that it is possible to rotate M_z into the transverse plane. If we consider the magnetization in a frame rotating at angular frequency ω relative to the laboratory frame, under an applied RF field of magnitude $B_1(t)$ at frequency ω_{RF} it can be shown[2] that the evolution of the transverse magnetization in the rotating frame, $M'_{x,y}$, can be expressed as

$$\frac{dM'_{\text{x,y}}}{dt} = -i\gamma M'_{\text{x,y}} \left(B_0 - \frac{\omega}{\gamma} \right) + i\gamma M_z B_1(t) e^{-i(\omega_{\text{RF}} - \omega)t}. \qquad [2.5]$$

If $\omega = \omega_{\text{RF}} = \gamma B_0$, then in the rotating frame $dM_{\text{x,y}}/dt = i\gamma M_z B_1(t)$. The longitudinal magnetization is rotated into the transverse plane. In this way it is possible to generate signal from M_z and so measure its behavior under T_1 relaxation. This is further discussed in §2.1.3.

The above mathematics gives a framework for describing (and modeling) relaxation parameters but says little about the source of the relaxation. The following section will further discuss the physical basis of relaxation.

2.1.2 *In vivo* mechanisms of T_1 and T_2 decay

While there is no complete model of relaxation in tissue[3], early work in NMR[4] and MRI has provided a quantitative understanding for idealized spin ensembles that can serve as a basis for qualitative understanding of the primary contributors to relaxation in a biological milieu. Longitudinal relaxation rate (T_1^{-1}) is sensitive to the Larmor frequency (and twice this frequency) relative to the local spin rotation, whereas transverse relaxation (T_2^{-1}) is sensitive to this and slowly moving components of the spin ensemble. In tissue, both forms of relaxation depend critically on interaction with macromolecules as well as paramagnetic particles.

A two pool model for water proton longitudinal relaxation describes the T_1 of pure water as a function of the spectral density of water proton oscillation at their resonance, whereas tissue water relaxation is largely determined by water interactions with macromolecules[5]. The water proton longitudinal relaxation in water can be expressed as[5,6]

$$\frac{1}{T_1} \propto \left(J^1(\omega) + J^2(2\omega) \right), \qquad [2.6]$$

where $J^1(\omega)$ and $J^2(2\omega)$ describe the proportion of water protons undergoing motions at the resonance and two times the resonance, respectively. Under a fast exchange two state (FETS) model, "free" water, away from proteins and other macromolecules, and "bound" water in the hydration layer around macromolecules, quickly exchange magnetization between these two pools. The resulting observable water proton T_1 is given as

$$\frac{1}{T_1} = \frac{b}{T_{1b}} + \frac{1-b}{T_{1f} + \tau_\epsilon} \qquad [2.7],$$

where b is the fraction of water in the macromolecular hydration layer, T_{1b} and T_{1f} are the longitudinal relaxation times of the water in the hydration layer and in the free water pool, respectively; and τ_ϵ is mean residence time for water in the hydration layer. The spectral density for free water is of the form

$$J^1(\omega) \propto \frac{1}{r^6} \frac{\tau_c}{1 + \omega^2 \tau_c^2}. \qquad [2.8]$$

Here, τ_c is the correlation time of the water proton, which is a measure of the time constancy of rotational or translational motion, and r is the average separation of the hydrogen protons in water. $J^2(2\omega)$ has a similar form. In pure water, it is known that $\tau_c \sim$ 1 ps, which gives $\omega^2 \tau_c^2 \ll 1$ for clinical MRI field strengths ($\sim$ T), so making T_{1f} independent of the resonant frequency. Distilled water, as stand-in for free water, is well known to have $T_1 \sim$ seconds, whereas tissue water varies widely over different tissue types and B_0[7]. For $\tau_\epsilon \ll T_{1f}$ the fraction of hydration water, b, and T_{1b} strongly influences, and possibly dominates, the observable longitudinal relaxation rate.

The characteristic transverse relaxation time (T_2) is derived from longitudinal relaxation processes as well as static magnetic field variations. The combined effect of

these processes effectively dephase otherwise coherent ensembles of magnetization. Like Eq. 2.6, T_2 for the proton can be modeled[5,6] as a function of spectral density functions

$$\frac{1}{T_2} \propto \left(\frac{J^0(0)}{4} + \frac{5J^1(\omega)}{2} + \frac{J^2(2\omega)}{4} \right) \qquad [2.9].$$

The $J^0(0)$ represents spectral density at zero frequency. Eq. (2.9) shows that transverse relaxation is composed of longitudinal relaxation processes as well processes for slowly moving particles. This is consistent with the intuitive idea that static magnetic fields will contribute to dephasing of the transverse magnetization, shortening T_2. *In vivo,* this manifests as so much shortening of the T_2 of protons in large macromolecules and those bonded to cellular membranes that these large structures become MRI-invisible to most human MRI systems/sequences. The static magnetic field variations contributions to T_2, depending on the motion of water, other tissue components, and sequence timing, act over larger distance than inter-particle dipole interactions and may be reversible.

Static components of magnetization dephasing due to meso- (> μm) and macro-scale changes in magnetic field generate an alternative form of transverse decay, with a characteristic time called T_2^*. These larger scale interactions may be due to susceptibility differences in tissue due to iron or inhomogeneity of the main magnetic field strength. In this model, transverse magnetization effects are felt over length scales much larger than the stochastic motion due to diffusion over the time of the MRI experiment.[8] Depending on the sequence timing and non-diffusive movements of the water and magnetic perturbations of the tissue, this dephasing may roughly be considered monoexponential and reversible. The reversibility of this static component of magnetic perturbation is the basis of the spin- (or Hahn-) echo[9], further discussed in §2.1.3.

Relaxation times may not be monospectral, but characteristic of multiple tissue compartments.[10] Exchange rates between these compartments can have a significant effect on the observed relaxation rates, which may complicate T_2 estimation in the case of intermediate or slow exchange rates (relative to their transverse relaxation rates).[11]

Fast exchange rates (relative to the longitudinal relaxation rates) may dominate T_1 relaxation times, which has an averaging effect on the observed T_1 values, but slowly exchanging tissue compartments may still may exist that give rise to multicomponent T_1 spectra[12,13]. Additionally, magnetization transfer contrast[14–16] may make water protons sensitive to macromolecular protons. In this model, short-T_2 macromolecular protons exchange magnetization with hydration layer water protons such that indirect estimates of the (macromolecular) bound proton fraction and exchange rates between the water and bound proton pool may be made.[17]

As discussed above, there is a static field dependence on T_1, and to a lesser degree T_2. Eq. (2.8) shows that the Larmor frequency of the water in relation to its spectral density determines longitudinal relaxation. On the other hand, the static component field inhomogeneity, in Eq. (2.9), that contributes to transverse relaxation, reduces the field dependence. These general arguments are supported by measurements of relaxation across a large array of field strengths.[5,18] At modern clinical MRI strengths of 1.5 an 3.0 T, these behaviors can also be observed.[7] Even prior to the inception of MRI, it was realized that the differences between relaxometry parameters between organs and pathological features could be used to generate image contrast.[19]

2.1.3 Conventional techniques for measuring T_1 and T_2

As discussed in §2.1.1, conventional techniques for measuring relaxometry parameters rely on measuring changes in the $M_z(t)$ and $M_{xy}(t)$. This is often accomplished by minimizing the contrast dynamics of the magnetization not under investigation, while maximizing that under study. However, faster estimation techniques are possible by relaxing the simplicity of the model, or by allowing both T_1 and T_2 contrasts to present simultaneously within a single sequence. While the total number of sequences for relaxometry are beyond the scope of this section, the techniques presented here provide a basis for further discussion in later sections and chapters.

The mathematically simplest form of T_1 estimation is inversion recovery, which is closely related to another method called saturation recovery. From Eq. (2.4), we can see

that if M_z is perfectly inverted from an equilibrium state and then rotated into the transverse plane after a delay from inversion time, T_I, the resulting signal will be

$$S(T_I) = C\big(1 - Ae^{(-T_I/T_1)}\big) \qquad [2.10],$$

where $A = 2$, C is constant to account for scaling of the signal due to magnetization density, incomplete rotation into the transverse plane (assumed to be constant through time), and the receive characteristics of the systems. If the magnetization is allowed to fully recover to equilibrium and the experiment is repeated at different T_Is, then we may solve for C and T_1 using a non-linear fit, thereby estimating T_1. Similarly, if the magnetization is saturated so that there is no longitudinal (or transverse) magnetization at $T_I = 0$, then we may use this model with $A = 1$. The inversion recovery method is practically complicated by incomplete inversion of the magnetization as well as the time requirement for full recovery to the equilibrium state. Saturation recovery is less sensitive than inversion recovery because the starting magnetization at $T_I = 0$ is closer to equilibrium, producing less contrast over the range of observed T_Is.

One method that speeds acquisition time and accounts for imperfect inversion of the magnetic field is the model for selective inversion recovery.[20,21] This sequence repeats the inversion after a time delay T_D, with the signal model

$$S(T_I) = C\big(S_f\big(1 - e^{(-T_D/T_1)}\big)e^{(-T_I/T_1)} + 1 - e^{(-T_I/T_1)}\big). \qquad [2.11]$$

Imperfect inversion is captured by S_f. This model assumes a complete saturation of the longitudinal magnetization prior to commencement of the delay time. Since $T_I + T_D$ may be much shorter than the T_R needed in a classical inversion recovery experiment to guarantee equal starting magnetization following inversion, selective inversion can improve sequence timing with more contrast than saturation recovery techniques. This mode of acceleration dovetails with imaging methods further discussed in §2.2.

A method for rapid T_1 estimation that is often employed in cardiac applications is the Look-Locker[22,23] sequence. In this sequence, inversion is followed by a series of low nutation (or flip) angle excitations, permitting greater sampling of the inversion curve near a given T_I. This has advantages in the imaging context, discussed further in §2.2. Combined with cardiac-gating and application of multiple acquisitions, the Look-Locker technique has been used to estimate T_1 of the myocardium[24].

Another technique that offers fast T_1 estimation is driven equilibrium single pulse observation of T_1 (DESPOT1)[25]. By applying a repeated nutation angle at short T_R and nulling ("spoiling") the remaining transverse signal before the next excitation pulse, it's possible to drive the system to equilibrium that is dependent on the signal's T_1. The short T_R in this case is conducive to rapid imaging. DESPOT1's counterpart, DESPOT2 (discussed below), permits rapid estimation of T_2 when the two methods are combined.

Estimation of T_2 is often achieved through spin- (or Hahn-[9]) echo techniques. In a typical MRI estimation of T_2, imperfect shimming of the static magnetic field or tissue susceptibility heterogeneity may induce changes in the observed transverse relaxation to cause T_2^* to be different than the inherent tissue T_2. However, the action of an excitation pulse induces a refocusing effect on the complex magnetization (see also §2.2.1). The refocusing has the effect of negating the phase of the transverse magnetization. If the magnetic susceptibility/static field deviations are constant over time and translational diffusion and exchange effects are neglected, then the dephasing due to these processes will be undone following the RF action. The result of this process is that for two RF pulses separation by a time $T_E/2$, there will be a maximum in the refocused magnetization $T_E/2$ after the second pulse: this is the spin-echo. This effect is maximal at a nutation angle of 180°. Since pure T_2 processes described by Eq. (2.9) act on the time scale of the water proton movement variations ($\tau_C \approx 1$ ps) and are stochastic in nature, these processes are not refocused, and the signal decays by a factor of $e^{(-T_E/T_2)}$. If the T_R is sufficiently long, or a series of "dummy" pulses are played at a given T_R without recording the signal, then the starting M_z at the time of excitation will be equal for 90° pulses, making T_1 effects contribute to scaling without confounding the estimation of T_2.

The burdensome timing requirements for classical spin-echo techniques can be improved by use of multiple refocusing angles in the Carr-Purcell-Meiboom-Gill (CPMG) sequence [26,27]. In this approach an initial 90° nutation with phase directed on a given axis is then followed at a time $\tau/2$ by a series of 180° pulses, separated by time τ, with a phase offset of $\pi/2$ from the initial pulse. This accomplishes three things: (1) repeated spin-echoes with ($T_E \ll T_R$) are acquired over many points in the decay curve, permitting more rapid estimation of T_2; (2) by repeatedly refocusing the magnetization at short time intervals, moving protons are repeatedly refocused so that the phase dispersion from inhomogeneous magnetic fields is decreased, relative to spin-echo at the same T_E, making T_2 estimates less diffusion sensitive; and (3) the $\pi/2$-phase rotation between the initial pulse and subsequent refocusing pulses reduces sensitivity to variations in B_{1+}. Contributions from non-ideal B_{1+} can still confound T_2 estimation using CPMG, but these can be reduced by modeling them, limiting the RF refocusing pulse sensitivity to B_{1+}[28], or using a gradient crusher scheme which limits the contribution to unwanted signals[29].

Further acceleration in T_2 estimation can be obtained by an MRI sequence called balanced steady-state free precession (bSSFP; §2.2.1)[30]. In particular, combined with the T_1 estimation from DESPOT1, DESPOT2[25] permits the estimation of T_2 through bSSFP's sensitivity to both T_1 and T_2. Like DESPOT1, DESPOT2 relies on a short T_R sequence, which permits rapid acquisition of the necessary nutation angles for parameter estimation.

2.2 Background on Conventional MR Imaging

The following section discusses conventional MRI pulse sequences for relaxometry and fat quantitation relevant to this work as well the basics of image reconstruction.

2.2.1. Conventional pulse sequences

We can broadly categorize pulse sequences into gradient echo (GRE) and spin echo sequences (SE). The primary difference between these sequences is that the GRE signal, which contains at least some component of longitudinal magnetization rotated into the

transverse plan (free induction decay)[i], relies on the immediate action of an RF pulse combined with a gradient (for imaging); whereas, the SE signal relies on the Hahn echo mechanism discussed in §2.1.3. Each of these expansive categories contain many subcategories including approaches to acquiring the necessary data to create an image, and differences in preparation before imaging to impart different contrast mechanisms. Here, we focus on subcategories that are most relevant to methods and modifications to those methods later employed in this work.

When considering GRE sequences, it is pertinent to consider the refocusing effects of transverse magnetization. For a given flip angle α at a given phase ϕ from an RF pulse (considered instantaneous in this context), the complex magnetization $\mathbf{M} = [M_+, M_-, M_z]^\mathrm{T}$, with $M_\pm = M_x \pm iM_y$, can be given as[31]

$$\mathbf{M}^+ = \begin{pmatrix} \cos^2\left(\frac{\alpha}{2}\right) & e^{2i\phi}\sin^2\left(\frac{\alpha}{2}\right) & -ie^{i\phi}\sin(\alpha) \\ e^{-2i\phi}\sin^2\left(\frac{\alpha}{2}\right) & \cos^2\left(\frac{\alpha}{2}\right) & ie^{-i\phi}\sin(\alpha) \\ -\frac{i}{2}e^{-i\phi}\sin(\alpha) & \frac{i}{2}e^{i\phi}\sin(\alpha) & \cos(\alpha) \end{pmatrix} \mathbf{M}^- = \mathrm{T}(\alpha)\mathbf{M}^-. \qquad [2.12]$$

Here, the $<\cdot>^\pm$ indicates after and before the RF pulse. We can see that for $\alpha = 180°$ ($\phi = 0$), $\mathrm{T}(\alpha)$ becomes

$$\mathrm{T}(180°) = \begin{pmatrix} 0 & 1 & 0 \\ 1 & 0 & 0 \\ 0 & 0 & -1 \end{pmatrix}. \qquad [2.13]$$

For non-zero transverse magnetization, the act of a refocusing pulse is to swap magnetization between the $M_\pm$ states by phase conjugation. Similarly, we can see that $\alpha < 180°$ also swaps information between these states. That is, for sequences with repeated

---

[i] Strictly speaking, this notion can be challenged in special cases, such as variable flip angle approaches where one of the flip angles is zero.

flip angles and $T_R \lesssim T_2$, refocused magnetization may contribute significantly to the signal for $\alpha < 180°$.

The spoiled gradient echo technique (SPGR) is a GRE sequence that severely attenuates or removes (spoils) the remaining transverse magnetization. A common way to achieve spoiling is by rotation of the RF phase between pulses in a quadratic fashion combined with a gradient spoiler that dephases the magnetization. Here the RF phase for the jth pulse, ϕ_j, can be given as[2]

$$\phi_j = \frac{1}{2}\phi_0(j^2 + j + 2), \qquad [2.14]$$

where ϕ_0 is an angle that is empirically derived to reduce contributions of refocused transverse magnetization. With RF spoiling, SPGR sequences can use $T_R \ll T_2$ with limiting effects from refocused magnetization. As an SPGR signal goes to the steady-state, its signal, s_{SPGR}, can be derived analytically as

$$s_{\text{SPGR}} = C \frac{1 - e^{-T_R/T_1}}{1 - e^{-T_R/T_1}\cos(\alpha)} e^{-T_E/T_2^*}\sin(\alpha). \qquad [2.15]$$

If the echo time, T_E, is fixed the T_2^* weighting can be folded into the scalar C. It is apparent that the SPGR signal is a function of T_1.

Steady-state free precession (SSFP) sequences are classes of GRE pulse sequences that do not spoil remaining transverse magnetization.[30] SSFP sequences are often divided into balanced (bSSFP) and unbalanced/non-balanced/gradient-spoiled (uSSFP) forms. In bSSFP, repeated flip angles with alternating sign are applied with zero net gradient across T_R. This has the effect of combining available FID signal from non-zero longitudinal magnetization as well as refocused components of the transverse magnetization. As such, the conventional steady-state bSSFP signal scales as $\sqrt{T_2/T_1}$.[32] If magnetization is sufficiently off-resonance so that the precession phase per T_R is π, the bSSFP signal is entirely nulled in the steady-state. This can produce banding artifacts on bSSFP images with

imperfect shimming or other sources of B_0 variation. Unbalanced SSFP relies on a gradient spoiling/crushing that introduces (generally) an integer number of phase cycles across a given imaging voxel. This crusher has the effect of nulling the signal for the next excitation, but this dephased magnetization me be later refocused. As discussed above, the RF action permits refocusing of the magnetization with conjugate phase. When a subsequent gradient crusher is applied to the dephased and conjugated magnetization, the magnetization is refocused and can contribute to signal. The uSSFP signal-to-noise ratio is generally reduced relative to that from bSSFP, but uSSFP does not suffer from banding artifacts. Depending on the magnitude of the crusher gradient, uSSFP sequences may experience diffusion weighting as the protons experience stochastic movements between excitations and have been subjected to dephasing gradients.

The SE sequence important for this work besides a basic Hahn echo technique, is a modified CPMG sequence. Under normal CPMG conditions, gradient crushers are used to suppress spurious signals from FID transverse components that contribute to the observed signal when $\alpha \neq 180°$. However, this does not prevent imperfect refocusing pulses from swapping magnetization from the transverse to the longitudinal direction and vice versa, like the GRE process of refocusing. These so-called stimulated echoes[9] decay by T_1 when they are in the longitudinal state, confounding T_2 estimation. Modulated gradient schemes for this have been formulated, which attempt to ensure stimulated echo contribution the signal is minimized. Key among these methods is the modified Poon-Henkelman approach, which utilizes a descending and alternating gradient strength so that stimulated echo coherent pathways cannot be easily refocused by subsequent crusher actions.[29] This violates the CPMG conditions, reducing the available signal for measurement, but drastically reduces the contributions from stimulated echoes so that T_2 estimated can be estimated from (demodulated) SE equation [Eq. (2.3)]. To reduce the imperfect refocusing sensitivity on B_{1+}, numerically optimized composite pulses can be used such as the Version S pulse,[28] which provides robust refocusing even with large deviations in B_{1+}.

2.2.2. Conventional image reconstruction in MRI

Beyond the simple Fourier relation between the signal domain and image domain, there are several modifications beyond basic clinical image reconstruction techniques pertinent to this work. These include non-uniform sampling, gridding, sample density compensation, and multi-coil image combination.

If the spatial-frequency domain (k-space) representation of a signal can be measured, using the (inverse) Fourier transform we can write the spatial domain signal, $s(\mathbf{r})$ as

$$s(\mathbf{r}) = \int_K s(\mathbf{k}) e^{i2\pi\mathbf{k}\cdot\mathbf{r}} d\mathbf{k}, \qquad [2.16]$$

where $\mathbf{r}$ denotes the spatial position, K is the region of support for the signal in the spatial frequency domain, and $\mathbf{k}$ is the spatial-frequency coordinate. The basis of MRI is to apply a magnetic field gradient in the magnetization with respect to the image encoding dimensions, $\mathbf{G} = \left[G_x, G_y, G_z\right]^{\mathrm{T}}$ ($G_r = \frac{\partial B_z}{\partial r}$), for some finite interval τ to measure the signal at $\mathbf{k}$ given as

$$\mathbf{k} = \frac{\gamma}{2\pi} \int_0^\tau \mathbf{G}(t) dt. \qquad [2.17]$$

If $\mathbf{k}$ is uniformly discretized so that $\mathbf{k}(t) = n\Delta\mathbf{k}, n = 0, 1, 2, \dots, N - 1$, we can write the spatial domain signal as the (inverse) discrete Fourier transform of its discretized spatial frequency counterpart

$$s(\mathbf{r}) = \sum_n s[n] e^{i2\pi\mathbf{k}[n]\cdot\mathbf{r}}, \qquad [2.18]$$

where $s[n] = s(\mathbf{k}[n]) = s(n\Delta\mathbf{k})$. Due to this sampling, the field-of-view (FOV) of the image is replicated at a spatial period of $1/\Delta\mathbf{k}$ and the resolution of the image $\Delta\mathbf{r} = 1/(N\Delta\mathbf{k})$.

The discrete image reconstruction can be sped by using fast Fourier transform algorithms.[33] These relations are relatively straightforward to implement if the image is sampled on a Cartesian grid, but that is not the case in radial or spiral k-space acquisitions.

To accommodate non-uniform sampling in k-space non-uniform FFT (NUFFT) algorithms have been developed.[34,35] Type I NUFFTs transform non-uniform data to a uniform sampling domain, whereas Type II NUFFTs do the reverse. In Type I NUFFTs, the k-space data are interpolated onto an oversampled grid with correction factors and reconstructed using standard FFT, thus is often referred to as "gridding." The Type II NUFFT is relevant for iterative methods of image reconstruction, where a current estimate of the image data can be (forward) projected onto the non-uniform k-space. This permits a least-squares solution to the non-uniform sampling image reconstruction problems. While this method has some guaranteed optimality, it is generally slower than gridding.[35]

Gridding depends on sampled density compensation (SDC) and interpolation. SDC is the re-weighting of the non-uniformly sampled data because k-space is more densely sampled in some areas than others. Without SDC, the resulting gridded image will be weighted more heavily in lower or higher resolution components of the image, concordant with higher sampling density in, respectively, the center or periphery of k-space. While SDC can be calculated analytically for certain idealized trajectories,[2] it can also be calculated numerically[36] for arbitrary k-space sampling trajectories. The interpolation is generally performed by convolution of the sampled k-space data with a Kaiser-Bessel function.[37]

In both Cartesian and non-uniform k-space sampling, multiple sets of data are often simultaneously acquired with several coils. To combine multi-coil data in the image domain for fully sampled data, a matched filter approach is optimal[38] for combining coils and methods for estimating coil sensitivities have been found[39]. Recent advances in coil combination permit calculation of the sensitivity maps from a calibration region in the acquired data.[40]

Spiral k-space trajectories are non-uniform trajectories that alter several aspects of reconstruction relative to conventional Cartesian sampling. The simplest of the spirals is the Archimedean spiral, which has uniform separation of its arms in k-space.[41] However, the design of spiral trajectories can be limited by maximum gradient amplitudes and slew

rates, supporting the development[42] of numerically calculated trajectories. This permits the calculation of variable density spirals, which can alter the spacing between adjacent arms. The efficiency of spirals as measured by SNR per unit time are improved relative to Cartesian sampling by avoiding acquisition of the corners of k-space and by center-out sampling.

2.3 Background on MRI Fat Quantitation

This section outlines models and methods for imaging triglycerides (i.e. fat) with conventional MRI. Early as well more recent methods for fitting for fat, water, and ΔB_0 are discussed.

2.3.1 An MR signal model for triglycerides

Electronic shielding of the proton studied in an MR experiment can introduce a chemical shift σ_s such that the magnetic field experienced by the nucleus $\widetilde{B_0}$ is given as

$$\widetilde{B_0} = B_0(1 - \sigma_s). \qquad [2.19]$$

This is particularly relevant to MR imageable triglycerides, which contain several moieties that have different chemical shifts, detailed in Table 2.1 adapted from Refs [43] and [44]. This table details the chemical shift of different protons from MR imageable triglycerides with the measured signal fraction, corrected for T_2, from murine gonadal white adipose tissue. Rows of different moieties have been combined when the peak intensity estimates were not separated in analysis.

Table 2.1 Chemical shifts and relative weightings in white adipose tissue.

δ (ppm)[1]	Name of moiety	Relative abundance in rodent white adipose tissue
0.9	Methyl	0.09
1.3	Bulk methylene	0.62
1.59	Methylene β to carbonyl	
2.03	Allylic methylene	0.15
2.25	Methylene α to carbonyl	
2.77	Diallylic methylene	0.02
4.1	Glycerol methylene	0.04
4.3	Glycerol methylene	
5.21	Glycerol methine	-
5.31	Olefinic methine	0.08

[1] Parts per million relative to tetramethylsilane.

While there are variations in the relative weights of the different moieties in triglycerides throughout the human body, these variations are relatively small between subcutaneous and visceral adipose tissue[45]. The deviation between fatty acid composition in white adipose tissue and brown adipose tissue is also thought to be small.[46] Unlike water, the T_1 relaxation of bulk methylene from white adipose tissue is generally thought to be constant throughout the body, which is important for certain forms of conventional fat suppression in MRI[47]. While there is some *in vitro* evidence that this may not be the case,[48] *ex vivo* evidence suggests that T_1 and T_2 of the different triglyceride moieties are relatively constant through different adipose tissue types[44]. As such, in the MR context, triglycerides that compose MR imageable fat are often treated as uniform composition throughout the body (see also Chapter 9).

The signal from water, $s_w(t)$, and fat, $s_f(t)$, as a function of time can be given as

$$s(t) = s_w(t) + s_f(t) = C\left((1 - \eta) + \eta \sum_{p=1}^{p=P} a_p e^{i2\pi f_p t}\right), \qquad [2.20]$$

where C is scaling constant that depends on the magnetization density as well as properties of the MRI hardware and acquisition setup, η is the fat signal fraction (FSF), $\{a_p\}$ is the set of relative weights of the fat moiety (i.e. the third column of Table 2.1) at the given chemical shift frequency $f_p = (\delta - \delta_{ref}) \cdot 10^{-6} \cdot f_0$ with f_0 the Larmor frequency, and relaxation is neglected. Commonly, the MRI signal is demodulated around the resonance frequency of free water $\delta_{ref} \approx 4.65$ ppm. Any phase offset in Eq. (2.20) is neglected for simplicity. The number of peaks, P, used to model the fat signal varies widely between different fat fitting algorithms, with one peak commonly being used to characterize the bulk methylene alone, up to six or more peaks, as seen in Table 2.1. It is known that monospectral fat models can bias estimation of fat fraction.[49] While often not directly considered in fat-water MRI, there is a close agreement between FSF and the fat mass fraction[50].

2.3.2 Confounding factors in the triglyceride signal model

The model given by Eq. (2.20) assumes a uniform B_0 field that is shimmed to δ_{ref} and does not consider susceptibility effects that may further distort the static field. Other complications to this model include T_1 effects and, potentially, J-coupling.

If a conventional MRI fat measurement relies on a sequence that spoils the remaining transverse magnetization at the end of T_R (see also §2.2), then a signal model for water and fat that consider shifts in the B_0-field as well dephasing effects due to

susceptibility variations at length scales smaller than the macroscale B_0 shifts can be given as

$$s(t) = C\left((1-\eta) + \eta \sum_{p=1}^{p=P} a_p e^{i2\pi f_p t}\right) e^{(i2\pi\Delta B_0 t - t/T_2^*)}. \qquad [2.21]$$

The first term within the last exponent accounts for phase offset as a function of time from ΔB_0, and the second term accounts for intra-voxel phase dispersion through the inclusion of T_2^*. Such complications to the model can substantially affect the estimate of FSF. For instance, if $\Delta B_0 \approx -430$ Hz at field strength of 3 T, one may find that water and the bulk methylene peak are swapped, depending on acquisition parameters and fitting approaches. However, estimating ΔB_0 may be equivalently confounded by the presence of fat. As discussed in §2.3.3, some effort in fat-water imaging is spent attempting to unravel this problem.

Relaxometry effects and J-coupling can also confound the signal model. As discussed in §2.1.2 water T_1 may vary substantially over the body, whereas the T_1 of fat is thought to be relatively fixed. During a short T_R sequence with repeated nutation angles and RF spoiling, the equilibrium signal will be T_1 dependent (Eq. 2.15). If the water and fat T_1 are not equal, the FSF will be biased depending nutation angle.[51,52] Imaging at a low nutation angle ($\leq 5°$) will often substantially mitigate this effect. J-coupling is the modulation of the proton resonance frequency mediated by electrons in through-bond interactions within the fat molecule. A number of different fat peaks experience J-coupling effects,[53] which can reduce signal[54] as the coupled protons in fat move in and out of phase with one another. While modeling for simple coupled systems[55] exist, empirical approaches[56] for J-coupling have also been employed.

2.3.3 Conventional and recent methods for MRI fat-water separation

Early MRI methods which used two images at different echo times to capture signal interference between the water signal and that of the bulk methylene for fat (two-point

22

method) have given way to techniques that acquire many images at different echo times and fit for B_0 and T_2^*. As such, fat-water post processing techniques have developed from simple image arithmetic to advanced discrete optimization techniques.

The foundation for much fat-water MRI is the Dixon technique[57]. In this approach,[58] Eq. (2.20) is used with a single peak of bulk methylene representing fat, and observations made at T_Es where water is entirely in-phase with fat ($T_{E,IP} = n/f_p, n = 0$, or 1, or 2, ...) and opposite phase with fat ($T_{E,OP} = n/f_p/2$, n = 1, or 3, ...). If we represent these two images as I_{IP} and I_{OP}, respectively, the estimate for the water image, W, and fat image, F, can be given as

$$W = \frac{I_{IP} + I_{OP}}{2} \qquad [2.22]$$

and

$$F = \frac{I_{IP} - I_{OP}}{2}. \qquad [2.23]$$

However, this neglects the other fat peaks and B_0 effects as we can see in Eqs. (2.20-21), which will bias these W and F estimates. More sophisticated three-point Dixon methods[59] have seen widespread use which image at different T_Es outside of in-phase and opposed-phase that permit estimation of B_0 effects. These methods have given way to a more general non-linear signal model for fat-water imaging.

If we observe at a set of N different T_Es, the image signal $\mathbf{s}$ at location $\mathbf{r}$ can be given as

$$\mathbf{s}(\mathbf{r}; T_E) = J \begin{bmatrix} s_w(T_{E,1}) & s_f(T_{E,1}) \\ s_w(T_{E,2}) & s_f(T_{E,2}) \\ \vdots & \vdots \\ s_w(T_{E,N}) & s_f(T_{E,N}) \end{bmatrix} \begin{bmatrix} W(\mathbf{r}) \\ F(\mathbf{r}) \end{bmatrix} \qquad [2.24],$$

where J is a diagonal matrix with entries $J_{n,n} = e^{iT_{\text{E},n}(2\pi\Delta B_0 - 1/T_2^*)}$, and s_{w} and s_{f} are the water and fat signal models. If ΔB_0 and T_2^* can be neglected, then the fat and water components can be estimated by linear regression using the Moore-Penrose pseudoinverse

$$\begin{bmatrix} \widehat{W} \\ \widehat{F} \end{bmatrix} = (A^H A)^{-1} A^H \mathbf{s} = A^\dagger \mathbf{s}, \qquad [2.25]$$

where A is the matrix composed of the water and fat signal model vectors, $\mathbf{s}_{\text{w}}$ and $\mathbf{s}_{\text{f}}$, and A^H is the conjugate transpose of A. However, with J not equal to the identity matrix, Eq. (2.24) is non-linear and requires iterative methods, such as Reeder *et al.*'s IDEAL technique,[60] or can be approached using variable projection.

Variable projection[61,62] operates on separable equations such as Eq. (2.24) where the linear aspects of the function ($A\mathbf{s}$) is separated form the non-linear portion ($J = f(\Delta B_0, T_2^*)$). Without loss of generality, we neglect T_2^*. If the values of the nonlinear parameter, ΔB_0, is known,

$$\mathbf{s} - \widetilde{A}\widetilde{A}^\dagger \mathbf{s} = \mathbf{0}, \quad [2.26]$$

where $\widetilde{A} = J(\Delta B_0)A$. This invites a least squares solution that depends only on the non-linear parameters:

$$\widehat{\Delta B_0} = \arg_{\Delta B_0} \min \left\| |\mathbf{R}| \right\|_2^2 \qquad [2.27]$$

with

$$\mathbf{R} = \left[I - \widetilde{A}\widetilde{A}^\dagger \right]\mathbf{s}. \qquad [2.28]$$

This formulation is dependent on a single variable, ΔB_0, and can be solved more readily than the problem with a higher number of variables. It has been adopted in a number of

different formulations of fat-water separation problem[43,62,63], including discrete optimization methods for solving for ΔB_0[64,65].

2.4 Background on MR Fingerprinting

This section presents an introduction to MRF and recent developments in this recently published technique. Balanced and unbalanced SSFP MRF sequences and their advantages and disadvantages are discussed. Modeling and compression techniques are presented, as well as optimization techniques and different MRF applications.

2.4.1 Relaxometry with high undersampling

The original MRF technique, developed at Case-Western by Dan Ma in the lab of Mark Griswold,[66] was based up on an inversion prepared bSSFP technique with a spiral k-space trajectory. Instead of fixed sequence parameters, flip angle and repetition times were varied in a pseudo-random pattern. And rather than try to capture all the necessary spiral interleaves at a constant signal to reconstruct an image, the contrast was permitted to vary each excitation. Only a single spiral interleaf is acquired each excitation before a different flip angle with a different T_R were then acquired. That is, the MRF signal exists in a transient state and is sampled in a highly undersampled way. Separate from the image acquisition, MRF used a series of discrete signal models (atoms)—parameterized by T_1, T_2, and ΔB_0—using a single isochromat Bloch simulation and normalized to unity. Aliased images were reconstructed for each excitation and then fit for T_1, T_2, and ΔB_0 by performing an inner product between each voxel's signal and all atoms of the dictionary. The best match was defined as the entry with maximum magnitude of the inner product. This dictionary of signals (or "fingerprints") highly constrains the possible fits for the signals, so that, despite the large amount of aliasing in the image, the correct parameter combination can be estimated at the given voxel. This assumes that the aliasing is essentially incoherent with the signal.

This bSSFP MRF technique permitted accurate relaxometry compared with conventional methods in a fraction of the time. Ma *et al*. compared their MRF estimates of T_1 and T_2 in a gadolinium-doped agarose phantom against conventional estimates from

saturation recovery and spin-echo measurements, as well as with DESPOT1/2. They found concordance correlation coefficients of MRF exceeded 0.970 for T_1 and T_2, and these concordances exceeded those from DESPOT1/2. The acquisition efficiency of T_1 and T_2 estimation, measured as the respective parameter estimate relative to the estimated noise in the parameter divided by the square root of the sequence time, was superior in MRF relative to DESPOT1/2. The scan duration of the MRF sequence was 12 s. *In vivo* brain T_1 and T_2 estimates were consistent with those from the literature.

Perhaps the most striking aspect of MRF is its ability to estimate parameters despite the large degree of aliasing noise. The bSSFP MRF technique reportedly used an undersampling factor of 48. However, the reconstructed magnetization density (and other parameter) maps showed little evidence of aliasing.

Despite the promise of fast relaxometry bSSFP MRF, there are some drawbacks to the sequence. Like its conventional version, bSSFP MRF is not immune to banding artifacts and integer multiples of off-resonance frequency $1/T_\mathrm{R}$ from $1/T_\mathrm{R}/2$. Also, the bSSFP MRF sequence is generally sensitive to ΔB_0, which may be advantageous if this is a parameter of interest, but in many cases, it is merely a nuisance parameter. The MRF signal dependence on the off-resonance likely limits bSSFP MRF's compressibility (see also §2.4.3).

2.4.2 Unbalanced SSFP MRF

To evade banding artifacts an unbalanced SSFP (uSSFP) MRF technique was developed[67] (also known as the non-vendor neutral fast-imaging with steady state precession {FISP} MRF). This sequence relies on an integer 2π gradient spoiling per nominal slice thickness in the slice select direction on top of the pseudo-random variation in α and T_R. As discussed in §2.1, the inclusion of the unbalanced gradient crusher generates coherent states that can be later refocused. Since these states are well characterized by many isochromats of different phase, the single isochromat Bloch simulation used for bSSFP MRF would not work as a model. Instead these states can be modeled using an extended phase graph (EPG) approach (§2.4.3). Like bSSFP MRF, uSSFP MRF permits T_1 and T_2 estimation concordant with conventional relaxometry techniques with large

undersampling factors. The lower SNR of the uSSFP sequence reduces the acquisition efficiency relative to the bSSFP approach, the cost of eliminating the banding artifacts.

Unbalanced SSFP was able to achieve high undersampling with seeming immunity to ΔB_0. The initial work on uSSFP MRF showed that T_1 and T_2 were roughly consistent despite substantial deviations in ΔB_0. The gradient crushing of the FID at the end of each T_R and variable T_R apparently reduced the sensitivity of the sequence on off-resonance effects relative to bSSFP MRF. However, the images and parameter maps generated from these poorly shimmed cases were not presented.

Variations of uSSFP have been employed in cardiac and volumetric imaging. For myocardial imaging, Hamilton *et al.*[68] customized the dictionary according to the subject-specific ECG trigger delays used during the MRF acquisition in order to estimate T_1 and T_2. Brain volumetric imaging[69] has been achieved by cycling through Cartesian slice encoding gradients in an undersampled and periodic fashion, as opposed to the spiral sampling for in-plane imaging. Intriguingly, the brain T_2 values in this study are over 10 ms lower than those typically reported from FSE measurements, but the MRF T_2 values have excellent agreement with those from conventional methods in an MRI system phantom with calibrated relaxometry contrast spheres.

2.4.3 MRF signal modeling, the extended phase graph formalism, and compressibility

The original bSSFP MRF manuscript[66] used the Bloch equations to model the signal response in their slice-selective sequence. Since any kind of phase dispersion of the magnetization within an imaging voxel was not considered, it was possible to model each dictionary element using a single isochromat. As such, this work used an idealized RF pulse response with the nominal flip angle that assumed a perfectly rectangular slice profile whose response is given by Eq. (2.12). Signal decay can be modeled using Eqs. (2.3-4). Including ΔB_0, over 500,000 dictionary atoms were created for the 1000 excitation sequence. In the case of uSSFP MRF, the unbalanced gradient causes a phase dispersion that may significantly slow a conventional Bloch simulation for MRF dictionary generation.

Unbalanced SSFP is more readily modeled with extended phase graphs (EPG)[31]. The EPG formalism describes how to operate excitation, relaxation, and gradient action in the

through-slice spatial frequency (k_z) domain, as opposed to the spatial domain approach of a conventional Bloch simulation. If a fixed crusher strength is used in the through-slice direction and causes integer 2π dephasing over the slice thickness, then, by the Fourier shift theorem, the phase dispersion can be modeled by a simple shift of the transverse magnetization k-space position (denoted by a shift operator S). Instead of using many isochromats to represent this phase dispersion, only a single k-space state must be non-zero valued to represent this operation. This makes it advantageous to use EPG in the uSSFP context over a Bloch simulation.

The EPG operators that describe the action of an idealized RF pulse and relaxation can be analytically determined. The RF transition operator is the same as Eq. (2.12), so that the EPG operation of RF in k-space, following the nomenclature of Weigel[31], is

$$
\mathbf{F}^+ = \begin{pmatrix} \cos^2\left(\frac{\alpha}{2}\right) & e^{2i\phi}\sin^2\left(\frac{\alpha}{2}\right) & -ie^{i\phi}\sin(\alpha) \\ e^{-2i\phi}\sin^2\left(\frac{\alpha}{2}\right) & \cos^2\left(\frac{\alpha}{2}\right) & ie^{-i\phi}\sin(\alpha) \\ -\frac{i}{2}e^{-i\phi}\sin(\alpha) & \frac{i}{2}e^{i\phi}\sin(\alpha) & \cos(\alpha) \end{pmatrix} \mathbf{F}^- = \mathrm{T}(\alpha)\mathbf{F}^- \qquad [2.29]
$$

where $\mathbf{F}^\pm = \mathcal{F}\{[M_+^\pm \ M_-^\pm M_z^\pm]^T\} = [F_+^\pm \ F_-^\pm \ F_z^\pm]^T$. The state matrix is the discrete Fourier transform of the through-slice direction, evaluated at $k = n\Delta k$, for $n = 0, 1, 2, ...$, rearranged into a matrix $\Omega(k) \in \mathbb{C}^{3xQ}$. The spacing in k-space, Δk, is generally given as $N_{\mathrm{crush}}/\Delta_{\mathrm{sl}}$, with N_{crush} the number of cycles per nominal slice thickness Δ_{sl}. The relationship between $F_+(n\Delta k) = F_+[n]$ and Ω is

$$
F_+[\mathrm{n}] = \begin{cases} \Omega^*[2, -n], & \text{for } 1 \le -n \le Q - 1 \\ \Omega[1, n], & \text{for } 0 \le n \le Q - 2 \end{cases} \qquad [2.30].
$$

The consequence of this discretization is that the shift operator, S, shifts the first row of Ω by a single index and shifts the second row in the opposite direction.

Transverse relaxation occurs only on the first two rows, longitudinal relaxation acts on the third row. The 3 x 3 matrix is

$$E = \text{diag}\{e^{-\frac{\tau}{T_2}}, e^{-\frac{\tau}{T_2}}, e^{-\frac{\tau}{T_1}}\}, \qquad [2.31]$$

for some time interval τ, and the relaxation operation can be given as

$$\Omega^+ = E\Omega^- + \left[0 \; 0 \; F_{z,0}\left(1 - e^{-\frac{\tau}{T_1}}\right)\right]^{\mathrm{T}} \tilde{\mathbf{I}}. \qquad [2.32]$$

The vector $\tilde{\mathbf{I}}$ denotes unity followed by $Q - 1$ zeroes. Putting the above together, EPG models excitation by Eq. (2.29), relaxation by Eqs. (2.31-32) and gradient crushing by the shift operator S.

The compressibility of MRF dictionaries can be evaluated and exploited using singular value decomposition (SVD). McGivney et al.[70] studied bSSFP and uSSFP MRF dictionary compression in the time domain with SVD. Paraphrasing this group's results, a dictionary $D \in \mathbb{C}^{N \times M}$ with N excitations and M atoms ($M > N$), using SVD, can be written as

$$D = USV^{\mathrm{H}} \qquad [2.33]$$

Where U, S, and V are the left singular vectors, diagonal matrix of singular values, and right singular vectors, respectively. The truncated SVD, composed of the first R columns/diagonal elements of the matrix of singular vectors/values is approximately equal to D,

$$D \approx U_R S_R V_R^{\mathrm{H}}. \qquad [2.34]$$

The accuracy of this low rank, R, approximation to D can be characterized by the energy of the elements of $S = \text{diag}(\sigma_i)$ such that the fractional energy

$$\epsilon(R) = \frac{\sum_{r=1}^{r=R} \sigma_r^2}{\sum_{r=1}^{r=N} \sigma_r^2}. \qquad [2.35]$$

The solution to the dictionary match problem for a signal vector $\mathbf{s}$ and parameters specified in the vector $\boldsymbol{\theta}$ is given as

$$\hat{\boldsymbol{\theta}} = \arg_j\max|\mathbf{s}^H\mathbf{d}_j| \qquad [2.36]$$

where $\mathbf{d}_j$ is the jth column (atom) of D. Since the truncated set of left singular vectors contain an orthonormal basis that nearly spans the space of dictionary and signal, $\mathbf{s}$ and D can be projected onto the left-singular vectors and then represented in Eq. (2.36) as follows,

$$|\mathbf{s}^H\mathbf{d}_j| \approx |(U_R U_R^H \mathbf{s})^H(U_R U_R^H \mathbf{d}_j)| \approx |\mathbf{s}^H U_R U_R^H \mathbf{d}_j| \qquad [2.37].$$

As R increases, $\epsilon \rightarrow 1$, and Eq. (2.37) is increasingly accurate. McGivney et $al.$ showed that for uSSFP MRF, that R can be as few as 10 and still capture a basis that nearly spans the space of the signals in D. It is important to note that this compressibility is sequence dependent, as well as the parameter space considered. A smaller sub-space of parameters may require still a lower rank for the same relative accuracy. Conversely, parameter specific modulations will tend to increase the rank. The bSSFP MRF dictionary required $R > 200$ elements to reach a nearly full representation of its dictionary, presumably due to the addition and interplay of ΔB_0 with T_1 and T_2. This compressibility can be exploited to speed dictionary matching, by reducing the inner product search from scalar $\sim N \times M$ multiplications to $\sim R \times M$ multiplications (once the dictionary and signal have been

compressed). This compressibility combined with dictionary modeling helps to clarify MRF as subset of low-rank model-based reconstruction techniques.

2.4.4 Optimization of MRF sequences

Several approaches have been taken to optimize MRF sequences. These techniques generally take a conventional approach by considering the aliasing to be normally distributed, or they use a heuristic to model the effects from undersampling. While these techniques may succeed in special cases, none of them provide a complete description of the noise propagation.

If the aliasing noise were normally distributed, then improving parameter estimation quality could be accomplished by increasing the orthogonality between dictionary entries through variation of the α and T_R schedule. To this end, Cohen *et al.*[71] tested a series of optimization algorithms on an objective function that penalizes non-zero inner products of two different dictionary atoms. On the other hand, Zhao *et al.*[72] used a Cramer-Rao lower bound estimation[73] calculation to optimize an MRF sequence. Both studies indicated T_2 accuracy could be substantially improved by optimization, compared to arbitrary sequence properties. However, outside of special situations, the aliasing in a given location will correlate with the unaliased signal, so is not normally distributed and may not be accurately modeled by conventional optimization approaches.

To address the non-normal distribution of the aliasing about the signal Sommer *et al.*[74] modeled the aliasing contribution as a non-stationary phenomenon that scales with MRF signal. This heuristic approach combined with optimization of the parameter estimation bias, demonstrated improved T_1 and T_2 estimation using MRF sequences with improved optimization scores relative to sequences with worse bias. Very recently, a more complete theoretical description of the bias propagation from aliasing in MRF has been made, permitting the authors to model relaxometry bias from aliasing that is comparable to measured results.[75]

2.4.6 MRF extensions beyond relaxometry

While the initial implementations of the MRF largely focused on T_1 and T_2 estimation, the general framework of MRF has shown to be applicable to several contrast mechanisms. These include perfusion, chemical exchange and magnetization transfer, diffusion, as well as fat signal fraction. A thorough review of these is beyond the scope of this introduction and has also been recently been reviewed elsewhere[76]. Instead, select MRF studies pertinent to this work as well as particular aspects are noted.

Quickly following the debut of MRF, it was proposed to estimate cerebral blood volume, mean vessel radius, and blood oxygen saturation using an MRF approach with a gradient-spin echo sequence[77]. In this vascular MRF (vMRF) technique, images were not undersampled and a conventional sequence was used. In a similar vein, another group estimated the same parameters in mice,[78] but using a more realistic model of the vasculature. Arterial spin labeling MRF has also been demonstrated[79] using pseudorandom labelling delays. In common to all these studies is the lack of undersampling and, to some degree, the use of conventional sequences. This points out the vagueness in what constitutes MR fingerprinting. While the vMRF approaches may model and fit signals like MRF, as well as estimate multiple parameters from the data, the similarities between the two techniques seem to end there. The legal protections granted MRF intellectual property notably require some variability in the sequence parameters in a non-conventional way. However, the precise boundaries of the definition of MRF are not necessary for this work moving forward.

Chemical exchange and magnetization transfer have been modeled with MRF sequences. While the Bloch-McConnell equations permit modeling of magnetization transfer effects, most effort in MRF has been given to modeling chemical exchange effects[80,81]. However, Malik *et al*. added to the EPG formalism to permit modeling of MT effects[82] in SSFP sequences, including MRF sequences.

The diffusion sensitivity of uSSFP MRF due to its crusher gradients has been studied.[83] This work indicated that long T_2 tissues with high gradient moments could experience substantial bias, but for many tissues at gradient moments $< 40\,\mathrm{mT} \cdot \mathrm{ms/m}$,

the bias from diffusion is relatively small. These biases will presumably be somewhat sequence dependent.

Fat quantitation in MRF prior to that presented in this work and those contemporaneously published (further detailed in Chapter 6) generally considered adipose tissue without partial volume effects, i.e. without considering voxels with both fat and water. In the earliest MRF works,[66,67] fat was modeled by its bulk methylene off-resonance and characteristic relaxometry values. Adipose tissue relaxometry values were measured in an early abdominal uSSFP work at 3 T, finding a T_1 and T_2 of 253 and 77 ms, respectively.[84]

2.5 Conclusions

The preceding chapters have provided a basis for the MRI and MRF developments and conventional measurements later discussed in this work. The original MRF developments noted above will be synthesized with the forthcoming (Chapter 3) introduction to nonalcoholic fatty liver in Chapter 4, which will discuss the potential role and challenges of MRF in liver imaging.

Chapter 3

BACKGROUND ON FATTY LIVER DISEASE AND ITS NON-INVASIVE IMAGING ASSESSMENT

3.1 Nonalcoholic Fatty Liver Disease

This section briefly reviews clinical features of nonalcoholic fatty liver disease (NAFLD). This includes its definition and sub-types, prevalence, and summaries of what is known about its etiology, prognosis, and treatment.

3.1.1 Characteristics of NAFLD

Nonalcoholic fatty liver disease, like the name suggests, is the ectopic deposition of fat in the liver in the absence of alcohol abuse. NAFLD encompasses a spectrum of pathological traits including steatosis and inflammation that may lead to hepatic fibrosis.[85] Historically, it has been overlooked, but has become an increasing health concern due to its high prevalence and relationship with fibrosis.

The NAFLD spectrum ranges from the excess storage of fat in the liver, nonalcoholic fatty liver (NAFL), to an inflammatory state that eventually progresses to fibrosis, nonalcoholic steatohepatitis (NASH). Both conditions are excluded by the presence of another hepatic disease/etiological source such alcohol abuse or Wilson's disease.[86] An hepatic fat fraction of >5% is considered abnormal, and is part of the basis of diagnosis of NAFL. NASH currently can only be confirmed by liver biopsy[87] and is characterized by hepatocellular ballooning degeneration and inflammatory activity, typically near the lobule central venule (acinar zone 3)[88]. Persistent inflammation can ultimately lead to development of fibrosis, impaired liver function, and eventually frank cirrhosis. There is no precise histological staging system for NAFLD/NASH, but several have been proposed.[89] The histological grading spans three or four stages from steatosis with mild inflammation to pervasive inflammation and ballooning degeneration[90–92]. While the National Institute of Diabetes and Digestive and Kidney Diseases has established the NASH Clinical Research Network NAFLD activity score (NAS)[93] to improve quantitation of NASH histology, this is

currently not the standard of care and is weighted more heavily in steatosis than inflammation[89].

While the presence of fibrosis is not required for the diagnosis of NASH, it is the most clinically relevant endpoint because of the relationship between fibrosis and liver function. Staging of NAFLD fibrosis is generally broken into five ordinal intervals from 0, 1, ..., 4.[91,94] These range from no fibrosis (0), zone 3/peri-sinusoidal fibrosis (1), zone 3 and portal fibrosis (2), bridging fibrosis between central venule and portal triad (3), to frank cirrhosis (4). As fibrosis advances, cirrhotic nodules form, and normal liver function is compromised, increasing risk of liver failure. Increased resistance to blood flow from hepatic stiffness can lead to portal hypertension and development of compensatory esophageal venous dilation called varices, which can be life-threatening, as well as extra-hepatic collection of proteinaceous fluids called ascites. The necrosing fibrotic milieu becomes conducive to development of hepatocellular carcinoma.[95]

NASH has only recently been delineated and its prevalence is increasing over time. It wasn't identified as its own disease until 1980.[96] Previously, its advanced stage presumably fell into the category of cryptogenic cirrhosis. The recent delineation of NASH as its own pathology may in part due to the rise in its prevalence. From a study period of 1988-1994 to 2005-2008, the prevalence of NAFLD increased by about twofold.[97] However, this depended on evaluation of serum blood markers for liver disease and may have undercounted NAFLD prevalence in either period. In a 2004 study of over >3,000 subjects from the Dallas area using magnetic resonance spectroscopy to define fat fraction, abnormal steatosis of the liver was found to be those subjects with >5.5% fat signal relative to water signal with an estimated prevalence of 34%.[98] Currently, it is estimated that approximately 30% of people in the United States may have NAFL, which is a similar prevalence to many other countries.[99] The prevalence may vary over ethnic group[100] and is generally high in obese populations[101]. The presence of NAFL and NASH are often correlated with diabetes mellitus[101] and metabolic syndrome[102]. The prevalence of NASH is only a fraction of those with NAFL, but is generally estimated to be ~3% of the general population in the United States[103] and may be much higher among some sub-populations[100].

35

3.1.2 Pathogenesis of NAFLD

The pathogenesis of NAFLD is not entirely understood, neither is the precise relationship between NAFL and NASH.[104,105] However, several general biological processes related to insulin resistance, lipotoxicity, and genetic factors have been shown to be important for development of fatty liver and steatohepatitis.

The accumulation of excess fat within hepatocytes is a result of an imbalance in the production of triglycerides and storage of free fatty acids (FFAs). In NAFLD subjects, approximately 60%, 25%, and 15% of accumulated triglycerides in NAFLD hepatocytes come from circulating FFAs, de novo lipogenesis, and diet, respectively.[106] It is not clear whether the elevation of serum FFAs is a product of (or even associated with) insulin resistance, or whether high serum FFA concentration is from adipose tissue dysfunction separate from insulin resistance.[107] Storage of FFAs in hepatocytes occurs after their esterification into neutral tri(acyl)glycerides (TGs) in macrovesicular lipid droplets surrounded by phospholipid monolayers that may exceed several μm in size.[108] These fatty acid chains can be broken into constitutive parts for energy production by the process of β-oxidization. TGs can also be exported to peripheral adipose tissue via very low-density lipoproteins (VLDLs). The presence of serum insulin upregulates transcription factors that promote liver lipogenesis[108,109] and attenuates breakdown of stored TGs[104]. In insulin resistant subjects, it follows that the chronic elevated levels of insulin may encourage overproduction of TGs through lipogenesis. Export of FFAs may be impaired or otherwise cannot keep pace with FFA production, causing hepatocytes to store the excess fat in lipid droplets.[109] As such, the accumulation of TG in hepatocytes may be considered a marker of underlying metabolic dysregulation rather than an etiological source of pathology.[110] The FFAs are known to have lipotoxic effects via the promotion of cytokines associated with inflammatory response in hepatic stellate cells.[105,110,111] Qualitative signaling models exist that explain a link between elevated serum FFA from adipocytes and hepatocellular injury.[110] Excess FFAs may also contribute to development of reactive oxygen species that stress the endoplasmic reticulum and hepatocyte mitochondria.[105,110] These pro-inflammatory events may be a foundation for the development of NASH.

Chronically inflamed liver cells may trigger a cascading reaction that results in the development of fibrosis. Repeated insults to hepatocytes result in cellular structural defects that appear as Mallory-Denk bodies and in apoptotic cell death via hepatocellular ballooning,[112] both of which appear as histological markers of NASH. Hepatic stellate cells (HSCs), which reside in the space of Disse, are thought to be activated by this prolonged cellular injury.[113,114] This activation causes HSCs to deposit extracellular matrix[115], in the form of fibrosis along the sinusoidal region[112]. The postprandial portal hypertension observed in subjects with late stage fibrosis[116] is presumably caused by the decreased capacity for vessel expansion during digestion. Progressive fibrosis leads to thick cirrhotic septa that surround regenerative nodules.[117]

The mechanisms by which hepatic steatosis forms and progresses to inflammatory response becomes pathological are thought to have sources beyond metabolism. Single nuclide polymorphisms associated with PNLP3 and other genes have been identified as being related to dysfunction of lipid metabolism in steatohepatitis and fibrosis.[108] While some of these associations have been repeatedly found to be associated with patients with NAFLD, these mutations in themselves are not sufficient to explain the presence or absence of NAFLD but likely interact with a host of other environmental and unknown genetic factors.[118]

3.1.3 Prognosis of NAFLD

Those with NAFLD are at higher risk of death by a factor of about 30%[119,120] than those without the disease. The stage of fibrosis is the largest determinant of this increased risk, whereas the relationship of NAFL or NASH without fibrosis remains uncertain.

It has been thought that the condition of NAFL alone generally is not a malignant condition, but other evidence makes this assumption controversial. As noted in §3.1.2 the role of TG accumulation in hepatocytes may be protective against FFA accumulation. As reviewed by Bertot and Adams,[121] studies of mortality risk in NAFL cohorts have shown a low excess mortality risk, but other studies have shown that about 25% of NAFL patients can transition to NASH with bridging fibrosis in less than 10 years. Their review[121] also outlines how the potential risk to patients with NAFL alone may also be revealed in the

fluidity of NAFL and NASH fibrosis changes with time using paired biopsies, with progression and regression rates of fibrosis stage of roughly 30% and 20%, respectively. It has been shown that there may be no difference in the proportion of NAFL and NASH subjects with fibrosis progression.[122]

The excess risk of mortality of those with NAFLD is largely determined by fibrosis. Ekstedt *et al*.[120] in a study of over 200 Swedish patients with biopsy-proven NAFLD followed for a mean of 26 years, found that those with fibrosis stage 3-4 had significantly higher overall mortality (hazard ratio > 3) than a reference population without NAFLD as well as higher disease specific mortality. Also of note in this study is that high NAS histology scores did not correlate with statistically significant higher mortality if fibrosis staging was low.

The complications of cirrhosis are multi-fold. Increased resistance to portal blood flow may result in increased pressure on the esophageal and gastric venous system. As noted above, the enlarged vessels, known as varices, may rupture and bleed, which is a life-threatening condition. Portal hypertension can encourage the formation of protein/albumin filled volumes outside of the liver known as ascites, which increases the risk of bacterial peritonitis. Those with advanced fibrosis and cirrhosis are at increased risk for the development of hepatocellular carcinoma,[120] which at the time of this writing has a five-year survival rate of 18.4% in the United States[123].

3.1.4 Treatment of NAFLD

The current treatments available for NAFL and NASH involve lifestyle changes as well as medications, but there are currently no FDA approved medications for NAFLD. The current guidance from the American Association for the Study of Liver Diseases[86] is that diet and possible medication with pioglitazone or vitamin E may benefit patients with NASH. Reduction of weight by $\geq$ 7% is thought to have a significant positive impact on NASH histological markers. The use of pioglitazone may be used with patients with or without type 2 diabetes whereas vitamin E may be used for nondiabetic patients. The use of pioglitazone is associated with weight gain and there may be an increased risked of prostate cancer for men taking an excess amount of vitamin E.

The concerns about safety of existing medications used for NAFLD have prompted the recent development of multiple other drugs, currently under Phase II and III trials.[124] As reviewed by Konerman et al.,[124] these new drugs, which broadly fall into the categories of modulators of hepatic metabolic and inflammatory pathways, are difficult to evaluate clinically because of the lack of non-invasive means to assess their effectiveness.

3.2 Diagnosis of NAFLD and Modality-Specific Strengths and Weaknesses

In this section, different methods for the diagnosis of NAFLD are discussed. The role of biopsy and blood tests are summarized. The role of non-invasive imaging methods of ultrasound, computed tomography, and MRI in NAFLD diagnosis and investigation are explored. The different modalities of MRI in chronic liver disease are given emphasis.

3.2.1 Histology and blood serum analysis

Histology is currently the only means to diagnose the hepatic necroinflammation that defines NASH.[87,112] The histological specimen is typically acquired percutaneously. The use of ultrasound image guidance reduces the risk of major complications, relative to blind biopsy.[125] Specimens are scored in a semi-quantitative grading on the presence and degree of steatosis, inflammatory infiltrates, Mallory-Denk bodies, and hepatocyte ballooning (as noted in §3.1.1). Using the Brunt system,[112] there are four fibrosis stages and three grades of NASH histology. The four stages closely match the consensus stages given in §3.1.1: (1) zone 3 perisinusoidal fibrosis, (2) stage (1) with portal fibrosis, (3) bridging fibrosis from the portal region to zone 3, and (4) cirrhosis. The three grades range from low to high steatosis and inflammation. While there is considerable variability in agreement amongst pathologists for scoring lobular inflammation and hepatocyte injury, the steatosis and fibrosis scoring are more consistent.[93] Despite these variabilities, this has historically been the only way to definitively diagnose NASH.

While histology is the gold standard for diagnosing NAFLD, it is not without its shortcomings. The biopsy procedure comes with a small risk of complications and substantial risk of pain,[125,126] making its use for longitudinal monitoring questionable. The biopsy core samples only a small fraction of the liver, so may be subject to sampling bias.

The repeatability of some biopsy metrics is variable,[127] making it difficult to accurately assess the sensitivity and specificity of any comparative diagnostic tests.

Blood serum analysis is routinely employed in the clinic to identify potential liver pathology. Composite scores of proteins related to liver pathology combined with other clinical metrics such as body mass index can be used to identify NAFLD patients with advanced fibrosis with area under the receiving operator curve (AUROC) of 0.85.[86] Recent advances in blood serum analysis tests show promise for identifying hepatocyte apoptosis, but markers of oxidative stress and inflammation specific to NASH have not advanced as far[87]. A particular challenge for any blood test for NASH is the potential non-specificity of the potential biomarker.

3.2.2 Medical imaging used in the diagnosis and investigation of NAFLD

3.2.2.1 Ultrasound and Computed Tomography of the liver

Ultrasound (US) is used clinically to diagnose steatosis as well as fibrosis. Brightness-mode US of the liver appear echogenic in fatty liver. In a large meta-analysis of US in the liver, AUROC for the diagnosis of steatosis has been reported to be 0.93 with an inter- and intra-rater reliability that varies from 0.44 to 1.0.[128] This is for a qualitative measure of steatosis. Recently, quantitative measures of hepatic steatosis with attenuation of amplitude mode US signal have been attempted, but there is substantial overlap in the attenuation metric between patients with and without steatosis.[129]

Fibrosis can be measured with US elastography using shear waves. Shear wave elastography measures mechanical properties of the liver based on a velocity measurement, which is then related to a stiffness metric. The generation of the shear waves can be done using longitudinal waves generated by mechanical external oscillation at low frequencies (~50 Hz), or by focused acoustic radiation, called acoustic radiation force impulse (ARFI). These technologies have success rates >90% and AUROCs > 0.82 for fibrosis stage $\geq$ 3.[130]

Challenges to US techniques include obesity and inflammation, which can confound measurements, as well the presence of ascites. Large body habitus can attenuate signal so

that is difficult to get a measure of steatosis or confound shear wave measurements. Inflamed tissue appears stiffer than normal tissue, which may bias estimates of stiffness due to fibrosis.[131] It is important that US have an acceptable acoustic window to probe the liver, which makes shadows from the ribs or pathology like ascites challenging in some cases.

Computed tomography (CT) can be used to detect hepatic steatosis. CT is sensitive to changes in the linear attenuation coefficient, which for soft tissue, scales closely with density. Since fat has a lower density than normal liver parenchyma, a fatty liver has lower Hounsfield units (the CT measure of linear attenuation) than surrounding organs. A liver that is less than 40 HU or more than 10 HU below the spleen is considered fatty.[132,133] Notably, CT is not sensitive to mild or low amounts of hepatic steatosis.[134]

3.2.2.2 Magnetic resonance imaging of NAFLD and chronic liver disease

3.2.2.2.i MR hepatic fat fraction imaging

Early work in MRI animal models of liver pathology had limited qualitative success in gauging steatosis from relaxometry, giving way to Dixon techniques. Stark *et al.*[135] estimated T_1 and T_2 in models of hepatitis and triglyceride accumulation. They found that the relaxometry parameters were more sensitive to changes in the tissue water environment than triglyceride accumulation, and estimations of fat fraction could not be made. Partly motivated by Stark *et al.*, Dixon[57] and an associated group[136] used the 2-point in-phase and opposed-phased MR images to estimate fat fraction in the liver in a 0.35 T magnet. These were the first works to quantify fat fraction *in vivo* in the human liver with an MRI technique. This set the foundation for a long history of studies using MRI in liver fat fraction estimation.

Improvements in fat fraction imaging in the liver have been made possible through accounting for confounding effects at higher field strengths. Building on Dixon's work, 3-point Dixon imaging[137] was used to correct for T_2^* effects. In this study, the inclusion of a another in-phase image, after the 2-point Dixon acquisition, to account for T_2^*, had only a maximum of 3% effect on the fat fraction estimate. Glover's development of 3-point Dixon

solution[138] and the subsequent development of IDEAL[60] permitted more accurate study of liver fat[139,140] by simultaneously estimating static field heterogeneities.

MRI fat fraction imaging for hepatic steatosis quantification is becoming the gold standard for non-invasive assessment of steatosis.[134] The hepatic proton density fat fraction has been shown to correlate with MR spectroscopy and quantitative histology estimates of fat fraction.[141] Current commercial MRI fat quantitation has also been shown to be reproducible across radiologists and different vendors.[142]

MRI-based fat fraction technology continues to advance and find greater clinical research utility. Increased echo time acquisitions have permitted characterization of triglycerides with MRI.[43] A study of 32 NAFLD subjects (12 with NAFL and 20 with NASH) incorporated fat fraction imaging, triglyceride characterization, as well as T_2^* and susceptibility estimates, found that saturated fat fraction was higher in NASH than in NAFL subjects.[143] Discrete optimization methods have improved simultaneous ΔB_0 fitting with fat-water separation.[64,65] The steady-state signal differences between fat and water, driven by their differing T_1s, can cause bias if not corrected in fat fraction estimates.[52] It has long been known that T_2^* can be a confounding factor in fat-water separation,[59] and recent methods[65] have been developed to robustly fit T_2^* with ΔB_0.

3.2.2.2.ii MR exogenous contrast imaging in the liver

Historically, gadolinium-, manganese-, and super-paramagnetic-iron-oxide- (SPIO) based contrast agents have found use in the liver for the detection and differentiation of solid tumors.[144] Chelates of gadolinium that remain in the extracellular space may provide information about vasculature and associated lesions. SPIOs are preferentially taken up by Kupffer cells, providing higher specificity of those agents to differentiate cancerous lesions, which more often devoid of these cells, from other lesions. A discontinued manganese-based contrast agent and a commercially available gadoxetic acid have shown specificity of uptake by hepatocytes, which can be useful for oncological radiology.[145]

Gadoxetic acid specificity for hepatocytes may have use in the study of NAFLD. Pre-clinical models of NAFLD have shown that contrast enhancement differs between steatosis alone and steatosis with fibrosis or inflammation.[146,147] Retrospective analysis of humans

with NAFL and NASH have also shown statistically significant differences in gadoxetic acid uptake between these groups.[148,149] Prospective studies on this have yet to be performed. Protocols involving gadoxetic acid in these studies required a 20 min delay between the injection of contrast and imaging during the hepatobiliary phase, which may prove burdensome to MRI facilities and patients if used on a large scale.

3.2.2.2.iii MRI elastography (MRE) in fibrotic liver

Like ultrasound, stiffness due to hepatic fibrosis can be monitored by transient shear-wave elastography of the liver using MRI. By placing an external oscillator on the subject, it is possible to induce mechanical oscillations that can be characterized by motion sensitive gradient moments using SE or GRE imaging.[150] From the phase information, shear wave velocity, shear modulus, and Young's modulus can be inferred. These tissue characterizations quantify the tissue stiffness.

MRE has seen extensive use in the fibrotic liver. In the context of NAFLD, histological fibrosis stages 3 and 4 are typically assessed with AUROCs > 0.90 using MRE.[151] The failure rate is reported to be 0-10%.[151]

MRE may be confounded by inflammation and is less sensitive to early fibrosis stages. Liver stiffness increases during hepatic inflammation[131] and MRE is likely sensitive to inflammation within NASH[152]. While this sensitivity may open MRE to have a greater role in NASH diagnosis[153], inflammation may confound MRE fibrosis measurements.

3.2.2.2.iv MRI relaxometry and magnetization transfer of chronic liver disease

The association of T_1 with hepatic fibrosis is longstanding, but the relationship between T_2 and fibrosis is less clear. By employing fat suppression techniques, it has been possible to estimate the T_1 of the MR visible water compartments of pathologic liver, but these estimates may be confounded by inflammation and other factors. Macromolecular pool fraction, as estimated by magnetization transfer, has also been used in the study of liver fibrosis.

In the early history of MRI, liver T_1 was known to be elevated in cirrhotic liver. The earliest report of *in vivo* human liver T_1 imaging was made in tandem with the first whole-

body human MRI system using imaging gradients[154] in Aberdeen, Scotland. The same group followed their technical development with a liver study of T_1 in 50 patients, 30 of which had established liver pathology.[155] A similar study followed in London.[156] Results from these early works at low fields (40-150 mT) found that cirrhotic liver had elevated T_1. Thomsen *et al.* later correlated elevated T_1 with biopsy proven cirrhosis.[157] However, it had already been noted at this point that T_1 alone (estimated at 80 mT) was not diagnostic for cirrhosis, even though it was generally elevated.[158] These earlier studies varied over field strength and did not have the means to compensate for respiratory motion or suppress fat, which has different T_1 than liver tissue at many field strengths.

More recent studies of in the pathological liver have found T_1 to be elevated in the presence of fibrosis. Using a respiratory-gated fat-suppressed echo-planar inversion-recovery spin-echo imaging sequence in a study of >100 subjects with chronic liver disease (mostly NAFLD), it was found that T_1 at 1.5 T was significantly higher in late stage (3-4) fibrosis, as evaluated by biopsy, than early stage (1-2).[159] Confounding factors in this study were inflammation and elevated iron that, respectively, raised and lowered T_1. This paralleled other studies at 1.5 T[160,161] that have also found T_1 elevated in cirrhotic livers relative to normal or early stage cirrhosis.

The behavior of T_2 in chronic liver disease remains unclear. Studies of cirrhosis in humans[160–162] and animal models[163] are conflicting: some studies show an increase in T_2 with fibrosis while others do not. However, of the human studies, two of these studies did not apparently control for fat content,[160,161] one did not monitor T_1,[162] and all of them had mixed etiologies in their study cohorts that included NAFLD. In a murine model of cholestatic cirrhosis induced by bile duct ligation, T_2 was more elevated than in a model of toxic cirrhosis induced by CCl_4 injection.[164] This pre-clinical study, which controlled for hepatic fat, suggests that T_2 provides some specificity for pathological mode.

Magnetization transfer effects of the fibrotic liver have been studied. Yarnykh *et al.*[165] estimated the macromolecular pool fraction (MPF) in 16 patients with viral hepatitis using an optimized SPGR-based two-point method. This group found that livers with significant biopsy-proven fibrosis had higher MPF than those with small amounts or no fibrosis, with the respective mean (and standard deviation {SD}) MPFs of the two cohorts

were 6.5% (SD 0.4%) and 5.9% (SD 0.3%). While these populations of differing liver fibrosis were separable with respect to MPF, the MPFs were very similar between the different fibrosis stages.

3.3 Conclusions

The label of NAFLD constitutes a spectrum of disease from NAFL to advanced NASH. Patients with NAFLD are at increased risk of mortality, especially at later stages of this disease spectrum. There is currently no reliable non-invasive method for monitoring disease progression at the early end of this disease spectrum, but MRI offers several possible metrics that may be sensitive to several stages of NAFLD progression. The next chapter will explore the motivation for advancing MRI techniques to study pathological liver.

Chapter 4

POTENTIAL FOR APPLICATION OF MAGNETIC RESONANCE FINGERPRINTING IN THE LIVER

4.1 Clinical and Scientific Needs That Could Be Addressed by MRF in the Liver

Fast estimation of hepatic fat fraction in the liver is important for clinical diagnosis as well as clinical and scientific inquiry, the utility of which may be enhanced by multi-parametric MRI. As discussed in §3.2.2, MRI-based fat fraction estimation is accurate and largely definitive in diagnosing NAFL, excluding other etiologies that promote hepatic steatosis. However, the relationship between NASH stage/grade and steatosis is less clear (§3.1.2). One means to investigate this is the longitudinal monitoring of fat fraction in NAFLD subjects. Rapid GRE MRI methods already exist for quantifying fat fraction, but these can be confounded by T_1 and T_2 effects (§2.3.3). Furthermore, since NASH histopathology extends outside of steatosis alone, other metrics may be useful to determine the relationship between NASH progression and steatosis. Sensitivity to MRI metrics that relate to NASH may better place fat fraction estimation in context of disease progression and improve specificity of clinically relevant parameters. Multi-parametric MRI of liver pathology may also be one means to address the clinical need for non-invasive and rapid assessment of novel therapeutic agents (§3.1.4) for NAFLD. MRF is one means to simultaneously estimate multiple MRI parameters.

The diagnostic test currently missing from the clinical repertoire is that which can diagnose NASH before the onset of fibrosis. Patients with type 2 diabetes with normal levels of plasma aminotransferases are at much higher risk for NASH than the general population.[166] Yet, it is currently only possible to use imaging to monitor the hepatic histopathology of these subjects with modalities that are most sensitive to later stages of fibrosis and cirrhosis, such as elastography (§3.2.2). By this point in disease progression it may be difficult for patients to make lifestyle changes necessary to combat NAFLD, as well as harder to tolerate other medical intervention. To address this, non-invasive diagnostic tests are needed that are sensitive to the hepatic metabolic dysregulation and inflammation association with early stages of NASH.

Longitudinal and transverse relaxation times may be sensitive to NASH early stage histology, but T_1 and T_2 require further study in the liver to determine their clinical utility. Elevated T_1, which correlates with fibrosis stage (§3.2.2), may be a sensitive indicator of NASH progression into the later stages, but it is confounded by other biological processes such as inflammation and iron content. The sensitivity of T_2 to iron[167,168] should reduce relaxation time in those subjects with excess hepatic iron, such as those with hemochromatosis. Conversely, inflammation should raise T_2 relative to the normal parenchyma.[163,164]

Fat fraction, T_1, and T_2 estimation separately correlate with NAFLD histology; but combined, their specificity may be improved. Elevation of T_1 should correlate with fibrosis and inflammation, whereas T_2 may help determine if changes in T_1 are more likely due to an inflammatory process or the onset of fibrosis. Steatosis may be present throughout NAFLD progression, but also may be reduced in later stages of fibrosis due to cross-talk between liver pathology and adipocytes[169]. MRF potentially permits simultaneous estimation of all these parameters.

An MRF technique that is sensitive to relaxation and fat signal fraction would permit exploration of the assumptions related to NAFLD disease progression, as well explore other questions. The goal of simultaneously estimating T_1 and T_2 from a single acquisition has already been demonstrated in MRF (§2.4), but further development is needed to incorporate fat-water separation. Because MRF generally estimates multiple parameters from a single acquisition, maps of parameter estimates will be inherently spatially registered. While spatial heterogeneity of fat in NAFL is thought to be minimal,[170] it is unclear if this true throughout disease progression and at high resolution. It is also unclear if spatial heterogeneity of T_1 and T_2 is greater than that of fat and how might these metrics change on average and spatially in early vs. late stages of NASH. These imaging metrics could be combined with other minimally invasive diagnostic tools such as blood serum analysis. Non-specific markers of inflammatory markers or metabolic function can be analyzed for correlations with imaging metrics to potentially improve specificity of diagnosis.

To address scientific and clinical questions about NAFLD using MRF, the sequence will have to overcome anatomical challenges and disease prevalence. One challenge is respiratory motion. Without gating, respiratory triggering, or an acquisition fast enough to be done in single breath-hold, degradation of parameter quality will likely occur due to hepatic motion under respiration. Another challenge is the high prevalence of NAFLD in the general population. If the sequence itself requires substantial amount of scanning time, it becomes impractical to execute any later established imaging biomarkers on a clinical scale, even as a secondary screening/monitoring method. The MRF sequence therefore should be fast enough or flexible enough to circumvent respiratory motion artifacts, as well as rapid enough to be a minimum time burden on patients and MRI facilities.

MRF developments made for the study of NAFLD will be broadly applicable to other pathologies and anatomies. Technical advances in MRF for liver imaging can be applied to anatomical sites without such stringent timing acquirements that still have some modicum of fat, such as the peri-orbital region of the brain. MRF with relaxometry and fat fraction estimation could also be applied to other more technically challenging organs that contain or are near adipose tissue, such as the kidneys, prostate, pancreas, and supraclavicular brown adipose tissue depots.

4.2 Technical Challenges Presented by MRF Fat-Water Separation in the Liver

To separate fat from water signal in MRF, several technical problems must be addressed before the method may be used to interrogate the aforementioned scientific questions concerning NAFLD. These include image blurring due to heterogenous B_0 and fat chemical shifts, undersampling effects, fat signal fraction estimation bias due to transient signal evolution and B_0 effects, applied radiofrequency sensitivity, and slice-profile effects.

The spiral acquisition methods used in MRF may cause blurring in MRF images and subsequent parameter maps. The original MRF developments used spiral acquisition (§2.4), which encouraged incoherent sampling from excitation-to-excitation as well as improved efficiency of gradient utility relative to other k-space trajectories.[41] However, it is well known that spiral acquisitions of finite duration in heterogeneous B_0 fields confound gradient encoding and cause blurring.[171] An example of this shown in Fig. 4.1, which depicts

a simulation of image blurring with 100 Hz off-resonance acquired with an idealized center-out k-space trajectory that has duration of 7 ms. This effect will also be present in regions of adipose tissue due to the chemical shift (Fig. 4.1c). The blurring in regions of fat may be further confounded by extra or reduced blurring due to deviations in B_0 due to susceptibility effects or imperfect shims (Fig. 4.1d).
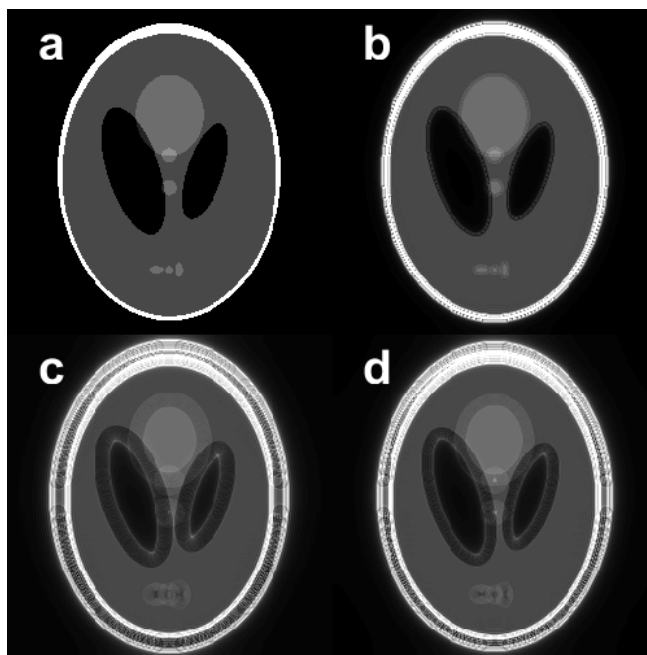
Fig. 4.1. Simulation of off-resonance blurring for a finite k-space trajectory. The unblurred image (a) is subject to blurring (b) using an idealized center-out k-space trajectory acquired in 7 ms and 100 Hz off-resonance. A chemical shift (-430 Hz), approximating the main methylene peak of fat, also produces blurring (c), and the off-resonance and chemical shift effects are additive (d). The blurring (d) appears slightly less severe than in (c), since the off-resonance is in the opposite direction as the chemical shift.

Besides blurring effects, ΔB_0 can bias fat-water fitting in MRF in a similar manner as conventional fat-water fitting methods. Off-resonance effects introduce a phase evolution that makes the different fat peaks more or less like water and vice versa. This B_0 effect may also compound with spiral blurring artifacts, making the problem even more difficult to unravel.

Undersampling is an inherent part of MRF and may bias fat estimation. In Dixon approaches to fat-water separation, fat and water components are estimated using a linear system (§2.3). If k-space is not fully sampled, aliasing will result in the image domain. It is unclear if inversion of the linear system will yield accurate estimates of fat and water components given the aliasing.

Another complication to fat-water separation with MRF is the transient state of the MRF signals. The linear fit of fat and water signals in GRE sequences (§2.3) generally assume that the fat and water signals are constant through multiple excitations. Because of varying nutation angle and other sequence variations in MRF, the steady state assumption is not valid. The resulting signal oscillations over the different MRF excitations will also be different for water and fat since they have different T_1 and T_2 values. Fits for fat and water components in such dynamic signals will be biased by these oscillations and relaxometry effects. A simplified model of one of these effects can be seen in Fig. 4.2. The fat and water signal magnitudes are modulated by a sine wave similar to how a smoothly oscillating MRF flip angle pattern might modulate the signal. The fat model experiences a phase oscillation at 430 Hz (corresponding the bulk methylene peak) that is modeled in the fit, but the transient magnitude behavior from the sequence flip angle modulation is not considered during fitting. The simulated signal is acquired for 32 echoes evenly spaced from 2 to 12 ms. The resulting fat signal fraction (FSF) calculation is substantially biased without incorporating transient contrast effects.

Slice profile effects and radiofrequency transmit sensitivity (B_{1+}) is known to affect MRF sequences. The original MRF formulations used single slice-selective excitation. It has been shown that bSSFP is sensitive to slice profile effects that produce bias in parameter estimates,[172,173] but this has been largely unstudied in uSSFP MRF. The dynamic signal shapes in MRF sequences depend on the sequence of nutation angles in a non-linear way. Sensitivity to B_{1+} scaling has been shown in bSSFP MRF.[172,173] In uSSFP sequences, there is degeneracy in the T_2 and B_{1+} parameter space such that one cannot simultaneously fit for the two parameters without sequence modifications.[174] Models of B_{1+} sensitivity in the liver at 3 T show substantial non-uniformity (>20%).[175] If B_{1+} cannot be fit directly with the MRF

sequence, an independent B_{1+} map will otherwise need to be acquired with similar speed/gating as the MRF sequence to minimize respiratory motion effects.
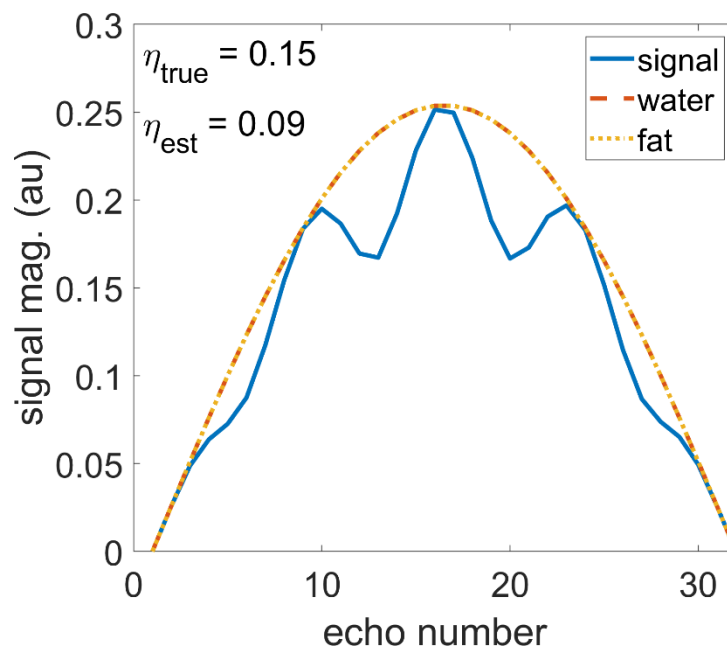
Fig. 4.2. Simulation of fat signal fraction (FSF; η) estimation with transient magnitude variations in fat and water. The transient state is a simplified representation of an MR fingerprinting-like signal. Without considering transient effects due to variations in sequence properties and relaxometry effects, the estimated FSF is biased.

4.3 Specific Aims of This Work

Take together the scientific/clinical questions concerning quantitative MRI in NAFLD with the technical advancements necessary to address these questions, and we arrive at several areas that constitute the unique body of work presented in this dissertation. The focused methodological advances and inquiries related to them can be expressed in the following three specific aims.

Aim 1 will use MR fingerprinting (MRF) to separate fat from water signal and quantify the fat signal fraction (FSF) with simultaneous estimation of water T_1 and T_2. This aim will permit improved quantification of these relaxometry metrics in fat-water

phantoms and healthy subjects relative to MRF estimates made without fat-water separation, as well as provide a method for quantifying steatosis.

Aim 2 will further optimize MRF for use in the abdomen by compensating for respiratory motion, and variation in B_{1+} and B_0 fields, and non-ideal slice profile effects. This aim will improve MRF T_1, T_2, and FSF measurement accuracy and uncertainty relative to measurements made without corrections.

Aim 3 will incorporate developed improvements in parameter estimation to quantify FSF with simultaneous estimation of water T_1 and T_2 in the liver of at least four healthy subjects to determine the intra-subject repeatability of these metrics, as well as show proof-of-concept that this MRF technique may be applied in NAFLD subjects. This will provide a baseline for measurement uncertainty and inform directions of future technical developments necessary to address specific scientific/clinical inquiries.

Since many of the technical advances addressed by these aims are interconnected, any given forthcoming chapter will, at times, pull from multiple aspects of these aims. In summary: Aim 1 borrows from developments in spiral blurring corrections discussed in Chapter 5 and MRF fat-water separation in Chapter 6; Aim 2 is addressed by the spiral blurring correction in Chapter 5, the ΔB_0 fitting incorporated in the fat-water separation discussed in Chapters 6 and 8, the incorporation of breath holding and B_{1+} correction in Chapters 6-8, and the slice profile corrections provided in Chapters 7 and 8; Aim 3 is addressed by improvements in slice profile corrections from Chapters 7-8, further refinements of the ΔB_0 correction from Chapter 6 in Chapter 8, and the liver *in vivo* results presented in Chapter 8.

Chapter 5

MULTI-FREQUENCY INTERPOLATION IN SPIRAL MAGNETIC RESONANCE FINGERPRINTING FOR CORRECTION OF OFF-RESONANCE BLURRING[ii]

5.1 Introduction

As discussed in §2.4, magnetic resonance fingerprinting (MRF) using undersampled spiral k-space readouts is an efficient method to estimate T_1 and T_2 using balanced steady-state free precession (bSSFP)[176] and unbalanced steady-state free precession (uSSFP)[67]. While the bSSFP sequence allows concomitant fitting of static magnetic field off-resonance frequencies (ΔB_0), it is subject to banding artifacts caused by off-resonance effects[177]. The uSSFP sequence circumvents banding, but has lower signal than bSSFP and was designed to be insensitive to ΔB_0[67]. The application of uSSFP MRF sequence has expanded to anatomical regions outside the brain that may have more prevalent B_0 heterogeneity[84,178].

It is well known that as spiral imaging acquisition time increases, B_0 inhomogeneity increases image blurring in proportion to the magnitude of the off-resonant frequency (see also §4.2). This blurring is present in both bSSFP and uSSFP implementations of MRF. Previous MRF work has shown accuracy despite B_0 non-uniformity in phantom and *in vivo.*[67] However, neither the effect of spatial blurring due to B_0 variations on parameter maps has been explored in detail, nor have explicit corrections been applied to compensate for the effect. Parametric maps generated by spiral-based MRF pulse sequences without blurring correction may have inaccurate values due to the off-resonance induced point spread function. This may have clinical relevance for regions close to air-tissue interfaces, tissue-tissue boundaries, or other regions of significant magnetic susceptibility gradients.

Many works have addressed correction of spatial blurring from off-resonance in spiral trajectories[179–182], and the work of Man *et al*. provides such a solution using multi-frequency interpolation (MFI)[183]. The MFI technique relies on a series of basis frequencies to express phase deviations in k-space caused by off-resonance. For each frequency in the

basis, each point in k-space is phase corrected according to the sample time after radiofrequency excitation. This basis set of phase-corrected k-spaces is transformed to the spatial domain, and a linear combination of the basis images are formed for each voxel according to ΔB_0 of that voxel obtained from a B_0 map. This linear combination of basis images closely approximates the image of that voxel without blurring. Recent work has begun to assess whether established blurring correction schemes can be used in MRF[184,185].

This chapter shows that uSSFP MRF phantom and *in vivo* data acquired using a spiral k-space trajectory may contain T_1 and T_2 parameter map distortions in the presence of ΔB_0. Results demonstrate that MFI corrections applied to the MRF images diminish those artifacts in the relaxation parameter maps and improve uncertainty in region-of-interest measurements.

5.2 Theory and Approach

As briefly stated in §5.1, the goal of MFI is to approximate the deblurred (conjugate phase) image as a linear combination of basis images that are formed from the measured image. Similar to the original MFI work,[183] we write the deblurred solution of the image I_{cp} $\in \mathbb{C}$ at position $\mathbf{r}$ with an associated off-resonance frequency f as

$$I_{cp}(\mathbf{r}; f) \approx I_{MFI}(\mathbf{r}; f) = \sum_{m=1}^{M} c_m(f) I_{f_m}(\mathbf{r}) \qquad [5.1]$$

where $c_m(f) \in \mathbb{C}$ is the weighting coefficient for $I_{f_m} \in \mathbb{C}$, which is the basis image formed from frequency f_m. The basis image I_{f_m} is given as

$$I_{f_m}(\mathbf{r}) = \mathcal{F}^{-1}\left\{S(\mathbf{k})e^{-i2\pi f_m t(\mathbf{k})}\right\} \qquad [5.2]$$

where $\mathcal{F}^{-1}$ is the inverse Fourier transform, $S(\mathbf{k})$ is the gridded and sample-density compensated k-space signal at discretized spatial frequency position $\mathbf{k}$, and $t(\mathbf{k})$ is the time following radiofrequency excitation for the given point in k-space. The accuracy of Eq. (5.1)

is dependent on the spacing in the frequency basis and the number of frequencies used in the basis.

Coefficient calculation of $\{c_m(f)\}$ for Eq. (5.1) can be performed on an ideal (noiseless) synthetic signal and solved with a linear system. The column vector $\mathbf{j}(f) \in \mathbb{C}^N$ is the complex exponential with row elements at discretized time t_n given as

$$j_n = \frac{1}{\sqrt{N}} e^{i2\pi t_n f} \tag{5.3}$$

and is related to the MFI coefficients $\mathbf{c}(f)$ as a column vector and system matrix A $\in \mathbb{C}^{N \times M}$ via the following linear relation

$$\mathbf{j}(f) = A\mathbf{c}(f). \tag{5.4}$$

The nth row and m^{th} column entry of A is given as

$$A_{nm} = \frac{1}{\sqrt{N}} e^{i2\pi t_n f_m} \tag{5.5}$$

The coefficients may be solved generally as

$$\mathbf{c}(f) = A^{\dagger}\mathbf{j}(f), \tag{5.6}$$

or, when A is in an orthonormal basis, as

$$\mathbf{c}(f) = A^{H}\mathbf{j}(f). \tag{5.7}$$

Here, $A^{\dagger}$ and A^{H} are the Moore-Penrose pseudoinverse and the complex conjugate transpose of A, respectively. The off-resonance frequency range and its map can be determined from an independently derived B_0 map. The coefficients for a finely spaced

array of off-resonance frequencies may be calculated and stored in a lookup table, and then applied with the discretized form of Eq. (5.2) to Eq. (5.1) to solve for the unblurred image. The timing information used in Eq. (5.2) can be solved analytically or mapped and is further discussed in other work.[179,183]

In the case of MFI applied to MRF, the images may be highly undersampled, creating spatial aliasing of the image. Despite this aliasing, spiral MRF has shown accuracy in parameter estimation, even up to undersampling factors of 48.[67] Like the standard MRF sequence, the MRF MFI aliasing at a given position is assumed to be incoherent with the sought-after signal.

5.3. Materials and Methods

5.3.1 Phantoms and human subjects

Three phantoms were used in this study. The first was composed of ten 50 mL conical centrifuge tubes filled with deionized water and variably doped with manganese chloride or gadopentate dimeglumine to provide a range of T_2 and T_1 contrast (10-tube phantom). The second phantom was a commercially available quantitative MRI system phantom (High Precision Devices, Inc., Colorado) with temperature calibrated T_1 and T_2 contrast spheres. As relaxation can be temperature dependent, the MRI system (Msys) phantom relaxation values were temperature corrected[186] before comparing to measurements. A Periodic Image Quality Test (PIQT) phantom (Philips Healthcare, The Netherlands) was used to determine geometric blurring improvement over the field-of-view.

One healthy subject underwent scanning after informed consent and with approval of the local institutional review board. The subject was scanned in the transverse plane superior to the orbits and nasal sinuses. Regions outside of the brain were masked because correction near the skull were difficult to identify as having sufficient signal to produce reliable parameter estimation and were also found to produce less robust blurring corrections.

5.3.2 Data acquisition and experimental design

Data were acquired on a Philips Achieva 3 Tesla scanner (Philips Healthcare, The Netherlands) with an eight-channel receive head coil for phantom and cranial *in vivo* acquisitions. MRF scans used an RF excitation of a Gaussian windowed sinc function with a time-bandwidth product of 10 and a minimum T_R of 17 ms (27.5 ms *in vivo*) (with T_R extensions detailed below) and T_E of 3.25 (3.5 *in vivo*) ms. A numerically designed variable density spiral[187–189] with zero net gradient over a single T_R and minimum/maximum undersampling factor of 24/48 (12 *in vivo*) was used for k-space encoding with a data acquisition time of ~3 to 7 ms per T_R (15 ms *in vivo*). The spiral was designed to not exceed an instantaneous gradient frequency greater than 1 kHz. The transition radius from least undersampled to most undersampled k-space sampling was 0.7 of the maximum k-space radius. The calculated spiral was rotated by an angle of 111.254° between successive excitations. For all phantom and *in vivo* scans, a field of view of 240 mm x 240 mm was used with an in-plane resolution and slice thickness of 1 mm x 1 mm and 5 mm, respectively. A single MRF planar acquisition consisted of 1000 excitations. B_0 maps were generated using a Cartesian sampled gradient-echo scan with two echo times spaced 1 ms apart and then reconstructed from the raw data and masked using `multithresh`, a multi-threshold implementation of Otsu's method[190] in MATLAB (v 8.5.0 Mathworks, Inc., Nattick, MA). In phantom cases where the off-resonance exceeded the available B_0 map bandwidth, an additive correction was applied above or below threshold to avoid frequency wraparound and confirmed by visual inspection. For the *in vivo* study, an inversion prepared T_1-weighted 3D spoiled gradient echo sequence with T_E/T_R of 4.6/8.3 ms, nutation angle of 9°, 1 mm x 1 mm x 1 mm voxels, with 884 Hz per voxel was acquired. For anatomical comparison with the thicker MRF slice, the T_1-weighted slice nearest the center of the MRF and nearest four slices were summed before display.

Phantom experiments consisted of evaluating geometric improvement in a standard image quality phantom and in relaxation contrast phantoms without and with B_0 heterogeneity, as well as evaluating the effect of MFI on MRF T_1 and T_2 maps. T_1 and T_2 maps used rainbow colormaps to visually enhance non-uniformities in the image. The PIQT

phantom was imaged in the coronal plane over a rectangular grid of water-filled pins. Linear shim settings were adjusted to provide a wide range of off-resonance frequencies over the field of view. The total acquisition time of the spiral was 3.76 ms (R = 48, uniform spiral). To evaluate spatial dependence and off-resonance magnitude on MFI correction, the 10-tube phantom was acquired with manually set shim values in longitudinal, transverse, and in-plane oblique directions to provide heterogeneous B_0 over a wide range of frequencies. The Msys phantom was imaged with a coronal orientation to cover the T_1 and T_2 contrast planes under both well shimmed and poorly shimmed conditions. Fourteen regions of interest (ROIs) were drawn on the magnitude image of each contrast slice of the well shimmed case and applied to all B_0/correction variations of the Msys experiment. These were numbered from 1 to 10 beginning at the 12 o'clock position moving clockwise, and from 11 to 14 beginning from the top left of the inner four contrast insets moving clockwise. Measurements were compared using boxplots to determine the effect of MFI on relaxometry values without and with B_0 heterogeneity. Concordance correlation coefficients (CCC) with confidence intervals[191] were calculated for all ΔB_0/correction variations using all ROIs and the Msys specifications as a reference.

5.3.3 MRF sequence, dictionary creation, and matching

The original MRF SSFP sequence with an inversion time of 7 ms and the same variable T_R extensions and relative flip angle evolution as described by Jiang *et al.*[67] was used in this study, with a maximum nutation angle of 70°. Two dictionaries were generated using an extended phase graph algorithm with the following T_1 and T_2 range and spacing (minimum:step:maximum), depending on the experiment. The first dictionary with T_1 values from 20:10:3000, 3200:200:5000 ms; and T_2 10:5:300, 350:50:2000 ms was used for all experiments except the Msys phantom. The Msys dictionary[192] spanned T_1 from 10:10:100, 120:20:1000, 1040:40:2000, 2100:100:3000 ms; and T_2 from 2:2:10, 15:5:100, 110:10:300, 350:50:800. Prior to matching, the dictionary and acquired MRF signal were normalized and compressed using a singular value decomposition method[70], preserving 99.99% of the singular value energy. The inner product was formed between the compressed signal with all compressed dictionary entries, and the highest magnitude of the

inner product determined the dictionary entry that defined T_1 and T_2 for each image voxel. The MRF compression and matching are further described in §2.4. The preceding and following reconstruction and analysis was performed in MATLAB unless otherwise noted.

5.3.4 MRF and MFI image reconstruction

Raw spiral k-space was first reconstructed without B_0 correction using gridding with iterative sample density compensation[36,188,193,194] and independently measured[195,196] k-space coordinates. Individual channel images for each excitation were combined using adaptive reconstruction described by Walsh *et al.*[39]. Adaptive coil combination coefficients were derived from the complex sum of the 1,000 MRF undersampled images for each channel. For each MRF excitation the derived coefficients were used to adaptively combine the different coil images. Each voxel in the coil-combined MRF image was then fit for T_1 and T_2 as discussed above.

The MFI correction coefficients were generated as previously described in Man *et al.* [183] and in §5.2. To generate the lookup table of coefficients, time t_n was discretized from 0 to $b(T_E + T_{acq})$ in N steps, with N set to the number of read points in the spiral, T_{acq} is the spiral acquisition time, and b a scale factor set to 1.2 in this work. The scale factor increases the time range in the columns of A. It was used because it was observed that regions near the endpoints in time of the modeled phase were least accurate, and this extension is like the time expansion used in the original work. As discussed by Man *et al.*, this system can be approximated by extracting $M - 1$ columns closest to $f_0 = 0$ from the DFT matrix and normalizing according to Eq. (5.5). So, A is composed of orthonormal columns of complex exponentials whose number is equal to the total number of basis frequencies chosen to represent all possible discretized off-resonant frequencies in the image over a time domain that is slightly larger than the k-space acquisition time. M was chosen to be 21 (31 *in vivo*) for reconstructions in this study, as it was found to keep the average root-mean-square error below approximately 1.5% for frequency deviations within +/- 700 Hz for the echo and acquisition times used here.

A linearly interpolated B_0 map was generated using the masked B_0 map using Delaunay triangulation[197] via MATLAB's `scatteredInterpolant` method. This helped

to overcome the missing off-resonance values in low signal regions of the image. For instance, signal from a voxel near a phantom or tissue surface may blur into adjacent voxel of air. If the air voxel's off-resonance is considered zero, this blurred information will not be returned to the correct voxel.

The linear system was then solved for all frequencies in the range of the median adjusted interpolated B_0 map discretized to 0.1 Hz over the expanded discretized time. Times before T_E and after T_E + T_{acq} were apodized as described in the original work to improve accuracy over the true acquisition window. The resulting interpolated coefficients were stored in a lookup table, and a coefficient map was created according to the linearly interpolated B_0 map.

MFI correction was applied before coil combination. To avoid gridding M basis k-space representations for 1000 MRF excitations for each coil, the previously saved coil images for all excitations were transformed back to gridded k-space. An acquisition time map[179] for gridded k-space was constructed, and each gridded k-space point was modulated in phase according to this time map for a given basis frequency following Eq. (5.2). This was repeated for all basis frequencies and transformed to the image domain to form M basis images. The coefficient map was then applied to the basis images to produce a single corrected frame using Eq. 5.1. The MFI-corrected undersampled images were then adaptively coil-combined as described previously.

5.4 Results

5.4.1 Reconstruction of PIQT phantom

The PIQT results show significant blurring correction using MFI over the field-of-view as seen in Fig. 5.1. The B_0 heterogeneity over the image spanned approximately 700 Hz asymmetrically about 0 Hz. This produced substantial blurring in regions of off-resonance that exceed approximately 200 Hz. The degree of blurring increases in proportion with off-resonance. The MFI corrected image shows very little if any residual blurring for any of the signal point sources across the field of view. Reduced signal of one

edge of the phantom is observable in both the uncorrected and corrected images due to low coil sensitivity at the edge of the phantom.
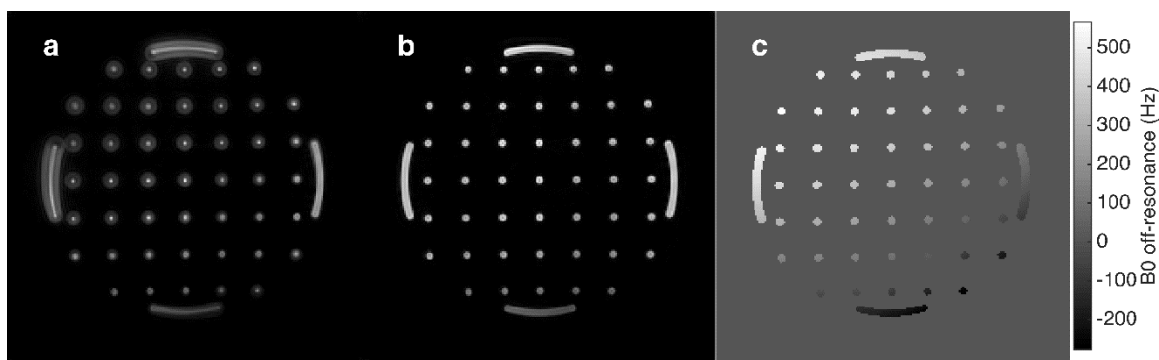
Fig. 5.1. The MFI correction for the Periodic Image Quality Test (PIQT) phantom. The magnitude image derived from the complex sum of all magnetic resonance fingerprinting excitations (a) exhibits blurring that increases with the magnitude of off-resonance mapped in (c). This geometrical blurring has been corrected by multi-frequency interpolation (b). Low signal regions can be seen at the bottom of the image, in regions of lower coil sensitivity in the uncorrected and corrected images.

5.4.2 MRF with B_0 inhomogeneity

Fig. 5.2 demonstrates MFI correction of T_1 and T_2 parameter maps under a variety of off-resonance patterns across the coronal section. Four examples of different off-resonance maps are given: less than +/-100 Hz variations in B_0, trans-axially spanning ~700 Hz, longitudinally spanning ~600 Hz, and ~700 Hz across an oblique axis. The uncorrected T_1 and T_2 maps show distortion of the phantom tube boundaries in all cases. The geometric integrity of these boundaries appears restored in three out of four cases. The fourth set of corrected off-resonance parameter maps (Fig. 5.2d) demonstrates partial restoration: some corrected cylinders still appear slightly distorted, though less than in the uncorrected maps. The T_1 values in the uncorrected maps relative to the corrected maps appear largely consistent. However, the T_2 maps show nonuniformity across phantom tubes in both uncorrected and corrected cases. The pattern of T_2 heterogeneity within a given phantom

61

tube changes between different B_0 heterogeneity patterns and between the uncorrected and MFI corrected reconstructions.
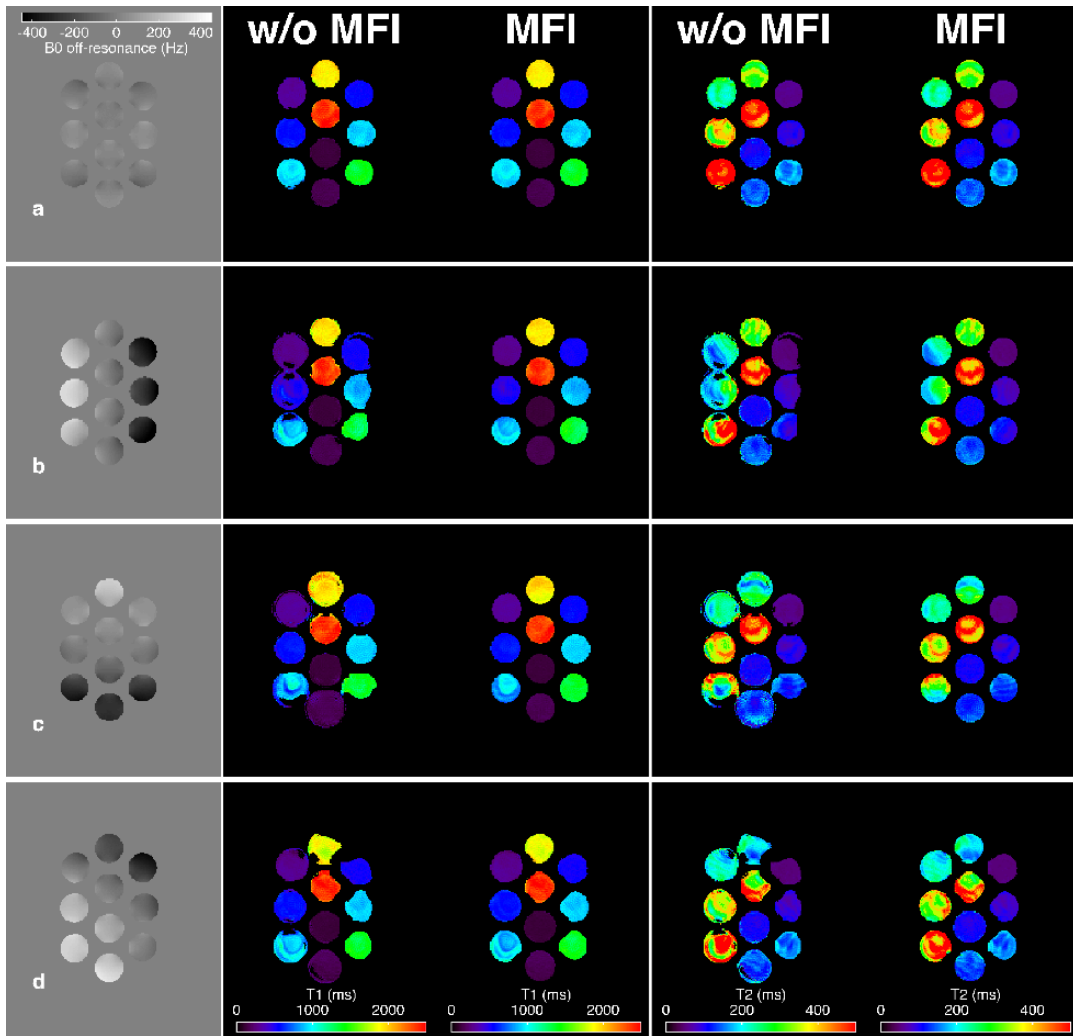
Fig. 5.2 The results before and after multi-frequency interpolation (MFI) correction of magnetic resonance fingerprinting T_1 and T_2 parameter maps of the 10-tube phantom for four instances of B_0 heterogeneities. Each row from left to right shows the B_0 map, uncorrected T_1, corrected T_1, uncorrected T_2, and corrected T_2 maps. The total off-resonance was minimized using pencil-beam volume shimming (a) and ramped transversely (b), longitudinally (c), and obliquely (d). The scaling for the parameter maps is the same between uncorrected and corrected cases for a given parameter type. MFI corrected reconstructions show geometrical improvement in all cases. The last row (d) exhibits some phantom boundary distortion after MFI correction.

5.4.3 MRI system phantom results

The Msys phantom imaged with poorly shimmed B_0 exhibits decreased blurring in magnitude images after MFI correction (Fig. 5.3). The B_0 maps from both the T_1 and T_2 contrast slices show that the contrast spheres span a range of ~300 Hz off-resonance asymmetrically about zero. Ring artifacts around the contrast insets are not apparent in the corrected image, and three fiducials outside the circumference of the spheres are more clearly resolved after MFI reconstruction. Additionally, susceptibility artifacts around the central T_1 spheres, which contain the highest concentrations of contrast agent, are improved in the MFI corrected image. The effects of the blurring and correction are also visible in the parameter maps (Fig. 5.4). In the uncorrected contrast maps, signal from the phantom background spreads into contrast spheres that are in regions of high off-resonance at the bottom and top portion of the phantom image. After correction, this background signal contamination is reduced.

The boxplots from ROI measurements of the T_1 and T_2 contrast spheres are shown in Fig. 5.5. Here, the well shimmed (ws) and poorly shimmed (ps) results are shown without (ws/ps) and with (ws+/ps+) MFI correction for each of the 14 contrast spheres of each relaxation type. The temperature-corrected specification value for each ROI is also shown for reference. The ws and ws+ show general agreement across all ROIs for T_1 and T_2. The ps and ps+ measurements have larger T_2 medians than ws and ws+ cases for the smaller T_2 ROIs (8 through 14). The T_1 and T_2 concordance correlation coefficients (CCCs) with 95% confidence intervals are shown in Table 5.1.
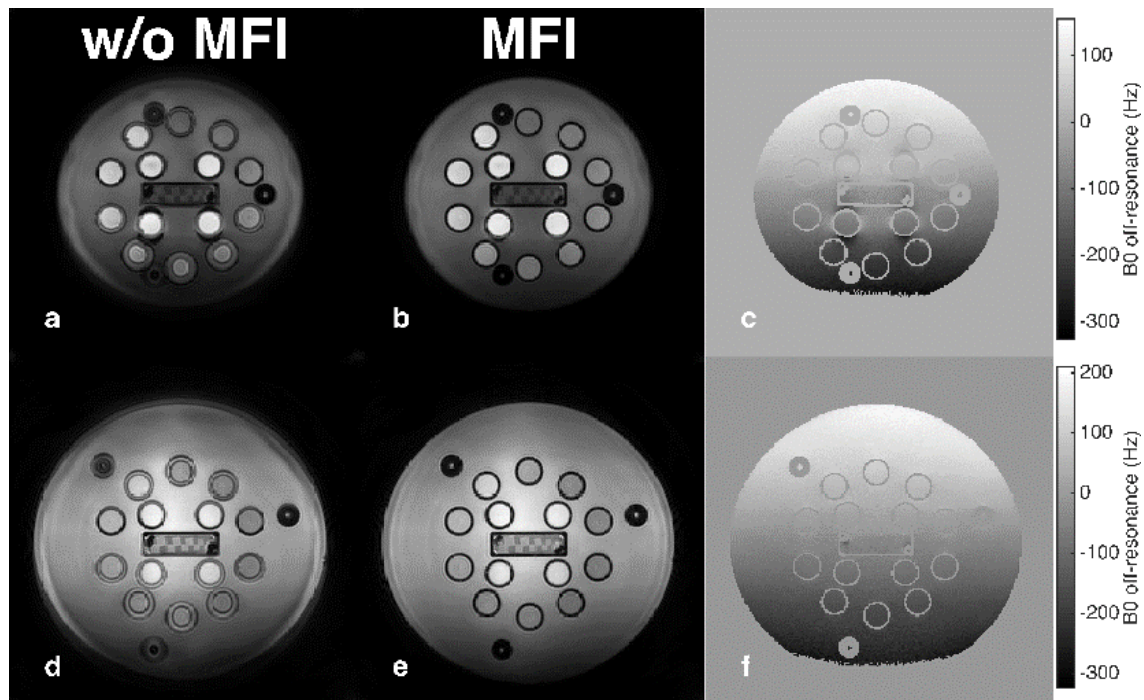
Fig. 5.3 The magnitude images for the T_1 (top row) and T_2 (bottom row) contrast slices of the MRI system phantom as well as B_0 maps. The uncorrected (a,d) and corrected (b,e) magnetic resonance fingerprinting magnitude images were derived from the complex sum of all MRF excitations. The B_0 maps (c,f) demonstrate a slope in off-resonance from the bottom to top of the image. Without multi-frequency interpolation (MFI) correction, the images show blurring in regions of off-resonance. The central spheres in (a) additionally show susceptibility artifacts that manifest as signal voids. The MFI corrected results (b,e) demonstrate a decrease in blurring in all regions.

Table 5.1. The concordance correlation coefficients of T_1 and T_2 without and with MFI correction for different shim settings.

Reconstruction	T_1 CCC[1] [CI][2]	T_2 CCC[1] [CI][2]
ws[3]	0.993 [0.982, 0.997]	0.995 [0.986, 0.999]
ws+[3]	0.993 [0.983, 0.997]	0.995 [0.986,0.999]
ps[3]	0.994 [0.988, 0.997]	0.974 [0.922, 0.992]
ps+[3]	0.995 [0.987, 0.998]	0.992 [0.977, 0.997]

[1]CCC, concordance correlation coefficient

[2]CI, confidence interval; numbers in brackets are the 95% CI

[3]ws, well shimmed; ws+, well shimmed with multi-frequency interpolation (MFI) correction; ps, poorly shimmed; ps+, poorly shimmed with MFI correction

Among the assessed ΔB_0/correction combinations, there is disagreement in the distribution of the T_1 and T_2 values for ROIs 5 through 7 (Fig. 5.5), which show more aberrant voxels for the ps case than the ws case. This effect is further quantified by the coefficient of variation (COV) plots (Fig. 5.6), which indicate an increase in COV for ps by a factor of approximately five in these ROIs relative to the COV values for ws. These ROIs (at the bottom of Figs. 5.3-4) are in the largest off-resonance region of the phantom. After MFI correction, the COVs of the poorly shimmed ROIs are comparable to the ws cases. Fig. 5.6 also shows 12 of 14 T_2 inserts of the ws+ have lower or equal COV than the ws cases,

indicating the MFI correction slightly lowered or did not affect the relative T_2 variation in absence of large off-resonance effects.
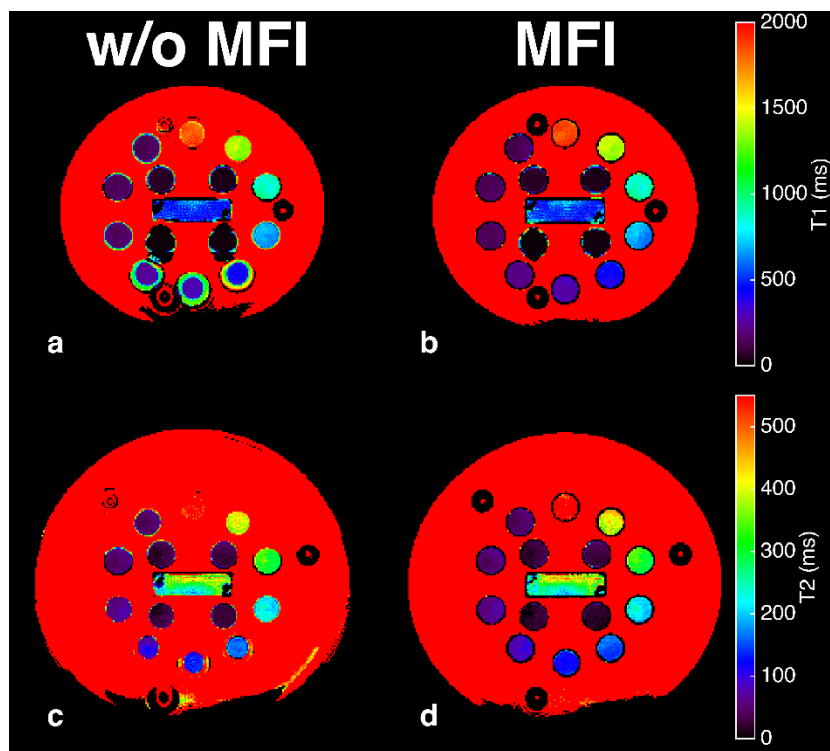
Fig. 5.4. The uncorrected and corrected T_1 (a,b) and T_2 (c,d) parameter maps from their respective slices in the MRI system phantom as shown in Fig. 5.3. Improvements in boundaries of the contrast spheres are visible, as well as reduction of bias from the high T_1 and T_2 background blurring.
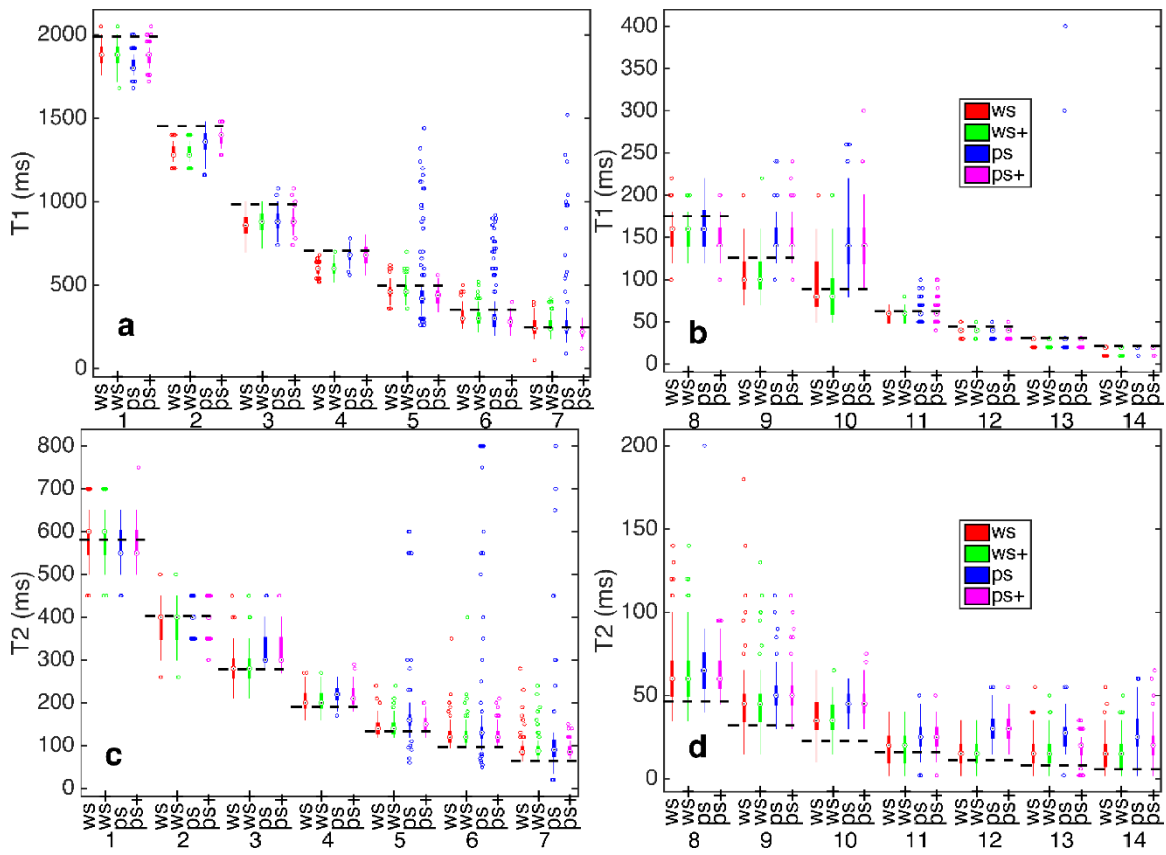
Fig. 5.5. Boxplots for all T_1 and T_2 contrast spheres in the MRI system (Msys) phantom. The results are divided into the longer half of T_1 (a) and T_2 (c) on the left and the shorter T_1 (b) and T_2 (d) on the right. Each numbered group consists of boxplots for regions of interest in the well shimmed (ws) and poorly shimmed (ps; Fig. 5.4) cases, as well as for the multi-frequency interpolation correction for the well shimmed (ws+) and poorly shimmed (ps+) cases. The horizontal dotted lines indicate the value of the Msys specifications.
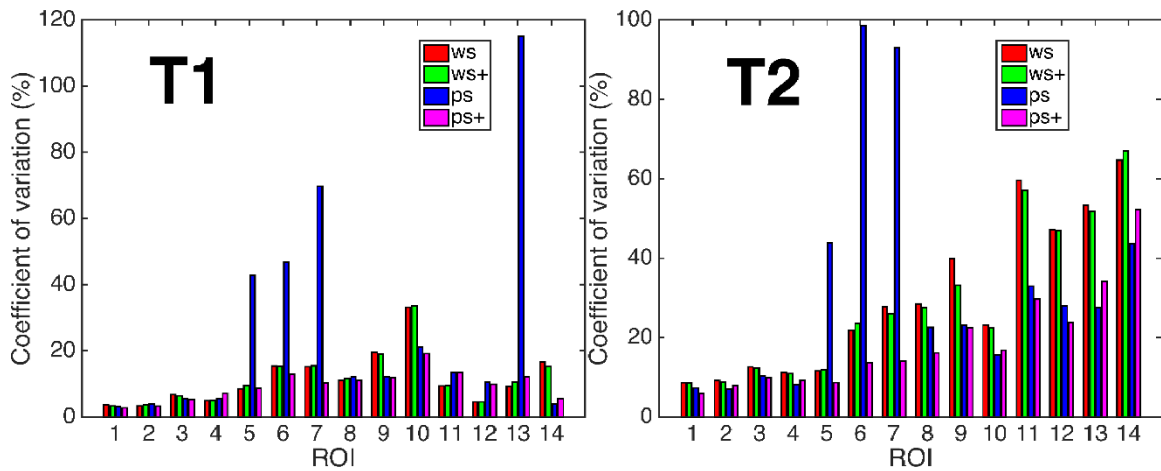
Fig. 5.6. The coefficient of variation (COV) for all regions of interest (ROIs) with and without multi-frequency interpolation (MFI). Each ROI COV is plotted for the well shimmed without MFI (ws), well shimmed with MFI (ws+), poorly shimmed (ps), and poorly shimmed with MFI (ps+). ROIs 5 through 7 for the ps cases demonstrate large COVs relative to the ws and ps+ cases. These ROIs correspond to the contrast spheres at the bottom of the images/maps of Figs. 5.3-4.

5.4.4 *In vivo* MRF MFI

The B_0 map, T_1-weighted anatomical reference, and T_1 and T_2 parameter maps for the transverse brain slice are shown in Fig. 5.7. The regions of highest off-resonance within the brain are in the frontal regions. Blurring is evident particularly at the midline, that appears less sharp on the uncorrected T_1 and T_2 maps relative to the corrected maps and the Cartesian sampled T_1-weighted anatomical reference. Fig. 5.8 plots the normalized signal magnitude across all excitations for a voxel in cerebrospinal fluid (CSF) (Fig. 5.8a) and in white matter (WM) (Fig. 5.8b). The CSF voxel rests in a region of higher off-resonance compared to that of the WM. The signal plot and parameter estimates from the CSF voxel are substantially different between the corrected and uncorrected cases, while those in the WM are relatively close.
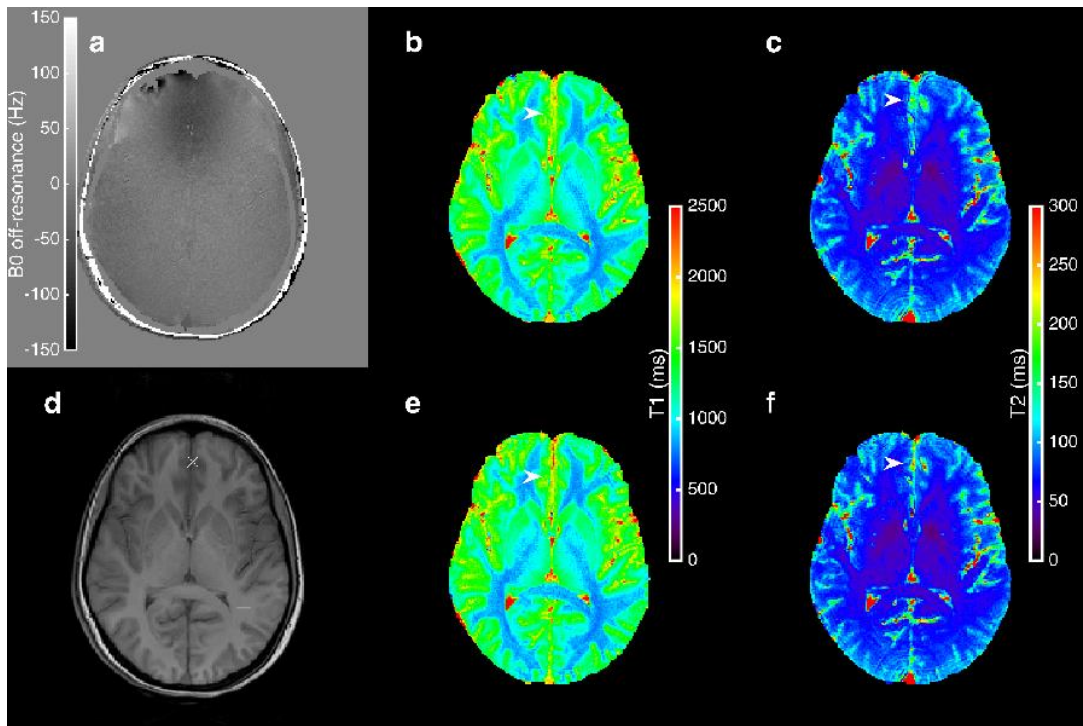
Fig. 5.7. A transverse slice of the brain superior to the orbits. The B_0 map shows increasing off-resonance near the frontal regions, referenced anatomically in the T_1-weighted image (d). Without multi-frequency interpolation (MFI), the uncorrected T_1 (b) and T_2 (c) maps exhibit an increased blurring near the midline (white arrowhead), which appears sharper in the T_1 (e) and T_2 (f) MFI-corrected maps. The 'x' and '+' in (d) are the voxels shown in Fig. 5.8(a) and (b), respectively.

5.5 Discussion

The results show that the effects of B_0 heterogeneity on unbalanced SSFP MRF parameter map details can be substantial due to spatial blurring, but the central regions of the phantom inserts are largely unchanged. The MFI correction applied to spiral-based MRF demonstrates good reconstruction in many cases of substantial B_0 heterogeneity and seems to fail where there is uncertainty in the B_0 map. The corrected PIQT phantom results show little to no blurring of the image. Similarly, the Msys phantom and 10-tube phantom showed dramatic improvement after MFI correction in the image as well as parameter maps. In the 10-tube phantom case of longitudinal or transverse B_0 gradient, the MFI

correction was able to restore images without noticeable geometric defect. An exception to this is the oblique B_0 pattern of heterogeneity in the 10-tube phantom, which showed significant but incomplete restoration of the circular phantom shapes. The more complicated off-resonance patterns seen in Fig. 5.2a do not confound MFI, but the off-resonance magnitudes do not much exceed 100 Hz in this case. MFI correction in the Msys phantom was able to substantially reduce blurring, even in areas of steep susceptibility gradients compounded with underlying low frequency B_0 variation (Fig. 3a-c). Thus, the regions where MFI fails are not necessarily at the extremes of off-resonance, but in cases where the linear interpolation of the B_0 map may fail and the magnitude of off-resonance is relatively large.

The proposed correction method helps to reduce uncertainty in T_1 and T_2 measurements and does not by itself alter relaxation estimates. The 10-tube and Msys phantom results demonstrate that MRF relaxation values in uniform contrast regions are degraded by B_0 heterogeneity. MRF quantitation near and inside contrast insert/tube boundaries are improved after MFI correction. This improvement can be seen in lower coefficient of variation and greater accuracy near the contrast edges in the poorly shimmed cases (ps vs ps+). Additionally, MFI correction applied to the Msys phantom in the well shimmed cases (ws vs ws+) did not show changes in the CCCs or worsening of COVs of relaxation values. Thus, MFI apparently does not alter ROI-based estimation of relaxation values by itself. While intra-tube T_2 heterogeneity in the 10-tube phantom experiments are evident in both uncorrected and corrected images, these variations without and with MFI suggests this may be flow or diffusion artifacts in the water-filled phantoms, or from other unknown effects. This is also supported by the greater homogeneity of T_2 across the Msys T_2 contrast inserts seen in Fig. 5.4 relative to the 10-tube phantom. However, it is unclear why there is an observable upward shift in the T_2 MRI system phantom results at the shorter end of T_2 for both the uncorrected and corrected poorly shimmed measurements. This contributes to the relatively higher COV of the well shimmed cases relative to the poorly shimmed cases at short T_2. The role of off-resonance effects in MRF T_2 estimation is explored more fully in Chapter 7.
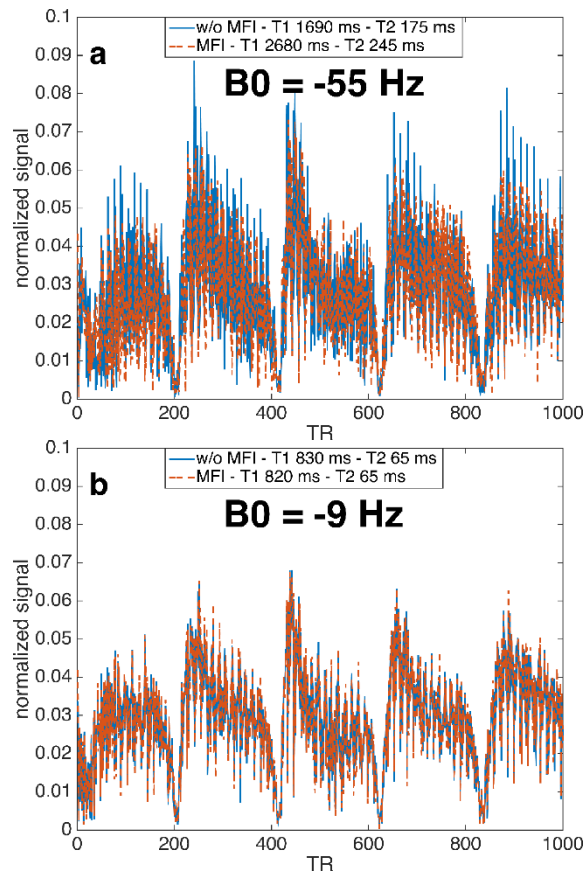
Fig. 5.8. The MRF signal evolution for cerebrospinal fluid (CSF) (a) marked as 'x' in Fig. 5.7(d), and white matter (WM) (b) marked as '+' in Fig. 5.7(d) without and with multi-frequency interpolation (MFI). The CSF is in a region of greater off-resonance and exhibits larger departures between corrected and uncorrected signals that are reflected in their different T_1 and T_2 values. The MFI correction in the low off-resonance region of (b) appears to match closely with the uncorrected signal. The T_1 and T_2 estimates in the WM are nearly identical.

The results in this work are largely consistent with the original MRF unbalanced SSFP report by Jiang *et al*[67]. They found that phantom measurements were largely unaffected by B_0 heterogeneity. This work found that CCC values appear greater than 0.97 in the presence of off-resonance, despite lying slightly outside of the 95% confidence interval for the T_2 well shimmed case. However, deviations in B_0 do produce blurring, and this blurring can largely be corrected by application of MFI.

72

The *in vivo* MFI results show expected improvements in the high signal brain areas, but they were masked in the skull region where signal was lower and correction less robust. The steep signal gradient and B_0 information of the skull spatially correlates with these effects. We also note that chemical shift of fat is not accounted for by MFI because the correction assumes a single off-resonance frequency at a given position (see also Chapters 2 and 4). Even pure fat has a multi-component spectral composition. Accounting for the presence of fat is further explored in Chapter 6. Despite areas for potential improvement, the current MRF MFI embodiment successfully demonstrates the positive impact of MFI on parameter map estimation in regions of off-resonance, as well as leaving unaffected white matter that do not need signal modulation (Figs. 5.7-8).

Other potential future improvements in off-resonance correction include accuracy of the interpolated map and possibly eliminating the need for a separately acquired ΔB_0 estimate. When there are only regions of high signal, a B_0 map can readily be calculated over the entire image. However, when there are regions of low signal, this information must be derived from surrounding high signal regions. While linear interpolation has shown much success in this study, under some circumstances this method may not produce the most optimal map for MFI correction. The separate acquisition of the B_0 map from the MRF scan reduces its efficiency and may reduce accuracy in situations where physiological motion may create differences in off-resonance between the MRF scan and B_0 map acquisition. Some of these problems may be improved by considering a form of MRF that integrates B_0 mapping such as bSSFP[176], or a reconstruction that uses a cost metric to implicitly define a B_0 map that minimizes the objective function. Simultaneous fitting of B_0 in uSSFP sequences is discussed in Chapter 6.

In support of reproducible research, the source code along with figure reproduction scripts and data are freely available for download at https://github.com/jostenson/MRI_Ostenson_MRF_MFI.

5.6 Conclusion

MFI correction in conjunction with spiral MRF reduces the effects of off-resonant blurring in images and parameter maps. This method has been demonstrated in phantoms

and *in vivo* under a variety of off-resonance magnitudes and patterns. This method can be further improved by incorporating ΔB_0 estimation into the MRF scan and better accounting for off-resonance values in regions of low signal or fat, all of which is addressed in Chapter 6.

Chapter 6

MR FINGERPRINTING WITH SIMULTANEOUS T_1, T_2, AND FAT SIGNAL FRACTION ESTIMATION WITH INTEGRATED B_0 CORRECTION[iii]

6.1. Introduction

Water T_1 and T_2 and fat content are important for tissue characterization in MRI. For example, T_1 and T_2 values are altered in several diseased states, such as cardiac[198,199], muscular[200], and others[201,202], in which the affected organs may contain or be near adipose tissue. The MRI-estimated fat signal fraction (FSF) is important in studies of healthy and pathological function, including brown adipose tissue[203] and abdominal organs[141,204,205]. Most relevant for this work, these metrics may be important indicators of pathological state in NAFLD (Chapters 3 and 4).

One approach to time-efficient, multi-parametric quantitative MRI is unbalanced steady state (uSSFP) MR fingerprinting (MRF) (§2.4). The uSSFP-MRF sequence permits the rapid, simultaneous estimation of T_1 and T_2 by acquiring signals over a train of pseudo-random nutation angles and T_R values.[67] This sequence has been applied to study regions with potential ectopic and visceral fat such as the abdomen[84], prostate[206] and heart[68].

In both conventional MRI and MRF, fat signals confound T_1 and T_2 estimates. The methylene peak of fat often has a shorter T_1 and longer T_2 than water.[44,207] Partial volume effects of fat may bias MRI T_1 estimates in the breast[208] and liver[209] and T_2 estimates in muscle[200]. Conventional MRI relaxometry approaches that exclude fat often rely on separate inversion recovery preparation, composite pulses, or chemically selective pulses to suppress the fat signal. Such techniques may increase the scan duration through their preparation or timing requirements, partially saturate water signal, inaccurately assume a single peak model for fat, or have sensitivity to non-ideal B_0 or B_{1+}.[47] Conversely, conventional Dixon MRI fat-water estimation is not generally employed to estimate longitudinal and spin-spin relaxation.

Fat-water separation is confounded by heterogeneous B_0, making fat-water separation a non-linear optimization problem[62]. This has been solved by a number of different approaches,[62–64,210] but these techniques generally assume a steady-state water signal, apart from B_0 effects. MRF uses non-steady-state water/fat signals to estimate T_1 and T_2 from the signal dynamics over many excitations. Because typical fat-water separation does not account for variable flip angles, the use of non-steady state signals may confound fat-water separation if a single, variable T_E is acquired after each excitation.

While the biases in T_1 and T_2 estimation due to fat have not been explicitly considered using MRF, MRF-based fat-water separation has been explored. The original MRF approach, based on balanced SSFP, permitted fat signal estimation through its sensitivity to off-resonance/relaxation effects.[66] However, partial volume effects were not considered. Cloos *et al*. explored fat imaging in the thighs using a two-point Dixon approach with a radial acquisition.[175] Several preliminary works have explored fat-water separation in uSSFP-MRF.[211–215] Recently, simultaneous fat-separated T_1, B_{1+}, and ΔB_0 estimation has been demonstrated at 1.5 T using MRF.[216] Yet, we are unaware of a full paper that has described an MRF approach for separating fat and water signals while simultaneously estimating the water-only T_1 and T_2 with B_0 correction.

Spiral acquisitions are commonly used in MRF, further complicating parameter estimation by introducing blurring from chemical shift and B_0 effects[212] (see also Chapters 4 and 5). While spiral blurring with fat-water separation remains an active topic of research[217], fat blurring in MRF spiral acquisition is relatively unexplored. Spiral blurring effects can be limited by using lower field strength, reduced spiral acquisition time, or radial acquisitions. However, these techniques lower the signal-to-noise ratio or restrict the timing of the image encoding.

The first goal of this chapter is to illustrate the potential for bias in MRF-derived T_1 and T_2 estimates of tissues containing composite fat-water signals. The second goal is to introduce an MRF method that separates fat and water signals, allowing B_0-corrected water T_1 and T_2 estimates with reduced levels of bias, as well an estimate of FSF. To do so, we propose modifications to the original uSSFP-sequence and reconstruction. By using a swept echo time and integrating a the reported B_0 correction method from Chapter 4[183,218] into

the reconstruction pipeline, we reformulate the parameter estimation problem into an optimization for ΔB_0. This optimization, along with an assumed multi-spectral fat model, results in corrected water and fat signal estimates. The outputs of the proposed approach are B_0-corrected, fat-separated water T_1 and T_2 maps and an FSF map with spiral deblurring.

6.2 Theory

We will first show that we can extend a k-space-based fat-water separation technique to MRF. We will then show that we can simultaneously estimate ΔB_0 with fat-water separation with variable T_E- and fixed T_R-MRF sequences using a form of conjugate-phase reconstruction.

6.2.1 MRF k-space fat-water separation

Brodsky *et al.*[219] showed that k-space-based fat-water separation is possible using a linear system of equations. We can extend this technique to MRF. An MRF signal vector through all N excitations not subject to B_0 deviations, $\mathbf{s}_o(\mathbf{k}) \in \mathbb{C}^N$, at a given k-space position $\mathbf{k}$ can be closely approximated as

$$\mathbf{s}_o(\mathbf{k}) \approx \mathrm{A}_k \mathbf{b}(\mathbf{k}), \qquad [6.1]$$

where A_k is the k-space position dependent system matrix and $\mathbf{b}(\mathbf{k}) \in \mathbb{C}^{M+1}$ are the coefficients that describe the water and fat components, with M defined below. A subscript on $\mathbf{s}$ is used to specify that B_0 effects outside of chemical shift are not considered in this model.

The system matrix in Eq. (6.1) can be given as

$$\mathrm{A}_k = [\mathbf{u}_1 \cdots \mathbf{u}_M | \mathbf{g}(t(\mathbf{k}))], \qquad [6.2]$$

where $\mathrm{A}_k \in \mathbb{C}^{N \times (M+1)}$, $\{\mathbf{u}_m\} \in \mathbb{C}^{N \times 1}$ are k-space independent singular vectors which describe the water dictionary in the time domain, and $\mathbf{g}(t(\mathbf{k}))$ is the fat model with k-space dependence through the finite trajectory timing (further defined below). McGivney *et al.* [70]

showed that the water dictionary is highly compressed in the time dimension. Since the compressibility of the water dictionary, as measured by the singular values, is invariant under transpose, we can similarly reason that the parameter dimension of the water dictionary is compressible. The vectors $\{\mathbf{u}_m\}$ can be calculated by singular value decomposition (SVD) of the water dictionary, using the left singular vectors to form $\{\mathbf{u}_m\}$ (for a dictionary $D \in \mathbb{C}^{N \times Q}$, with Q dictionary atoms). The value of M, the number of members in the set $\{\mathbf{u}_m\}$, is determined by the fraction of singular value energy one wishes to retain. Increasing the value of M, increases the model accuracy of Eqs. (6.1-2). The last column of A_k describes the MRF fat model in k-space, $\mathbf{g}(t(\mathbf{k})) \in \mathbb{C}^{N \times 1}$, with the nth element of $\mathbf{g}$ given as

$$g_n(t(\mathbf{k})) = \frac{1}{b_o(\mathbf{k})} \sum_{p=1}^{p=P} b_{p,n}\, e^{i2\pi f_p \left(T_{\mathrm{E},n} + t(\mathbf{k}) \right)}. \qquad [6.3]$$

Here, $b_o(\mathbf{k})$ is a k-space dependent normalization factor that gives $\mathbf{g}(t(\mathbf{k}))$ unit norm, $b_{p,n}$ a triglyceride peak weighting that accounts for MRF sequence T_1/T_2 contrast effects for excitation n and the moiety's weighting relative to the whole triglyceride, f_p is the pth peak's chemical shift frequency, $T_{E,n}$ is the echo time following excitation n, and $t(\mathbf{k})$ is the time to reach $\mathbf{k}$ through the k-space trajectory. In this work, we assume that the echo time starts at the beginning of the spiral readout at the k-space origin. The coefficient estimates at each k-space position, $\hat{\mathbf{b}}(\mathbf{k}) \in \mathbb{C}^{M+1}$, may be solved by pseudo-inverse of A_k using Eq. (6.1).

The water dictionary does not contain phase evolution through time, and $\{\mathbf{u}_m\}$ are orthonormal by definition. The fat signal, $\mathbf{g}$, does exhibit complex periodic phase through time that lends a certain amount of orthogonality to the water dictionary basis. As a result, we find that the conditioning of A_k is reasonable throughout k-space for the trajectory timing and T_Es used in this work.

The Fourier transform of $\hat{\mathbf{b}}(\mathbf{k})$ gives coefficient images represented by $\hat{\mathbf{b}}(\mathbf{r})$, for a given spatial position $\mathbf{r}$. These images are representations of the coefficients in the spatial domain. The coefficients in the spatial domain can then be multiplied by the water ($\{\mathbf{u}_m\}$)

and fat (**g**) model vectors at each **r** to reconstruct the estimated MRF water and fat signals. The fat coefficient estimate, the last entry of $\hat{\mathbf{b}}(\mathbf{r})$, is multiplied by **g** with $t = 0$ in Eq. (6.3). Under this condition, $A_k = A$ is independent of k-space and can be applied in the image domain to on-resonance signals. This reconstructed representation of the MRF fat signal does not exhibit blurring due to chemical shift, since the phase accrual in k-space has been fit using Eq. (6.3). While this fat-water separation does resolve blurring due to chemical shift, it does not consider B_0 effects that may confound the fat-water fitting due to blurring or frequency shift.

6.2.2 ΔB_0 fitting with MRF fat-water separation

We can extend the concept of a conjugate phase reconstruction technique called multi-frequency interpolation (MFI)[183,218] to correct for ΔB_0 blurring and fat-water separation bias. If the MRF T_Rs are fixed, and the slice profiles and crushers are ideal (see also Chapter 7), the uSSFP MRF sequence will refocus off-resonance magnetization contributing to signal at the beginning of every excitation.[2,220] Using MFI, the demodulated MRF signal in the image domain $\mathbf{s}_o(\mathbf{r})$ at position **r** is

$$\mathbf{s}_o(\mathbf{r}) \approx \sum_{l=1}^{l=L} a_l\big(\mathbf{r}; \Delta B_o(\mathbf{r})\big)\, \mathbf{s}_l(\mathbf{r}), \qquad [6.4]$$

where $\{a_l(\mathbf{r})\}$ depend only on $\Delta B_o(\mathbf{r})$ and $\{\mathbf{s}_l(\mathbf{r})\}$ are image domain MRF signals from the Fourier transforms ($\mathfrak{F}$) of the corresponding k-space representations of the demodulated MRF signals $\{\mathbf{s}_l(\mathbf{k})\}$. That is,

$$s_{n,l}(\mathbf{r}) = \mathfrak{F}^{-1}\{s_{n,l}(\mathbf{k})\} = \mathfrak{F}^{-1}\{e^{-i2\pi f_l(T_{E,n}+t(\mathbf{k}))}s_n(\mathbf{k})\}, \qquad [6.5]$$

where f_l is the lth MFI basis frequency. The accuracy of Eq. (6.4) is limited by the number of basis frequencies used, as well as[179,182] by non-zero B_0 gradients. Eq. (6.4) can be used to help determine an estimate of $\Delta B_o(\mathbf{r})$ in the presence of fat as follows.

If we enforce consistency between the spatial representation of Eq. (6.1) and Eq. (6.4), and apply variable projection[61] (see also §2.3), we can form an objective function that depends on $\Delta B_o(\mathbf{r})$ and the given measurement. The signal is demodulated using Eq. (6.5), then fit for water and fat by Eq. (6.1) for each MFI basis frequency to give $\mathbf{s}_l(\mathbf{k})$ that is adjusted for fat blurring, then Fourier transformed to the image domain (see also §6.3.1.3). The problem statement is

$$\widehat{\Delta B}_0(\mathbf{r}) = \arg\min_{\Delta B_0} \left\| [I - AA^\dagger] \sum_{l=1}^{L} a_l(\Delta B_0(\mathbf{r}))\mathbf{s}_l(\mathbf{r}) \right\|_2^2. \qquad [6.6]$$

The matrix $A^\dagger$ denotes the pseudo-inverse of A {Eq. (6.2)}. Here, we have used the standard signal model assumption that the image is instantaneously acquired at the echo time. As mentioned above, the matrix A can be applied in the image domain by letting $t = 0$ in Eq. (6.3). The definition and dimensions of A are otherwise the same as in Eq. (6.2).

The memory requirements implied by Eq. (6.6) may be reduced by SVD compression. Depending on the number of MFI basis frequencies, *L*, solution implementation requires enough memory to store at least *L* MRF data sets. To reduce this, a basis set of orthonormal vectors, stored in a matrix $U \in \mathbb{C}^{N \times M'}$ that describe any $\mathbf{s}_l$, can be formed by SVD of an MRF dictionary that includes off-resonance/chemical shift effects. The number of columns M' in U is defined similarly to M, as the number of singular values necessary to capture a specified singular value energy. A set of coefficients $\{\mathbf{c}_l(\mathbf{k})\}$ that describe $\mathbf{s}_l(\mathbf{k})$ is given as

$$\mathbf{c}_l(\mathbf{k}) = U^H \mathbf{s}_l(\mathbf{k}). \qquad [6.7]$$

The spatial representations of these coefficients $\mathbf{c}_l(\mathbf{r})$ can be calculated as the (inverse) Fourier transform of their k-space representations. Combining Eq. (6.6) and (6.7) gives

$$\widehat{\Delta B}_0(\mathbf{r}) = \arg\min_{\Delta B_0} \left\| [I - AA^\dagger] \sum_{l=1}^{L} a_l\big(\Delta B_0(\mathbf{r})\big) U\mathbf{c}_l(\mathbf{r}) \right\|_2^2 . \qquad [6.8]$$

Eq. (6.8) can be solved by exhaustive search as discussed in Methods. MRF is known to estimate T_1 and T_2 accurately despite undersampling factors as large as 48.[67] Similarly, we test if the above expressions yield accurate fat-water separation with B_0 compensation in highly aliased/undersampled MRF data using the following phantom and *in vivo* experiments.

6.3. Materials and Methods

6.3.1 MRF image acquisition and processing

6.3.1.1 MRF sequences

To implement the proposed solution and compare it to standard MRF approaches, we designed three different MRF sequences. The proposed sequence permits chemical shift encoding through variable T_E. The next two sequences, based on standard MRF approaches, have fixed T_E and do not encode chemical shift information[iv]. All sequences used adiabatic inversion with an inversion time (T_I) of 40 ms, excitation with a sinc-gauss pulse and a time-bandwidth product of 10 to minimize B_1+ heterogeneity in the slice profile[173] and slice thicknesses of 5 to 30 mm (see below). Images were encoded using a numerically optimized spiral[42] with a fixed undersampling factor of 32, an acquisition time of approximately 5 ms and rotated 11.25° between excitations. In-plane image resolution ranged from 1.0 to 1.5 mm (see below).

[iv] An uSSFP MRF sequence with variable T_R and fixed T_E will experience non-zero phase evolution under $\Delta B_0 \neq 0$. In theory, such a sequence can store chemical shift information like a variable T_E sequence. However, in the original uSSFP publication, the pseudo-random variation in T_R was not intended to produce a coherent phase representation that can be used to estimate ΔB_0 or fat content. Rather, this reference reported insensitivity to off-resonance effects. As such, we do not directly consider direct fitting of fat or ΔB_0 using variable T_R MRF sequences in this work, though it may be an interesting subject of independent study.
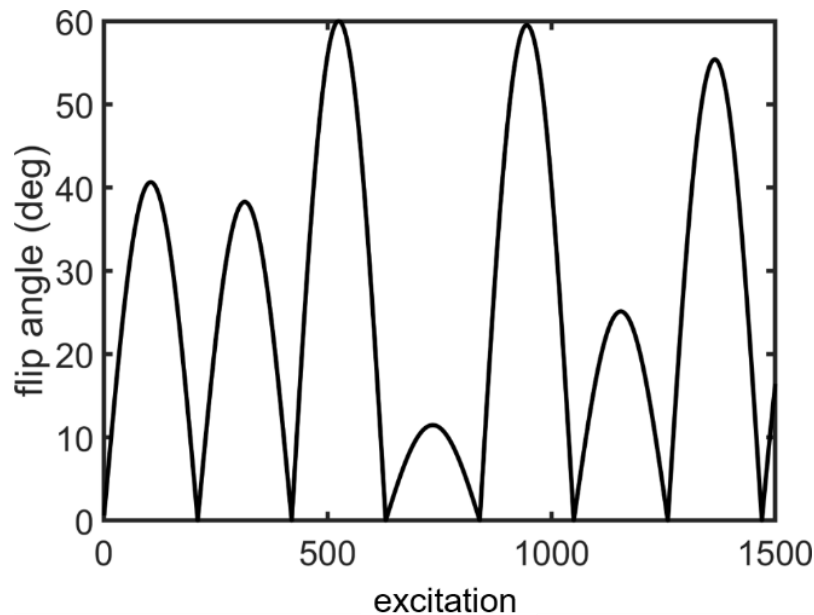
Fig. 6.1. Flip angle pattern for the variable T_E MR fingerprinting (MRF-varTE) and fixed T_E MRF sequence (MRF-fixTE).

The three MRF sequences differed as follows. The proposed variable T_E uSSFP MRF sequence (MRF-varTE) used 1500 excitations, fixed T_R of 16 ms, a linearly swept T_E from 3.5 to 7.5 ms over the 1500 excitations, fixed radiofrequency phase and a variable flip angle pattern (Fig. 6.1). The flip angle pattern was designed from half-sinusoids with randomly varying maximum amplitudes[67] no greater than 60°. The scan duration was 24 s. The first fixed T_E uSSFP MRF sequence (MRF-fixTE) used 1500 excitations, fixed T_R of 16 ms, a T_E of 4.65 ms, and the same flip angle pattern as MRF-varTE, for a scan duration of 24 s. The second fixed T_E MRF sequence used a variable T_R (MRF-varTR) with variable flip angle and T_R patterns (Fig. 6.2) with fixed T_E = 3.5 ms, adapted from the first MRF uSSFP (FISP) sequence[67]. The scan duration was 17.5 s.

All images were acquired on a 3T Philips Ingenia (Philips Healthcare, The Netherlands) with a 32-channel head coil for phantom experiments and brain acquisitions, a 16-channel transmit-receive knee coil for knee acquisitions, and a multi-channel anterior coil with integrated tabletop posterior coil for abdominal acquisitions.
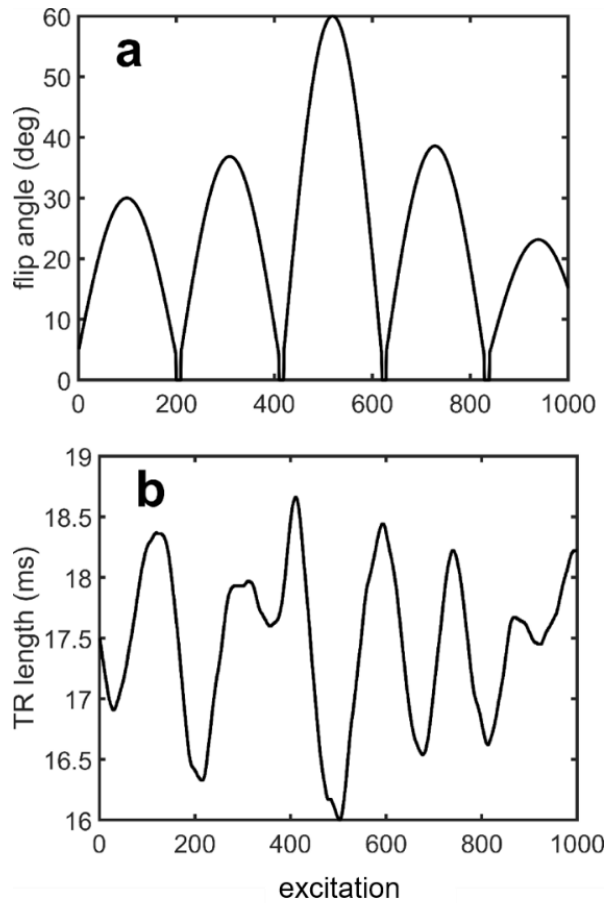
Fig. 6.2 Flip angle pattern (a) and repetition time length (b) for the variable T_R MR fingerprinting sequence (MRF-varTR). The flip angle sequence shape (with different scaling) and extension from minimum TR were adapted from Ref [67].

6.3.1.2 Image reconstruction and MRF T_1/T_2 estimation

Following k-space data acquisition, we reconstructed the undersampled MRF data using iterative sample density compensation[36] derived from fully-sampled k-space coordinates combined with SVD virtual coil compression by a factor of two, sensitivity map estimation using eSPIRIT[40], and gridding and coil combination using the Berkeley Advanced Reconstruction Toolbox (BART)[221]. The k-space trajectory was measured using an implementation[196] of the Duyn method[195]. The input for eSPIRIT used low resolution reconstructions generated from the inner 30 x 30 grid of k-space positions of each virtual

coil's MRF image stack. All processing was performed in MATLAB (The MathWorks, Natick, MA, USA).

Estimates for T_1/T_2 were made in the following way. We used an extended phase graph algorithm[31] to construct an on-resonance water dictionary using the following range of T_1, T_2, and B_{1+} values: (min:step:max): T_1 (ms) 10:10:90, 100:20:1000, 1040:40:2000, 2050:100:3000; T_2 (ms) 2:2:8, 10:5:100, 110:10:300, 350:50:800, 900:100:1500 (adapted from Ref[222]); B_1+ 0.5, 0.6, 0.7 0.75, 0.8:0.025:1.2, 1.25 1.3, 1.4, 1.5. MRF-fixTE and MRF-varTR T_1s and T_2s were fitted using the inner product of the compressed signal and time-compressed dictionary[70] constrained from independently measured 3D B_{1+} maps using the Yarnykh[223] method (except as noted) with high in-plane (2 mm x 2 mm) resolution and a 1.5-2 min acquisition time to ensure sufficient SNR. MRF-varTE water T_1s and T_2s were estimated in the same way but using the water signal following fat-water separation.

6.3.1.3 Implementation of MRF fat-water separation

Figure 6.3 provides a flowchart describing the fundamental steps of the proposed solution. The basic workflow is to reconstruct and combine coil images, perform a demodulation in k-space using the MFI basis frequencies, do a k-space fat-water separation, and then transform to the image domain and fit a B_0 map that yields the B_0-corrected coefficients used to reconstruct the fat and water signals.
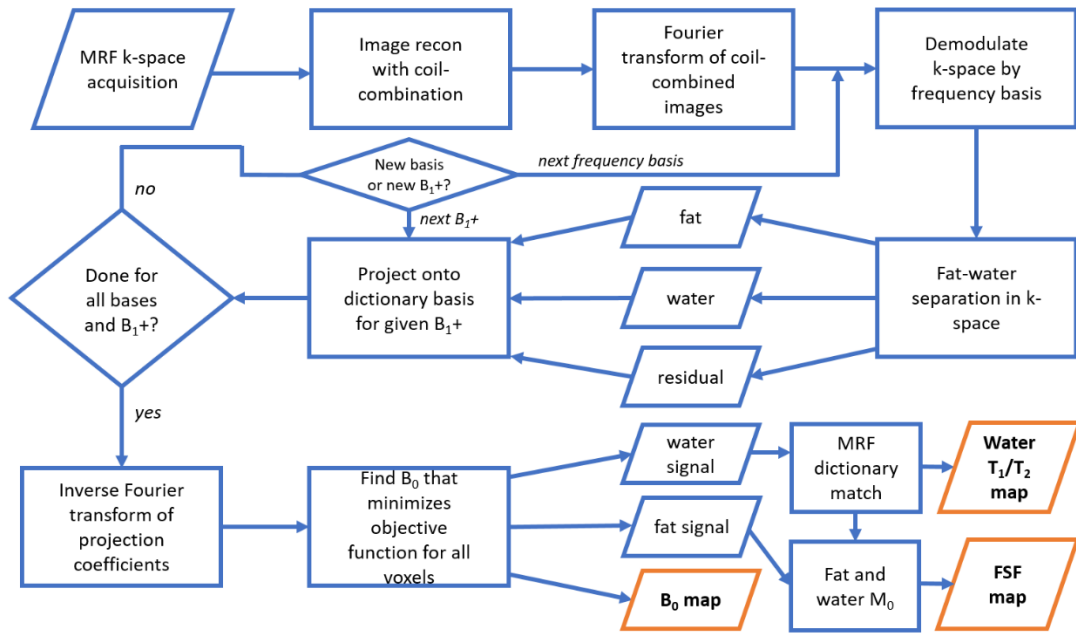
Fig. 6.3. A flowchart of the implementation for the proposed MR fingerprinting (MRF) fat-water separation technique. A fixed-T_R, linear swept T_E is used for the MRF acquisition. Following gridding and coil-combination, the MRF stack is transformed back into k-space and demodulated as described in §6.2. Fat-water-residual separation is performed in k-space for each demodulation frequency and each discretized B_{1+}. The water, residual, and deblurred fat components are projected onto an approximate basis of a dictionary that includes T_1, T_2, and off-resonance effects. The coefficients of this projection are transformed to the image domain and smoothed (not shown), and ΔB_0 at each voxel is fitted. The ΔB_0 estimate is then used to appropriately combine the water and fat coefficients to yield fat signal fraction (FSF), and water T_1 and T_2 maps.

The gridded and coil-combined k-space data were demodulated for each basis frequency and then separated into their fat-water-residual components. We defined basis frequencies as the 31 central Fourier basis frequencies over the time interval from $T_E = 0$ to 20% larger than the sum of the latest T_E and spiral acquisition time, discretized into the

number of spiral read points from a single interleaf with apodization as originally described for MFI[183]. This produced coefficients for B_0 values with normalized RMSE <1.5% over a frequency range of ±700 Hz within the shortest T_E to the longest T_E plus the spiral acquisition time. This bandwidth is sufficient to capture chemical shift combined with significant B_0 effects. The number of basis vectors in U (in Eqs. 6.7-8) and in $\{\mathbf{u}_m\}$ {in Eq. (6.2)} were defined as the rank of the SVD of the respective dictionaries that captured 99.99% of the singular value energy. The multi-peak fat model was defined as in Eq. (6.3) and used previously reported chemical shifts and estimated T_1/T_2 values of white adipose tissue[44] (Table 6.1). The fat-water fit was repeated for all discretized B_{1+} values. The fitted fat coefficients were projected onto the fat model $\mathbf{g}$ with $t = 0$ in Eq. (6.3). The resulting estimated fat and water signals and residuals were projected on the off-resonance dictionary basis for each voxel in gridded k-space for each discretized B_1+ value and frequency demodulation. The k-spaces of the fit coefficients were then converted to the image domain.

Following fat-water separation for all of k-space and conversion to the image domain, we smoothed the coefficient maps using a Gaussian kernel of 1.5 voxels. It was found empirically that this smoothing removed single voxel outliers in the ΔB_0 fits. We then fit for the B_0 map.

The ΔB_0 fitting was performed using Eq (6.8). The possible ΔB_0 values were discretized by 10 Hz increments and restricted to a range of ±250 Hz. For each voxel, linear combinations of the reconstructed signal were made with the precalculated coefficients $\{a_l(\Delta B_o)\}$ for all discretized ΔB_0 values to determine the ΔB_0 that minimized the objective function as stated in Eq. (6.8). The B_0-corrected water signal T_1 and T_2 values were estimated as described above. The water (W) and fat (F) magnitudes for each voxel were defined as the magnitudes of their respective M_0 estimates. M_0 for fat and water were calculated as the complex inner product of the B_0-corrected fat and water signal estimates with their respective signal models. The FSF, η, at each voxel was given as

$$\eta = \frac{F}{W+F}.$$
[6.9]

Table 6.1. Fat model parameters[†]

Model ppm	Descriptor	T_1 (ms)	T_2 (ms)	Peak weight*
5.3	Olefinic methine	421	44.1	0.122
4.65	Water	not fixed	not fixed	not fixed
4.2	Glycerol methylene	154	50**	0.064
2.75	Diallylic methylene	284	46.2	0.033
2.1	Methylene alpha to carbonyl	202	51.9	0.241/2***
2.1	Allylic methylene	249	51.9	0.241/2***
1.3	Methylene beta to carbonyl	240	54.7	0.500***
1.3	Bulk methylene	280	54.7	0.500***
0.9	Terminal methylene	543	80.1	0.144

[†]Adapted from observations from Hamilton *et al*. [44]

*Peak weights are relative to peaks at 1.3 ppm

**Not reported/estimated

***T_1/T_2 estimates of methylene alpha to carbonyl and allylic methylene from the observations by Ref. [44] were fitted at the same chemical shift and cannot be separated, so the peak weights for each peak were divided by two. The same rule was applied to the methylene beta to carbonyl and bulk methylene peaks.

6.3.1.4 Dictionary MRF fat-water separation

To compare with the proposed solution, we implemented an MRF fat-water separation in the image domain using an MRF dictionary with fat signal, without adjusting for spiral blurring. The fat-water dictionary was composed of discretized FSF (η = 0.0:0.05:1.0) using linear combinations[212] of the water dictionary and the multi-peak fat model with the MRF-varTE sequence. Reconstructed MRF images were then matched to the fat-water dictionary on a voxelwise basis to estimate water T_1, water T_2, and η.

6.3.2 Simulation studies

6.3.2.1 Simulation of T_1 and T_2 Bias Due to Fat

To understand better the potential for fat bias in MRF T_1 and T_2 estimates under ideal conditions, we numerically simulated fully-sampled MRF-varTE, MRF-fixTE and MRF-varTR signals. We then estimated the T_1 and T_2 for all sequences with fat-water separation for MRF-varTE and without fat-water separation for MRF-fixTE and MRF-varTR. The multi-peak fat model was defined as above. Linear combinations of the normalized fat and water signals with varying FSFs were simulated and matched against the water dictionary. The following T_1/T_2 combinations and FSF values were simulated: 500/30, 800/30, 1200/50, 1600/100, 2250/100 ms and η = 0.0:0.05:1.0. The simulation assumed zero noise. T_1 and T_2 were estimated as described above.

6.3.2.2 MRF Image Simulations

To assess the performance of the proposed method relative to MRF T_1 and T_2 estimation methods that do not account for fat, simulated measurements with undersampling and varying levels of noise were generated from a digital phantom. Since we were unaware of any consensus digital fat phantoms with varying water T_1 and T_2, we used a digital 240 x 240 Shepp-Logan phantom and arbitrarily assigned different segments of the phantom an FSF and one of the T_1/T_2 combinations used in §6.3.2.1. The FSF values were 0.0, 0.25, 0.5, 0.6, and 0.8. The total magnetization density was kept uniform throughout the image. The parameter assignments to each phantom segment are detailed in Figure 6.4 and Table 6.2. All simulated MRF stacks were subjected to ΔB_0 = 150 Hz.

Table 6.2. Image simulation segment properties

Segment	T_1 (ms)	T_2 (ms)	η
1	2250	100	0.60
2	1200	50	0.00
3	1600	100	0.50
4	500	30	0.25
5	800	30	0.80
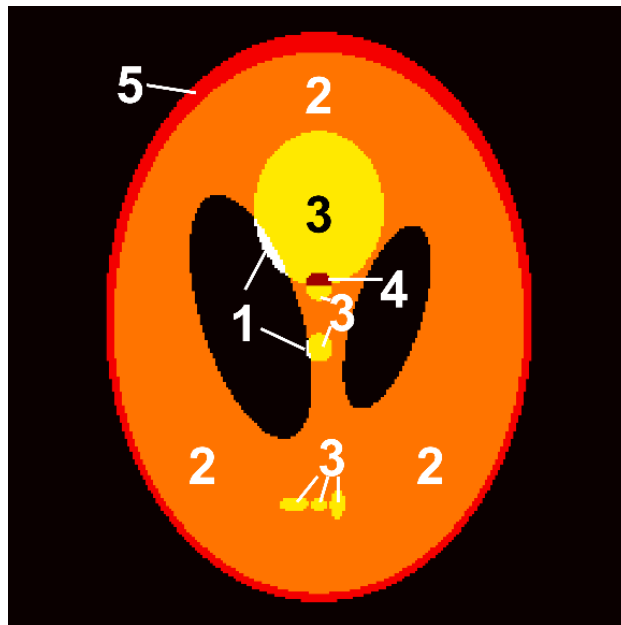
Fig. 6.4. The image simulation segmentation. Each numbered segment has the parameter values given in Table 6.2.

The undersampled spiral MRF acquisitions were simulated as described by Zhao *et al*[224]. Undersampled spiral images were generated by non-uniform fast Fourier transform[35] from a measured k-space trajectory used in this study. Blurring effects from chemical shifts and off-resonance were simulated using a spiral acquisition time of 5.0 ms and the measured trajectory. Complex white Gaussian noise was added in k-space to yield SNR values of 28, 32, and 38 dB as well as no added noise, as described in Ref[224]. All parameters were estimated for the proposed fat-water separation method using the MRF-varTE

simulations. T_1 and T_2 were estimated without fat separation for the MRF-fixTE and MRF-varTR simulations. Parameter bias for each voxel was calculated as the difference from ground truth. Uncertainty was quantified as the standard deviation (SD) of voxel bias to permit comparison of segments with differing T_1/T_2. Mean bias and SD of the bias were calculated for the entire non-zero image defined by ground truth.

6.3.3 Phantom experiments

6.3.3.1 FSF estimation with MRF direct match vs. k-space fitting

The proposed method, as well as a dictionary-based fat estimation, were used to measure FSF in a fat-water phantom. The phantom was composed of 50 mL conical centrifuge tubes filled with differing concentrations of peanut oil and aqueous agar doped with a gadolinium-based contrast agent.

The phantom was imaged with the MRF-varTE and spoiled gradient echo (SGPR) sequences. The images were reconstructed as described above, with an FOV of 240 mm x 240 mm, in-plane resolution of 1 mm x 1 mm and slice thickness of 8 mm. A 3D spoiled gradient echo (SPGR) sequence with 6 T_Es ($T_{E,min}$ = 1.5 ms, ΔT_E = 1.1 ms) with a flip angle of 3° was acquired and processed with a graph-cut-based fat-water separation algorithm with simultaneous B_0 and R_2^* correction[64], serving as FSF reference. The FSF was also estimated from MRF-varTE using the proposed solution and the dictionary-based fat-water separation.

The concordances of the two MRF FSF estimation methods with the SPGR reference were calculated. ROIs were manually drawn within each imaged phantom tube on a SPGR reference image. The means of the ROIs' FSFs were used to calculate the concordance correlation coefficients (CCC)[225] for the two MRF methods.

6.3.3.2 Variability of water T_1 and T_2 estimation with partial volume of oil

We constructed a phantom of distinct water and oil compartments with varying water T_1 and T_2 to test the proposed method across a broad range of water contrasts. Nine 50 mL conical centrifuge tubes were filled with 25 mL of deionized water with different concentrations of $MnCl_2$, over which 25 mL of peanut oil were added. This produced separated water and oil layers in each tube (Fig. 6.5). The tubes were then placed in a rectangular plastic container filled with a 2% aqueous agar gel to serve as a background signal. This fat-water layer phantom was imaged in cross-section with 3 cm slice thickness. Seven slice offsets were used, generating a different FSF for each slice. This permitted different T_1 and T_2 combinations across seven different fat fractions.
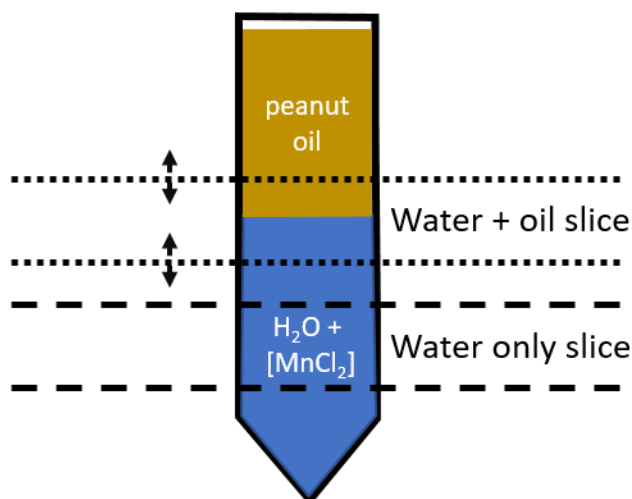
Fig. 6.5. Phantom and acquisition design of oil-water layer phantom (not to scale). Nine 50 mL conical centrifuge tubes were filled with 25 mL of $MnCl_2$-doped water and 25 mL of peanut oil. A 3 cm slice was used to acquire a water-only slice as well as several slices with different fractions of oil and water. This enabled many fat-fraction observations over nine different T_1/T_2 water combinations.

At each offset, images were acquired with all MRF sequences and a 2D SPGR sequence with the same echo time spacing and in-plane resolution described in §6.3.3.1. The through-slice position of the SPGR sequence was corrected by 1.2 mm to adjust for the different positions of the bulk methylene-water interface relative to the different RF

bandwidths of the MRF and reference SPGR sequences. This partially corrected for differences in the height of the oil-water interface from the different bandwidth pulses.

To assess the relative biases in water T_1 and T_2 estimation due to fat signal contamination, the deviations in each sequence's T_1 and T_2 estimates from consensus values were calculated as functions of oil content. The T_1 and T_2 values were estimated by all three MRF sequences in a slice that contained only water. These were averaged to yield water T_1 and T_2 consensus values for each tube. For each slice and MRF sequence, the T_1 and T_2 consensus estimates from each tube were subtracted from estimates with different fat fractions to determine the relative bias in estimated T_1 and T_2 for each FSF and MRF sequence. The SPGR data with graph cut processing (as in §6.3.3.1) was calculated for all slices/fat fractions and tubes for reference FSF values.

The accuracies of T_1/T_2 estimates in water for all MRF sequences were separately verified in a NIST-traceable MRI system phantom. All MRF sequences as well as conventional selective inversion recovery (SIR) and spin-echo (SE) sequences were used to estimate the T_1 and T_2 maps in an MRI system phantom (HPD, Boulder, Colorado) with NIST-traceable T_1/T_2 contrast spheres[186]. The SIR sequence used 11 T_Is: 50, 100, 200, 300, 500, 750, 1000, 1500, 2000, 3000 and 6000 ms. The SE sequence used 6 T_Es: 15, 30, 60, 120, 240 and 500 ms. Measurements were acquired at the specification temperature in the T_2 contrast spheres filled with $MnCl_2$. T_1 and T_2 estimates were made as described in §6.3.4 with the exception that the SE used a two-parameter fit without a noise bias correction because of the large range of T_2 values relative to the echo times.

6.3.3.3 Effect of B_0 on Proposed Method

To explore the effect of the in-line ΔB_0 fitting, the oil-water layer phantom was imaged under heterogeneous B_0 conditions and processed with and without the proposed B_0 correction. Cross-sectional acquisitions with the MRF-varTE and 2D SPGR sequence were selected at a single slice to produce FSF values ranging from ~10-30% across the different phantom tubes. Pencil-beam shimming was used to produce a reference scan with minimal B_0 variation, then the shimming was manipulated to produce a heterogeneous off-resonance pattern. The MRF data were processed with k-space fat separation with and

without the ΔB_0 fitting portion of the code, and the SPGR images were processed as in §6.3.3.1.

6.3.4. *In vivo* experiments

To assess the *in vivo* differences of the MRF methods, as well as the feasibility of the fat-water separation method proposed here, three subjects were imaged in three anatomical sites after providing informed consent and with the approval of the local institutional review board.

One subject was imaged in a sagittal plane in the left knee with all MRF sequences using in-plane resolution of 1 mm x 1 mm, 5 mm slice thickness, and an FOV 240 mm x 240 mm. For reference, we acquired the following scans: a six-echo 3D SPGR sequence with $T_{E,min}$ = 1.4 ms and ΔT_E = 1.1 ms; a fat-suppressed single-shot gradient echo inversion recovery (IR-TFE) sequence using a water excitation 1-3-3-1 binomial pulse, inversion times of 50, 100, 200, 500, 1000, 2000, and 6000 ms, and delay time (T_D) of 2500 ms with 2 averages; a fat-suppressed 20-echo multiple spin-echo (MSE) sequence using spectral adiabatic inversion recovery and extra olefinic saturation prepulse, Version S refocusing[28], minimum T_E = 20 ms, echo spacing 20 ms, T_R = 3000 ms; and T_1-weighted turbo spin echo (TSE) sequence with a T_R/T_E = 700/11 ms and TSE factor of 3. Besides the in-plane resolution for the MSE and IR-TFE acquisitions of 2 mm x 2 mm, all other spatial resolutions and slice thickness equaled those of the MRF sequences. All reference scans were reconstructed to the same FOV and in-plane resolution as the MRF images. FSF estimates from the SPGR were made as described in §6.3.3.1. The proposed fat-water separation was performed for the MRF-varTE sequence. T_1 and T_2 estimates were made using the acquired images (MRF-fixTE, -varTR) and the water images (MRF-varTE) as described above. For the IR-TFE acquisition, T_1 was estimated using a non-linear fit to the magnitude images with the following three-parameter signal model[226]

$$S(TI) = \left| S_o \left[S_f \left(1 - e^{\frac{-T_D}{T_1}} \right) e^{\frac{-T_I}{T_1}} + 1 - e^{\frac{-T_I}{T_1}} \right] \right|. \qquad [6.10]$$

Here, $S(T_{\mathrm{I}})$ is the signal at T_{I}, S_o is the equilibrium signal intensity, and S_f scales for imperfect inversion. T_2 was estimated from the magnitude MSE images using the following three parameter signal model

$$S(T_{\mathrm{E}}) = S_o e^{\frac{-T_{\mathrm{E}}}{T_2}} + \epsilon_o. \qquad [6.11]$$

Here, $S(T_{\mathrm{E}})$ is the signal at the given T_{E}, S_o is a scaling factor, and ϵ_o accounts for a noise floor. To better evaluate parameter estimates, T_1 and T_2 maps were masked using the SPGR water image with a threshold based on Otsu's method[190].

The second subject was also imaged with SPGR and MRF sequences in the transverse direction in the brain at the level of the orbits. The resolution, FOV and SPGR T_{E}s were the same as those for the knee.

To provide proof-of-concept of the proposed method in a region sensitive to respiratory motion, the third subject was imaged in a transverse plane in the abdomen with the MRF-varTE sequence and processed with the proposed method. The resolution and FOV were 1.5 mm x 1.5 mm with slice thickness 8 mm, and 480 mm x 480 mm, respectively. To permit faster acquisition, a B_{1+} map was estimated using dual refocused echo acquisition mode sequence[227] with a scan duration of 8 s. Separate end-exhalation breath-holds were used for the MRF and B_{1+} acquisitions.

6.4. Results

6.4.1. Simulation Studies

Figure 6.6 shows the results of simulations of T_1 and T_2 biases due to fat for the different MRF sequences. The fitted T_1s are unbiased for the MRF-varTE (with fat separation) for $\eta < 1.0$ (Fig. 6.6a). They decline approximately linearly for the MRF-fixTE sequence (Fig. 6.6b), and sharply increase then decrease for the MRF-varTR simulations (Fig. 6.6c). Biases without fat-separation exceed several hundred ms and even saturate for

the MRF-varTR results at the 3000 ms limit of T_1 in the dictionary. The simulated water T_2 estimates are unbiased for the MRF-varTE with the proposed method (Fig. 6.6d) and vary for the MRF sequences without fat separation (Figs. 6.6e, f).
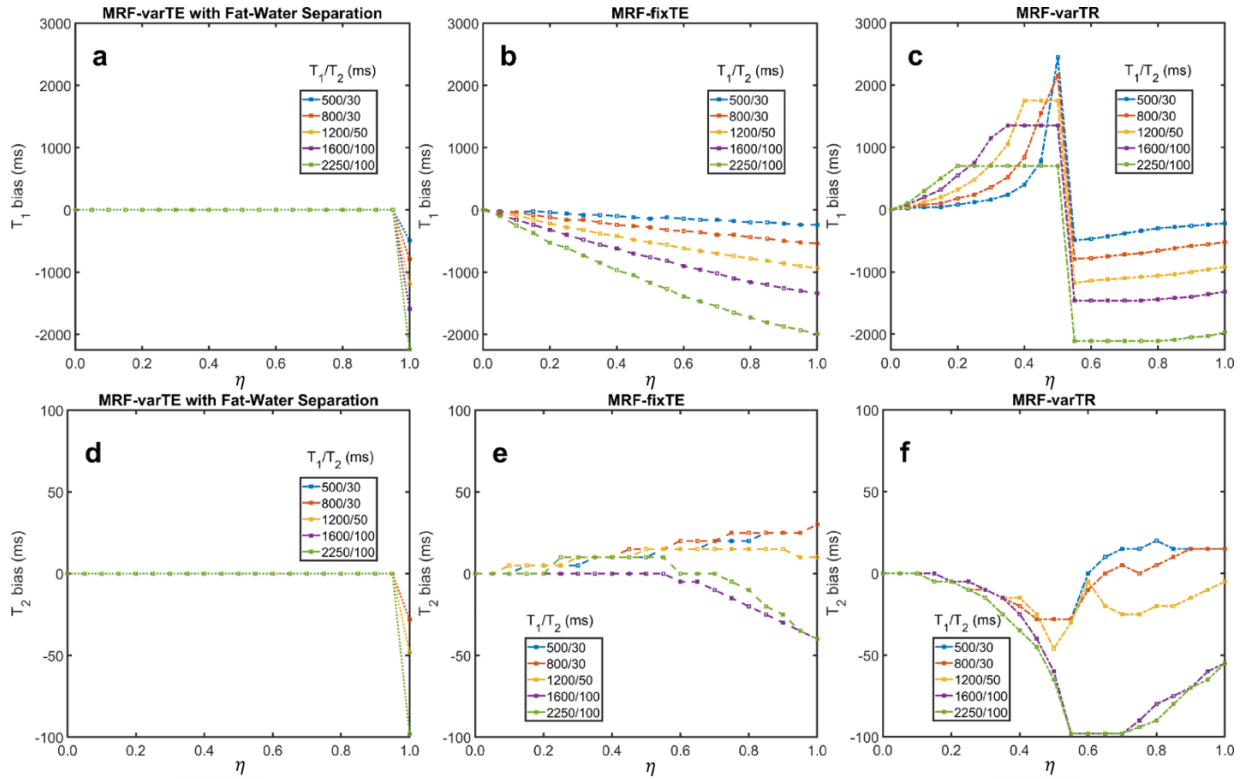
Fig. 6.6. Simulated water T_1 and T_2 bias from fat using MRF sequences. This simulation used the variable T_E MR fingerprinting (MRF) sequence with the proposed fat-water separation (MRF-varTE), as well as the fixed T_E (MRF-fixTE) and fixed T_E/variable T_R MRF sequence (MRF-varTR) without fat-water separation. The simulated signals were fully sampled without blurring effects, noiseless and matched against a water-only dictionary for fat signal fractions (FSF) from 0.0 to 1.0 in increments of 0.05. The T_1 bias (a-c) and T_2 bias (d-f) for five listed T_1/T_2 combinations as a function of fat signal fraction (η) are shown. MRF-fixTE is in-phase with the main methylene peak of fat whereas MRF-varTR is approximately opposed phase. Water T_1 and T_2 bias in the proposed method (a, d) occur only when water is entirely absent (η = 1.0) and is otherwise zero. The T_1 positive bias is so large for the MRF varTR sequence (c) that it is saturated due to the maximum T_1 used in this study (3000 ms).

The image simulation results show that the proposed method reduces T_1 and T_2 bias and uncertainty, relative to MRF without fat separation. Figure 6.7 presents the ground truth and estimated parameters from all MRF sequences for the lowest SNR simulated (28 dB). Bias and blurring from fat signal and from off-resonance B_0 can be seen in the MRF-fixTE and MRF-varTR T_1 and T_2 maps. In comparison, the MRF-varTE parameter maps show closer agreement to the ground truth T_1 and T_2 as well as sharper geometric definition. The mean T_1 bias without fat separation drops from about -150 ms to less than 5 ms with fat separation (Fig. 6.7c). Bias reduction using the proposed method can also be observed for T_2. The standard deviations (SDs) of the bias for the proposed method are reduced by a factor of approximately three to five for T_2 and T_1, respectively (Fig. 6.7c). Decreases in SDs can be seen for the proposed method as the noise level decreases. The proposed technique has bias in $\eta \leq 0.017$ (≤ 0.025 SD) and ΔB_0 bias ≤ 1 Hz (≤ 6 Hz SD) for all noise levels.
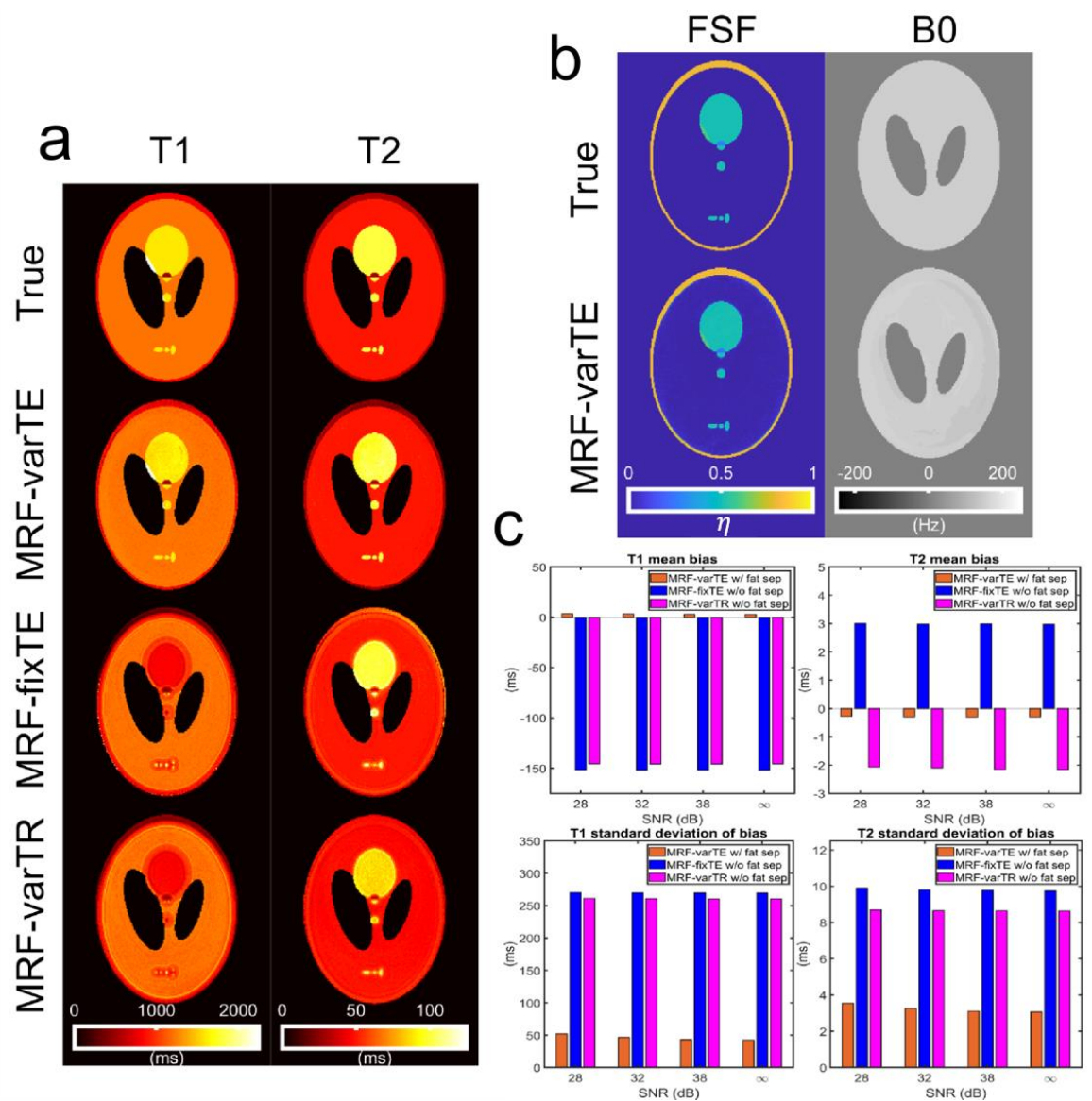
Fig. 6.7. Example parameter estimates for the MR fingerprinting image simulations and associated bias plots. The example maps here use an SNR of 28 dB, an undersampling factor of 32, and a spiral acquisition time of 5.0 ms. The T_1 and T_2 maps (a) from the MRF-varTE sequence with fat separation exhibit reduced bias compared to the MRF-fixTE and MRF-varTR which do not use fat separation or account for spiral blurring due to ΔB_0/fat chemical shift. The fat signal fraction and B_0 map for the MRF-varTE method (b) generally agrees with the ground truth. T_1 and T_2 estimation bias and the standard deviation of the bias are reduced at all noise levels for the MRF-varTE with fat separation simulations relative to the MRF techniques without fat separation (c).

If the parameter estimates are made from fully-sampled and zero-noise images, the mean T_1 and T_2 biases and SDs drop to zero for the proposed method (Figs. 6.8-9). In contrast, the biases and SDs of all segments for the MRF estimates without fat separation approximately equal those from the undersampled, noisy simulations.
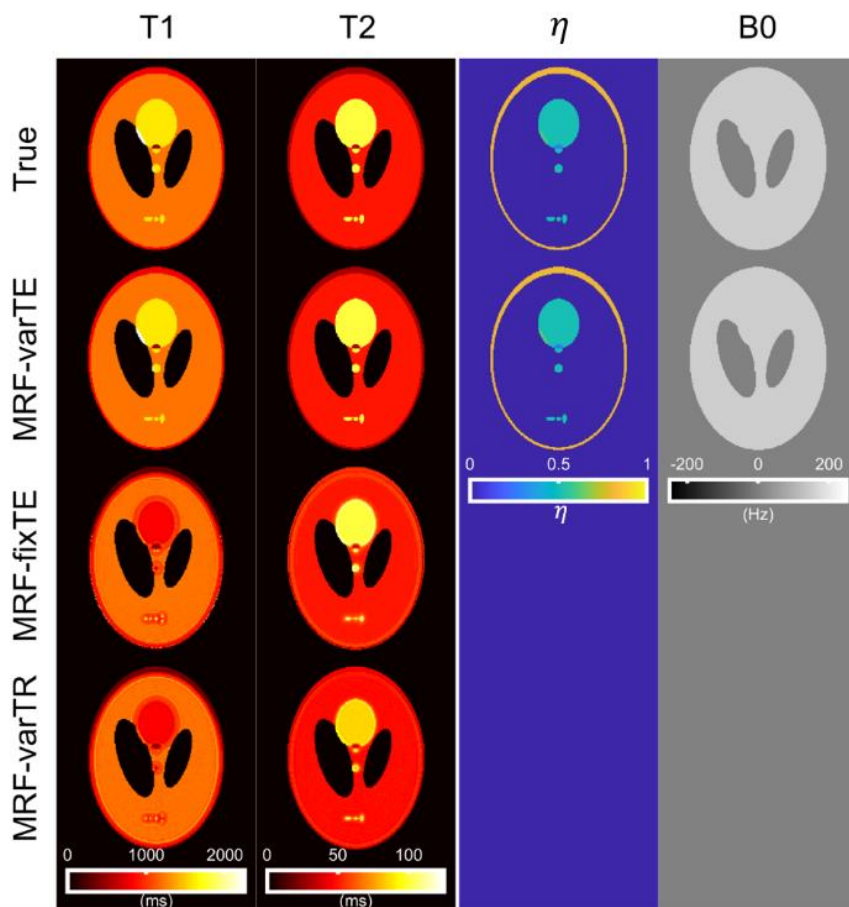
Fig. 6.8. Simulated image parameter maps from the fully sampled simulations without noise. This figure corresponds to Fig. 7, except fully-sampled Cartesian encoded data was used for fitting and no noise was added. Simulated acquisition timing matched that in Fig. 7, which results in the same blurring for MRF-fixTE and MRF-varTR as in Fig. 6.7. The bias and standard deviation of the bias are shown in Fig. 6.9.
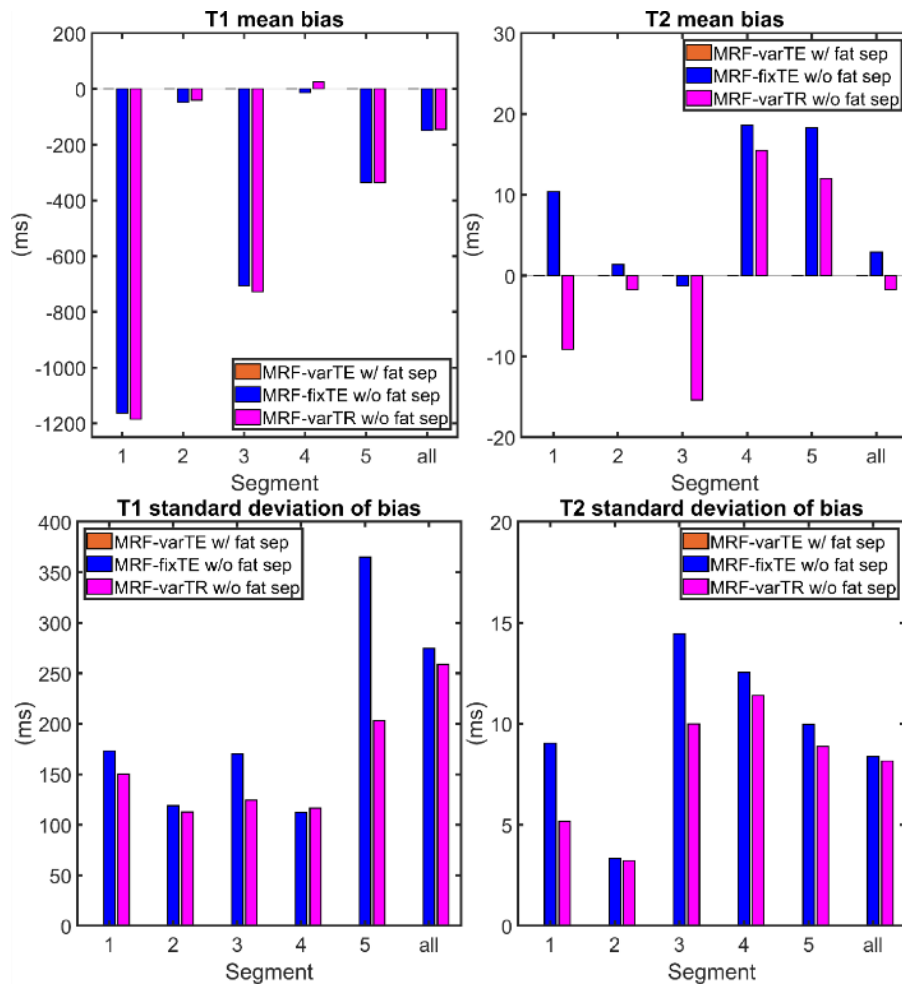
Fig. 6.9. Bias plots for the fully sampled image simulations without noise. All segments correspond to those in Fig. 6.4 and Table 6.2. The parameter maps can be seen in Fig. 6.8. The bias and standard deviations for the proposed technique are effectively zero.

6.4.2 Phantom Studies

The concordance of the dictionary and k-space MRF fat-separation methods with the SPGR-derived estimate for FSF exceeded 0.980 in both cases (Fig. 6.10). However, the dictionary-based method has blurring artifacts on the outer edges of the phantom tubes due to the fat chemical shift. There are also asymmetric features that are likely due to B_0 inhomogeneity. The k-space method with B_0 correction FSF map does not show these artifacts.
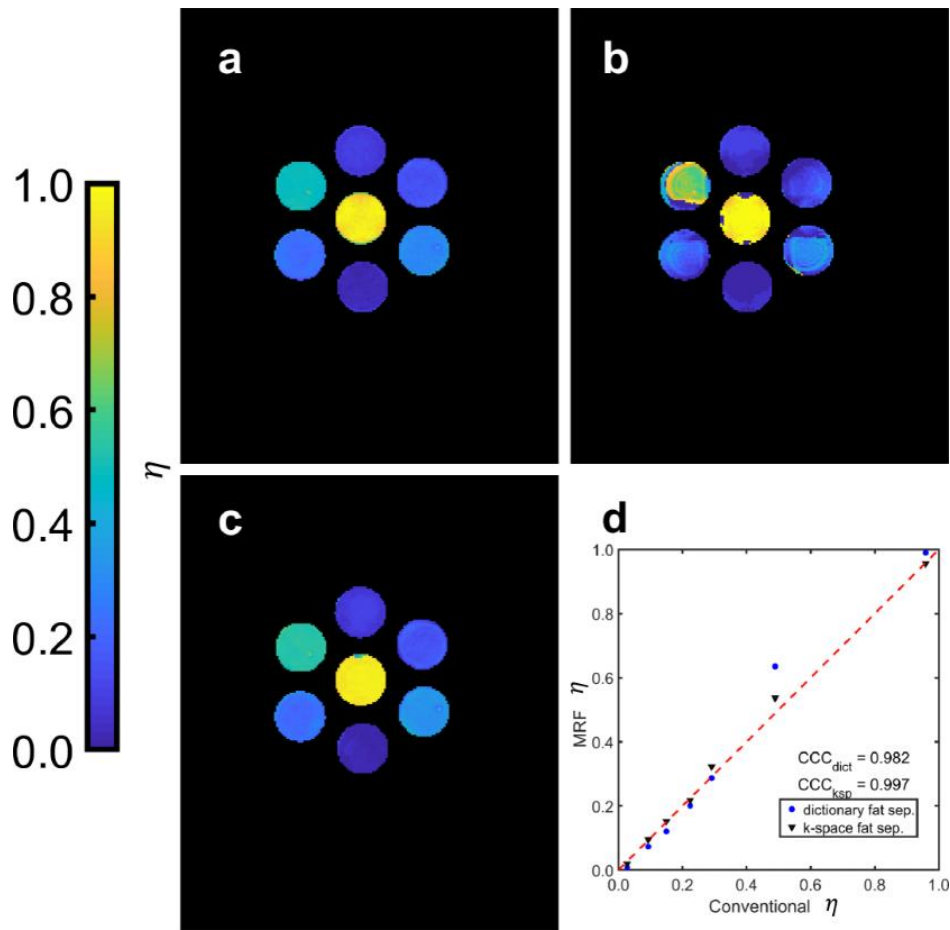
Fig. 6.10. Fat signal fraction (η) fitting with conventional and MRF techniques. The fat signal fraction maps from a spoiled gradient echo (SPGR) sequence (a), a variable-TE fixed-TR (MRF-varTE) sequence estimated via direct dictionary matching (b) and the proposed k-space based method (c) are shown for a phantom with different fat fraction emulsions. The concordance of the two MRF methods with the SPGR method is graphed in (d) with calculated concordance correlation coefficients (CCC) and a line representing perfect concordance for visual reference. Asymmetries and ring artifacts can be seen in the direct matching map (b).

The CCCs of all MRF and conventional T_1 and T_2 estimates in the MRI system phantom relative to specifications were ≥ 0.988 and ≥ 0.978, respectively (Fig. 6.11).

For the oil-water phantoms, the T_1 and T_2 deviations from water reference values with increasing oil-fraction are smaller for the MRF-varTE than for the MRF methods without fat separation. Figure 6.12 shows example T_1 and T_2 maps in the water-only slice

100

and a slice that contains ~30 to 50% fat signal. The water T_1s and T_2s range from approximately 300 to 1500 ms and 30 to 180 ms, respectively. The MRF T_1 and T_2 estimates in the water layer were consistent; the maximum absolute difference between each MRF sequence's estimate and the averaged values for each tube were 17 ms and 3 ms for T_1 and T_2, respectively. The T_1 values for the oil-water slice are mostly lower than those from the water-only slice, with the MRF-varTR sequence changes being the most variable. The MRF-fixTE and MRF-varTR exhibit greater deviations than the MRF-varTE with fat separation (Fig. 6.12a-f). The T_2 maps in Fig. 6.12 appear to show slightly reduced, relatively unchanged, and widely varying changes in the oil-water slice relative to the water-only slice for the MRF-varTE with fat separation, MRF-fixTE and MRF-varTR, respectively.
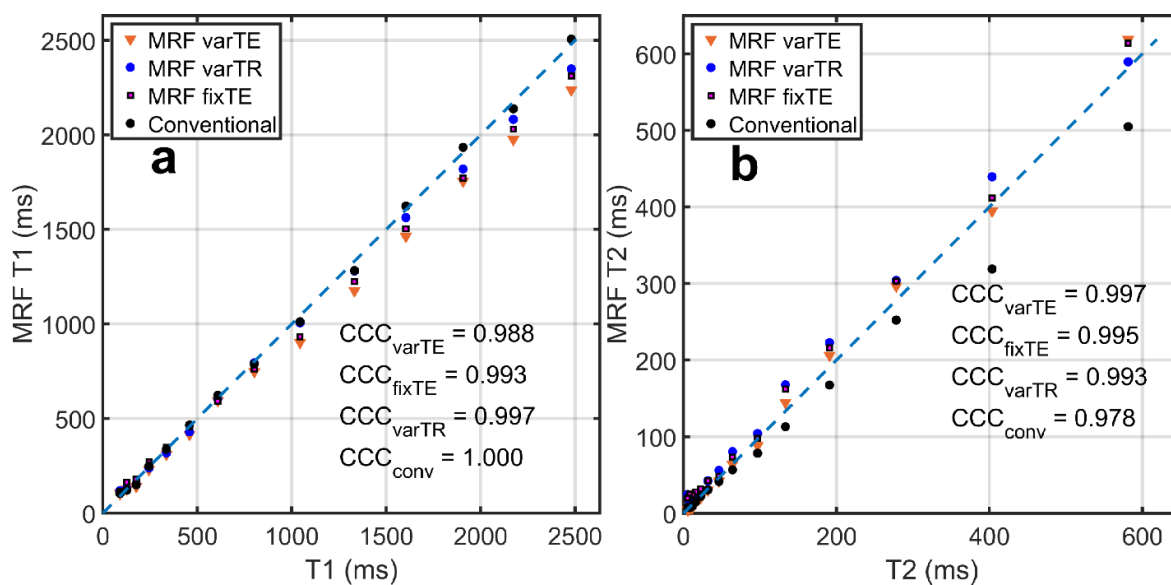
Fig. 6.11. Comparison of T_1 and T_2 estimates from MRF and conventional techniques. MR fingerprinting variable T_E with proposed fat-water separation (MRF-varTE), fixed-T_E (MRF-fixTE), variable T_R (MRF-varTR) and conventional selective inversion recovery (SIR) and spin-echo (SE) sequences were used to estimate the T_1 and T_2 maps in an MRI system phantom. Concordance correlation coefficients (CCC) for each acquisition is listed relative to the specification values.

Figure 6.13 plots the differences in T_1 and T_2 estimates from the water-only slice consensus values for all tubes and all oil-water slices as a function of FSF (including water

only). At $\eta > 0.15$, much wider perturbations in estimated T_1 are seen with the MRF-fixTE and MRF-varTR than with MRF-varTE with fat separation. The T_2 deviations of the MRF-varTR are greater than those of the MRF-varTE and MRF-fixTE, whereas MRF-varTE deviations are more negative than those of MRF-fixTE. The general variation in T_1 with increasing FSF are similar to the simulation (Fig. 6.6) results for each sequence.
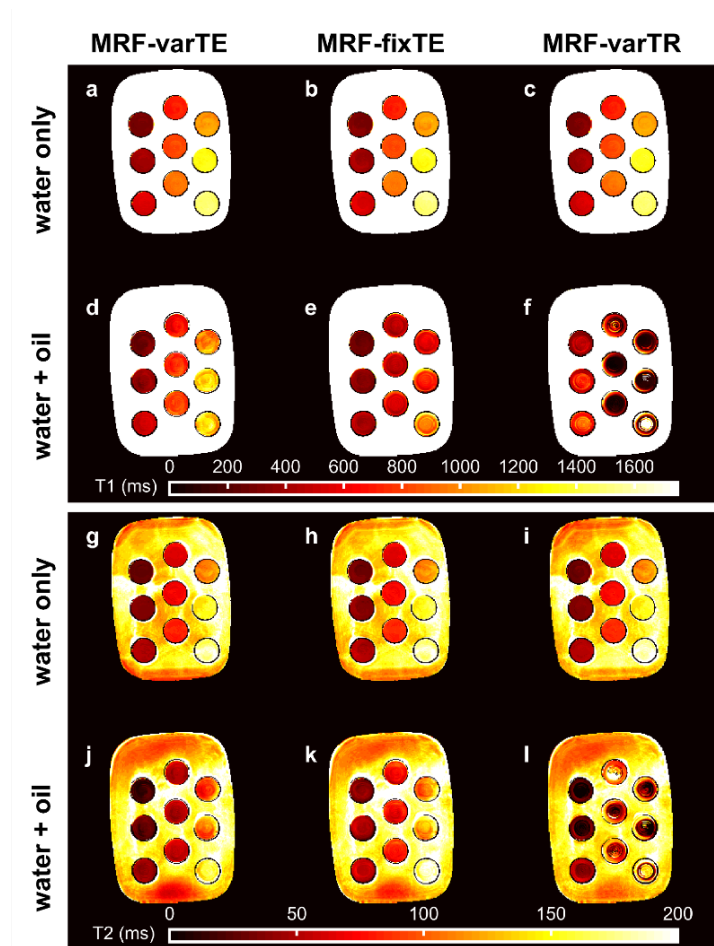
Fig. 6.12. The MR fingerprinting (MRF) T_1 and T_2 maps from the oil-water phantom. The MRF-varTE sequence uses the proposed k-space fat-water separation whereas the MRF-fixTE and MRF-varTR sequences do not separate fat from water. The T_1 estimates from a pure water layer within the phantom tubes (a-c) are shown above the T_1 estimates from an oil-water layer (d-f). The T_2 estimates are arranged as the T_1 maps with water-only T_2 estimates in (g-i) above the oil-water T_2 estimates (j-l) and the same MRF sequence order from left to right. The largest deviations from the water-only T_1 and T_2 values can be seen in (e, f, l).
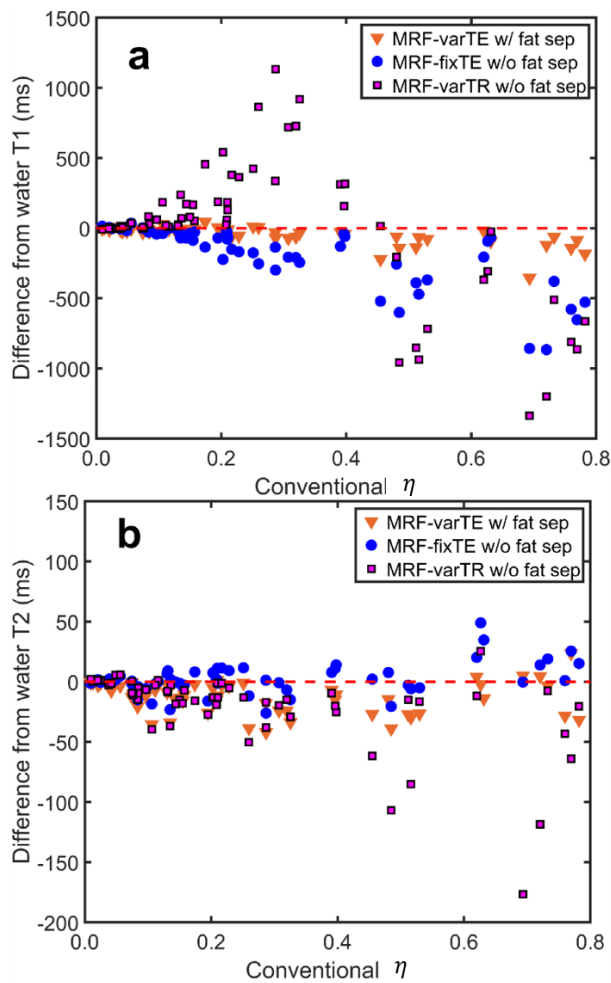
Fig. 6.13. The deviations in MR fingerprinting (MRF) estimated T_1 and T_2 with fat signal fraction (η) in the oil-water phantom. The difference from the consensus T_1 estimates for all T_1/T_2 tube combinations and all measured slices is shown for the proposed k-space fat-water separation (MRF-varTE) and fixed-T_E/variable-T_R MRF methods without fat-water separation, plotted against η estimated from a spoiled gradient echo sequence (a). The changes in estimated T_2 versus η are plotted in (b).

Figure 6.14 plots FSF estimates from the proposed MRF method against the SPGR-derived values for all tubes and oil-water slices. Example FSF and B_0 maps are also shown. The FSF maps indicate general agreement between the FSF and graph cut fat-water separation across the phantom tubes. The B_0 maps show perturbations within 100 Hz, with more discretization and lower B_0 estimates in the MRF map relative to the SPGR derived

map. The FSF estimates are concordant with CCC = 0.990 across the different tubes with differing T_1 and T_2.
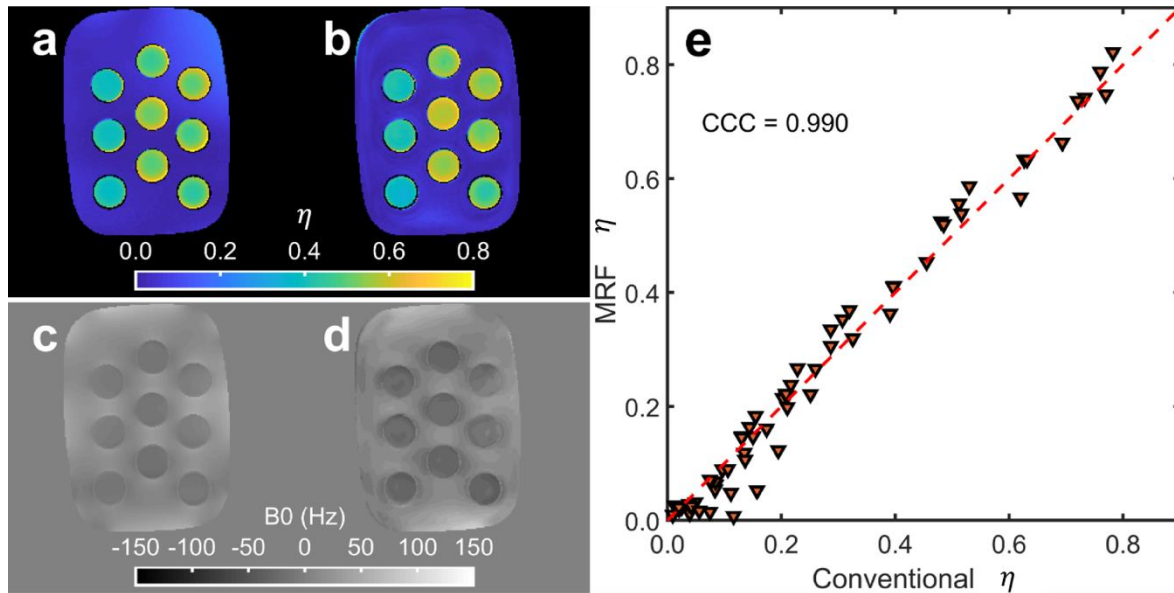
Fig. 6.14. Example fat signal fraction (η), B_0 maps and η concordance over a large range of T_1/T_2s from the oil-water phantom. The conventional spoiled gradient echo (SPGR) (a) and proposed MR fingerprinting (MRF) (b) η estimates are shown with the estimated SPGR (c) and MRF (d) B_0 maps from the oil-water phantom slice shown in Fig. 6.12. The η concordance between the MRF and SPGR method is plotted in (e) for all measured water/oil-water layers across all T_1/T_2 tube combinations with the concordance correlation coefficient (CCC) displayed.

Figure 6.15 shows the results from the poorly shimmed condition at an FSF layer of ~10 to 30%. Without B_0 correction, the k-space-based MRF fat-water separation FSF bias is substantial in regions with high B_0. The B_0 estimate from the graph cut processing appears more negative than that from the MRF method. Fat-water swaps are visible at the extreme limbs of the phantom of both methods.

Figure 6.16 provides example T_1 and T_2 maps from the well shimmed and poorly shimmed slice, without and with B_0 correction. Without B_0 correction, substantial deviations in T_1 and T_2 are observed in regions of B_0 perturbation. These deviations are reduced by > 100 ms in some cases with the proposed B_0 correction.
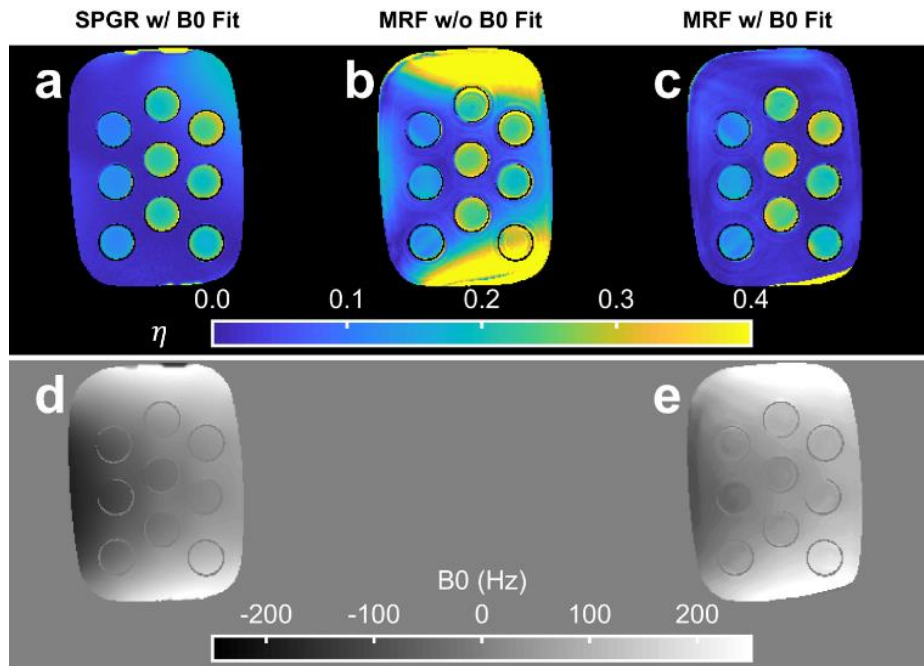
Fig. 6.15. The fat signal fraction (η) and ΔB_0 estimate from conventional and MR fingerprinting (MRF) methods. The FSF maps for a single slice in the oil-water phantom with heterogeneous B_0 are shown for the reference spoiled gradient echo (SPGR) with graph cut processing (a), the MRF k-space based fat separation method without B_0 correction (b) and the MRF k-space based fat separation method with B_0 correction (c). The estimated SPGR (d) and MRF (e) B_0 maps are also displayed. The data are from the same slice as depicted in Fig. 6.16.
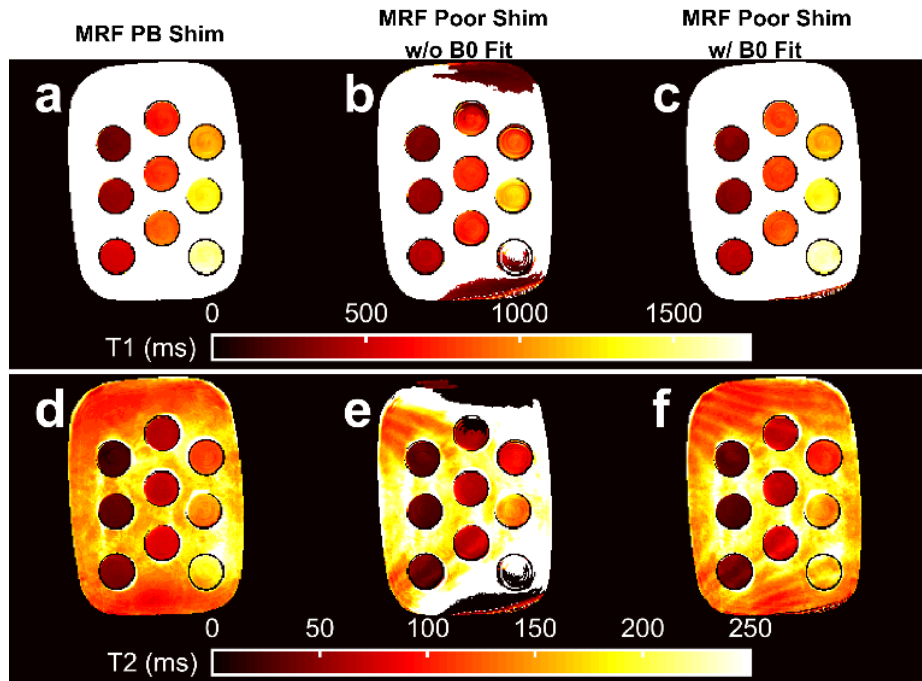
Fig. 6.16. The MR fingerprinting (MRF) estimated T_1 and T_2 maps without and with B_0 correction. Variable T_E MRF T_1 and T_2 maps with pencil-beam (PB) shimming (a, d) are shown for comparison with poorly shimmed T_1 and T_2 maps from MRF k-space fat-water separation without B_0 correction (b, e) and k-space fat-water separation with B_0 correction (c, f). The data are from the same slice as depicted in Fig. 6.15.

6.4.3 *In vivo* studies

Figures 6.17 and 6.18 show the FSF, T_1 and T_2 maps from the knee and brain. The knee FSF maps between the SPGR and MRF data appear largely consistent (Fig. 6.17b). Compared to the SPGR measurement, the MRF FSF appears slightly lower in the gastrocnemius and biceps femoris and slightly higher in the subcutaneous and intermuscular fat regions. The fat-suppressed IR-TFE and MSE measurements appear mostly uniform across the main muscle groups visible in the parameter maps (Fig. 6.17c, d). The MRF T_1s appear lower than the IR-TFE measurements within the main muscle bodies and higher in T_2 than the MSE measurements. The MRF-fixTE and MRF-varTR T_1 and T_2 exhibit bands of lower and higher T_1 and T_2 estimates near the muscle-fat interfaces throughout the FOV. The B_0 and FSF maps from the brain from the proposed method are similar to the SPGR reference maps (Fig. 6.18). The periorbital fat is clearly defined on the

FSF maps, with low FSF in the brain and optic nerve tracts. The conventional and MRF B_0 maps both reveal increases in B_0 superior to the temporal bone. Deviations from the FSF and B_0 maps include fat-water swapping in the anterior orbits and in a small region in the optic nerves, as well as a posterior circular flow artifact. T_1 and T_2 maps in the brain appear similar in all MRF methods except for the orbits, optical nerve, and regions near extracranial fat.

The abdominal MRF data was successfully acquired in a single breath hold and can be seen in Fig. 6.19. Fine features of visceral, subcutaneous and marrow fat can be visualized in the FSF map. The fat-separated T_1 and T_2 estimates of the liver are 1,093 and 19 ms, respectively. In comparison, 3 T MR spectroscopy water relaxometry estimates of the liver from the literature are 990 (SD 89) ms for T_1 and 30 (SD 2) ms for T_2.[228]
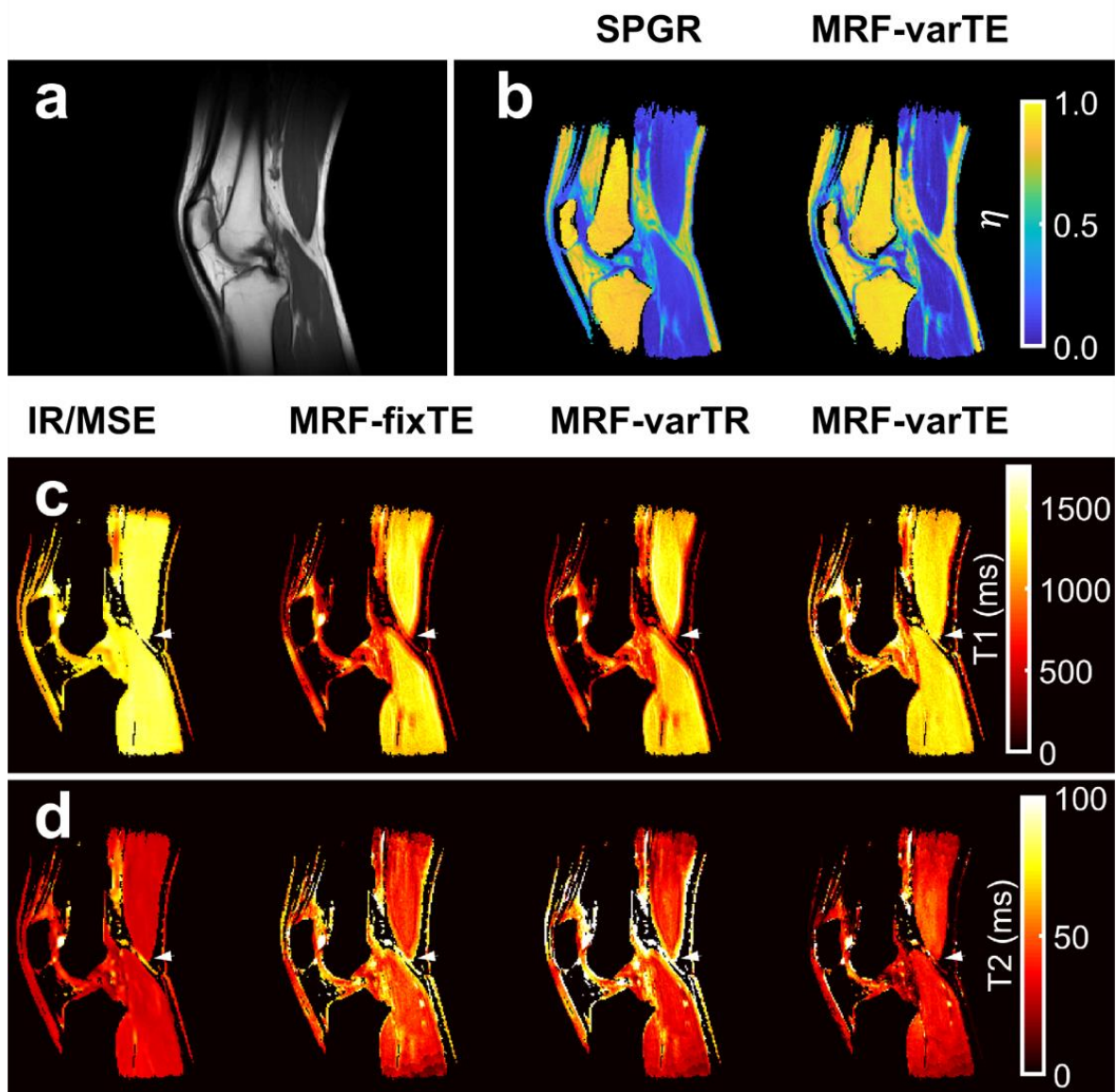
Fig. 6.17. Multi-parametric knee maps. An anatomical reference from T_1-weighted images (a) with fat signal fraction (η) maps from spoiled gradient echo (SPGR) and the proposed MR fingerprinting fat-water separation methods (b) are shown. The T_1 maps (c) from fat-suppressed inversion recovery (IR-TFE) are shown next to the MRF fixed T_E (MRF-fixTE), MRF variable T_R (MRF-varTR) without fat-water separation and the proposed method with fat-water separation using MRF variable T_E (MRF-varTE). The fat-suppressed multiple spin-echo (MSE) T_2 maps are shown adjacent to the MR-fixTE, MRF-varTR and proposed method acquired with MRF-varTE T_2 estimates (d). Parameter maps were masked using the SPGR derived water image and threshold. Bands of lower T_1 and higher T_2 appear near fat-muscle

interfaces in the MRF-fixTE and MRF-varTR parameter maps, which do not account for fat. An arrowhead marks a point on all T_1/T_2 knee parameter maps where there are multiple fat-muscle interfaces and the banding effect is pronounced.
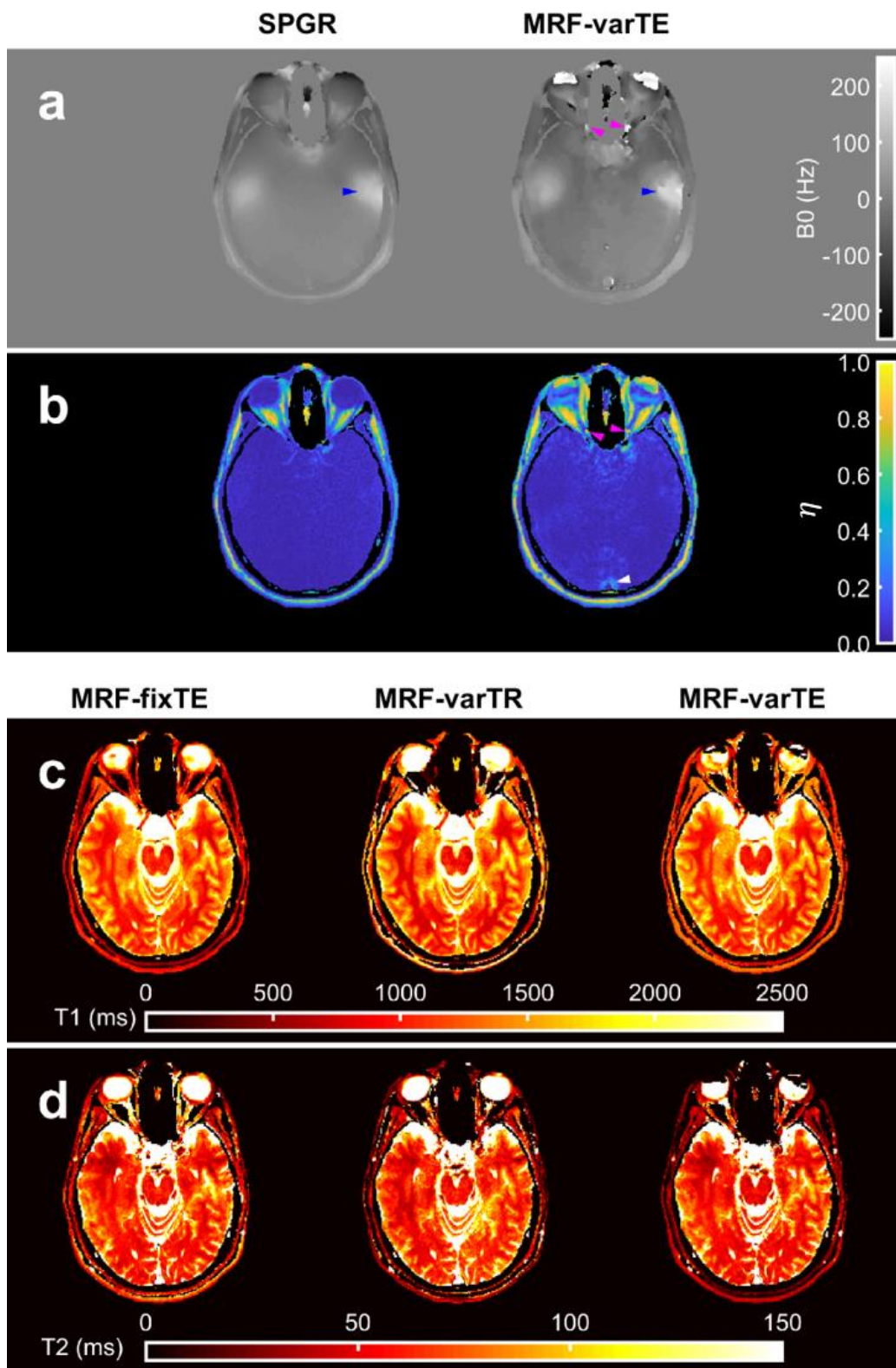
Fig. 6.18. (Previous page) Multi-parametric maps of the brain. The B_0 maps from the spoiled gradient sequence with graph cut processing (SPGR) and the proposed MR fingerprinting (MRF) fat-water and B_0 estimation method with variable T_E (MRF-varTE) are shown (a), with the corresponding fat signal fraction maps (b). The MRF method has general agreement with the SPGR. Blue arrows indicate a region superior to the temporal bone featuring increased B_0 heterogeneity in both methods, which is also present on the contralateral side (unmarked). Deviations between the methods include fat-water swapping in the anterior orbits and small sections of the optic nerves (magenta arrows), and the MRF FSF map indicates an area of a flow artifact (white arrow). The MRF T_1 (c) and T_2 maps are shown for the MRF methods without fat-water separation (MRF-fixTE/-varTE) and the proposed fat-water separation using MRF-varTE. The slice thickness (5 mm) is thicker than the optic nerve diameter so may include a partial volume of CSF.
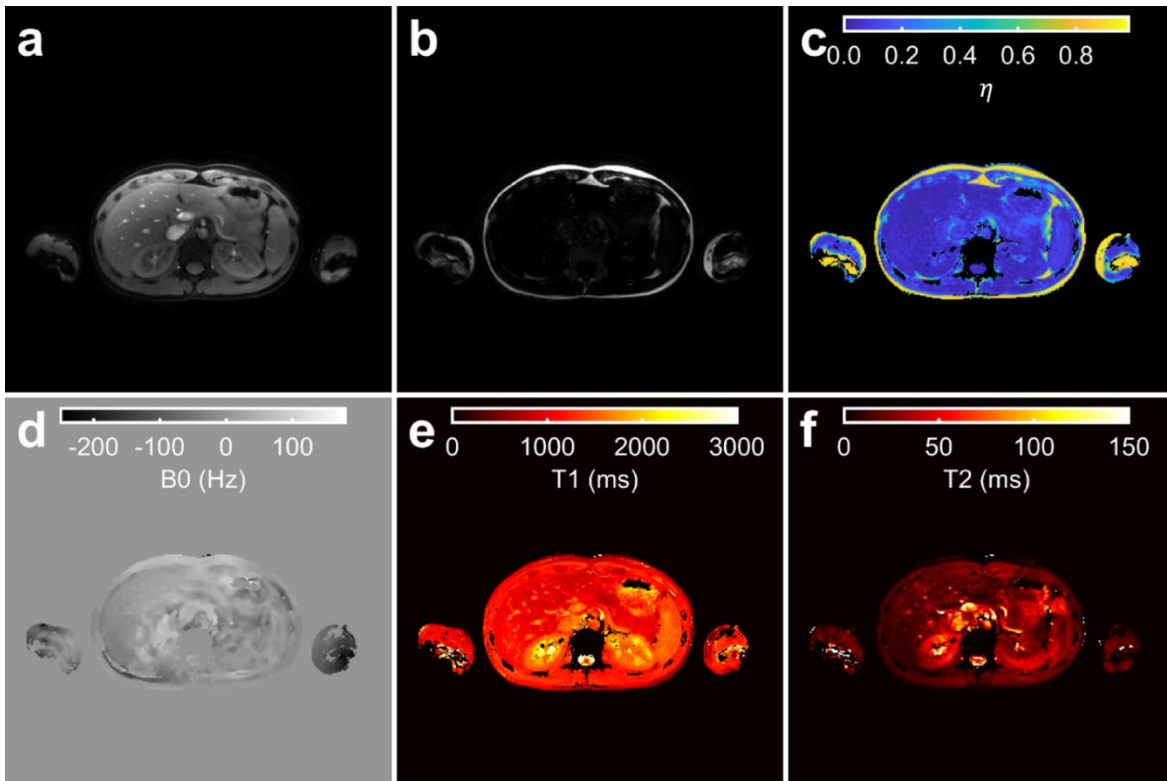
Fig. 6.19. The proposed MR fingerprinting method applied in the abdomen. The water (a) and fat (b) images, and fat signal fraction (η) (c), B_0 (d), T_1 (e) and T_2(f) maps estimated by the proposed technique are shown for a single slice in the liver. Parameter maps (c-f) were masked using the sum of the water (a) and fat (b) magnitude images with a threshold. The MRF and B_{1+} acquisitions were separately acquired using end-expiration breath holds.

6.5 Discussion

The results indicate that small fractions of fat signal significantly bias T_1 and T_2 water estimates from MRF techniques that do not consider fat. The proposed MRF method ameliorates these biases, circumvents spiral blurring, and incorporates a B_0 correction that substantially improves parameter map quality.

The simulation, phantom, and *in vivo* results all show that fat biases MRF T_1 and T_2 estimation. This bias in T_1 can exceed 200 ms at $\eta > 0.2$ (Figs. 6.6-9,6.13). From the image simulations, the noiseless, fully sampled MRF parameter estimates without fat separation

were equally biased as the noisy, undersampled estimates, suggesting that fat signal contamination may in some cases be the dominate form of bias, relative to instrument noise or aliasing. The knee results (Fig. 6.17) showed that in regions which do not contain fat, bias may be avoided by excluding regions close to fat from analysis. However, fat signal contamination of the T_1 and T_2 estimates may be inescapable if fat is diffusely spread throughout, or immediately adjacent to, the tissue of interest. This is common in nonalcoholic fatty liver disease[112], pancreatic steatosis[229], fat-infiltrating myopathies[200], and pericardial fat[230].

The proposed MRF fat separation method reduces bias of T_1 and T_2 due to fat, relative to the MRF-fixTE and MRF-varTR techniques; it also provides FSF estimates. Figures 6.6-9 and 6.13 show that the proposed method substantially reduces the bias in T_1, relative to MRF without fat-separation. The MRF-fixTE (in-phase T_E) and -varTR (~opposed-phase T_E) results likely indicate that in-phase T_E reduces T_1 and T_2 bias when fat separation is not used. The FSF CCC of 0.990 between the MRF and SPGR measurements (Fig. 6.14) includes a broad range of T_1 and T_2 combinations, suggesting that water T_1/T_2 are not biasing the MRF FSF estimate. While high concordance can be achieved with spiral MRF directly estimating FSF with a dictionary matching scheme in the image domain, Fig. 6.10 shows that blurring due to chemical shift may degrade parameter map quality.

The B_0 correction from the proposed technique improves FSF, T_1, and T_2 estimation compared to those estimates made without the correction. MFI approximates the true B_0 correction because of the finite number of basis frequencies and the nonzero gradient of B_0. However, the proposed correction still helps to significantly improve the relaxometry estimates in regions of $\Delta B_0 > 100$ Hz (Fig. 6.16) and mostly follows the reference B_0 map in the brain with the noted exceptions (Fig. 6.18). Figures 6.15-16 shows that without the proposed B_0 correction, the phase modulation may confound the variable echo time MRF sequence needed to encode fat chemical shift information, as well as confound the T_1 and T_2 estimation using the dictionary that does not contain off-resonance information.

The *in vivo* data suggest this technique may be applied to improve MRF extra-cranial relaxometry and FSF measurements. The knee FSF maps (Fig. 6.17) appear concordant between MRF and conventional techniques in the marrow and intermuscular fat. The MRF

113

T_1/T_2 maps (Fig. 6.17) indicate bias near fat regions without fat separation, in agreement with the phantom results. While T_2* is not explicitly considered in this work, the spin-spin (T_2) component of T_2* is considered, leaving the refocusable transverse relaxation (T_2') unmodeled. The *in vivo* magnitude of this potential bias from T_2' is not clear but can potentially be included in the fitting with modifications to the above theory, which we leave for future work. Nevertheless, the addition of FSF and B_0 estimates to relaxometry increases the amount of information available from a single MRF sequence, supporting its continued study for potential applications in clinical research. The MRF data for fat-separated multi-parametric abdominal study (Fig. 6.19) were acquired in 24 s with a single breath hold. Future quantitative MRI studies in the extremities, abdomen, thorax or neck may be made more practicable by using the proposed technique.

Limitations of this study include the fixed fat model assumption, regularization of the B_0 fitting, aliasing, independent B_1+ mapping, and the *in vivo* study size. Allowing an unconstrained fitting for fat T_1 and T_2 and signal amplitude would likely dramatically increase the memory requirements of the solution as well as make the k-space fat-water separation increasingly ill-posed. However, the extent to which any potential variability in *in vivo* fat relaxation properties quantitatively impact the observed signals is not clear. For instance, inversion recovery-based fat suppression generally assumes a fixed T_1 for fat. A recently described MRF approach to multi-compartment relaxometry [231] could potentially be applied to this problem, but is outside the scope of this work. The image simulations suggest that aliasing contributes to uncertainty: the relaxometry standard deviations are zero for the proposed method when fully-sampled (Figs. 6.8-9) but are non-zero when aliasing is introduced without any noise (Fig. 6.7). Incorporation of matrix completion[232] or low-rank[233] reconstruction methods may reduce these uncertainties. The fat-water swapping in Fig. 6.18 may be reduced by more rigorous incorporation of spatial roughness penalties or other regularization to limit sudden changes in estimated ΔB_0. Consideration of non-idealities such as imperfect slice profile and crushing action may also improve ΔB_0 fitting as well as T_2 estimates (see also Chapters 7 and 8). The MRF scan durations reported in this proof-of-concept study do not include the time required to acquire independent B_1+ mapping. However, methods such as dual refocused echo acquisition mode[227] (Fig. 6.19)

and Bloch-Siegert shift[234] can map B_1+ on the order of seconds and have been previously employed in MRF to this end[173]. Bloch-Siegert-based B_{1+} mapping is used in following studies in this work (Chapter 7 and 8). Integrating B_1+ mapping into the MRF sequence is an active area of research.[235] The *in vivo* MRF T_1 and T_2 estimates *outside* of fatty regions generally agreed with each other in the knee and the brain, but further study with more subjects are needed to understand the difference between MRF with/without fat-separation and conventional techniques in different organs.

In support of reproducible research, the source code along with figure reproduction scripts and data are freely available for download at https://github.com/jostenson/MRI_Ostenson_MRF_FSF.

6.6 Conclusions

We have developed a means to simultaneously estimate T_1, T_2, and FSF with in-line B_0 correction using a single MRF sequence. The method improves T_1 and T_2 estimation in regions of fat over non-fat separating MRF methods and adds to the parameters available for estimation via MRF. This unification of multi-parametric estimation increases the amount of information gathered by the MRF sequence and extends MRF's possible utility. In the next chapter some of the model assumptions used in this chapter as well as uncertainties relating to ΔB_0 and T_2 estimation are further explored.

Chapter 7

SLICE-SELECTIVE EXTENDED PHASE GRAPHS IN GRADIENT-CRUSHED, TRANSIENT-STATE FREE PRECESSION SEQUENCES[v]

7.1 Introduction

Gradient-crushed transient-state free precession sequences, such as those used in unbalanced "steady-state" free precession (uSSFP) MR fingerprinting (MRF; §2.4, Chapters 5-6),[67] have states of partial or fully defocused magnetization that may interact with slice selection, biasing parameter estimates. These sequences can be modeled with Bloch simulations or extended phase graphs (EPG) using idealized slice profiles. The repeated dephasing of the crusher gradients motivates the use of EPG modeling, but current EPG methods idealize the slice profile or the crusher gradient in a way that may bias these models.

The EPG formalism is a method for modeling signals from pulsed MRI experiments (§2.4.3).[31] EPG is particularly useful for calculating the effects of coherence pathways, states of dephased magnetization that may later be refocused and manifest as spin-echoes or stimulated echoes. These echoes may contribute substantially to the observed signal in a given gradient-crushed sequence. The equivalence of EPG to a conventional Bloch simulation has been shown.[236] EPG was employed for signal modeling in the original uSSFP MRF work[67] using idealized slice profiles.

EPG has been used to improve signal modeling accuracy of slice-selective sequences with inhomogeneous slice profiles.[237,238] The approach taken by Lebel and Wilman[237] for slice-selective multiple spin-echo (MSE) T_2 estimation is to discretely partition the slice profile based on precomputed excitation and refocusing profiles. The partitioned components are each fed through an EPG algorithm, then summed to determine the cumulative effect of the non-uniform excitation/refocusing profile. A similar approach has been adopted in slice-selective uSSFP MRF.[174,175] It is known that slice-selective balanced

116

SSFP MRF relaxometry estimates improve with slice profile modeling using Bloch simulations,[172,173] but uSSFP MRF is often modeled with EPG because of the contributions of multiple coherence pathways to the signal. This complex signal evolution suggests the partitioned EPG (pEPG) approach used in MSE. However, pEPG idealizes gradient crushing action and has not been closely studied in the context of MRF.

Gradient crushers of insufficient strength and non-uniform slice profiles may lead to inaccurate pEPG signal models. As an example, consider a pulse profile that is a scaled delta function and a finite strength crusher. After a single pulse and crusher, the crusher will have caused an offset of phase of the transverse magnetization but no dephasing: ignoring relaxation effects, the signal magnitude is unchanged. On the other hand, pEPG predicts complete annihilation of the signal by the crusher. While this example is extreme, it illustrates how the partitioning method may fail to accurately model the signal due to slice profile inhomogeneity. Furthermore, pEPG models the crusher gradients as completing prior to an instantaneous RF excitation, which also may lead to bias.

Parameter estimates in uSSFP may also be complicated by static field heterogeneity. Recent preliminary work has shown that off-resonance effects may bias T_2 estimates made with uSSFP MRF.[239,240] This effect was attributed to insufficient dephasing prior to radiofrequency (RF) excitation. Since the dephasing gradient strength and slice-selective gradient are coupled, this off-resonance effect may need to be modeled to obtain accurate parameter estimates.

In this work, we propose slice-selective EPG (ssEPG) to study transient-state, gradient-crushed/spoiled sequences with a focus on uSSFP MRF. Unlike previous EPG slice profile methods, the ssEPG model operates entirely in k-space. It uses a hard-pulse approximation method to closely approximate soft RF signal responses, integrated with the conventional EPG method. The ssEPG method accurately accounts for crusher/slice profile interactions, works in EPG state-space using familiar transition and shift operators, and accurately models intra-slice signal evolution in the transient state. We use ssEPG to examine relaxometry bias in uSSFP MRF due to slice profile effects as well as interactions with static field heterogeneity.

7.2 Theory

In this section we introduce the mathematical framework for ssEPG. Using a spatial-frequency representation of the Bloch equations, as well as an hard-pulse approximation, we show that we may write the effect of an RF pulse in terms of shift and transition operators familiar to conventional EPG. These operations apply to the normal EPG state matrix using conventional notation[31].

7.2.1 The Bloch equations in the Fourier domain for an applied radiofrequency pulse

The magnetization $\mathbf{M} = [M_x, M_y, M_z]^T$ in the RF rotating frame under the influence of an applied radiofrequency field in a slice-selective pulsed MRI sequence, neglecting relaxation, at time t is related to its time derivative as

$$\frac{d\mathbf{M}}{dt} = \begin{pmatrix} 0 & \omega & -\omega_1 \sin(\phi) \\ -\omega & 0 & \omega_1 \cos(\phi) \\ \omega_1 \sin(\phi) & -\omega_1 \cos(\phi) & 0 \end{pmatrix} \mathbf{M}(t). \qquad [7.1]$$

Here $\omega = \gamma G z$, with gyromagnetic ratio γ, gradient amplitude G, and slice position z; $\omega_1 = \gamma B_1(t)$ where $B_1(t)$ is the amplitude of the applied radiofrequency and ϕ is its phase. By expressing this form of the Bloch equations in complex magnetization (i.e. $M_+ = M_x + iM_y$ and $M_- = M_x - iM_y$) and taking the Fourier transform in z, it can be shown that Eq. (7.1) is equivalent to

$$\frac{\partial \mathbf{F}(k_z, t)}{\partial t} = \begin{pmatrix} \frac{\gamma}{2\pi} G \frac{\partial}{\partial k_z} & 0 & i\omega_1 e^{i\phi} \\ 0 & -\frac{\gamma}{2\pi} G \frac{\partial}{\partial k_z} & -i\omega_1 e^{-i\phi} \\ \frac{i\omega_1}{2} e^{-i\phi} & -\frac{i\omega_1}{2} e^{i\phi} & 0 \end{pmatrix} \mathbf{F}(k_z, t). \qquad [7.2]$$

Here $\mathbf{F}(k_z, t) = \mathcal{F}_z\{[M_+, M_-, M_z]^T\}$ is the Fourier transform of the complex magnetization, and $\frac{\partial}{\partial k_z}$ represents the partial derivative operator with respect to the spatial-frequency in the z dimension.

118

7.2 Solution of the k-space representation of the Bloch equations by the hard-pulse approximation

Splitting the matrix in Eq. (7.2) we can write

$$\frac{\partial \mathbf{F}(k_z, t)}{\partial t} = (A + B)\mathbf{F}(k_z, t), \qquad [7.3]$$

where

$$A = \begin{pmatrix} 0 & 0 & i\omega_1(t)e^{i\phi} \\ 0 & 0 & -i\omega_1(t)e^{-i\phi} \\ \frac{i\omega_1(t)}{2}e^{-i\phi} & \frac{-i\omega_1(t)}{2}e^{i\phi} & 0 \end{pmatrix}, \qquad [7.4]$$

and

$$B = \begin{pmatrix} \frac{\gamma}{2\pi}G\frac{\partial}{\partial k_z} & 0 & 0 \\ 0 & -\frac{\gamma}{2\pi}G\frac{\partial}{\partial k_z} & 0 \\ 0 & 0 & 0 \end{pmatrix}, \qquad [7.5]$$

where $\omega_1(t)$ is the applied RF over the time t to $t + \Delta t$, which the RF is considered constant in a hard-pulse approximation. The matrix operators A and B do not commute. By splitting the matrices as we have done, we may use an approximation accurate to the second-order[241] for a bounded magnetization over a finite region of support

$$\mathbf{F}(k_z, t + \Delta t) \approx e^{A_t\Delta t/2}e^{B\Delta t}e^{A_t\Delta t/2}\mathbf{F}(k_z, t). \qquad [7.6]$$

Eq. (7.6) is a convenient expression if we use the conventions of Ref [31]. The matrix exponential $e^{A_t\Delta t/2}$ is the normal EPG transition matrix for half of the flip-angle $\omega_1(t)\Delta t$,

which we denote as T_n for n^{th} time interval in the RF pulse. The matrix exponential of diagonal matrix B is given by the exponentiation of the diagonal elements

$$e^{B\Delta t} = \text{diag}\left\{e^{\frac{\gamma}{2\pi}\Delta t G \frac{\partial}{\partial k_z}}, e^{-\frac{\gamma}{2\pi}\Delta t G \frac{\partial}{\partial k_z}}, 1\right\} \qquad [7.7]$$

and

$$e^{\pm\frac{\gamma}{2\pi}\Delta t G \frac{\partial}{\partial k_z}}F_\pm(k_z, t) = F_\pm\left(k_z \pm \frac{\gamma}{2\pi}\Delta t G, t\right). \qquad [7.8]$$

Eq. (7.8) describes the conventional EPG gradient shift operator denoted as S. The accuracy of Eq. (7.6) is limited by the discretization in t.

The effect of the entire RF pulse of length τ, discretized into N_{RF} components, can then be given as $\mathbf{F}(k_z, \tau) = T_{N_{\text{RF}}}ST_{N_{\text{RF}}}T_{N_{\text{RF}}-1}ST_{N_{\text{RF}}-1}\cdots T_1ST_1\mathbf{F}(k_z, 0)$. Discretizing k-space into units of $\Delta k_z = \frac{\gamma}{2\pi}\Delta t G$, we can solve for the EPG state matrix $\Omega(t) = [\mathbf{F}(0, t), \mathbf{F}(\Delta k_z, t), \mathbf{F}(2\Delta k_z, t), \cdots] \in \mathbb{C}^{3\times Q}$ as

$$\Omega(\tau) = T_{N_{\text{RF}}}ST_{N_{\text{RF}}}T_{N_{\text{RF}}-1}ST_{N_{\text{RF}}-1}\cdots T_1ST_1\Omega(0). \qquad [7.9]$$

The hard-pulse and matrix splitting approximations give the response of a soft RF pulse in terms of the native EPG representation of the magnetization using shift and transition operations. The standard EPG framework for interpulse relaxation and gradient dephasing is used to model the remainder of the pulse sequence. The signal magnitude at each echo time T_E is the first entry of $\Omega(T_E)$ (i.e. the DC component of k-space). If desired, the slice profile can be calculated from the Fourier transform of the $F_+(k_z; t)$ (see also §7.7).

The spacing between EPG states in ssEPG are coupled to the product of the slice-select gradient strength G and hard-pulse time interval Δt (Eq. 7.8). As a result, coupled relationships between the RF pulse profile characteristics and the uSSFP gradient crusher emerge. These are detailed in §7.7.

7.3 Methods

7.3.1 Numerical and experimental validation of ssEPG

To validate the proposed method of slice profile computation, we calculated slice profiles from a soft RF pulse in a 10 excitation uSSFP sequence using a linear ordinary differential equation (ODE) solver of the Bloch equations and using the proposed ssEPG method. For reference, the sequence was also modeled with EPG using an idealized slice profile. All computations were performed in MATLAB (v. 2018a; MathWorks, Natick, MA). A Hanning-windowed sinc excitation pulse with time-bandwidth product (TBW) of four and a nominal flip angle of 90° was used. Slice thickness was 8 mm; the gradient crushing introduced four cycles of phase across the nominal slice thickness; T_1 and T_2 were 1000 and 100 ms, respectively; and the T_E/T_R were 3/15 ms. We used a nonstiff ODE solver based on the Runge-Kutta method (MATLAB function ode45) with 5000 isochromats over four times the nominal slice thickness. The number of states Q used for the ssEPG method was defined to match the resolution of the Bloch simulation.

The measured transient slice profiles were compared to modeled slice profiles and signals from ssEPG and pEPG. A 50 mL conical centrifuge tube was filled with 3% aqueous agar (w/w) and doped with 1.0 mM gadolinium-based contrast agent. All MRI experiments were performed on a 3T Philips Ingenia (Philips Healthcare, The Netherlands). The tube was imaged with an uSSFP sequence with crusher strengths of one and four cycles per nominal slice thickness of 6 mm. The sequences were 10 excitations in length and used Hanning-widowed sinc pulses with TBWs of two, four, and eight for excitation. Three nominal flip angles of 30°, 60°, and 90° were used. The readout gradient was along the through-slice direction with an FOV of 32 mm and a resolution of 125 μm. The body coil was used for signal reception to minimize coil sensitivity changes over the slice. Thirty-two averages were used with a time delay of 5.5 s between averages to permit full recovery of magnetization between averages. The T_1 and T_2 of the agar phantom were estimated using single voxel MR spectroscopy. ssEPG slice profiling modeling matched the resolution of the measurement. The pEPG method used 256 partitions to match the resolution of the measurement. The slice profile partitions were calculated by ssEPG from equilibrium using

the respective RF pulse type and flip angle. Signal magnitude root-mean-square-errors (RMSE) were calculated for the normalized EPG signal models using the normalized signal measurement as a reference.

7.3.2 ssEPG applied to MRF in phantom

To assess EPG's effect on parameter estimation accuracy using uSSFP MRF, we estimated T_1 and T_2 in an MRI system phantom with ssEPG and pEPG slice profile modeling, as well as EPG without slice profile modeling. The same RF pulses used in the agar slice profile experiment were used to image the system phantom[186] (High Precision Devices, Boulder, CO) composed of $MnCl_2$-doped calibrated contrast spheres temperature corrected with conventional measurements. The MRF acquisition used the first 1250 excitations of a previously used flip-angle pattern from this work[242] (Fig. 6.1), fixed T_R = 16 ms, a T_E ramped linearly through the repetitions from 3 to 7 ms, and a crusher strength of one or four cycles per nominal slice thickness. The readout used 32 spiral interleaves rotated 11.25° between excitations, with an in-plane resolution of 1 mm x 1 mm and 8 mm slice thickness. The pEPG dictionary used 50 partitions for four times the nominal slice thickness. All dictionaries used the same T_1s and T_2s ranging from 10 to 3000 ms and 2 to 1500 ms, respectively. The B_{1+} was modeled from 1.0 to 1.35, which matched the range of a separately acquired B_{1+} map[243] over the contrast spheres. Comparison of relaxometry estimates between MRF and the reference were made using the concordance correlation coefficient[225].

To speed ssEPG dictionary modeling, the code was parallelized for use with MRF. GPU functionality within MATLAB as well as a modified CUDA kernel from an EPG-based fast dictionary modeling approach[244] were employed to speed calculations. Dictionaries were generated using an NVIDIA TITAN RTX (Nvidia Corp., Santa Clara, CA). Errors in ssEPG modeling will come from truncation of the state matrix: if Q is too small relative to the number of states spanned by repeated gradient crushing (each of number ΔN), information can be lost. Using the relationships in §7.7, we optimized Q for each TBW and crusher strength used in the MRF sequence. Over a physiological range of T_1 (300 to 1500 ms) and T_2 (5 to 150 ms) we selected 10 log-spaced values for both T_1 and T_2, and used all 100 pairings from all combinations of each metric's 10 values. We generated high resolution

signal models using ssEPG for all these T_1 and T_2 pairings for each RF pulse and crusher strength. For each set of signals, we sequentially incremented the value of $Q/\Delta N$, which defined Q for the given pulse and crusher strength, and then modeled all T_1 and T_2 combinations and 2% above and below the query values (i.e. the dictionary had 9 closely spaced atoms $\times$ 100 log-spaced atoms = 900 atoms). The unbiased ssEPG high resolution signals were then matched against the truncated dictionary and $Q/\Delta N$ was increased until the maximum absolute error in the estimated T_1 and T_2 for all 100 signals was zero.

7.3.3 ssEPG MRF B_0 effects and *in vivo* application

To model slice profile effects *in vivo*, we must consider the interaction of static field heterogeneity with slice profile effects. It is difficult to achieve the same homogeneity of the static field *in vivo* as in a phantom, so we model B_0 deviations under free precession within the EPG model using the relation in §7.7.

The ssEPG slice profiles for several off-resonance frequencies were calculated for the second excitation of the MRF sequence described above using a T_1 and T_2 of 1320 and 30 ms, respectively. The ΔB_0s were defined in relation to the fundamental frequency of repetition time of the MRF sequence at the following factors of $1/T_R$: 0, 1/4, 1/2, 5/4, and 3/2. We also modeled the magnitude and phase of the MRF signals for the given T_1 and T_2 sequence at the same frequencies. We investigated the off-resonance frequency periodicity of the slice profile, magnitude and phase modulations.

We evaluated the bias of MRF T_1 and T_2 when fitting with ΔB_0 modeling against dictionaries with slice profile effects without ΔB_0 effects for TBWs of four and eight at nominal crusher cycles per nominal slice thickness of one and four. The bias calculations were done for the following T_1/T_2 combinations (in ms) as rough estimates of mono-exponential relaxation times of skeletal muscle, liver, gray matter, and white matter[207]: 1320/30, 800/30, 1400/85, and 800/65, respectively. These evaluations of bias were evaluated for the following sequences: the MRF sequence described above (variable T_E/fixed T_R), the MRF sequence described above without variations in echo time (fixed T_E/fixed T_R), and an MRF sequence with variable T_R (fixed T_E/variable T_R). To reduce discretization effects in fitting, all three dictionaries were generated over a finely spaced

domain of 35 T_1s and 165 T_2s log-spaced over the ranges of 100 to 3000 ms and 2 to 300 ms, respectively. The variable T_R sequence is similar to the first reported uSSFP MRF sequence[67], using the same T_R extension with a minimum T_R of 16 ms, as well as the same flip angle modulation pattern with a maximum flip angle of 60°, and 1000 excitations. The mean relative bias and standard deviation of the query parameter estimates were calculated for each TBW, crusher strength, dictionary type, and ΔB_0 across the four physiological T_1 and T_2 combinations.

A single volunteer was imaged in the calf after informed consent and with approval from the local institutional review board. The (variable T_E/fixed T_R) MRF sequence in the MRI system phantom experiment was used for acquisition with an FOV of 320 mm × 320 mm, and in-plane and through-plane resolution of 1.25 mm × 1.25 mm and 5 mm, respectively. A 16-channel transmit-receive knee coil was used for image acquisition. Images were reconstructed used the Berkley Advanced Reconstruction Toolbox[221] with numerically calculated sampled density compensation[36]. Dictionaries with EPG, pEPG, ssEPG, and ssEPG with B_0 effects were used to fit the T_1 and T_2 from the calf data. For the calf, B_{1+} was modeled from 0.7 to 1.15, which matched the range of a separately acquired B_{1+} map[243].

7. 4 Results

7.4.1 Numerical and experimental validation of ssEPG

The ssEPG slice profile model closely matches the ODE Bloch solution (Fig. 7.1). The relatively long T_2 (100 ms), relative to the T_R (15 ms), permits the development of multiple coherence pathways that modulate the slice profile, manifesting as oscillations in the profile magnitude. These oscillations in the pulse profile are in close agreement between the two models. The normalized signal from the ssEPG simulation has an RMSE of 0.002 relative to the signal to the Bloch simulation. The normalized signal from the standard EPG model without slice profile modeling has an RMSE of 0.115.
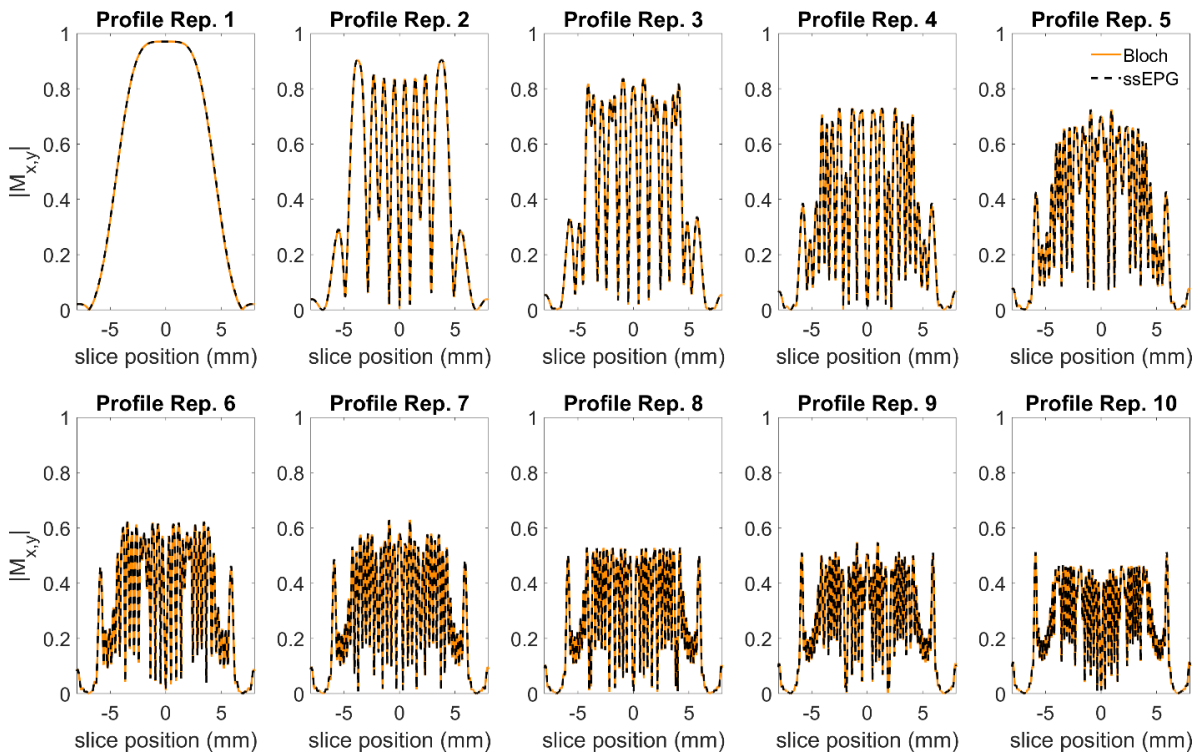
Fig. 7.1 The magnitudes of the simulated, transient slice profiles calculated by numerical solution to the Bloch equations and the slice-selective extended phase graph (ssEPG) techniques. The unbalanced SSFP sequence uses an Hanning-windowed sinc pulse with a time-bandwidth factor of four, a nominal flip angle of 90°, and four crusher cycles per nominal slice thickness, which produces large dynamic oscillations in the profiles.

7.4.2 ssEPG applied to MRF in phantom

The ssEPG model of the pulse profile in agar closely matches that of the measurement, and the ssEPG signal model error is lower than that of the pEPG method. An example plot of the measured and modeled slice profiles, scaled by their root-mean-square values of the first profile, shows general agreement between the slice shapes (Fig. 7.2). The oscillations in the measured profile are generally matched in the ssEPG model. High frequency components visible in ssEPG appear slightly attenuated in the 1D projection measurement. pEPG does not model these oscillations. Fig. 7.3 shows that the signal RMSEs of the various EPG modeling methods.
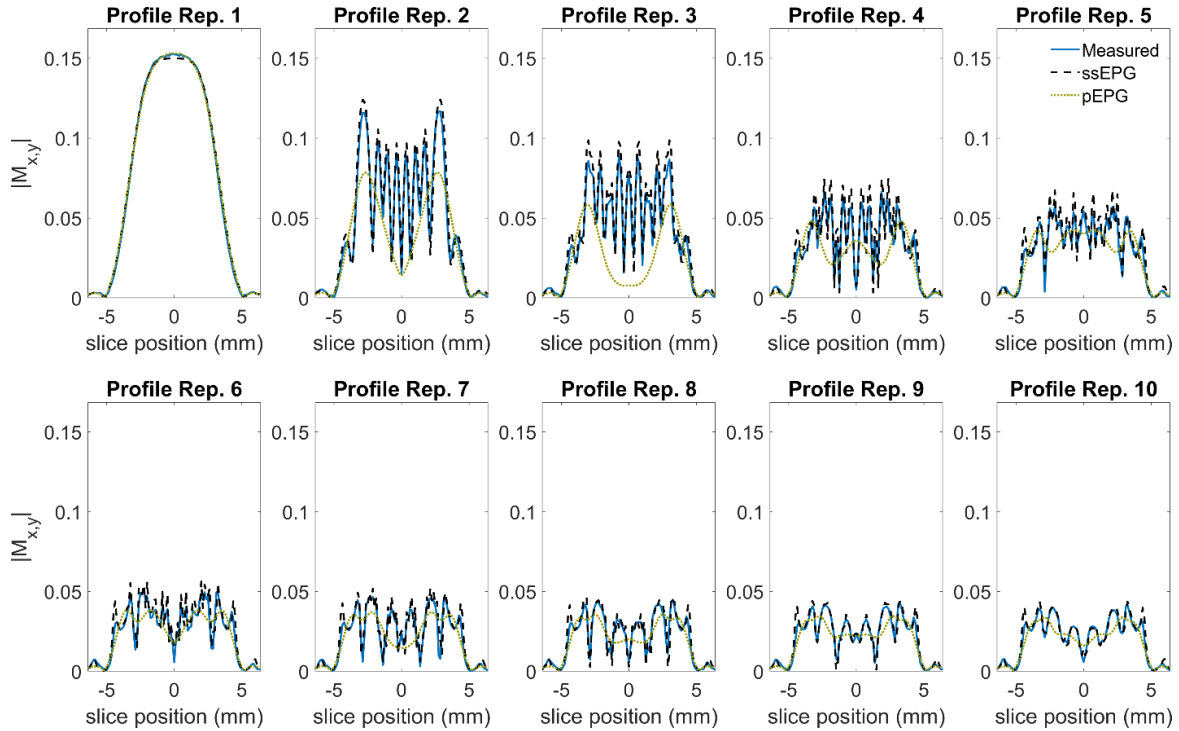
Fig. 7.2 The measured and simulated magnitudes of the slice profiles from the agar phantom. The measured, slice-selective EPG (ssEPG), and partitioned EPG (pEPG) profiles were scaled by the root-mean-square of their respective first profiles.

The T_2 estimates of the MRI system phantom from ssEPG modeling more closely match the ground truth than those from other EPG methods. The plots of T_2 estimates over a physiological range of T_2 (0 to 100 ms) are shown in Fig. 7.4a-c. The CCCs in this T_2 range are shown in Fig. 7.4d. Over the full dynamic range, the mean CCCs over all RF pulses and crusher strengths for T_1 are 0.994, 0.999, and 0.999 for EPG, pEPG, and ssEPG, respectively; and over the full range of T_2s they are 0.919, 0.975, 0.996 for EPG, pEPG, and ssEPG, respectively. As measured by an independent B_0 mapping, the ΔB_0 of the MRI system phantom contrast inserts did not deviate more than 6.6 Hz, using the mean ΔB_0 for each insert.
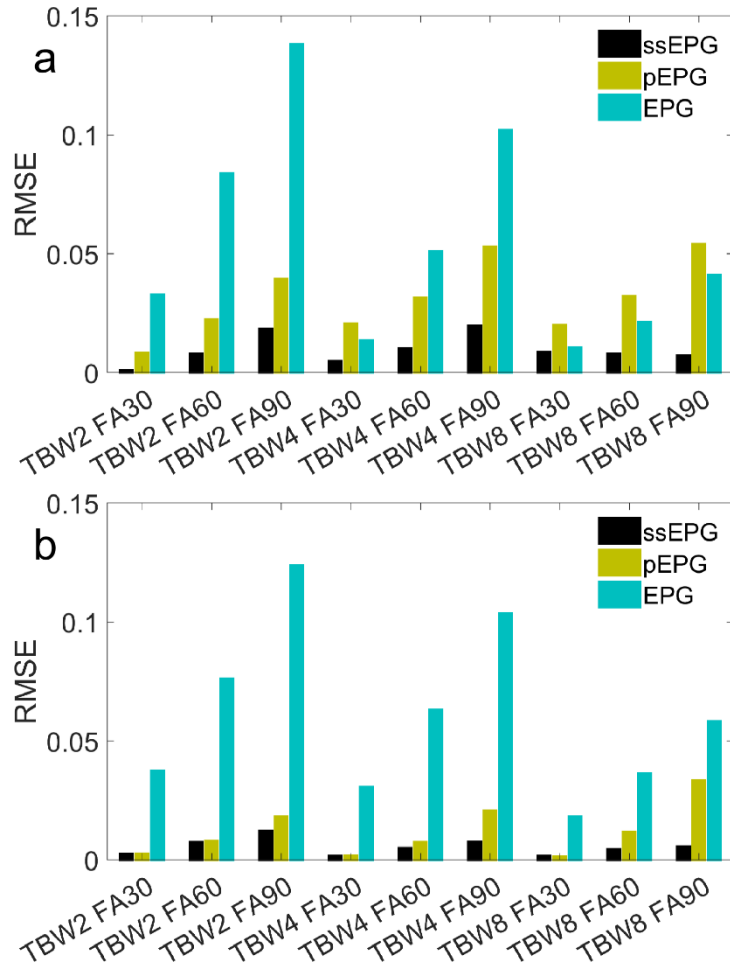
Fig. 7.3 The root-mean-square error (RMSE) of the normalized signals magnitudes modeled by slice-selective (ssEPG), partitioned (pEPG), and conventional EPG without slice profile modeling, relative to the measured signal from the agar phantom over 10 excitations for a crusher strength of one cycle per nominal slice thickness (a), and for four cycles (b). The time-bandwidth product (TBW) of the Hanning-windowed sinc pulses and the nominal flip angles (FA) in degrees are listed.
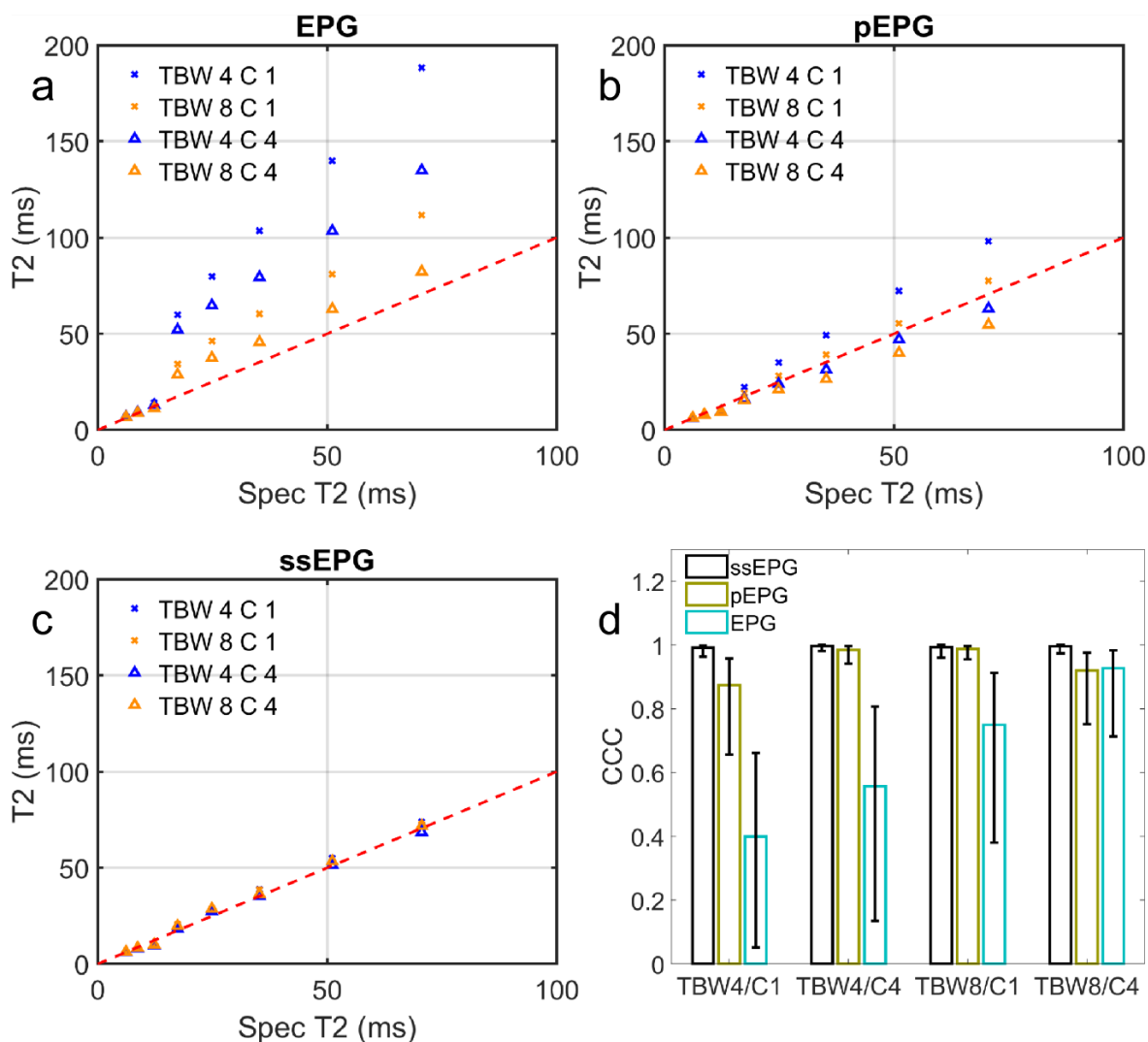
Fig. 7.4 The MRF T_2 estimates over a physiological range in the MRI system phantom and concordance correlation coefficients (CCC) from different slice profile modeling techniques for different RF time-bandwidth products (TBW) and crusher strengths (C). The EPG without slice profile corrections are shown in (a), the partitioned EPG (pEPG) results in (b), and the slice-selective EPG (ssEPG) estimates in (c). The dotted line is that of perfect concordance. The CCCs are in panel (d) with error bars indicating 95% confidence intervals.

7.4.3 ssEPG MRF B_0 effects and *in vivo* application

The simulation of B_0 effects in the variable T_E/fixed T_R MRF sequence modeled with ssEPG are shown in Fig. 7.5. For a fixed T_R sequence such as this, there are modulations in the slice profile magnitude and these modulations are periodic in ΔB_0 by frequencies of

$1/T_R$. Fig. 7.5a shows that the slice profile magnitudes of $\Delta B_0 = 1/(4T_R)$ and $1/(2T_R)$ are equal to $5/(4T_R)$ and $3/(2T_R)$, respectively. The MRF signal magnitudes at these off-resonant frequencies are also modulated (Fig. 7.5b). These modulations in magnitude also follow the periodicity of the slice profiles. The phase modulations (Fig. 7.5c) of the MRF signals show monotonic as well as oscillatory behavior. Again, assuming the fixed T_R MRF sequence, we find that the phase modulations for $|\Delta B_0| > 1/T_R$, for MRF signal s_n at excitation n, can be modeled by multiplying the modulo $1/T_R$ frequency by the added complex phase,

$$s_n(T_E, \Delta B_0 = a) = e^{i2\pi\frac{m}{T_R}T_E} s_n\left(T_E, \Delta B_0 = a \bmod \frac{1}{T_R}\right) \qquad [7.10],$$

where $m = T_R\left[a - \left(a \bmod \frac{1}{T_R}\right)\right]$, so m is an integer. Two examples of using Eq. (7.10) to construct higher order frequencies can be seen in Fig. 7.5c, denoted by asterisks. Using Eq. (7.10), B_0 effects for a given T_1, T_2, and B_{1+} can be modeled if the signal is known for $0 \leq \Delta B_0 < 1/T_R$.

The modeled T_1 biases from B_0 effects were generally small for the fixed T_E sequences, but the relative bias increased with ΔB_0 values from the variable T_E sequence. The maximum magnitude of relative T_1 bias for the fixed T_E sequences was < 1% for all TBW and crusher strength combinations. For the variable T_E sequence, the T_1 bias increased steadily with ΔB_0. The maximum magnitude of relative T_1 bias for the variable T_E sequence for all TBW and crusher strength combinations was < 1%, < 1%, 10%, 22%, and 35% for ΔB_0 values (in units of $1/T_R$) of 0, 1/4, 1/2, 5/4, 3/2, respectively.

Substantial T_2 bias can be observed at low ΔB_0 values for several sequences. The relative bias in T_2 from signals with B_0 effects fit against ssEPG dictionaries without B_0 effects are shown in Fig. 7.6. The T_2 bias for sequences with $\kappa/2 \geq N_{\text{crush}}$ (TBW = κ) increases from ΔB_0 of $1/(4T_R)$ to $1/(2T_R)$ and decreases from $1/(2T_R)$ to $5/(4T_R)$. Relative to this, the T_2 bias is reduced for sequences with $\kappa/2 < N_{\text{crush}}$. The T_2 bias from the fixed T_E/fixed T_R sequence is equal between steps in ΔB_0 of $1/T_R$. The bias of the variable T_E/fixed

T_R sequence for the three lowest ΔB_0 values is generally equal to or less than that from the other sequences. The contributions to the total crusher strength from the slice-selective gradient before the isodelay and added dephasing gradient (calculated using relations given in §7.7) for each TBW and crusher combination are given in Table 7.1.

Table 7.1. MRF T_2 bias for different RF pulses and crusher strengths

TBW	C	$N_{crush,ss}$	$N_{crush,g}$	Max. Rel. T_2 bias†
4	1	2	-1	0.933
4	4	2	2	0.057
4	8	2	6	0.011
8	1	4	-3	0.543
8	4	4	0	0.504
8	8	4	4	0.028

TBW – time-bandwidth product

C – number of crusher cycles per nominal slice thickness

$N_{crush,ss}$ – number of crusher cycles from slice-select gradient before isodelay

$N_{crush,g}$ – number of crusher cycles from dephasing gradient

† - maximum relative T_2 bias from fixed T_R/fixed T_E MRF sequence from the data used in Fig. 7.6
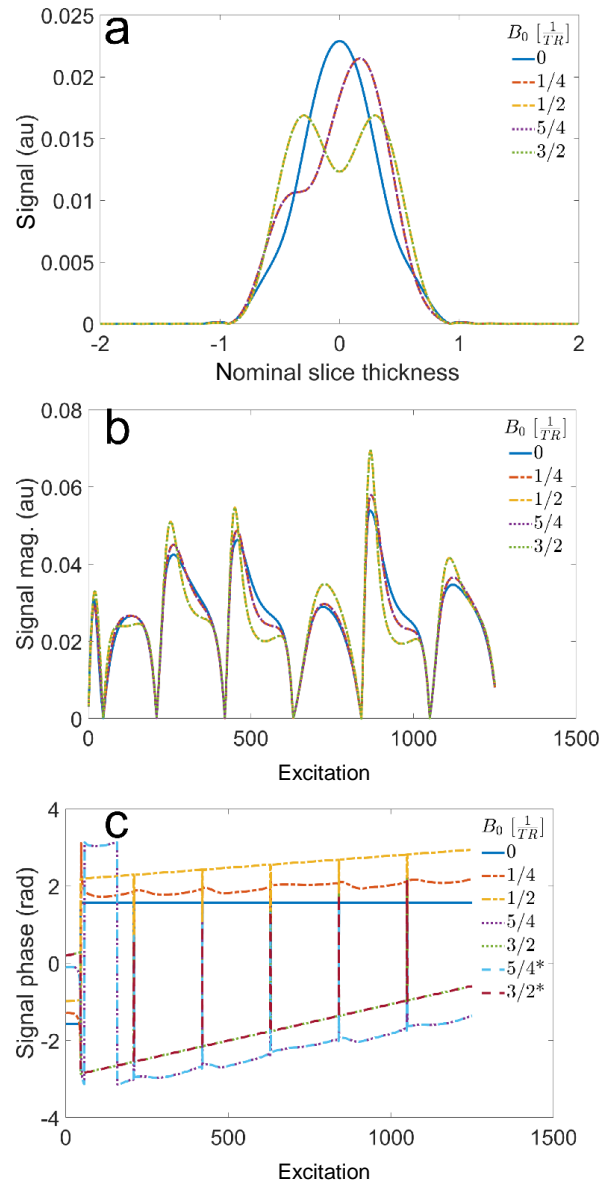
Fig. 7.5. The magnitude of the slice profiles from the second excitation of the MRF sequences for a TBW of four RF pulse and one cycle per nominal slice thickness gradient crusher at the listed ΔB_0s (a). The magnitude of the of MRF signals modeled at the listed ΔB_0s (b). The slice profiles and signal magnitudes of $\Delta B_0 = 1/4$ and 1/2 overlap with 5/4 and 3/2, respectively, in (a) and (b). The phase of the MRF signals are shown in (c). The 5/4* and 3/2*ΔB_0 signals were reconstructed from the 1/4 and 1/2 ΔB_0 signals, respectively, using Eq. (7.10). These reconstructed signals overlap with the explicitly calculated 5/4 and 3/2 ΔB_0 signals.
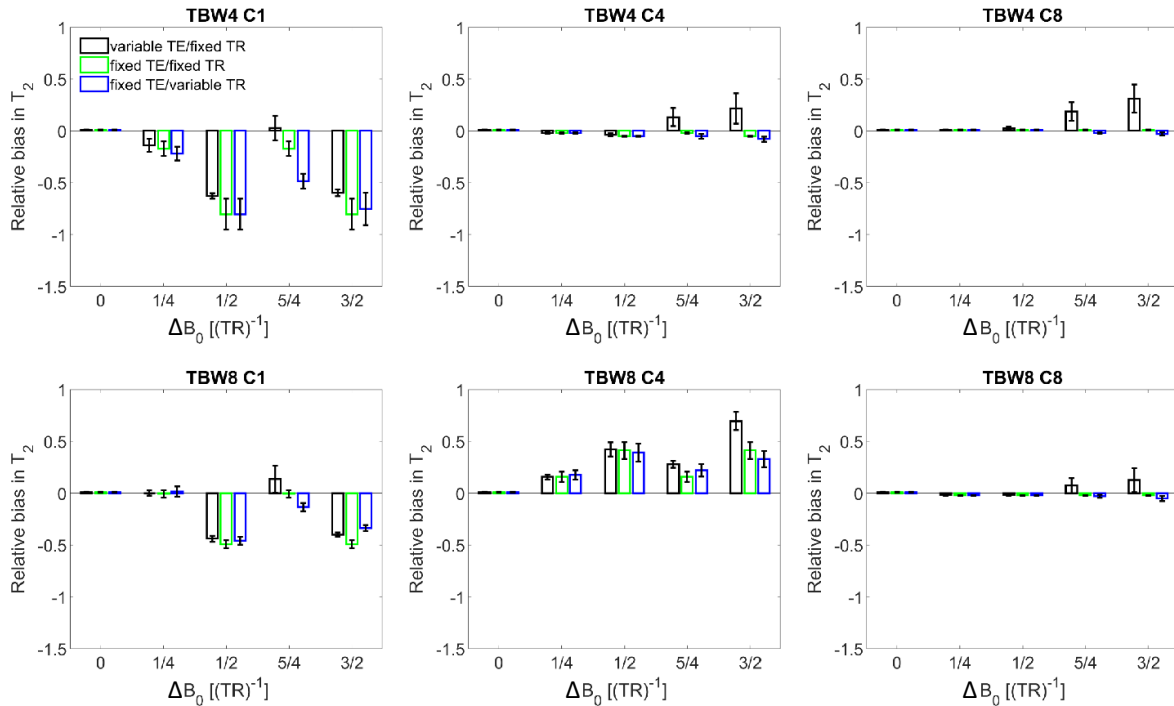
Fig. 7.6 The mean relative T_2 bias from MRF signals modeled with B_0 effects, fitted against models without B_0 effects for three different MRF sequences and six different time-bandwidth (TBW) and crusher cycles per nominal slice thickness (C) combinations. The mean is across four physiological T_1/T_2 combinations noted in the text. Error bars represent the standard deviation of the relative bias.

The *in vivo* parameter maps from the calf using EPG fitting can be seen in Fig. 7.7. The T_1 maps (Fig. 7.7a) of the three different crusher strengths and four different EPG fitting models yield similar results. The EPG T_1 estimates without profile effects in the calf muscles appear slightly lower than those from the other EPG modeling. The T_2 estimates (Fig. 7.7b) are substantially biased using EPG without slice profile effects. The pEPG and ssEPG show drops or abrupt increases in the T_2 estimates in the lateral aspects of the calf muscles. These deviations are reduced in the ssEPG with B_0 modeling. The mean T_1 for the entire non-zero parameter maps for EPG, pEPG, ssEPG, and ssEPG with B_0 modeling are 1231, 1289, 1290, and 1282 ms, respectively; for T_2 they are 63, 22, 24, and 23 ms, respectively.

Further analysis of the *in vivo* calf data can be seen in Fig. 7.8. The coefficient of variation (COV) across the different crushers for the different EPG fitting methods (Fig. 7.8a) show that ssEPG with B_0 modeling has the lowest COV across the different measurements. Regions that are within 30% of the an off-resonance magnitude of $1/(2T_R)$ (Fig. 7.8c) correspond to regions of highest COV in ssEPG without B_0 modeling. These regions have reduced COV after B_0 is considered.
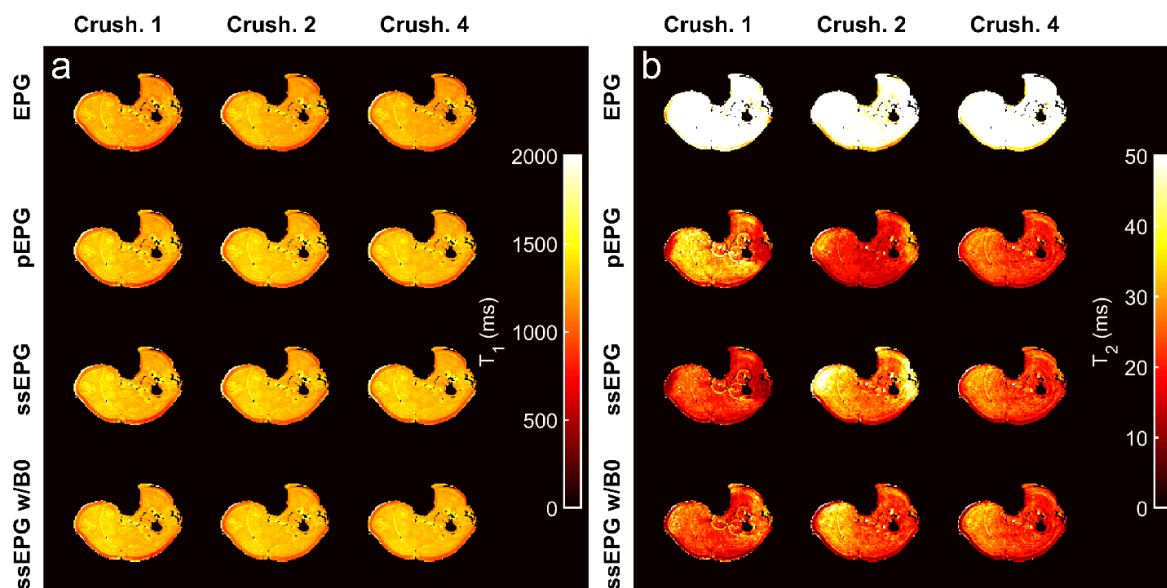
Fig. 7.7 The MRF T_1 (a) and T_2 (b) maps of the calf from three different crusher strengths fit by four different EPG models for a TBW of four RF excitation pulse. The "EPG" fits do not consider slice profile effects. The "pEPG" method accounts for slice profile effects from the RF pulse but idealizes crusher action. The "ssEPG" method accounts for RF pulse and the differences in crusher strength. The T_2 of the "EPG" method exceeds the dynamic range of the color mapping, which is reduced to better capture variations in the other fitting models.
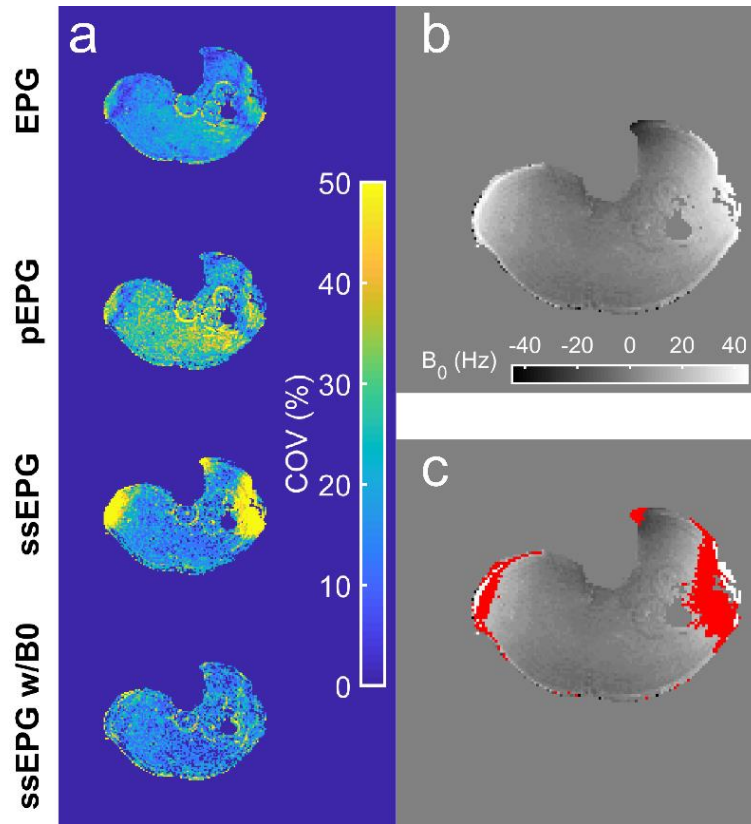
Fig. 7.8 The coefficient of variation (COV) of T_2 across the different crusher strengths in the calf for the four different fitting methods (a). The mean B_0 map in (b) is estimated from the slice-selective EPG (ssEPG) with B_0 modeling. An overlay shows regions of ΔB_0 that are within 30% of an integer multiple of ΔB_0 of $1/T_R$ from $1/(2T_R)$ (c).

7.5 Discussion

Slice profile effects can substantially bias relaxometry estimates in gradient-crushed, free precession sequences. The ssEPG method proposed here accounts for soft RF pulse effects. It also improves on other EPG methods, by accounting for the non-idealized gradient crushing interaction.

The simulation, phantom, and *in vivo* results demonstrate that ssEPG accurately models slice profiles and associated effects on signal. The simulations with ssEPG indicate that it accurately captures the highly variable magnitudes of slice-selective profiles that result from unbalanced gradients. Such slice profile modulations may be relevant in the context of partial volume effects, and possibly in multicompartment MRF parameter

estimation,[245,246] depending on the length scale of the heterogeneity of the tissue. The ssEPG model has the lowest RMSE (Fig. 7.3) and highest CCC (Fig. 7.4) compared to other EPG methods. The MRI system phantom and *in vivo* results show that the ssEPG modeling translates to more accurate relaxometry estimates using uSSFP MRF in regions of the $|\Delta B_0|$ ≈ 0 relative to other EPG-based methods.

The pEPG method markedly improves slice profile modeling effects relative to EPG without slice profile considerations, but it is not as accurate as ssEPG over a physiological range of T_2 due to its simplification of crusher action. The RMSE (Fig. 7.3) and relaxometry estimates (Fig. 7.4) from the phantom measurements are better than those from EPG without profile modeling. While the accuracy of pEPG in the agar phantom at the larger crusher strength is similar to that of the ssEPG method, pEPG used in MRF apparently exhibits variable relaxometry bias depending on crusher strength and TBW (Fig. 7.4). The pEPG model has more variability in T_2 across crusher strengths for the given TBW *in vivo*.

The effect of ΔB_0 on MRF uSSFP T_2 relaxometry is substantial and pertains to both fixed and variable T_R MRF sequences, whereas the T_1 estimates were relatively unbiased by B_0 effects. Matching what has been previously reported,[239,240] we observe periodicity in the T_2 bias at frequency of $1/T_R$, which parallels the modulation of the slice profile over ΔB_0. Fig. 7.6 shows that the T_2 bias from the fixed and variable T_E MRF sequence are similar at $\Delta B_0 = 1/(2T_R)$ indicating it is not the phase dispersion of the variable T_E causing the bias seen *in vivo* variable T_E/fixed T_R MRF T_2 maps in Figs. 7.7-8. Table 7.1 shows that the source of the T_2 bias is insufficient crushing before the slice-select gradient: off-resonance signal components are being transferred by RF action to refocusing and longitudinal states prior to their complete dephasing, later contributing to the net signal. A higher TBW does not reduce this bias, but Table 7.1 indicates the majority of the T_2 bias is eliminated if the signal following each excitation has been crushed/dephased well beyond $k_z = 0$ prior to the beginning of the next RF pulse. Fig. 7.8 demonstrates that incorporation of B_0 into ssEPG reduces the variability of *in vivo* T_2 estimates, particularly in regions of ΔB_0 near integer multiples of $1/T_R$ from $1/(2T_R)$.

Depending on the crusher strength and TBW, the ΔB_0 effects and the MRF contrast effects in a fixed T_R MRF sequence are not separable as they are with idealized

crushing[220,242]. However, B_0 effects are still separable for higher order frequencies as shown in Eq. (7.10) and Fig. 7.5. This separability should be restored for higher crusher strengths and most 3D acquisitions. Yet, in cases where rapid acquisition is required, 3D may not be an option, and diffusion effects[247] may limit the use of high crusher strengths.

A limitation of this study is the uncertainty of all sources of influence on *in vivo* T_2 estimates. Slice profile effects are only one component that contribute to relaxometry errors. Undersampling effects in MRF have shown to limit the accuracy of MRF.[75] Multi-compartment effects, with or without exchange, may bias parameter estimates.[11] Notably, a 3D MRF uSSFP study of the brain showed T_2 values much less than those from conventional estimates.[69] The skeletal muscle T_1 and T_2 values in this study are, respectively, consistent with and lower than conventional estimates[207]. Conversely, the ssEPG T_2 estimates in phantom (Fig. 7.4) are entirely consistent with conventional measurements. Despite this limiting uncertainty, we have shown: ssEPG provides accurate signal and slice profile calculations, MRF T_2 estimation can be improved using ssEPG, gradient crusher interactions with slice-selective excitation may lead to bias that can be corrected with ssEPG modeling, and a simple relationship between TBW and crusher strength can be applied to ameliorate T_2 bias in uSSFP MRF without explicit modeling.

While the focus of this work was to apply ssEPG to transient state uSSFP slice profiles, such as those in MRF, this modeling technique could be applied to slice-selective MSE measurements, as well. In situations of low gradient crusher strength or inhomogeneous pulse profiles, ssEPG may yield improvements in T_2 estimation. However, further investigation is required to determine ssEPG's utility in MSE.

In support of reproducible research, the source code along with figure reproduction scripts and data are freely available for download at https://github.com/jostenson.

7.6 Conclusions

Transient gradient-spoiled/crushed sequences such as uSSFP MRF are sensitive to slice profile effects. These profile effects are dependent on RF pulse, crusher strength, and ΔB_0. All these effects can be modeled with ssEPG to improve MRF relaxometry estimates as well as to provide insights into the source and relationship of different modes of bias.

Some of these improvements will be combined with MRF fat-water separation in Chapter 8.

7.7. Appendix

The following is a description of relationships between RF model properties, crusher gradient, and spatial/frequency resolution in ssEPG. The action of off-resonance frequency under free precession in EPG is also noted.

If we define the constant slice-selective gradient strength G, in terms of time-bandwidth product κ, RF pulse approximated in N_{RF} discrete steps of duration $\tau = N_{\mathrm{RF}}\Delta t$, and slice thickness Δ_{sl} as

$$G = \frac{2\pi\kappa}{\gamma\tau\Delta_{\mathrm{sl}}} \qquad [7.11]$$

and insert this into the definition of Δk_z from Eq. (7.8), we can see that spatial-frequency discretization can also be given as

$$\Delta k_z = \frac{\kappa}{N_{\mathrm{RF}}\Delta_{\mathrm{sl}}}. \qquad [7.12]$$

The EPG state matrix is $\Omega \in \mathbb{C}^{3\times Q}$, with Q states, has the effective field-of-view equal to the reciprocal of Eq. (7.12). The discrete spatial-frequency representation of the complex magnetization

$$F_+[\mathrm{n};t] = \begin{cases} \Omega^*[2,-n;t], & \text{for } 1 \leq -n \leq Q-1 \\ \Omega[1,n;t], & \text{for } 0 \leq n \leq Q-2 \end{cases}, \qquad [7.13]$$

where $F_+ \in \mathbb{C}^{2Q-2}$, with spacing between states of Δk_z and Ω^* is the complex conjugate of Ω. For a given resolution in the spatial domain Δ_z, using Eq. (7.12), Q can be given as

$$Q = \frac{\Delta_{sl} N_{RF}}{2\Delta_z \kappa} + 1. \qquad [7.14]$$

A gradient crusher may be applied to Ω, shifting its transverse states by multiples of Δk_z. If N_{crush} is the number of crusher cycles per nominal slice thickness, and f_r is the fraction of the RF duration before the isodelay, then the number of discrete steps applied by the gradient crusher N_{cycle} is

$$-N_{cycle} = f_r N_{RF} - \frac{\frac{N_{crush}}{\Delta_{sl}}}{\Delta k_z}. \qquad [7.15]$$

Combining Eqs. (7.12) and (7.15) we can write

$$N_{cycle} = N_{RF}\left(\frac{N_{crush}}{\kappa} - f_r\right). \qquad [7.16]$$

The net number of discrete steps, ΔN, taken in a time T_R from the gradient crusher and the portion of slice-select gradient before the isodelay is given by

$$\Delta N = f_r N_{RF} + N_{cycle} = \frac{N_{crush} N_{RF}}{\kappa}. \qquad [7.17]$$

From this expression and Eq. (7.14) we can write the number of ssEPG states relative to the net shift in state-space each over T_R as

$$\frac{Q}{\Delta N} = \frac{1}{N_{crush}}\left(\frac{\Delta_{sl}}{2\Delta_z} + \frac{\kappa}{N_{RF}}\right). \qquad [7.18]$$

From Eqs. (7.15-17), N_{cycle} comes from the slice-select and separate dephasing gradient contributions. The number of cycles per nominal slice thickness advanced by the slice-select gradient, $N_{crush,ss}$, is $f_r \kappa$. The remainder from the dephasing gradient is

138

$N_{\text{crush,g}} = N_{\text{crush}} - N_{\text{crush,ss}}$. So, for $f_r = 1/2$, there will be at least one cycle of dephasing prior to RF excitation for

$$N_{\text{crush}} \geq \frac{\kappa}{2} + 1. \qquad [7.19]$$

Under free precession, complex transverse magnetization $M_{\pm}$ at position z experiencing an off-resonance of frequency ΔB_0 for a time τ can be written as

$$M_{\pm}(\tau + t; z) = e^{\pm i 2\pi \Delta B_0 \tau} M_{\pm}(t; z). \qquad [7.20]$$

By taking the Fourier transform of Eq (7.20) and assuming that B_0 is independent of z over a slice selection, we can write

$$F_{\pm}(\tau + t; k_z) = e^{\pm i 2\pi \Delta B_0 \tau} F_{\pm}(t; k_z). \qquad [7.21]$$

Chapter 8

APPLICATION OF MRF FAT-WATER SEPARATION TO THE LIVER

8.1 Introduction

This work was motivated by the potential role for a rapid, MRI-based approach to characterizing liver pathology. The MRF fat-water separation technique discussed in Chapter 6, incorporating the conjugate phase spiral blurring correction, was applied to a single subject in the liver. However, since that study was completed, we have implemented several other technical advancements; and there remains a need to evaluate the measurement properties of the sequence.

Regarding the MRF sequence itself, the sequence described in Chapter 6 used a 24 s total acquisition time, making it slightly too long for some subjects to hold their breath. This length of breath-hold is expected to be particularly burdensome for some patients. In addition, the post-processing methods described in Chapter 6 exhibited fat-water swaps. Given the location of the liver relative to the lungs, respiratory motion, proximity of subcutaneous and visceral adipose tissue and the ribs, as well the liver's large volume, it can be difficult to shim B_0 sufficiently to avoid large variations in static field across the image. All these factors help promote errors that may lead to fat-water swapping. As mentioned in §6.5, a possible remedy for these swaps is to regularize the fit for ΔB_0 to reduce abrupt changes in static field that come with fat-water swaps. Furthermore, the slice-profile corrections described in Chapter 7 were implemented after the liver imaging in Chapter 6. Depending on the time-bandwidth product (TBW) and nominal crusher cycles, it was shown that these slice profile effects could make a substantial difference in the T_2 estimates. Lastly, the repeatability and accuracy of the fully implemented sequence, relative to conventional relaxometry methods, needs to be studied.

Therefore, the purpose of this chapter is to apply improvements to the MRF fat-water separation developed in Chapter 6, as well as slice profile modeling (Chapter 7), to determine the repeatability of MRF relaxometry metrics in the liver. We also show proof-

of-concept that MRF fat-water separation can be performed in a subject with biopsy-proven NASH.

8.2 Methods

8.2.1 Image acquisition

A total of six volunteers were imaged following informed consent and with approval of the local institutional review board. Five volunteers without a reported history of liver disease were recruited to study repeatability of MRF metrics in the liver and one subject with biopsy-proven NASH was imaged to evaluate MRF performance in pathological liver. All subjects were asked to fast for at least four hours prior to imaging to avoid potential post-prandial effects on repeatability. One subject was not compliant with fasting. All subjects without liver disease compliant with fasting were included in the repeatability cohort. The repeatability cohort had an age range of 23-30 and no reported history of metabolic diseases, prescription medication use varied among the subjects. Two of the four subjects were taking prescription medications. The NASH subject (62 y, male) had stage 3 bridging fibrosis on percutaneous image guide liver histology, no reported steatosis or inflammation, with a history of diabetes mellitus.

All subjects were imaged on a Philips Achieva 3 T (Philips Healthcare, The Netherlands) using an anterior body coil array and integrated posterior tabletop coil array. Conventional imaging and spectroscopy were acquired for reference and comparison with MRF-derived estimates: a six echo Dixon sequence with vendor reconstructed fat fraction, T_2^*, and B_0 mapping (mDixon Quant); a spin-echo based custom Bloch-Siegert mapping sequence[243]; and two subjects' livers were measured with two forms of single voxel stimulated echo acquisition mode spectroscopy (STEAM-MRS). To estimate T_1, the first MRS sequence used saturation recovery with 12 approximately log-spaced variable T_{RS} (325 to 3000 ms, T_M = 15 ms, T_E = 8.3 ms), a voxel size of 21.5 mm x 21.5 mm x 8 mm, and BW = 2 kHz and 512 samples. To accommodate respiratory motion a total scan duration for a single average, including two dummy pulses prior to acquisition, was < 20 s. The signals from three separate breath holds (three averages) were separately acquired and

concatenated to fit T_1. To fit T_2, the same MRS voxel and T_M were used in a 10 spin-echo (9, 24, 39, 54, 69, 84, 99, 114, 129, 144 ms) measurement with T_R = 1500 ms. Like the variable T_R MRS, two separate breath holds were used to acquire two averages, separately, from which the measurements were concatenated to estimate T_2. MRS fitting is further detailed in §8.2.2.

The MRF sequence used in this work was the variable T_E/fixed T_R sequence reported in Chapter 7 and very similar to that reported in Chapter 6. Briefly, the sequence used 1250 excitations with oscillating flip angles ranging from 0 to 60°, and a linearly ramped T_E from 3 to 7 ms, and T_R of 16 ms. The total scan duration was 20 s, done in a single breath hold. For subjects in the repeatability cohort, the MRF sequence was acquired at least three times. For the first three MRF acquisitions, the subjects were removed from the scanner bore and asked to stand up between scans. Two of the subjects were scanned a fourth time without being removed from the scanner bore.

8.2.2 Reconstruction and fitting techniques

The MRS data were apodized, phase and center frequency corrected. The real part of each water peak was fit with a Gaussian curve to estimate a scaling factor for the subsequent relaxometry curve fit. The T_1 and T_2 were estimated using an EPG simulation of the stimulated echo signal with simultaneous fitting for imperfect B_{1+}. The estimated T_1 and flip angle correction were used to fit the for T_2 using the variable T_E MRS data.

The MRF images were reconstructed as described in Chapter 6. Following MRF image reconstruction and coil combination, the image data were processed in different ways to test the effects of different post-processing steps on liver imaging.

Since variable T_E (or T_R) is required to encode the chemical shift information necessary for FSF estimation, the MRF data were processed with and without the MRF fat-water separation to observe the effect of phase dispersion from the variable T_E due to chemical shift and off-resonance effects. The T_1 and T_2 estimation without fat separation used the standard dictionary matching discussed in §2.4. The MRF fat-water separation with ΔB_0 fitting used the method discussed in Chapter 6. Example M_0, T_1 and T_2 maps for

each method from a subject with significant subcutaneous fat and off-resonance within the liver were generated for comparison.

To improve ΔB_0 fitting, an iterative fitting method[64] developed for conventional multi-echo Dixon imaging was adapted for MRF fat-water separation method used in Chapter 6. This method penalizes the square of the changes of the gradient of ΔB_0. Using this regularization, Eq. (6.6) becomes

$$\widehat{\Delta B}_0(\mathbf{r}) = \arg\min_{\Delta B_0} \left\| [I - AA^\dagger] \sum_{l=1}^{L} a_l(\Delta B_0(\mathbf{r}))\mathbf{s}_l(\mathbf{r}) \right\|_2^2$$
$$+ \mu \sum_{k}^{K} w_{r,k}(\Delta B_0(\mathbf{r}) - \Delta B_{0,k})^2, \qquad [8.1]$$

where μ is a weighting factor that controls the smoothness, μ = 0.02 in this study, the summation is around the K = 8 nearest voxels to the voxel at position r, $w_{r,k}$ is the voxel-specific weighting factor given in Ref [64] that ensures proper scaling of the off-resonance penalty, and $\Delta B_{0,k}$ is the current estimate of off-resonance at voxel k. By initializing $\widehat{\Delta B}_0(\mathbf{r})$ for all $\mathbf{r}$ using the first term in Eq. (8.1), the solution method in Chapter 6, this equation can be used to iteratively update the solution for $\widehat{\Delta B}_0(\mathbf{r})$. Forty iterations were used in this study. Example B_0 and FSF maps from a single subject without and with the iterative method were compared for differences in these post-processing methods.

To improve parameter fitting, slice profile effects were modeled for fat and water components. As discussed in Chapter 7, profile effects may bias the signal model needed for accurate fitting of parameters using MRF signals. The design matrix A contains models of the water and fat signals, which are coupled to ΔB_0 in (Eq. 8.2). To partially account for slice-profile effects, the MRF water and fat signals were modeled for the specific RF pulse used in the MRF acquisition (gaussian-windowed, κ = 10). These profile improvements were combined with the iterative ΔB_0 fitting for the repeatability study. Magnetization density M_0 was defined as the sum of the fat and water magnetization densities.

8.2.3 Statistical techniques

For each abdominal MRF M_0 map, the liver was manually contoured and further masked using Otsu's method[190]. This segmentation was further thresholded to exclude major vessels by masking regions that had $T_1 > 1500$ ms or $T_2 > 60$ ms. This segmentation was then applied to the T_1, T_2, and FSF maps to determine the mean hepatic parameter value from the respective maps. A smaller, focal region of interest, away from all major vessels in a given subject, was also evaluated. The fat-separated MRF water T_1 and T_2 repeatability was assessed using the intra-subject coefficient of variation[248]. The hepatic FSF repeatability was not assessed (but the hepatic FSF is plotted) since none of the subjects had known steatosis, and white adipose tissue has high fat fraction such that its repeatability is not entirely germane to hepatic steatosis. Absolute and relative changes in T_1 and T_2 between different processing methods were evaluated. Significance was P < 0.05, evaluated using a paired t-test.

8.3 Results

The comparison of parameter maps with and without fat-water separation is shown in Fig. 8.1. Substantial off-resonance within the liver parenchyma and chemical shift with the subcutaneous regions cause blurring in the M_0 maps (Fig. 8.1a). The phase dispersion confounds T_1 and T_2 fitting without the inline ΔB_0 correction provided with fat-water separation. With the ΔB_0 fitting, the blurring and parameter map quality is markedly improved.

The addition of iterative ΔB_0 fitting is exemplified in Fig. 8.2. Without the iterative solution, lateral and posterior aspects of the abdomen experience fat-water swaps seen most readily in the B_0 maps. With the iterative solution, the fat-water swaps are resolved and the B_0 map appears smoother than without iteration.
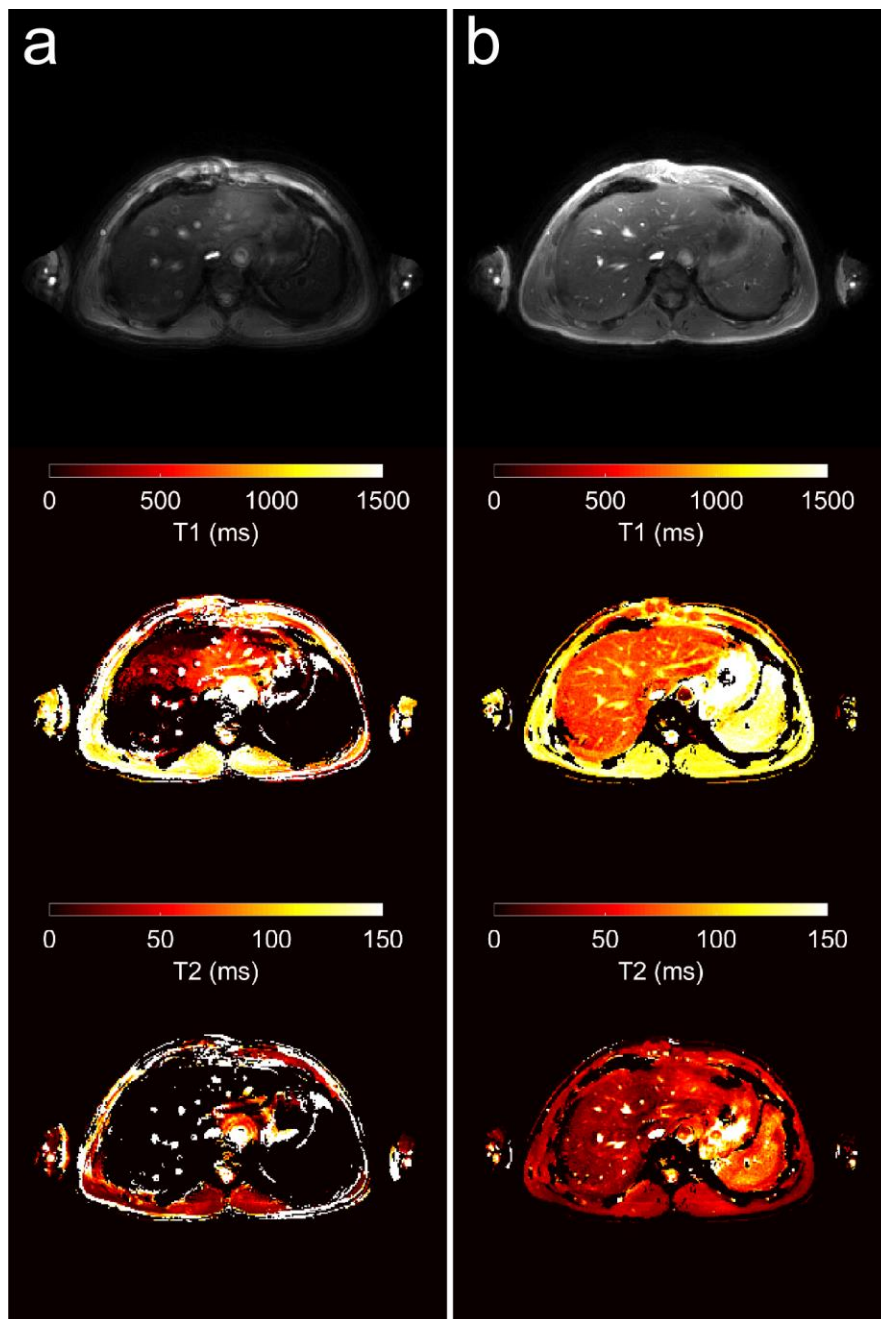
Fig. 8.1 MRF parameter maps without (a) and with (b) fat-water separation. The image data was the same for the two different sets of parameter maps. The top row shows the proton density images from the respective matches. In the case of (b) the fat and water proton density maps are summed. Phase dispersion from the variable T_E MRF sequence confounds T_1 and T_2 fitting (a) without the ΔB_0/fat fitting that is used in (b).
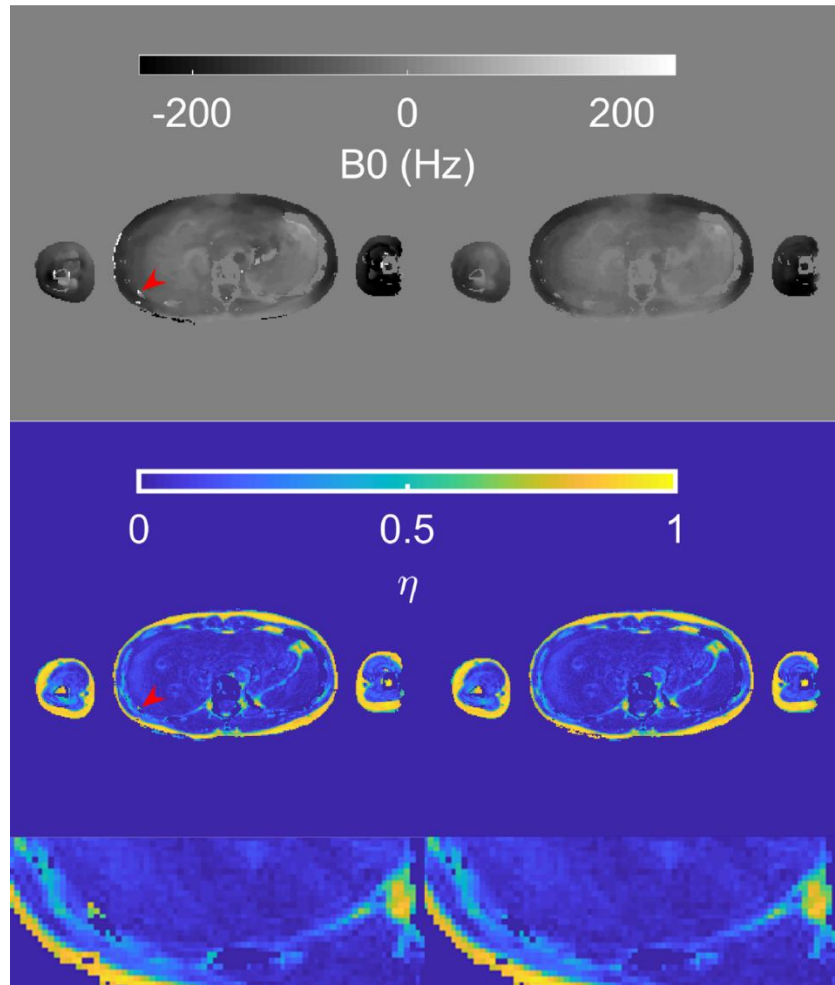
Fig. 8.2 The B_0 and fat signal fraction (η) maps without (left) and with (right) the iterative ΔB_0 solution from the same image data set. A red arrowhead denotes a region near the hepatic right lower lobe that experiences a fat-water swap in the non-iterative solution, resolved in the iteratively derived maps. A detail from the FSF maps near the fat-water swap is shown at the bottom.

Another example of combining the iterative ΔB_0 fitting with the addition of slice profile corrections can be seen in Fig. 8.3. A significant fat-water swap can be seen in the left antero-lateral aspect of the subcutaneous adipose tissue that is resolved with the enhanced ΔB_0 fitting. From the parameter maps using iterative ΔB_0 fitting without the profile correction (not shown), most of this observed correction in Fig. 8.3 is from the ΔB_0

fitting improvement. Flow artifacts around the major vessels can be seen in the FSF maps in both post-processing techniques.
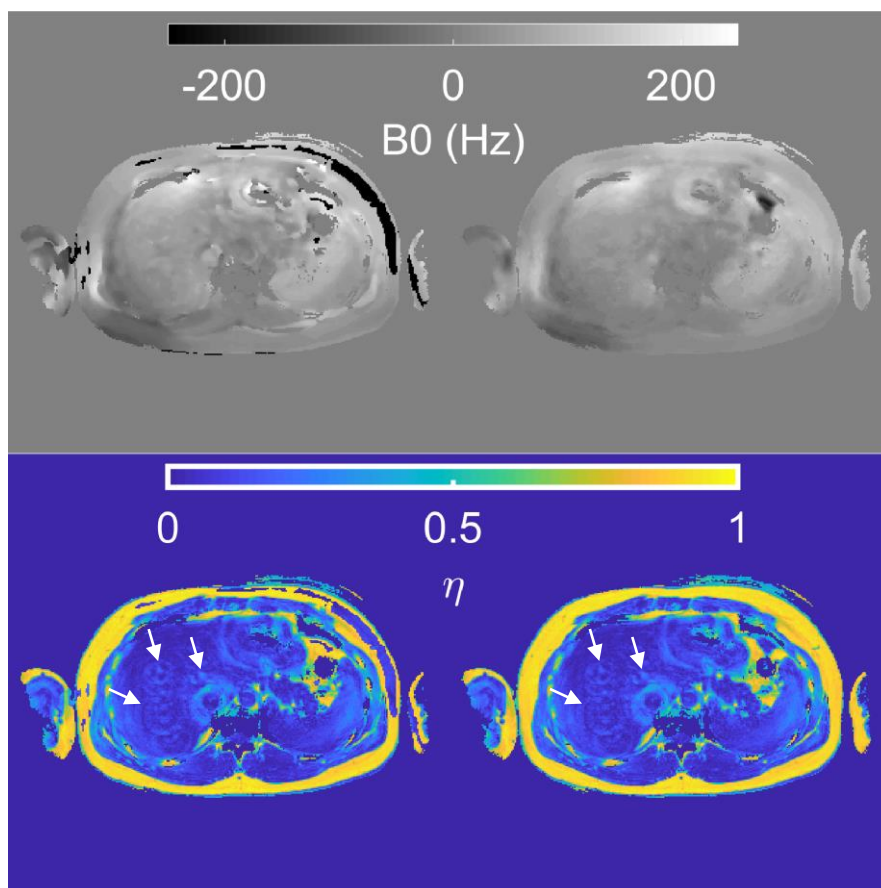
Fig. 8.3 An example of fat signal fraction (η) and ΔB_0 maps without (left) and with (right) the iterative ΔB_0 fitting and slice profile correction. Fat-water swaps can be seen throughout the subcutaneous adipose tissue without improvements to the fitting (left), that are mostly resolved with improvements to the fitting (right). Flow artifacts (arrows) can be seen near the inferior vena cava and within the liver in the FSF maps.

Changes in estimated liver T_1 and T_2 without and with iterative ΔB_0 fitting and slice profile correction in the repeatability cohort can be seen in Fig. 8.4. The mean change in the estimated T_1 is 24.9 ms (mean relative change 3.0%) and the mean change in the

estimated T_2 is -6.9 ms (mean relative change -25.2%). Both metric estimate changes are significant ($P < 10^{-5}$).
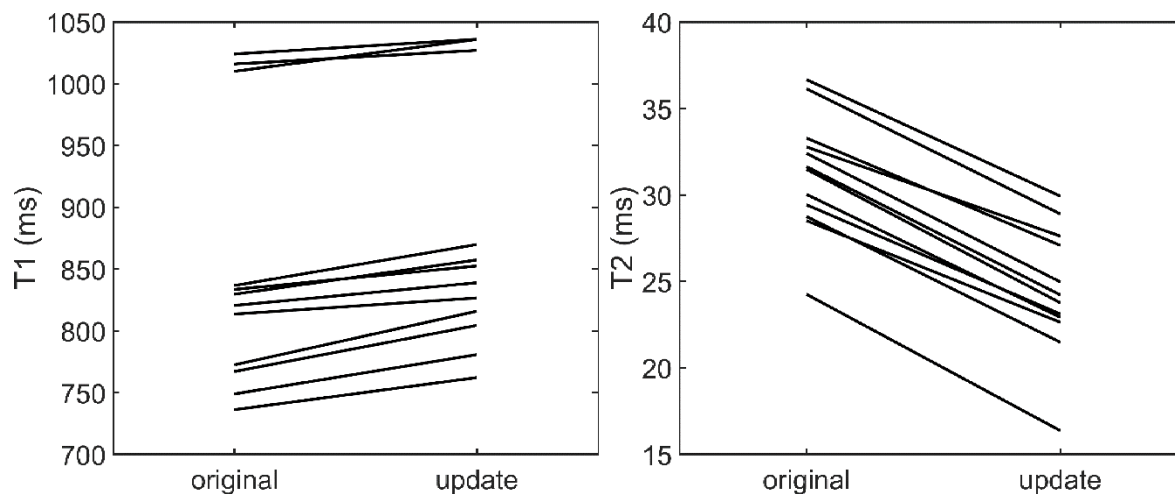
Fig. 8.4 The changes in estimated hepatic T_1 and T_2 from the repeatability cohort. The "original" processing label denotes the fat-water separation used in Chapter 6. The "update" label denotes the fat-water separation with iterative ΔB_0 fitting and slice profile modeling.

The T_1, T_2, FSF, and B_0 maps from the first three repetitions of the repeatability cohort are shown in Figs. 8.5-8. The mean hepatic T_1, T_2, and FSF from the repeatability cohort are plotted in Fig. 8.9. The intrasubject COVs are listed in Table 8.1. All subjects in the repeatability cohort were able to complete the requested breath holds and scanning. The mean T_1, T_2, and η over all subjects were 876 ms, 24.4 ms, and 0.07, respectively. The standard deviations between subjects were 109 ms, 2.9 ms, and 0.004, respectively. Small intra-subject variations in T_1 estimates were observed (Table 8.1, Fig. 8.9.a), whereas the T_2 estimate variations were proportionally much more and had higher variations across the liver, as evidenced by higher COV and standard errors of the mean (Table 8.1, Fig. 8.9b). The mDixon estimated fat fraction (not shown) was $\lesssim$ 2% throughout the liver for all subjects in the repeatability cohort.
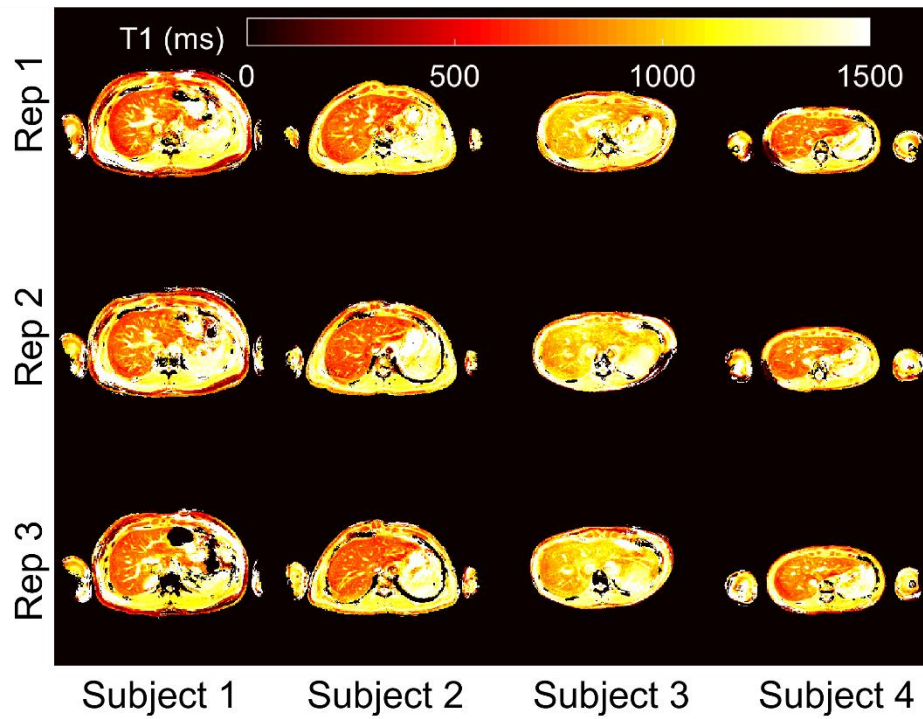
Fig. 8.5 The T_1 maps from the first three repetitions of the repeatability cohort.
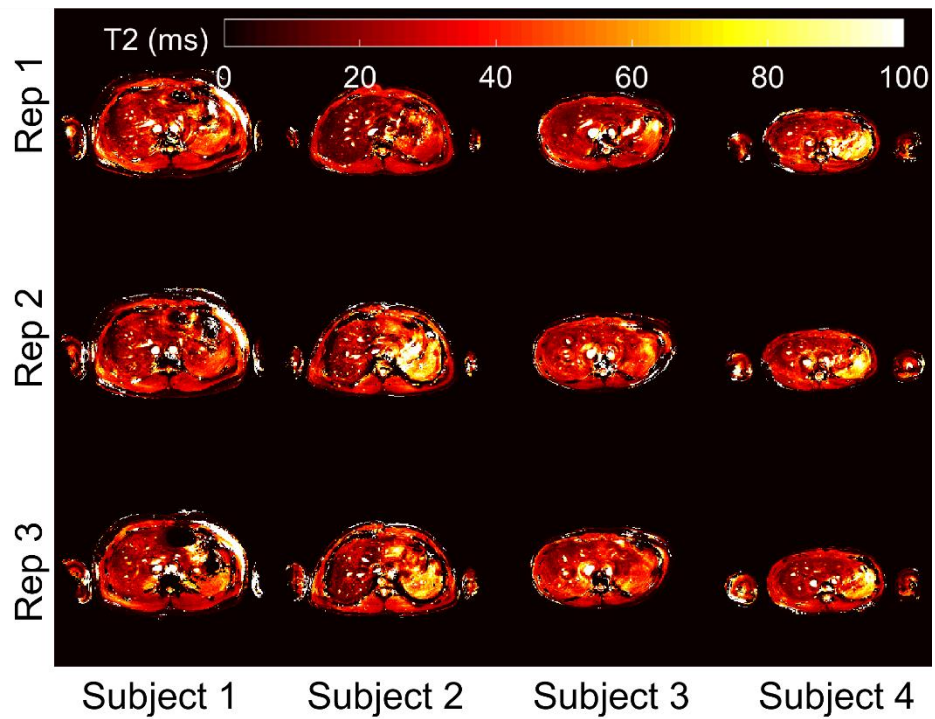
Fig. 8.6 The T_2 maps from the first three repetitions of the repeatability cohort.
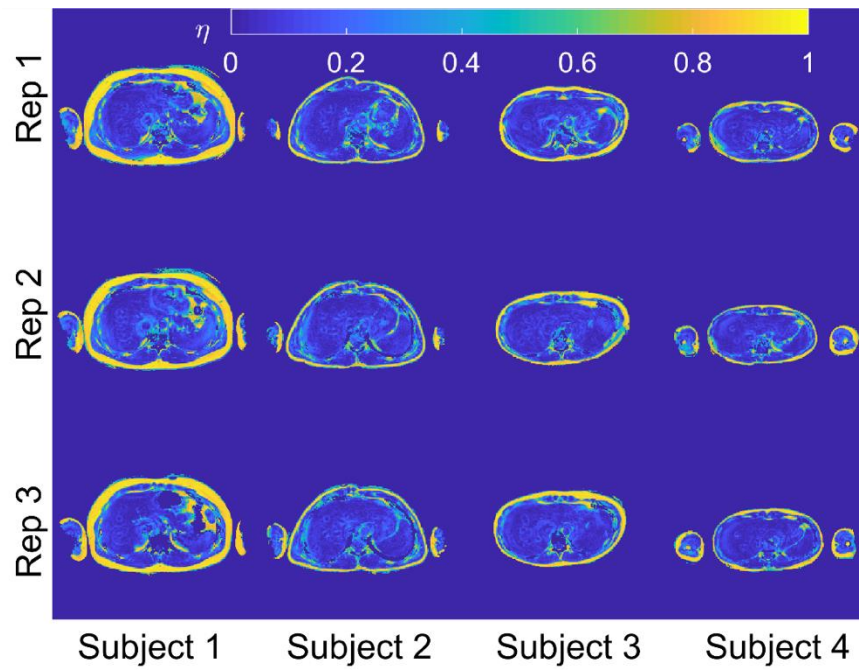
Fig. 8.7 The fat signal fraction (η) maps from the first three repetitions of the repeatability cohort.
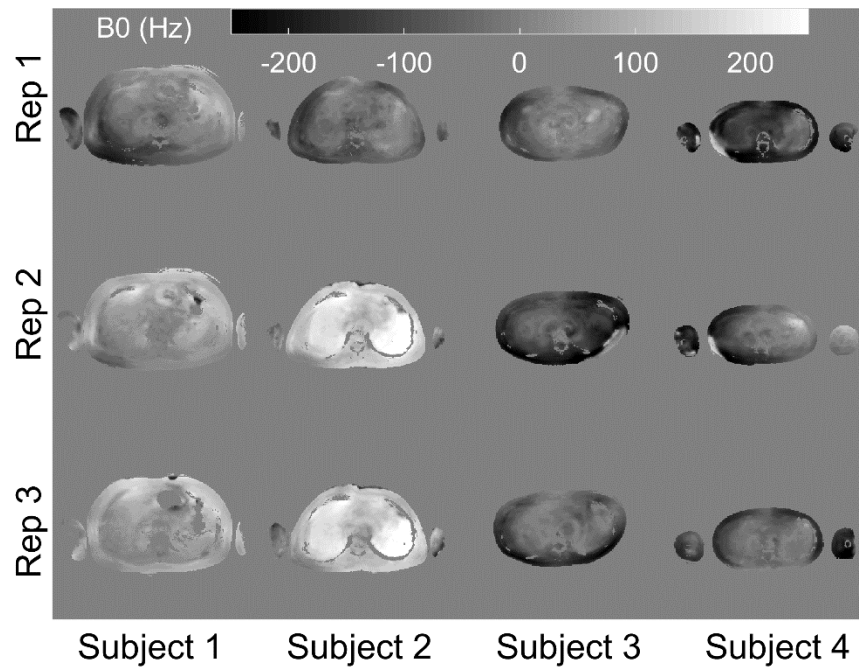
Fig. 8.8 The B_0 maps from the first three repetitions of the repeatability cohort.
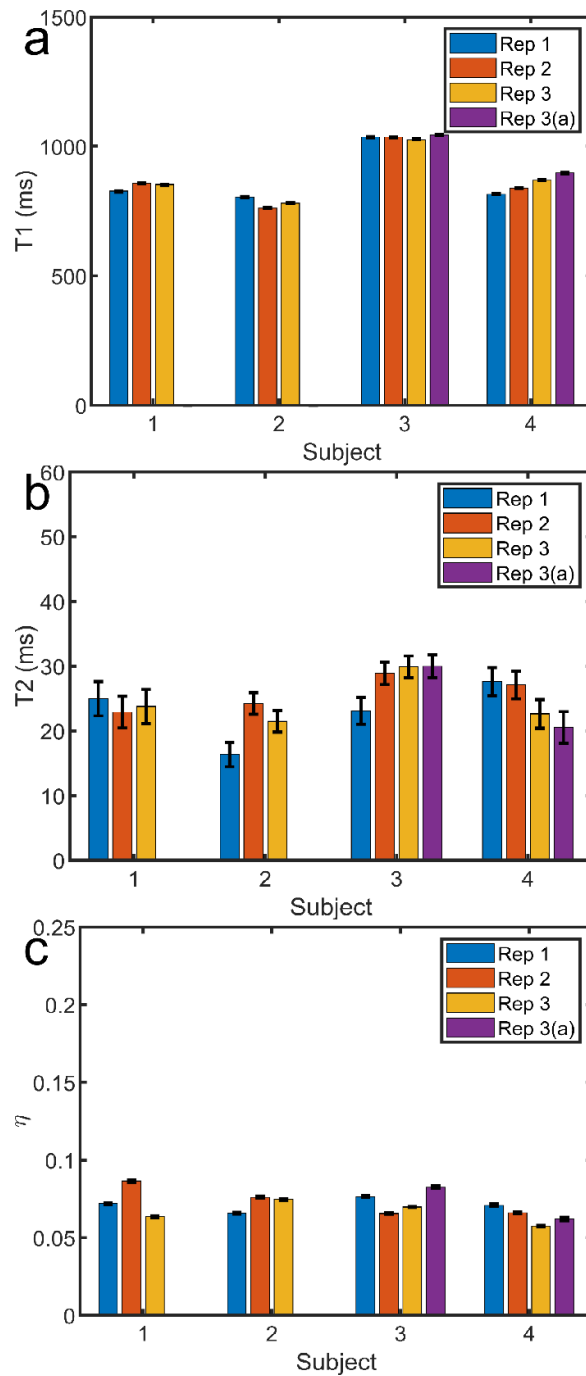
Fig. 8.9 The MRF mean hepatic T_1 (a), T_2 (b), and fat signal fraction (η; c) of the four repeatability cohort subjects for all repetitions (Rep) of the measurement. Subjects were removed from the scanner and the scanner bed between Reps 1-3. Scans were repeated without removal from the scanner bore (Rep 3a) for Subjects 3 and 4. Estimates were made using the iterative ΔB_0 fitting and slice profile correction. Error bars are standard errors of the reported means.

Table 8.1 Hepatic relaxometry coefficients of variation (COV)

	T1 COV (95% CI[a])	T2 COV (95% CI[a])
Intra-subject mean	2.4% (1.2 – 3.5%)	14.6% (7.2 – 22.4%)
Intra-subject focal[b]	5.5% (2.8 – 8.4%)	11.6% (5.8 – 17.8%)
Inter-subject mean	12.4%	11.7%

[a]CI confidence interval

[b]focal liver area is a region of interest liver of $\sim 1000 \ mm^3$

The MRS voxels overlaid on the corresponding MRF T_1 and T_2 parameter maps are shown in Fig. 8.10. The estimated MRF and MRS T_1 and T_2 from the voxel in Fig. 8.10 are given in Table 8.2.
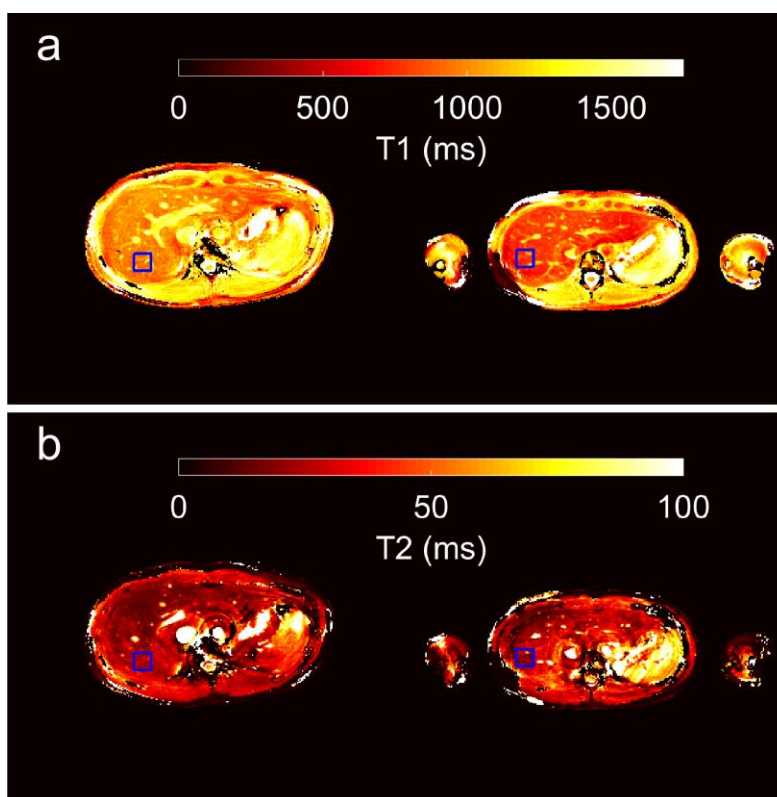
Fig. 8.10 The MRS voxel is overlaid (blue box) on the T_1 (a) and T_2 (b) parameter maps of subjects 3 (left) and 4 (right). The MRS and MRF parameter estimates are given in Table 8.2.

Table 8.2 The MRS and MRF relaxometry estimates

	T_1 (ms)[a]		T_2 (ms)[a]	
	MRF	MRS	MRF	MRS
Subject 3	992 (8)	1099	25.0 (0.4)	29.2
Subject 4	806 (8)	893	23.7 (0.6)	23.0

[a]Relaxometry estimates are listed with standard errors

The parameter maps for the NASH subject are shown in Fig 8.11. Relative to the repeatability cohort, this subject has higher visceral adipose tissue content (Fig. 8.11c), higher T_2 (Fig. 8.11f), and higher T_1 than 3/4 of the repeatability cohort (Fig. 8.11e). The T_2 increases from ~15 ms to > 50 ms posteriorly to anteriorly. The mean liver T_1, T_2, and η (with SE) are 937 ms (1.6), 32.1 ms (0.2), and 0.094 (0.001), respectively. The mDixon $\eta \lesssim$ 5%, slightly higher than that of the repeatability cohort.
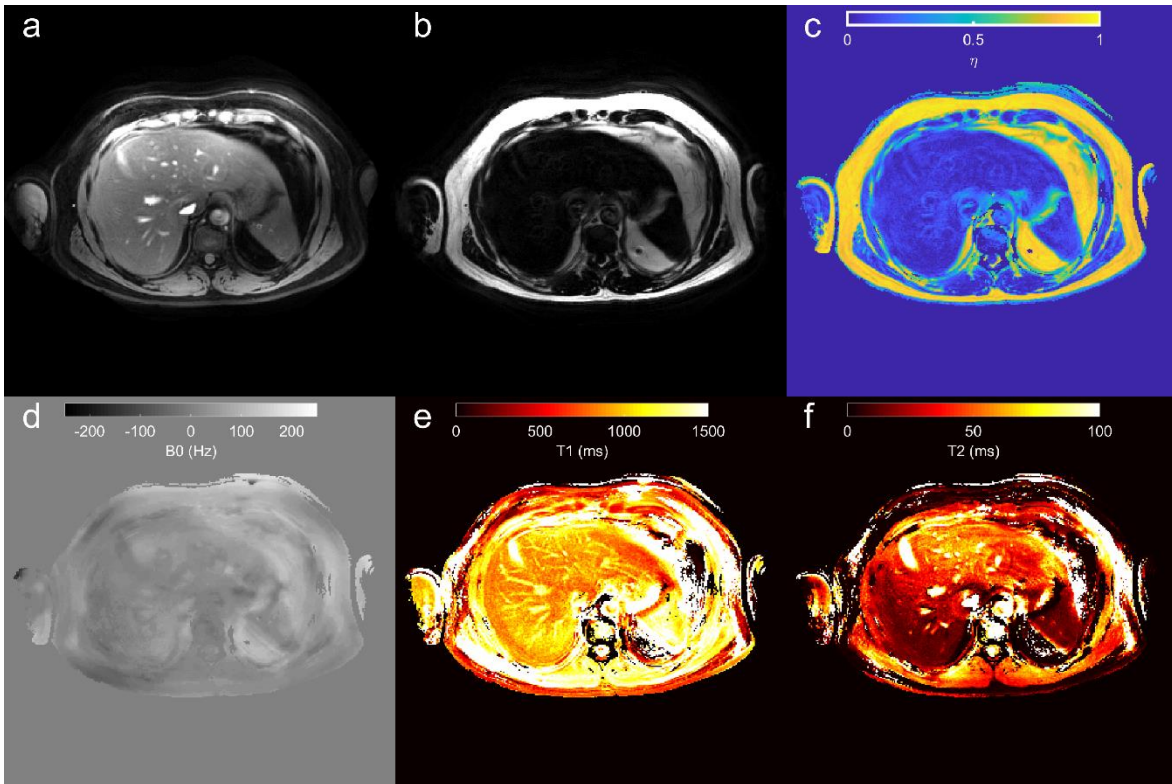
Fig. 8.11 The parameter maps from the NASH subject. The water (a) and fat (b) M_0 maps yield the fat signal fraction (η) map in (c). The B_0 map is shown in (d), with the fat-separated water T_1 (e) and T_2 (f) maps adjacent.

8.4 Discussion

The results of the MRF liver imaging and parameter estimation show repeatable T_1, anatomically consistent FSF that is positively biased in the liver, and T_2 values that are approximately consistent with MRS estimates but have poor repeatability.

The inline ΔB_0 estimation and iterative fitting markedly improve hepatic MRF image and parameter map quality. Compensation of blurring and phase dispersion from off-resonance effects is essential given the spiral trajectory and variable T_E required for chemical shift encoding. Without this fitting/compensation parameter mapping of the liver is not possible (Fig. 8.1). Conversely, a fixed T_E MRF sequence could be used to reduce the effects bias from off-resonance, but this would not compensate for spiral blurring without an independently measured B_0 map. Hepatic relaxometry with a fixed T_E MRF sequence

154

would also require prior knowledge that fat fraction is low enough not to bias the T_1/T_2 estimates (as discussed in Chapter 6). The spatial roughness penalty on ΔB_0 reduces fat-water swapping in adipose tissue as well regions within/ near the liver (Figs. 8.2-3).

The changes in hepatic T_1 and T_2 slice profile modeling are consistent with the general results of Chapter 7. Like the phantom and *in vivo* results of Chapter 7, with slice profile modeling the T_1 estimates increase a small amount and the T_2 estimates decrease a proportionally greater amount.

The MRF mean liver T_1s and T_2s are consistent with the literature, but substantial inter-subject variation in T_1 can be seen in the repeatability cohort. Reported hepatic T_1s and T_2s of subjects without liver pathology at 3 T have ranged from 717-990 ms[228,249,250] and 30-34 ms[228,249], respectively, estimated using imaging techniques or ^{1}H-spectroscopy. Imaging studies of liver relaxometry at 3 T have not used fat-water separation in cohorts without liver pathology. Given the high prevalence of NAFLD and that it can be asymptomatic, this calls into question relaxometry studies without fat fraction estimation that have not been screened for hepatic steatosis. In the fat-water separated MRF results here, one subject from the MRF repeatability cohort has higher mean water T_1 than the NASH subject. The controls on the repeatability cohort were not sufficient to guarantee the absence of variation in liver relaxometry such as prescription medications, lifestyle differences, and previously undiagnosed clinical conditions. Further study with a larger number of subjects without liver pathology is needed to understand the inter-subject variability of normal hepatic water T_1 and T_2.

The higher estimated T_1 in the NASH subject's liver, relative to non-pathological liver, follows the results of previous studies, but the T_2 estimates in this work need greater study to interpret. The higher T_1 of the NASH subject relative to the repeatability cohort mean T_1 is consistent with the expected increase of T_1 with fibrosis (see also Chapter 3). The estimate of T_2 is slightly higher than those of the repeatability cohort, but highly uncertain given the dynamic range across this subject's liver. In comparison to the MRF results, a study of 64 subjects with biopsy-proven NAFLD or were at high risk for having NAFLD, Hamilton *et al*.[251] reported a mean (and SD) hepatic water T_1 and T_2 of 822 ms (123) and 24.1 ms (4.5), respectively. However, like many relaxometry studies, it is not clear to

what degree these results were affected by incomplete modeling of non-idealities such as imperfect B_{1+}.

The intra-subject repeatability values of T_1 and T_2 are, respectively, low and high relative to the expected differences between healthy and fibrotic/inflamed liver, while the hepatic FSF values are biased. An estimate for the difference between fibrotic and non-fibrotic liver T_1 is 10%[159], and, given the sparsity of T_2 estimation in hepatic inflammation, we suppose the same relative 10% difference between the T_2 of hepatitic and healthy liver. The T_1 and T_2 intra-subjective repeatability values reported here are, respectively, low enough and too high to observe these expected differences in an individual subject. Given the intra-subject T_1 COV (Table 8.1), with further validation of the accuracy of T_1 *in vivo*, this metric may be employed for longitudinal studies in the liver. However, the intra-subject variability of T_2 is much higher and the parameter maps exhibit large changes across the liver (Figs. 8.6, 8.10-11). The potential source of these variations is further discussed below. The mean hepatic FSF estimated by mDixon suggest that all subjects within the repeatability cohort have negligible steatosis, but the mean MRF FSF values are notably higher. This is apparently due to elevations around the major vessels. The NASH subject mDixon fat fraction measurement was slightly elevated relative to the repeatability cohort and parallels the slightly larger MRF FSF estimate in the NASH subject relative to the other subjects. Notably, no steatosis was reported on clinical biopsy.

The mean hepatic T_1s and T_2s reported in this study depend on the segmentation used to define the liver parenchyma. In this study, thresholds on T_1 and T_2 were used to exclude major vessels, but further investigation is needed to determine the sensitivity of mean hepatic relaxometry estimates on these thresholds and the presence of major vessels. Conversely, the liver is often idealized as homogenous parenchyma, but it's clear from the 1.5 mm x 1.5 mm spatial resolution of the MRF T_1 parameter maps that perfusion of blood/bile throughout the liver is a multi-scale feature even far from the biliary tree, portal vein, and hepatic artery. The heterogeneity of relaxometry metrics across the liver may deserve separate study. In any event, the MRF parameter shows that the liver is not homogeneous and parameter estimates may depend on the location and region of interest within the liver.

Several limitations in the current method may need to be resolved before some of the MRF metrics can be used effectively for studies in the pathological liver. The large intra-hepatic and intra-subject variability of MRF T_2 may be explained by the bias in this metric with ΔB_0 (Chapter 7). Given the RF TBW (10) and number of nominal crusher cycles per nominal slice thickness (four) used in this study, we expect to see modulations in phase and magnitude of the MRF signals for a given T_1, T_2, and B_{1+} depending on ΔB_0 that may confound fat-water fitting. The slice profile corrections provided in this work do not account for this ΔB_0 dependency, which is further discussed in Chapter 9. However, a simple solution may be to decrease the TBW/increase the crusher strength so that the ΔB_0 effects are separable. Another source of bias is the apparent flow artifacts around major vessels, which particularly bias MRF fat fraction estimates. This may be addressed by incorporating flow suppression or by directly fitting the flow effects in the MRF data, further discussed in Chapter 9.

8.5 Conclusions

Despite some limitations, this preliminary study has shown that MRF fat-water separation can be done in a single breath hold in the abdomen in healthy and diseased subjects. Improvements to fat-water separation fitting reduce fat-water swaps. Mean liver relaxometry estimates are approximately consistent with the literature. T_1 is a more repeatable metric than T_2, and the upper limits of repeatability were determined for mean hepatic T_2. An observed increase in MRF-estimated T_1 in the NASH subject relative to the repeatability cohort is consistent with previous findings in fibrotic livers. Further developments to improve the accuracy and uncertainty of MRF parameter estimates are discussed in Chapter 9.

Chapter 9

CONCLUSIONS AND FUTURE DIRECTIONS

9.1 Conclusions

This work was motivated by the need for a rapid quantitative MRI sequence capable of imaging pathological liver. The challenges of MRF spiral blurring correction, MRF fat-water separation, and slice-profile modeling were all addressed in this work, as well as others. This dissertation makes substantial progress on the specific aims noted in Chapter 4. The advancement on these technical and measurement developments, as well as remaining areas for improvement, are discussed below. A section on future directions follows this section.

This work has addressed multiple facets of blurring in spiral MRF. While significant portions of recent MRF developments have used radial acquisitions, presumably in part to avoid blurring, the gradient efficiency of spiral k-space trajectories may be higher. The initial development of uSSFP MRF reported limited sensitivity to ΔB_0 effects, but it can be seen from Chapters 4-6 and 8 that as $t_{acq}\Delta B_0 \gtrsim 1/2$, where t_{acq} is the spiral acquisition time, blurring is noticeable in the image domain. Clearly, this blurring is not unique to uSSFP. Any spiral MRF sequence with large enough t_{acq} or ΔB_0 will be subject to blurring. In Chapter 5 MRF spiral blurring was partly resolved using a form of conjugate-phase reconstruction, also demonstrating that blurring was coupled to parameter estimation accuracy in regions of heterogeneous T_1 or T_2. Relaxometry bias in blurred voxels was reduced with the MFI correction.

A limitation in Chapter 5 was the need for independent B_0 mapping, which was addressed in Chapter 6. Simultaneous fitting for ΔB_0 was resolved by using the variable projection technique with a multi-T_E MRF sequence. This enabled simultaneous estimation of ΔB_0 with fat-separated water T_1 and T_2, and fat signal fraction (FSF). To use variable projection, the off-resonance modeling in Chapter 6 exploited the separability of ΔB_0 from the MRF contrast effects under the idealized slice profile/instantaneous RF assumption. This separability was also used to model a basis for MRF signals with off-resonance effects,

avoiding the more time-consuming approach of explicitly modeling each ΔB_0. That is, for the fixed TR uSSFP MRF sequences described in Chapters 6-8 the MRF signal vector for any off-resonance frequency f, under the separable assumption, can be computed as

$$\mathbf{s}(T_1, T_2, B_{1+}, f) = \mathrm{J}_\mathrm{f}\,\mathbf{s}(T_1, T_2, B_{1+}, 0), \qquad [9.1]$$

where J_f is a diagonal matrix with entries $j_{n,f} = e^{i2\pi f T_{\mathrm{E},n}}$. Since it likely takes much longer to directly compute the off-resonance effects with the MRF contrast effects than to compute the MRF contrast effects than the off-resonance phase modulations by Eq. (9.1), this dramatically improves the timing of modeling of off-resonance. To form the MRF basis with off-resonance in Chapter 6, a set of frequencies that (in linear combination) could model any phase evolution on the diagonal of J_f with MFI was used to generate a storage basis using this separable approach. While not discussed explicitly in Chapter 6, this is an alternative use of the MFI technique: deblurring is accomplished by demodulation through the k-space trajectory acquisition window with conventional MFI, whereas the basis for phase modulation of each excitation of the linearly swept T_E MRF sequence is modeled by this repurposed form of MFI. Chapter 6 also addressed another limitation of Chapter 5, where the blurring from chemical shift confounded the blurring from other off-resonance effects.

To uncouple fat blurring from non-chemical shift blurring, the deblurring correction was accomplished by two different ways in the fat-water separation technique from Chapter 6. Building on Chapter 5, MFI was incorporated into the ΔB_0 fitting to resolve non-chemical shift related blurring, but direct k-space fitting was used to resolve blurring from fat. This approach resolved the dual deblurring problem noted in Chapter 4, where fat blurring adds with off-resonance blurring without pre-existing knowledge of the off-resonance map or fat distribution. Other recent forms of fat-water MRF using spirals have used dictionary-based approaches to directly fit for ΔB_0 and then fit for water and fat parameters (without T_2)[216] or used repeated fixed T_E MRF acquisitions, with different T_Es each acquisition, to directly apply Dixon fat-water separation on each frame[252,253] ("Dixon-

MRF"). In the former case, fitting for fat properties can be confounded by ΔB_0, presumably because the off-resonance was fit sequentially instead of simultaneously with fat. The reported dictionary-based method also used RF spoiling, so did not attempt to account for any form of refocused transverse relaxation. However, this study did account for B_{1+} effects. The Dixon-MRF approach to MRF fat-water separation theoretically offers greater versatility than the method proposed in this work because a simultaneous fat-water separation with ΔB_0 is accomplished at the outset of processing with a well-established method, which then permits an independent analysis of the fat and water signals. This permits relaxometry estimates of the fat. Unfortunately, each T_E requires an independent MRF acquisition, expanding the scan duration, which makes it difficult to acquire in a single breath hold. A recent study using Dixon-MRF for cardiac applications overcame the timing constraints by inclusion of low a low-rank reconstruction technique (see also §9.2) and avoided blurring altogether by using a radial k-space trajectory.[253] Without blurring, it may be possible to simplify the method in Chapter 6 to directly fit with variable projection in the image domain.

It remains to be seen under what circumstances it is better or worse to use the proposed MRF method's acquisition of ~1000 independent echo times with a fixed fat model over the Dixon-MRF approach. The closely spaced echoes should improve fat-water fitting relative to coarse discretizations in echo time by providing a high bandwidth for fat/ΔB_0 determination, but smoothing was still required in practice to avoid fat-water swaps in Chapters 6 and 8. In theory, many echo times over a large span of echoes may improve resolution/differentiation of multi-peak fat models. This is further discussed in §9.2.

Chapter 6 showed that fat-water separation was essential to make unbiased relaxometry estimates of the water. A common theme throughout MRI is the tension between suppressing or fitting unwanted signals such as those from fat. Insofar as the fat and water signal models are accurate, fitting for fat permits complete recovery of the water signal without the extra scan duration/sequence constraints required for lipid signal suppression. This is true to the spirit of MRF, which attempts to minimize the time necessary to acquire the data by modeling effects that cannot be fit by conventional

analytical assumptions. A complication to fat-water separation noted in Chapter 6 is that accurate fitting of fat required the assumption that triglyceride (TG) relaxometry properties were unchanged. This assumption is perhaps controversial. On one hand, *in vitro* mixtures of fat with water, have shown to have a significant effect on fat relaxometry values.[48] On the other hand, *in vivo* TG storage in hepatocytes occurs within lipid droplets surrounded by phospholipid monolayers,[108] which likely restricts TG interactions with proteins to a greater degree than water interactions with proteins. This may limit relaxometry variability within fat. Supporting this hypothesis, a study[44] of excised intact white adipose tissue and brown adipose tissue have shown only small differences in T_1 and T_2 between the two fat types.

The initial validations of FSF estimation in Chapter 6 suggest that J-coupling does not strongly influence the MRF fat-water separation. The high concordance between MRF and conventional FSF estimates supports this claim. This may be due to a combination of the relatively short T_R used in the MRF sequence, which will help to reduce J-coupling effects relative to longer refocusing periods, and the contribution of FID to the uSSFP MRF signal sampled at short T_E (~3 ms) relative to the J-coupling period (~ 140 ms).

The developments in slice profile modeling illuminate results from previous chapters, as well as provide unresolved challenges in MRF fat-water separation. Bloch simulations have mostly been used to model slice profile effects in bSSFP MRF. As noted in Chapter 7, the use of EPG has been popular in uSSFP MRF signal modeling because the large (and possibly unknown) number of isochromats necessary to capture a coherence pathway with conventional Bloch simulation can often be characterized by a relatively small number of states in EPG. The framework of ssEPG attempts to bridge the gap between a conventional (Bloch) spatial-domain approach without altogether abandoning EPG. While the advantage of the reduced number of EPG coherence states relative to the number of Bloch simulation isochromats may be compromised when slice-profile modeling is included, it is not clear in which circumstances one approach may be advantageous over another. Nonetheless, the development of ssEPG and associated relationships helped to shed light on the mechanism by which bias was observed in T_2 depending on time-bandwidth product and crusher strength. The ssEPG approach may also be applied to other

problems such slice-selective multiple spin-echo signal modeling and, potentially, to RF/sequence optimization problems.

The bias in MRF estimated T_2 with off-resonance and slice-profile related effects may explain some of the phantom and *in vivo* results in Chapters 6 and 8. For instance, the reduction in T_2 bias with increasing FSF (Fig. 6.13) was not as much as expected according to the simulations and the T_1 results in the same phantom. A possible explanation for this was the contribution of the highly dynamic slice profiles observed in Chapter 7 that interacted with the water-oil boundary to produce bias. In addition to this, imperfect B_0 shimming and incomplete modeling of the fat signal from chemical shifts could bias results. In the liver, T_2 was found to be more variable than T_1, and was likely biased in some cases. For instance, the NASH subject's intra-hepatic T_2 estimation variability may be explained by ΔB_0 effects in the context of Chapter 7. Besides sequence changes to reduce these sources of bias, further slice profile modeling (see also §9.2) may be possible to account for them.

Another potential source of bias in hepatic MRF T_1 estimates is magnetization transfer (MT). The MRF and MRS results from the liver in Table 8.2 suggest that MRF T_1 measurements may be negatively biased relative to MRS. The repeated on-resonance action of the MRF excitation may saturate the hepatic macromolecular pool, which then may result in dynamic signal changes not currently modeled. However, given the small difference in macromolecular pool fraction reported between non-fibrotic and fibrotic liver (3.2.2.2.iv), any MT bias in MRF T_1 estimates may be similar between healthy and diseased liver. Furthermore, the accuracy of the single breath-hold saturation recovery MRS method used to estimate T_1 in Chapter 8 needs further study to firmly establish it as a reference.

Irrespective of the remaining challenges for MRF fat-water parameter estimation in the liver, the work presented here has brought multi-fold developments and improvements to MRF. MRF spiral blurring has been evaluated and a solution to correct for this was found. Accurate fat-signal fraction estimation with simultaneous estimation of water T_1 and T_2, and ΔB_0 has been demonstrated with a spiral blurring correction. Reduction of T_1 and T_2 estimation bias in the presence of fat has been shown. Incorporation of an established form of regularization to improve ΔB_0/FSF estimation improved MRF fat-water fitting. The extended phase graph formalism has been further extended to account for slice profile

effects. Aggregated, these developments have been employed in healthy and diseased liver. The intra-subject repeatability of hepatic T_1 and T_2 using these MRF techniques has been determined. Additionally, the role of ΔB_0 in slice-selective unbalanced free precession sequence T_2 bias has been further explained. To promote reproducibility, the code for chapters based on publications has been or will be publicly released. The local MRI scanner was coded to allow: spiral MRF acquisition with design control; undersampled acquisition; options for variations of MRF T_R, T_E, and flip angle pattern; projection imaging for slice profile measurements; and custom radiofrequency pulses. All these MRI system developments are available for local institutional use.

9.2 Future Directions

In Chapter 6, aliasing from undersampled MRF k-space trajectories produced bias in the parameter maps. One means to overcome this is to incorporate low-rank[233] reconstruction or matrix completion[232]. In these iterative methods, the problem of aliasing or missing k-space data is resolved by forming an orthogonal signal basis either from a pre-calculated dictionary or from a fully-sampled calibration region in k-space. Low rank reconstruction has been recently applied to cardiac Dixon MRF fat-water separation.[253] In this form of reconstruction, the vectorized image coefficient estimates $\hat{\mathbf{x}}$ (of the basis vectors in U) can be given as

$$\hat{\mathbf{x}} = \arg_{\mathbf{x}} \min ||\mathrm{PUFS}\mathbf{x} - \mathbf{k}||_2^2. \qquad [9.2]$$

In Eq. (9.2), P represents a sampling operator that takes fully sampled k-space into its undersampled representation, F is a non-uniform Fourier transform operator, S is the coil sensitivity weightings, and $\mathbf{k}$ is the measured k-space data. Regularized versions of this add other terms to Eq. (9.2). The challenge of using this approach with the MRF method proposed in Chapter 6 is the rank of U may be too high such that there are not enough measurements to adequately recover the missing data. The signal T_1 and T_2 contrast remain relatively low rank, but the variable T_E provides phase sensitivity that may compound the rank of U such that too many observations are needed for accurate reconstruction without

increasing the scan duration. However, MRF low rank techniques have been recently enhanced by enforcing image sparsity.[254] Adding this and other constraints may help to limit the possible solution space so that low rank reconstruction is more effective for the MRF methods proposed in this work.

Another area to improve or expand fat-water MRF is TG definition and characterization. The fat model used in the current MRF fat-water separation is based on *ex vivo* MRS measurements of white adipose tissue. While the fat signal fraction models in Chapter 6 produce FSF estimates consistent with conventional methods in a fat-water phantom, more precise measurements of the relaxometry properties of the different fat moieties may yield more accurate results. Conversely, with further sequence optimization, it may be possible to assess differences in TG properties like degree of saturation/number of double bonds in the acyl chains. This has been done using conventional MRI.[43,255] If a series of accurate signal models for TG could be generated, a "TG dictionary" can be formed. The resulting design matrix for water and TG signals is

$$A = [U_w \ U_f]. \qquad [9.3]$$

This matrix forms a signal basis for water and fat, where U_w and U_f represent the left singular vectors of the water and TG dictionaries, respectively. If some degree of orthogonality between the TG atoms and the water atoms was maintained, as it is in the current MRF fat-water separation, then A may be reasonably conditioned. Alternatively, Eq. (9.3) could include some form of regularization to improve its conditioning. After fat-water separation, a second fitting/dictionary match can be done on the reconstructed fat signals to determine the TG atom at each voxel that best matches the signal.

As discussed in Chapter 4, MRF fat-water separation advances designed for liver imaging are applicable to other anatomical sites. As example, brown adipose tissue (BAT) in adults is of great research interest because of its metabolic/thermogenic properties.[256] However, BAT is a challenging tissue to study with MRI because it is predominately located near the supraclavicular fossa near the apex of the lung. The partial volume of fat, respiratory motion, B_0 heterogeneity, and dynamic metabolism suggest that a rapid multi-

parametric fat-water separation such as those employed in this work may be useful for its study. As a proof-of-concept we imaged a volunteer in their BAT depot at 3 T. Following informed consent and with approval of local institutional review board, the single breath hold MRF with the variable T_E MRF sequence from Chapter 6 was acquired. The parameter maps from this subject are shown in Fig. 9.1. Many of the successes and needs for improvements apparent in Fig. 9.1 are like those from the liver imaging in this work. MRF developments for liver imaging translate to developments in other areas of the body.
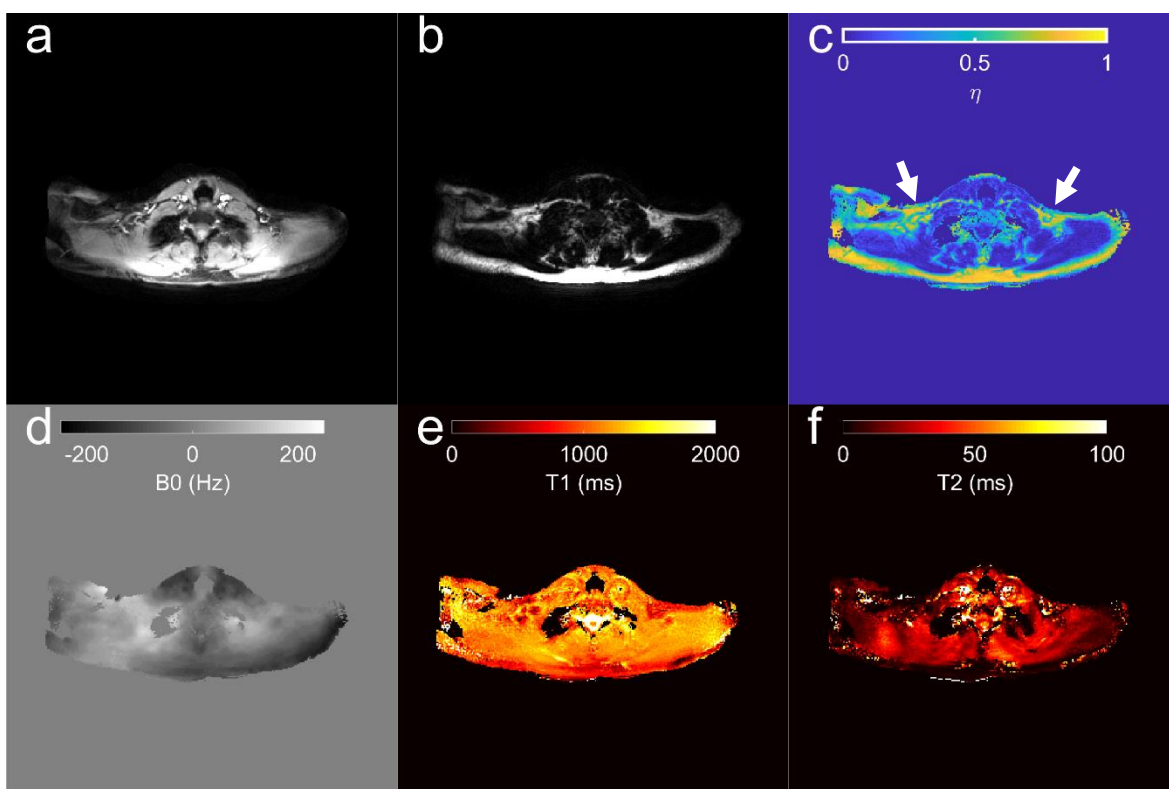
Fig. 9.1 The MRF parameter maps from a transverse slice through the brown adipose tissue (BAT) depot near the supraclavicular fossa. The water (a) and fat (b) maps are shown adjacent to the fat signal fraction (η) map (c) with arrows indicating the BAT depots. The B_0 map (d) is shown adjacent to fat-separated T_1 and T_2 maps.

A semi-separable solution may be used to help resolve bias in MRF T_2 estimation with fat-water separation. A major improvement required for robust MRF relaxometry is resolving the ΔB_0 dependent T_2 bias. The source of this bias came from small fluctuations

in magnitude and phase depending on these two parameters. This presents a problem for the technique introduced in Chapter 6, which requires MRF T_2 effects to be separable from ΔB_0. A possible solution is to include the small magnitude and phase modulations in the MRF signal in the calculation of the water basis sets. While this is not strictly accurate, since these signal modulations occur for $\Delta B_0 \neq 0$, which is outside the span of the basis used during k-space water-fat separation, it may still permit fat-water separation if these modulations are not parallel with the fat signal and do not much increase the rank of the water basis. That is, the fat-water design matrix A from Chapter 6 becomes

$$A = \begin{bmatrix} \widetilde{U} & \widetilde{f} \end{bmatrix}. \qquad [9.3]$$

Here, $\widetilde{U}$ represents the left singular vectors of with all ΔB_0-dependent phase and magnitude modulations at $T_E = 0$ with MRF T_1 and T_2 contrast modeled out to the full T_E, and $\widetilde{f}$ represents the fat signal model vector using a full B_0 modeling (discussed further below). More simply, Eq. (9.3) supposes that the water basis spans a larger space than necessary but does not span into the space of the signal basis of fat much more than the idealized approach taken in Chapter 6. To improve slice-profile models of the large fat chemical shift, the fat model would need to be modeled without the simplifying free precession assumption. Examples of an MRF slice profile, signal magnitudes and phases from fat modeled with and without free precession are shown in Fig. 9.2. Both model types used the same fat model from Chapter 6. The "RF interaction" model type, unlike the free precession model, modeled chemical shift during the RF pulse. Differences in the signal magnitude and phase can be seen between the models.
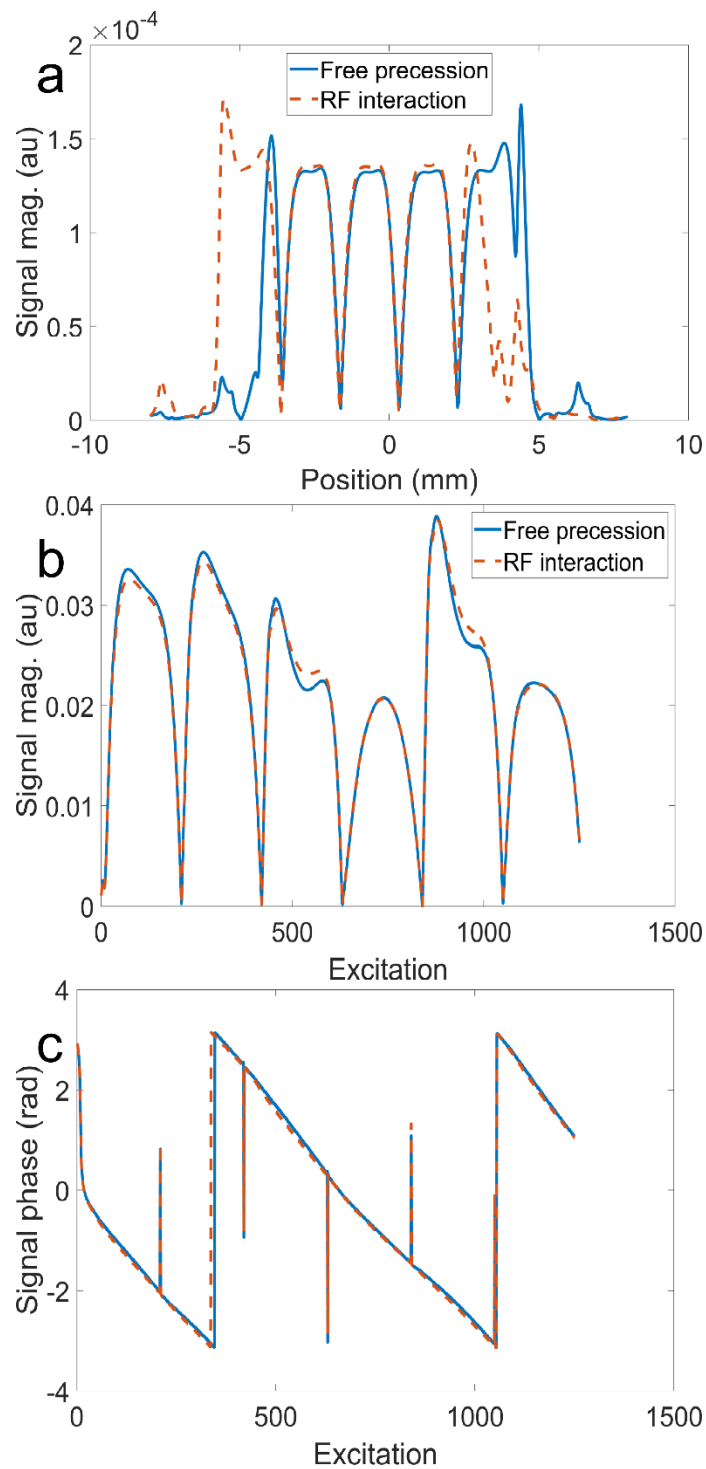
Fig. 9.2 The simulation of MRF fat profiles and signals under the free precession model of chemical shift effects, as well as a model where chemical shifts occur during the RF pulse. The magnitude of the slice profile (a) is from the excitation where the signal magnitude (b) deviation is large (excitation #543). The phase of the fat signal is shown in (c).

Flow compensation is likely an area of future work that will benefit parameter map quality. MRF methods have been developed outside this work that are flow sensitive.[257] Unfortunately, from the MRF *in vivo* parameter maps in this work, sensitivity to flow with spiral acquisition appears to unintentionally confound fitting, particularly of FSF. The source of these artifacts is not certainly flow, but it is notable that the radius of blurring appears to be dependent on the vessel diameter. This is consistent with phase dispersion proportional to vessel radius during the spiral acquisition, but further analysis is needed to determine if this is the cause. Remediation of flow artifacts will likely require explicit modeling of the flow so that its contributions may be fit out of the data set. Alternatively, flow suppression may be built into the MRF sequence, or a fast, radial acquisition may be used to minimize blurring effects due to flow.

Volumetric acquisition would likely benefit the utility of MRF fat-water separation. Single-slice, histologically correlated MRI metrics would drastically increase sampling relative to a single needle-core biopsy. However, for diagnostic utility and to reduce estimation variability, volumetric imaging would be preferred. Based on the experience in this work, the timing requirement for a single breath-hold acquisition is ~20 s scan duration. While reductions in the scan time may be achieved by further sequence optimization and low rank reconstruction discussed above, alternative strategies may be needed to acquire more through-plane data. One approach is simultaneous multi-slice (SMS) acquisition,[258] which, as the name suggests, simultaneously excites multiple slices of data. This has been demonstrated for MRF without fat-water separation,[259,260] but further exploration is required to determine if this can be adapted to k-space based fat-water separation.

Related to volumetric acquisition is respiratory motion compensation, which imposes timing constraints on abdominal imaging. Triggered acquisition strategies have been used in cardiac MRF,[68,253] so may be useful in liver imaging. The use of respiratory navigators could also be employed to prospectively or retrospectively gate MRF acquisition. An alternative to these strategies is free-breathing image acquisition. A recent application to cardiac MRF, showed that free breathing without ECG triggering was possible using a low-rank tensor approach with a fully sampled calibration region in k-space.[261] Applied to

the abdomen, such an approach may allow very high resolution volumetric parameter mapping previously unobtainable in the liver.

The work presented here provides a basis or a departure point for many future studies that may have broad influence over many aspects of quantitative MRI. These future developments may help address many current challenges to MRF, extracranial quantitative MRI in the liver and other anatomical locations, and in a variety of human diseases and pathologies.

BIBLIOGRAPHY

1. Bloch F. Nuclear Induction. *Phys Rev*. 1946;70(7-8):460-474. doi:10.1103/PhysRev.70.460

2. Bernstein MA, King KF, Zhou XJ. *Handbook of MRI Pulse Sequences*. Academic Press; 2004. https://www.elsevier.com/books/handbook-of-mri-pulse-sequences/bernstein/978-0-12-092861-3.

3. Gore JC, Brown MS. Pathophysiological Significance of Relaxation. In: *Magnetic Resonance Imaging, Vol. II*. ; 1988:1070-1074.

4. Bloembergen N, Purcell EM, Pound R V. Relaxation effects in nuclear magnetic resonance absorption. *Phys Rev*. 1948;73(7):679-712. doi:10.1103/PhysRev.73.679

5. Bottomley P. Frequency Dependence of Tissue Relaxation Times. In: *Magnetic Resonance Imaging, Vol. II*. ; 1988:1075-1098.

6. Blumich B. *NMR Imaging of Materials*. Vol 57. OUP Oxford; 2000.

7. Stanisz GJ, Odrobina EE, Pun J, et al. T1, T2 relaxation and magnetization transfer in tissue at 3T. *Magn Reson Med*. 2005;54(3):507-512. doi:10.1002/mrm.20605

8. Kiselev VG, Novikov DS. Transverse NMR relaxation in biological tissues. *Neuroimage*. 2018;182(December 2017):149-168. doi:10.1016/j.neuroimage.2018.06.002

9. Hahn EL. Spin echoes. *Phys Rev*. 1950;80(4):580-594. doi:10.1103/PhysRev.80.580

10. Go KG, Edzes HTES. Water in Brain Edema. *Arch Neurol*. 1975;32(7):462. doi:10.1001/archneur.1975.00490490066006

11. Does MD. Inferring brain tissue composition and microstructure via MR relaxometry. *Neuroimage*. 2018;182(December 2017):136-148. doi:10.1016/j.neuroimage.2017.12.087

12. Does MD, Beaulieu C, Allen PS, Snyder RE. Multi-component T1 relaxation and magnetisation transfer in peripheral nerve. *Magn Reson Imaging*. 1998;16(9):1033-

1041. doi:10.1016/S0730-725X(98)00139-8

13. Deoni SCL, Rutt BK, Arun T, Pierpaoli C, Jones DK. Gleaning multicomponent T 1 and T 2 information from steady-state imaging data. *Magn Reson Med*. 2008;60(6):1372-1387. doi:10.1002/mrm.21704

14. Edzes HT, Samulski ET. Cross relaxation and spin diffusion in the proton NMR of hydrated collagen. *Nature*. 1977;265(5594):521-523. doi:10.1038/265521a0

15. Henkelman RM, Huang X, Xiang Q-S, Stanisz G, Swanson S, Bronskill M. Quantitative interpretation of magnetization transfer. *Magn Reson Med*. 1993;29(6):759-766. doi:10.1002/mrm.1910290607

16. Morrison C, Mark Henkelman R. A Model for Magnetization Transfer in Tissues. *Magn Reson Med*. 1995;33(4):475-482. doi:10.1002/mrm.1910330404

17. de Boer RW. Magnetization Transfer Contrast. *Philips Med Syst MedicaMundi*. 1995;40:64-73.

18. Bottomley PA, Foster TH, Argersinger RE, Pfeifer LM. A Review of Normal Tissue Hydrogen NMR Relaxation Times and Relaxation Mechanisms from 1-100 MHz. *Med Phys*. 1984;11(4):425-448.

19. Damadian R. Tumor detection by nuclear magnetic resonance. *Science*. 1971;171(3976):1151-1153. http://www.ncbi.nlm.nih.gov/pubmed/5544870.

20. Gochberg DF, Gore JC. Quantitative magnetization transfer imaging via selective inversion recovery with short repetition times. *Magn Reson Med*. 2007;57(2):437-441. doi:10.1002/mrm.21143

21. Li K, Zu Z, Xu J, et al. Optimized inversion recovery sequences for quantitative T1 and magnetization transfer imaging. *Magn Reson Med*. 2010;64:491-500. doi:10.1002/mrm.22440

22. Look DC, Locker DR. Time saving in measurement of NMR and EPR relaxation times. *Rev Sci Instrum*. 1970;41(2):250-251. doi:10.1063/1.1684482

23.   Kay I, Henkelman RM. Practical Implementation and Optimization of One-shot T1 imaging. *Magn Reson Med*. 1991;22(2):414-424. doi:10.1002/mrm.1910220249

24.   Messroghli DR, Radjenovic A, Kozerke S, Higgins DM, Sivananthan MU, Ridgway JP. Modified Look-Locker Inversion Recovery (MOLLI) for High-Resolution T 1 Mapping of the Heart. *Magn Reson Med*. 2004;52:141-146.

25.   Deoni SCL, Peters TM, Rutt BK. High-resolution T1 and T2 mapping of the brain in a clinically acceptable time with DESPOT1 and DESPOT2. *Magn Reson Med*. 2005;53(1):237-241. doi:10.1002/mrm.20314

26.   Carr HY, Purcell EM. Effects of Diffusion on Free Precession in Nuclear Magnetic Resonance Experiments. *Phys Rev*. 1954;94(3):630-638. doi:10.1103/PhysRev.94.630

27.   Meiboom S, Gill D. Modified Spin-Echo Method for Measuring Nuclear Relaxation Times. *Rev Sci Instrum*. 1958;29(8):688-691. doi:10.1063/1.1716296

28.   Poon CS, Henkelman RM. 180° Refocusing Pulses Which Are Insensitive To Static and Radiofrequency Field Inhomogeneity. *J Magn Reson*. 1992;99(1):45-55. doi:10.1016/0022-2364(92)90154-Y

29.   Poon CS, Henkelman RM. Practical T2 quantitation for clinical applications. *J Magn Reson Imaging*. 1992;2(5):541-553. doi:10.1002/jmri.1880020512

30.   Hargreaves BA. Rapid gradient-echo imaging. *J Magn Reson Imaging*. 2012;36(6):1300-1313. doi:10.1002/jmri.23742

31.   Weigel M. Extended phase graphs: Dephasing, RF pulses, and echoes - Pure and simple. *J Magn Reson Imaging*. 2015;41(2):266-295. doi:10.1002/jmri.24619

32.   Bieri O, Scheffler K. Fundamentals of balanced steady state free precession MRI. *J Magn Reson Imaging*. 2013;38(1):2-11. doi:10.1002/jmri.24163

33.   Cooley JW, Tukey JW. An Algorithm for the Machine Calculation of Complex Fourier Series. *Math Comput*. 1965;19(90):297. doi:10.2307/2003354

34.   Dutt A, Rokhlin V. Fast Fourier Transforms for Nonequispaced Data. *SIAM J Sci Comput*. 1993;14(6):1368-1393. doi:10.1137/0914081

35.   Fessler JA, Sutton BP. Nonuniform fast fourier transforms using min-max interpolation. *IEEE Trans Signal Process*. 2003;51(2):560-574. doi:10.1109/TSP.2002.807005

36.   Zwart NR, Johnson KO, Pipe JG. Efficient sample density estimation by combining gridding and an optimized kernel. *Magn Reson Med*. 2012;67(3):701-710. doi:10.1002/mrm.23041

37.   Jackson JI, Meyer CH, Nishimura DG, Macovski A. Selection of a Convolution Function for Fourier Inversion Using Gridding. *IEEE Trans Med Imaging*. 1991;10(3):473-478. doi:10.1109/42.97598

38.   Roemer PB, Edelstein WA, Hayes CE, Souza SP, Mueller OM. The NMR phased array. *Magn Reson Med*. 1990;16(2):192-225. doi:10.1002/mrm.1910160203

39.   Walsh DO, Gmitro a F, Marcellin MW. Adaptive reconstruction of phased array MR imagery. *Magn Reson Med*. 2000;43(5):682-690. http://www.ncbi.nlm.nih.gov/pubmed/10800033. Accessed August 28, 2012.

40.   Uecker M, Lai P, Murphy MJ, et al. ESPIRiT - An eigenvalue approach to autocalibrating parallel MRI: Where SENSE meets GRAPPA. *Magn Reson Med*. 2014;71(3):990-1001. doi:10.1002/mrm.24751

41.   Delattre BMA, Heidemann RM, Crowe LA, Vallée J-P, Hyacinthe J. Spiral demystified. *Magn Reson Imaging*. 2010;28(6):862-881. doi:10.1016/j.mri.2010.03.036

42.   Pipe JG, Zwart NR. Spiral trajectory design: A flexible numerical algorithm and base analytical equations. *Magn Reson Med*. 2014;71(1):278-285. doi:10.1002/mrm.24675

43.   Berglund J, Ahlström H, Kullberg J. Model-based mapping of fat unsaturation and

chain length by chemical shift imaging--phantom validation and in vivo feasibility. *Magn Reson Med*. 2012;68(6):1815-1827. doi:10.1002/mrm.24196

44.   Hamilton G, Smith DL, Bydder M, Nayak KS, Hu HH. MR properties of brown and white adipose tissues. *J Magn Reson Imaging*. 2011;34(2):468-473. doi:10.1002/jmri.22623

45.   Hamilton G, Schlein AN, Middleton MS, et al. In vivo triglyceride composition of abdominal adipose tissue measured by 1H MRS at 3T. *J Magn Reson Imaging*. 2017;45(5):1455-1463. doi:10.1002/jmri.25453

46.   Dawkins MJR, Stevens JF. Fatty Acid Composition of Triglycerides from Adipose Tissue. *Nature*. 1966;209(5028):1145-1146. doi:10.1038/2091145a0

47.   Del Grande F, Santini F, Herzka DA, et al. Fat-suppression techniques for 3-T MR imaging of the musculoskeletal system. *Radiographics*. 2014;34(1):217-233. doi:10.1148/rg.341135130

48.   Hu HH, Nayak KS. Change in the proton T 1 of fat and water in mixture. *Magn Reson Med*. 2010;63(2):494-501. doi:10.1002/mrm.22205

49.   Reeder SB, Cruite I, Hamilton G, Sirlin CB. Quantitative assessment of liver fat with magnetic resonance imaging and spectroscopy. *J Magn Reson Imaging*. 2011;34(4):729-749. doi:10.1002/jmri.22580

50.   Hu HH, Li Y, Nagy TR, Goran MI, Nayak KS. Quantification of Absolute Fat Mass by Magnetic Resonance Imaging: a Validation Study against Chemical Analysis. *Int J Body Compos Res*. 2011;9(3):111-122. http://www.ncbi.nlm.nih.gov/pubmed/23204926.

51.   Bydder M, Yokoo T, Hamilton G, et al. Relaxation effects in the quantification of fat using gradient echo imaging. *Magn Reson Imaging*. 2008;26(3):347-359. doi:10.1016/j.mri.2007.08.012

52.   Kühn J-P, Jahn C, Hernando D, et al. T1 bias in chemical shift-encoded liver fat-

fraction: Role of the flip angle. *J Magn Reson Imaging*. 2014;40(4):875-883. doi:10.1002/jmri.24457

53.   Hamilton G, Middleton MS, Bydder M, et al. Effect of PRESS and STEAM sequences on magnetic resonance spectroscopic liver fat quantification. *J Magn Reson Imaging*. 2009;30(1):145-152. doi:10.1002/jmri.21809

54.   Hardy PA, Henkelman RM, Bishop JE, Poon ECS, Plewes DB. Why fat is bright in rare and fast spin-echo imaging. *J Magn Reson Imaging*. 1992;2(5):533-540. doi:10.1002/jmri.1880020511

55.   Stables L a, Kennan RP, Anderson WA, Gore JC. Density matrix simulations of the effects of J coupling in spin echo and fast spin echo imaging. *J Magn Reson*. 1999;140(2):305-314. doi:10.1006/jmre.1998.1655

56.   Gajdošík M, Chmelík M, Just-Kukurová I, et al. In vivo relaxation behavior of liver compounds at 7 Tesla, measured by single-voxel proton MR spectroscopy. *J Magn Reson Imaging*. 2014;40(6):1365-1374. doi:10.1002/jmri.24489

57.   Dixon WT. Simple proton spectroscopic imaging. *Radiology*. 1984;153(1):189-194. doi:10.1148/radiology.153.1.6089263

58.   Pauly J. Dixon Reconstruction. *Stanford Lect Notes*. 2007:1-6.

59.   Glover GH. Multipoint dixon technique for water and fat proton and susceptibility imaging. *J Magn Reson Imaging*. 1991;1(5):521-530. doi:10.1002/jmri.1880010504

60.   Reeder SB, Pineda AR, Wen Z, et al. Iterative decomposition of water and fat with echo asymmetry and least-squares estimation (IDEAL): Application with fast spin-echo imaging. *Magn Reson Med*. 2005;54(3):636-644. doi:10.1002/mrm.20624

61.   Golub G, Pereyra V. Separable nonlinear least squares: The variable projection method and its applications. *Inverse Probl*. 2003;19(2). doi:10.1088/0266-5611/19/2/201

62.   Hernando D, Haldar JP, Sutton BP, Ma J, Kellman P, Liang ZP. Joint estimation of

water/fat images and field inhomogeneity map. *Magn Reson Med*. 2008;59(3):571-580. doi:10.1002/mrm.21522

63. Doneva M, Börnert P, Eggers H, Mertins A, Pauly J, Lustig M. Compressed sensing for chemical shift-based water-fat separation. *Magn Reson Med*. 2010;64(6):1749-1759. doi:10.1002/mrm.22563

64. Hernando D, Kellman P, Haldar JP, Liang ZP. Robust water/fat separation in the presence of large field inhomogeneities using a graph cut algorithm. *Magn Reson Med*. 2010;63(1):79-90. doi:10.1002/mrm.22177

65. Berglund J, Skorpil M. Multi-scale graph-cut algorithm for efficient water-fat separation. *Magn Reson Med*. 2017;78(3):941-949. doi:10.1002/mrm.26479

66. Ma D, Gulani V, Seiberlich N, et al. Magnetic resonance fingerprinting. *Nature*. 2013;495(7440):187-192. doi:10.1038/nature11971

67. Jiang Y, Ma D, Seiberlich N, Gulani V, Griswold MA. MR fingerprinting using fast imaging with steady state precession (FISP) with spiral readout. *Magn Reson Med*. 2015;74(6):1621-1631. doi:10.1002/mrm.25559

68. Hamilton JI, Jiang Y, Chen Y, et al. MR fingerprinting for rapid quantification of myocardial T 1 , T 2 , and proton spin density. *Magn Reson Med*. 2017;77(4):1446-1458. doi:10.1002/mrm.26216

69. Ma D, Jiang Y, Chen Y, et al. Fast 3D magnetic resonance fingerprinting for a whole-brain coverage. *Magn Reson Med*. 2018;79(4):2190-2197. doi:10.1002/mrm.26886

70. McGivney DF, Pierre E, Ma D, et al. SVD compression for magnetic resonance fingerprinting in the time domain. *IEEE Trans Med Imaging*. 2014;33(12):2311-2322. doi:10.1109/TMI.2014.2337321

71. Cohen O, Rosen MS. Algorithm comparison for schedule optimization in MR fingerprinting. *Magn Reson Imaging*. 2017;41:15-21. doi:10.1016/j.mri.2017.02.010

72. Zhao B, Haldar JP, Liao C, et al. Optimal Experiment Design for Magnetic Resonance

Fingerprinting: Cramér-Rao Bound Meets Spin Dynamics. *IEEE Trans Med Imaging*. 2019;38(3):844-861. doi:10.1109/TMI.2018.2873704

73.   Cavassila S, Deval S, Huegen C, van Ormondt D, Graveron-Demilly D. Cramér-Rao bounds: an evaluation tool for quantitation. *NMR Biomed*. 2001;14(4):278-283. doi:10.1002/nbm.701

74.   Sommer K, Amthor T, Doneva M, Koken P, Meineke J, Börnert P. Towards predicting the encoding capability of MR fingerprinting sequences. *Magn Reson Imaging*. 2017;(2016). doi:10.1016/j.mri.2017.06.015

75.   Stolk CC, Sbrizzi A. Understanding the Combined Effect of k-Space Undersampling and Transient States Excitation in MR Fingerprinting Reconstructions. *IEEE Trans Med Imaging*. 2019;38(10):2445-2455. doi:10.1109/TMI.2019.2900585

76.   Poorman ME, Martin MN, Ma D, et al. Magnetic resonance fingerprinting Part 1: Potential uses, current challenges, and recommendations. *J Magn Reson Imaging*. 2019:jmri.26836. doi:10.1002/jmri.26836

77.   Christen T, Pannetier NA, Ni WW, et al. MR vascular fingerprinting: A new approach to compute cerebral blood volume, mean vessel radius, and oxygenation maps in the human brain. *Neuroimage*. 2014;89:262-270. doi:10.1016/j.neuroimage.2013.11.052

78.   Pouliot P, Gagnon L, Lam T, et al. Magnetic resonance fingerprinting based on realistic vasculature in mice. *Neuroimage*. 2017;149:436-445. doi:10.1016/j.neuroimage.2016.12.060

79.   Su P, Mao D, Liu P, et al. Multiparametric estimation of brain hemodynamics with MR fingerprinting ASL. *Magn Reson Med*. 2017;78(5):1812-1823. doi:10.1002/mrm.26587

80.   Zhou Z, Han P, Zhou B, et al. Chemical exchange saturation transfer fingerprinting for exchange rate quantification. *Magn Reson Med*. 2018;80(4):1352-1363. doi:10.1002/mrm.27363

81.   Cohen O, Huang S, Mcmahon MT, Rosen MS, Farrar CT. Rapid and quantitative chemical exchange saturation transfer (CEST) imaging with magnetic resonance fingerprinting (MRF). *Magn Reson Med*. 2018;(October 2017):1-15. doi:10.1002/mrm.27221

82.   Malik SJ, Teixeira RPAG, Hajnal J V. Extended phase graph formalism for systems with magnetization transfer and exchange. *Magn Reson Med*. 2018;80(2):767-779. doi:10.1002/mrm.27040

83.   Kobayashi Y, Terada Y. Diffusion-weighting Caused by Spoiler Gradients in the Fast Imaging with Steady-state Precession Sequence May Lead to Inaccurate T 2 Measurements in MR Fingerprinting. 2018:1-9. doi:10.2463/mrms.tn.2018-0027

84.   Chen Y, Jiang Y, Pahwa S, et al. MR Fingerprinting for Rapid Quantitative Abdominal Imaging. *Radiology*. 2016;279(1):278-286. doi:10.1148/radiol.2016152037

85.   McCullough AJ. Update on nonalcoholic fatty liver disease. *J Clin Gastroenterol*. 2002;34(3):255-262. doi:10.1097/00004836-200203000-00013

86.   Chalasani N, Younossi Z, Lavine JE, et al. The diagnosis and management of nonalcoholic fatty liver disease: Practice guidance from the American Association for the Study of Liver Diseases. *Hepatology*. 2018;67(1):328-357. doi:10.1002/hep.29367

87.   Alkhouri N, McCullough AJ. Noninvasive Diagnosis of NASH and Liver Fibrosis Within the Spectrum of NAFLD. *Gastroenterol Hepatol (N Y)*. 2012;8(10):661-668. http://www.ncbi.nlm.nih.gov/pubmed/24683373.

88.   Kleiner DE, Makhlouf HR. Histology of Nonalcoholic Fatty Liver Disease and Nonalcoholic Steatohepatitis in Adults and Children. *Clin Liver Dis*. 2016;20(2):293-312. doi:10.1016/j.cld.2015.10.011

89.   Puri P, Sanyal AJ. Nonalcoholic fatty liver disease: Definitions, risk factors, and workup. *Clin Liver Dis*. 2012;1(4):99-103. doi:10.1002/cld.81

90.   Younossi ZM, Gramlich T, Liu YC, et al. Nonalcoholic fatty liver disease: assessment of variability in pathologic interpretations. *Mod Pathol*. 1998;11(6):560-565. http://www.ncbi.nlm.nih.gov/pubmed/9647594.

91.   Brunt EM, Janney CG, Di Bisceglie AM, Neuschwander-Tetri BA, Bacon BR. Nonalcoholic steatohepatitis: a proposal for grading and staging the histological lesions. *Am J Gastroenterol*. 1999;94(9):2467-2474. doi:10.1111/j.1572-0241.1999.01377.x

92.   Matteoni CA, Younossi ZM, Gramlich T, Boparai N, Yao Chang Liu, McCullough AJ. Nonalcoholic fatty liver disease: A spectrum of clinical and pathological severity. *Gastroenterology*. 1999;116(6):1413-1419. doi:10.1016/S0016-5085(99)70506-8

93.   Kleiner DE, Brunt EM, Van Natta M, et al. Design and validation of a histological scoring system for nonalcoholic fatty liver disease. *Hepatology*. 2005;41(6):1313-1321. doi:10.1002/hep.20701

94.   Bedossa P. Intraobserver and Interobserver Variations in Liver Biopsy Interpretation in Patients with Chronic Hepatitis C. *Hepatology*. 1994;20(1):15-20. doi:10.1002/hep.1840200104

95.   Ramakrishna G, Rastogi A, Trehanpati N, Sen B, Khosla R, Sarin SK. From Cirrhosis to Hepatocellular Carcinoma: New Molecular Insights on Inflammation and Cellular Senescence. *Liver Cancer*. 2013;2(3-4):367-383. doi:10.1159/000343852

96.   Ludwig J, Viggiano TR, McGill DB, Oh BJ. Nonalcoholic steatohepatitis: Mayo Clinic experiences with a hitherto unnamed disease. *Mayo Clin Proc*. 1980;55(7):434-438. http://www.ncbi.nlm.nih.gov/pubmed/7382552.

97.   Younossi ZM, Stepanova M, Afendy M, et al. Changes in the Prevalence of the Most Common Causes of Chronic Liver Diseases in the United States From 1988 to 2008. *Clin Gastroenterol Hepatol*. 2011;9(6):524-530.e1. doi:10.1016/j.cgh.2011.03.020

98.   Browning JD, Szczepaniak LS, Dobbins R, et al. Prevalence of hepatic steatosis in an urban population in the United States: Impact of ethnicity. *Hepatology*.

2004;40(6):1387-1395. doi:10.1002/hep.20466

99.   LaBrecque DR, Abbas Z, Anania F, et al. World Gastroenterology Organisation
       Global Guidelines. *J Clin Gastroenterol*. 2014;48(6):1.
       doi:10.1097/MCG.0000000000000116

100.   Williams CD, Stengel J, Asike MI, et al. Prevalence of nonalcoholic fatty liver disease
       and nonalcoholic steatohepatitis among a largely middle-aged population utilizing
       ultrasound and liver biopsy: A prospective study. *Gastroenterology*.
       2011;140(1):124-131. doi:10.1053/j.gastro.2010.09.038

101.   Bellentani S, Scaglioni F, Marino M, Bedogni G. Epidemiology of non-alcoholic fatty
       liver disease. *Dig Dis*. 2010;28(1):155-161. doi:10.1159/000282080

102.   Hamaguchi M, Kojima T, Takeda N, et al. The metabolic syndrome as a predictor of
       nonalcoholic fatty liver disease. *Ann Intern Med*. 2005;143(10):722-728.
       doi:10.7326/0003-4819-143-10-200511150-00009

103.   Younossi Z, Anstee QM, Marietti M, et al. Global burden of NAFLD and NASH:
       Trends, predictions, risk factors and prevention. *Nat Rev Gastroenterol Hepatol*.
       2018;15(1):11-20. doi:10.1038/nrgastro.2017.109

104.   Cohen JC, Horton JD, Hobbs HH. Human Fatty Liver Disease: Old Questions and
       New Insights. *Science (80-)*. 2011;332(6037):1519-1523.
       doi:10.1126/science.1204265

105.   Buzzetti E, Pinzani M, Tsochatzis EA. The multiple-hit pathogenesis of non-alcoholic
       fatty liver disease (NAFLD). *Metabolism*. 2016;65(8):1038-1048.
       doi:10.1016/j.metabol.2015.12.012

106.   Donnelly KL, Smith CI, Schwarzenberg SJ, Jessurun J, Boldt MD, Parks EJ. Sources of
       fatty acids stored in liver and secreted via lipoproteins in patients with nonalcoholic
       fatty liver disease. *J Clin Invest*. 2005;115(5):1343-1351. doi:10.1172/JCI23621

107.   Karpe F, Dickmann JR, Frayn KN. Fatty Acids, Obesity, and Insulin Resistance: Time

for a Reevaluation. *Diabetes*. 2011;60(10):2441-2449. doi:10.2337/db11-0425

108. Gluchowski NL, Becuwe M, Walther TC, Farese R V. Lipid droplets and liver disease: From basic biology to clinical implications. *Nat Rev Gastroenterol Hepatol*. 2017;14(6):343-355. doi:10.1038/nrgastro.2017.32

109. Kawano Y, Cohen DE. Mechanisms of hepatic triglyceride accumulation in non-alcoholic fatty liver disease. *J Gastroenterol*. 2013;48(4):434-441. doi:10.1007/s00535-013-0758-5

110. Leamy AK, Egnatchik RA, Young JD. Molecular mechanisms and the role of saturated fatty acids in the progression of non-alcoholic fatty liver disease. *Prog Lipid Res*. 2013;52(1):165-174. doi:10.1016/j.plipres.2012.10.004

111. Reccia I, Kumar J, Akladios C, et al. Non-alcoholic fatty liver disease: A sign of systemic disease. *Metabolism*. 2017;72:94-108. doi:10.1016/j.metabol.2017.04.011

112. Brunt EM, Tiniakos DG. Histopathology of nonalcoholic fatty liver disease. *World J Gastroenterol*. 2010;16(42):5286-5296. doi:10.3748/wjg.v16.i42.5286

113. McCuskey RS. Morphological mechanisms for regulating blood flow through hepatic sinusoids. *Liver*. 2000;20(1):3-7. doi:10.1034/j.1600-0676.2000.020001003.x

114. Poisson J, Lemoinne S, Boulanger C, et al. Liver sinusoidal endothelial cells: Physiology and role in liver diseases. *J Hepatol*. 2017;66(1):212-227. doi:10.1016/j.jhep.2016.07.009

115. Friedman SL. Hepatic stellate cells: Protean, multifunctional, and enigmatic cells of the liver. *Physiol Rev*. 2008;88(1):125-172. doi:10.1152/physrev.00013.2007

116. O'Brien S, Keogan M, Patchett S, McCormick PA, Afdhal N, Hegarty JE. Postprandial changes in portal haemodynamics in patients with cirrhosis. *Gut*. 1992;33(3):364-367. doi:10.1136/gut.33.3.364

117. Faria SC, Ganesan K, Mwangi I, et al. MR imaging of liver fibrosis: current state of

the art. *Radiographics*. 2009;29(6):1615-1635. doi:10.1148/rg.296095512

118. Anstee QM, Day CP. The genetics of NAFLD. *Nat Rev Gastroenterol Hepatol*. 2013;10(11):645-655. doi:10.1038/nrgastro.2013.182

119. Adams LA, Lymp JF, St. Sauver J, et al. The natural history of nonalcoholic fatty liver disease: A population-based cohort study. *Gastroenterology*. 2005;129(1):113-121. doi:10.1053/j.gastro.2005.04.014

120. Ekstedt M, Hagström H, Nasr P, et al. Fibrosis stage is the strongest predictor for disease-specific mortality in NAFLD after up to 33 years of follow-up. *Hepatology*. 2015;61(5):1547-1554. doi:10.1002/hep.27368

121. Bertot LC, Adams LA. The natural course of non-alcoholic fatty liver disease. *Int J Mol Sci*. 2016;17(5). doi:10.3390/ijms17050774

122. McPherson S, Hardy T, Henderson E, Burt AD, Day CP, Anstee QM. Evidence of NAFLD progression from steatosis to fibrosing-steatohepatitis using paired biopsies: Implications for prognosis and clinical management. *J Hepatol*. 2015;62(5):1148-1155. doi:10.1016/j.jhep.2014.11.034

123. Liver and Intrahepatic Bile Duct Cancer - Cancer Stat Facts. https://seer.cancer.gov/statfacts/html/livibd.html. Accessed October 27, 2019.

124. Konerman MA, Jones JC, Harrison SA. Pharmacotherapy for NASH: Current and emerging. *J Hepatol*. 2018;68(2):362-375. doi:10.1016/j.jhep.2017.10.015

125. Al Knawy B, Shiffman M. Percutaneous liver biopsy in clinical practice. *Liver Int*. 2007;27(9):1166-1173. doi:10.1111/j.1478-3231.2007.01592.x

126. Karanjia RN, Crossey MME, Cox IJ, et al. Hepatic steatosis and fibrosis: Non-invasive assessment. *World J Gastroenterol*. 2016;22(45):9880-9897. doi:10.3748/wjg.v22.i45.9880

127. Ratziu V, Charlotte F, Heurtier A, et al. Sampling variability of liver biopsy in nonalcoholic fatty liver disease. *Gastroenterology*. 2005;128(7):1898-1906.

doi:10.1053/j.gastro.2005.03.084

128. Hernaez R, Lazo M, Bonekamp S, et al. Diagnostic accuracy and reliability of ultrasonography for the detection of fatty liver: A meta-analysis. *Hepatology*. 2011;54(3):1082-1090. doi:10.1002/hep.24452

129. Desai NK, Harney S, Raza R, et al. Comparison of controlled attenuation parameter and liver biopsy to assess hepatic steatosis in pediatric patients. *J Pediatr*. 2016;173:160-164.e1. doi:10.1016/j.jpeds.2016.03.021

130. Zhang YN, Fowler KJ, Ozturk A, et al. Liver fibrosis imaging: A clinical review of ultrasound and magnetic resonance elastography. *J Magn Reson Imaging*. 2019:1-18. doi:10.1002/jmri.26716

131. Mueller S, Sandrin L. Liver stiffness: a novel parameter for the diagnosis of liver disease. *Hepatic Med Evid Res*. May 2010:49. doi:10.2147/HMER.S7394

132. Hamer OW, Aguirre DA, Casola G, Lavine JE, Woenckhaus M, Sirlin CB. Fatty liver: Imaging patterns and pitfalls. *Radiographics*. 2006;26(6):1637-1653. doi:10.1148/rg.266065004

133. Schwenzer NF, Springer F, Schraml C, Stefan N, Machann J, Schick F. Non-invasive assessment and quantification of liver steatosis by ultrasound, computed tomography and magnetic resonance. *J Hepatol*. 2009;51(3):433-445. doi:10.1016/j.jhep.2009.05.023

134. Lee SS, Park SH. Radiologic evaluation of nonalcoholic fatty liver disease. *World J Gastroenterol*. 2014;20(23):7392-7402. doi:10.3748/wjg.v20.i23.7392

135. Stark DD, Bass NM, Moss AA, et al. Nuclear magnetic resonance imaging of experimentally induced liver disease. *Radiology*. 1983;148(3):743-751. doi:10.1148/radiology.148.3.6192464

136. Lee JK, Dixon WT, Ling D, Levitt RG, Murphy WA. Fatty infiltration of the liver: demonstration by proton spectroscopic imaging. Preliminary observations.

Radiology. 1984;153(1):195-201. doi:10.1148/radiology.153.1.6089264

137. Levenson H, Greensite F, Hoefs J, et al. Fatty infiltration of the liver: quantification with phase-contrast MR imaging at 1.5 T vs biopsy. *Am J Roentgenol*. 1991;156(2):307-312. doi:10.2214/ajr.156.2.1898804

138. Glover GH, Schneider E. Three-point dixon technique for true water/fat decomposition with B0 inhomogeneity correction. *Magn Reson Med*. 1991;18(2):371-383. doi:10.1002/mrm.1910180211

139. Zhang X, Tengowski M, Fasulo L, Botts S, Suddarth SA, Johnson GA. Measurement of fat/water ratios in rat liver using 3D three-point dixon MRI. *Magn Reson Med*. 2004;51(4):697-702. doi:10.1002/mrm.20005

140. Kovanlikaya A, Mittelman SD, Ward A, Geffner ME, Dorey F, Gilsanz V. Obesity and fat quantification in lean tissues using three-point Dixon MR imaging. *Pediatr Radiol*. 2005;35(6):601-607. doi:10.1007/s00247-005-1413-y

141. Kukuk GM, Hittatiya K, Sprinkart AM, et al. Comparison between modified Dixon MRI techniques, MR spectroscopic relaxometry, and different histologic quantification methods in the assessment of hepatic steatosis. *Eur Radiol*. 2015;25(10):2869-2879. doi:10.1007/s00330-015-3703-6

142. Serai SD, Dillman JR, Trout AT. Proton Density Fat Fraction Measurements at 1.5- and 3-T Hepatic MR Imaging: Same-Day Agreement among Readers and across Two Imager Manufacturers. *Radiology*. 2017;284(1):244-254. doi:10.1148/radiol.2017161786

143. Leporq B, Lambert SA, Ronot M, Vilgrain V, Van Beers BE. Simultaneous MR quantification of hepatic fat content, fatty acid composition, transverse relaxation time and magnetic susceptibility for the diagnosis of non-alcoholic steatohepatitis. *NMR Biomed*. 2017;(May):e3766. doi:10.1002/nbm.3766

144. Gandhi SN, Brown MA, Wong JG, Aguirre DA, Sirlin CB. MR Contrast Agents for Liver Imaging: What, When, How. *RadioGraphics*. 2006;26(6):1621-1636.

doi:10.1148/rg.266065014

145.   Thian YL, Riddell AM, Koh D-M. Liver-specific agents for contrast-enhanced MRI: role in oncological imaging. *Cancer Imaging*. 2013;13(4):567-579. doi:10.1102/1470-7330.2013.0050

146.   Tsuda N, Okada M, Murakami T. Potential of Gadolinium-ethoxybenzyl-diethylenetriamine Pentaacetic Acid (Gd-EOB-DTPA) for Differential Diagnosis of Nonalcoholic Steatohepatitis and Fatty Liver in Rats Using Magnetic Resonance Imaging. *Invest Radiol*. 2007;42(4):242-247. doi:10.1097/01.rli.0000258058.44876.a5

147.   Ding Y, Rao S-X, Meng T, Chen C, Li R, Zeng M-S. Usefulness of T1 mapping on Gd-EOB-DTPA-enhanced MR imaging in assessment of non-alcoholic fatty liver disease. *Eur Radiol*. 2014;24(4):959-966. doi:10.1007/s00330-014-3096-y

148.   Wu Z, Matsui O, Kitao A, et al. Usefulness of Gd-EOB-DTPA-enhanced MR imaging in the evaluation of simple steatosis and nonalcoholic steatohepatitis. *J Magn Reson Imaging*. 2013;37(5):1137-1143. doi:10.1002/jmri.23921

149.   Bastati N, Feier D, Wibmer A, et al. Noninvasive Differentiation of Simple Steatosis and Steatohepatitis by Using Gadoxetic Acid–enhanced MR Imaging in Patients with Nonalcoholic Fatty Liver Disease: A Proof-of-Concept Study. *Radiology*. 2014;271(3):739-747. doi:10.1148/radiol.14131890

150.   Low G, Kruse SA, Lomas DJ. General review of magnetic resonance elastography. *World J Radiol*. 2016;8(1):59. doi:10.4329/wjr.v8.i1.59

151.   Kennedy P, Wagner M, Castéra L, et al. Quantitative elastography methods in liver disease: Current evidence and future directions. *Radiology*. 2018;286(3):738-763. doi:10.1148/radiol.2018170601

152.   Chen J, Talwalkar JA, Yin M, Glaser KJ, Sanderson SO, Ehman RL. Early Detection of Nonalcoholic Steatohepatitis in Patients with Nonalcoholic Fatty Liver Disease by Using MR Elastography. *Radiology*. 2011;259(3):749-756.

doi:10.1148/radiol.11101942

153. Yin M, Glaser KJ, Manduca A, et al. Distinguishing between hepatic inflammation and fibrosis with MR elastography. *Radiology*. 2017;284(3):694-705. doi:10.1148/radiol.2017160622

154. Edelstein WA, Hutchison JMS, Johnson G, Redpath T. Spin warp NMR imaging and applications to human whole-body imaging. *Phys Med Biol*. 1980;25(4):751-756. doi:10.1088/0031-9155/25/4/017

155. Smith FW, Mallard JR, Reid A, Hutchison JM. Nuclear magnetic resonance tomographic imaging in liver disease. *Lancet (London, England)*. 1981;1(8227):963-966. doi:10.2214/ajr.138.2.193

156. Doyle FH, Pennock JM, Banks LM, et al. Nuclear magnetic resonance imaging of the liver: initial experience. *AJR Am J Roentgenol*. 1982;138(2):193-200. doi:10.2214/ajr.138.2.193

157. Thomsen C, Christoffersen P, Henriksen O, Juhl E. Prolonged T1 in patients with liver cirrhosis: An in vivo MRI study. *Magn Reson Imaging*. 1990;8(5):599-604. doi:10.1016/0730-725X(90)90137-Q

158. Board GH. Magnetic resonance imaging of parenchymal liver disease: a comparison with ultrasound, radionuclide scintigraphy and X-ray computed tomography. *Clin Radiol*. 1987;38(5):495-502. doi:10.1016/S0009-9260(87)80131-9

159. Hoad CL, Palaniyappan N, Kaye P, et al. A study of T 1 relaxation time as a measure of liver fibrosis and the influence of confounding histological factors. *NMR Biomed*. 2015;28(6):706-714. doi:10.1002/nbm.3299

160. Heye T, Yang S-R, Bock M, et al. MR relaxometry of the liver: significant elevation of T1 relaxation time in patients with liver cirrhosis. *Eur Radiol*. 2012;22(6):1224-1232. doi:10.1007/s00330-012-2378-5

161. Cassinotto C, Feldis M, Vergniol J, et al. MR relaxometry in chronic liver diseases:

Comparison of T1 mapping, T2 mapping, and diffusion-weighted imaging for assessing cirrhosis diagnosis and severity. *Eur J Radiol*. 2015;84(8):1459-1465. doi:10.1016/j.ejrad.2015.05.019

162. Guimaraes AR, Siqueira L, Uppal R, et al. T2 relaxation time is related to liver fibrosis severity. *Quant Imaging Med Surg*. 2016;6(2):103-114. doi:10.21037/qims.2016.03.02

163. Chow AM, Gao DS, Fan SJ, et al. Measurement of liver T_1 and T_2 relaxation times in an experimental mouse model of liver fibrosis. *J Magn Reson Imaging*. 2012;36(1):152-158. doi:10.1002/jmri.23606

164. Luetkens JA, Klein S, Traber F, et al. Quantification of Liver Fibrosis at T1 and T2 Mapping with Extracellular Volume Fraction MRI: Preclinical Results. *Radiology*. 2018:180051. doi:10.1148/radiol.2018180051

165. Yarnykh VL, Tartaglione E V., Ioannou GN. Fast macromolecular proton fraction mapping of the human liver in vivo for quantitative assessment of hepatic fibrosis. *NMR Biomed*. 2015;28(12):1716-1725. doi:10.1002/nbm.3437

166. Portillo-Sanchez P, Bril F, Maximos M, et al. High Prevalence of Nonalcoholic Fatty Liver Disease in Patients With Type 2 Diabetes Mellitus and Normal Plasma Aminotransferase Levels. *J Clin Endocrinol Metab*. 2015;100(6):2231-2238. doi:10.1210/jc.2015-1966

167. Wood JC, Enriquez C, Ghugre N, et al. MRI R2 and R2* mapping accurately estimates hepatic iron concentration in transfusion-dependent thalassemia and sickle cell disease patients. *Blood*. 2005;106(4):1460-1465. doi:10.1182/blood-2004-10-3982

168. Wood JC, Zhang P, Rienhoff H, Abi-Saab W, Neufeld EJ. Liver MRI is more precise than liver biopsy for assessing total body iron balance: A comparison of MRI relaxometry with simulated liver biopsy results. *Magn Reson Imaging*. 2015;33(6):761-767. doi:10.1016/j.mri.2015.02.016

169. van der Poorten D, Samer CF, Ramezani-Moghadam M, et al. Hepatic fat loss in advanced nonalcoholic steatohepatitis: Are alterations in serum adiponectin the cause? *Hepatology*. 2013;57(6):2180-2188. doi:10.1002/hep.26072

170. Bonekamp S, Tang A, Mashhood A, et al. Spatial distribution of MRI-determined hepatic proton density fat fraction in adults with nonalcoholic fatty liver disease. *J Magn Reson Imaging*. 2014;39(6):1525-1532. doi:10.1002/jmri.24321

171. Noll DC, Meyer CH, Pauly JM, Nishimura DG, Macovski A. A homogeneity correction method for magnetic resonance imaging with time-varying gradients. *IEEE Trans Med Imaging*. 1991;10(4):629-637. doi:10.1109/42.108599

172. Hong T, Han D, Kim MO, Kim DH. RF slice profile effects in magnetic resonance fingerprinting. *Magn Reson Imaging*. 2016;41:73-79. doi:10.1016/j.mri.2017.04.001

173. Ma D, Coppo S, Chen Y, et al. Slice Profile and B 1 Corrections in 2D Magnetic Resonance Fingerprinting. *Magn Reson Med*. 2017;00:1-9. doi:10.1002/mrm.26580

174. Buonincontri G, Sawiak SJ. MR fingerprinting with simultaneous B1 estimation. *Magn Reson Med*. 2015;00:1-9. doi:10.1002/mrm.26009

175. Cloos MA, Knoll F, Zhao T, et al. Multiparametric imaging with heterogeneous radiofrequency fields. *Nat Commun*. 2016;7:12445. doi:10.1038/ncomms12445

176. Ma D, Gulani V, Seiberlich N, et al. Magnetic resonance fingerprinting. *Nature*. 2013;495(7440):187-192. doi:10.1038/nature11971

177. Scheffler K, Lehnhardt S. Principles and applications of balanced SSFP techniques. *Eur Radiol*. 2003;13(11):2409-2418. doi:10.1007/s00330-003-1957-x

178. Yu AC, Ponsky LE, Dastmalchian S, Rogers M, Mcgivney D, Griswold MA. Development of a Combined MR Fingerprinting and Diffusion Examination for Prostate. 2017;000(0):1-10. doi:10.1148/radiol.2017161599

179. Schomberg H. Off-resonance correction of MR images. *IEEE Trans Med Imaging*. 1999;18(6):481-495. doi:10.1109/42.781014

180. Nayak KS, Tsai CM, Meyer CH, Nishimura DG. Efficient off-resonance correction for spiral imaging. *Magn Reson Med*. 2001;45(3):521-524. doi:10.1002/1522-2594(200103)45:3<521::AID-MRM1069>3.0.CO;2-6

181. Fessler JA, Lee S, Olafsson VT, Shi HR, Noll DC. Toeplitz-based iterative image reconstruction for MRI with correction for magnetic field inhomogeneity. *IEEE Trans Signal Process*. 2005;53(9):3393-3402. doi:10.1109/TSP.2005.853152

182. Eggers H, Knopp T, Potts D. Field inhomogeneity correction based on gridding reconstruction for magnetic resonance imaging. *IEEE Trans Med Imaging*. 2007;26(3):374-384. doi:10.1109/TMI.2006.891502

183. Man LC, Pauly JM, Macovski A. Multifrequency interpolation for fast off-resonance correction. *Magn Reson Med*. 1997;37(5):785-792. http://www.ncbi.nlm.nih.gov/pubmed/9126954.

184. Koken P, Amthor T, Doneva M, et al. Improving Accuracy in MR Fingerprinting by Off-Resonance Deblurring. *Proc Intl Soc Mag Reson Med*. 2017:5607.

185. Ostenson J, Robison RK, Zwart NR, Welch EB. Off-Resonance Correction for MR Fingerprinting Using Multiple Frequency Interpolation. *Proc Intl Soc Mag Reson Med*. 2017:0938.

186. Keenan KE, Stupic KF, Boss MA, et al. Multi-site, multi-vendor comparison of T1 measurement using ISMRM/NIST system phantom. In: *Proc Intl Soc Mag Reson Med*. ; 2016:3290.

187. Pipe JG, Zwart NR. Spiral trajectory design: a flexible numerical algorithm and base analytical equations. *Magn Reson Med*. 2014;71(1):278-285. doi:10.1002/mrm.24675

188. ISMRM MRI Unbound. ISMRM website. http://www.webcitation.org/6okjuKEpG. Published 2017. Accessed March 3, 2017.

189. Pipe JG. Mri Unbound - Spiral Gen (Spiral Waveform Generation) -

Spiralgen_Jgp_12Oct.Zip. January 2012. doi:10.5281/ZENODO.401058

190. Otsu N. A Threshold Selection Method from Gray-Level Histograms. *IEEE Trans Syst Man Cybern*. 1979;9(1):62-66. doi:10.1109/TSMC.1979.4310076

191. Crawford SB, Kosinski AS, Lin H-M, Williamson JM, Barnhart HX. Computer programs for the concordance correlation coefficient. *Comput Methods Programs Biomed*. 2007;88(1):62-74. doi:10.1016/j.cmpb.2007.07.003

192. Jiang Y, Ma D, Keenan KE, Stupic KF, Gulani V, Griswold MA. Repeatability of magnetic resonance fingerprinting T $_1$ and T $_2$ estimates assessed using the ISMRM/NIST MRI system phantom. *Magn Reson Med*. 2016;00(September):1-6. doi:10.1002/mrm.26509

193. Zwart NR. Mri Unbound - Sdc 3D (Sampling Density Calculation) - Sdc3_Nrz_11Aug.Zip. January 2011. doi:10.5281/ZENODO.401057

194. Zwart NR, Turley DC, Johnson KO, Pipe JG. Mri Unbound - Grid 3D (Gridding) - Grid3_Dct_11Aug.Zip. January 2011. doi:10.5281/ZENODO.401036

195. Duyn JH, Yang Y, Frank JA, van der Veen JW. Simple correction method for k-space trajectory deviations in MRI. *J Magn Reson*. 1998;132(1):150-153. doi:10.1006/jmre.1998.1396

196. Welch EB, Robison RK, Harkins KD. Robust k-space trajectory mapping with data readout concatenation and automated phase unwrapping reference point identi cation. In: *Proc Intl Soc Mag Reson Med*. ; 2017:1387.

197. Amidror I. Scattered data interpolation methods for electronic imaging systems: a survey. *J Electron Imaging*. 2002;11(2):157. doi:10.1117/1.1455013

198. Taylor AJ, Salerno M, Dharmakumar R, Jerosch-Herold M. T1 Mapping Basic Techniques and Clinical Applications. *JACC Cardiovasc Imaging*. 2016;9(1):67-81. doi:10.1016/j.jcmg.2015.11.005

199. Giri S, Chung Y-C, Merchant A, et al. T2 quantification for improved detection of

myocardial edema. *J Cardiovasc Magn Reson*. 2009;11:56. doi:10.1186/1532-429X-11-56

200. Arpan I, Forbes SC, Lott DJ, et al. T2 mapping provides multiple approaches for the characterization of muscle involvement in neuromuscular diseases: A cross-sectional study of lower leg muscles in 5-15-year-old boys with Duchenne muscular dystrophy. *NMR Biomed*. 2013;26(3):320-328. doi:10.1002/nbm.2851

201. Wei Y, Wu S, Gao F, et al. Esophageal carcinoma: Ex vivo evaluation by high-spatial-resolution T2 -mapping MRI compared with histopathological findings at 3.0T. *J Magn Reson Imaging*. 2016:1609-1616. doi:10.1002/jmri.25509

202. Sabouri S, Chang SD, Savdie R, et al. Luminal Water Imaging: A New MR Imaging T2 Mapping Technique for Prostate Cancer Diagnosis. *Radiology*. 2017;284(2):451-459. doi:10.1148/radiol.2017161687

203. Hu HH, Smith DL, Nayak KS, Goran MI, Nagy TR. Identification of brown adipose tissue in mice with fat-water IDEAL-MRI. *J Magn Reson Imaging*. 2010;31(5):1195-1202. doi:10.1002/jmri.22162

204. Tang A, Tan J, Sun M, et al. Nonalcoholic Fatty Liver Disease: MR Imaging of Liver Proton Density Fat Fraction to Assess Hepatic Steatosis. *Radiology*. 2013;267(2):422-431. doi:10.1148/radiol.12120896

205. Pokharel SS, Macura KJ, Kamel IR, Zaheer A. Current MR imaging lipid detection techniques for diagnosis of lesions in the abdomen and pelvis. *Radiographics*. 2013;33(3):681-702. doi:10.1148/rg.333125068

206. Yu AC, Badve C, Ponsky LE, et al. Development of a Combined MR Fingerprinting and Diffusion Examination for Prostate Cancer. *Radiology*. 2017;283(3):729-738. doi:10.1148/radiol.2017161599

207. Bojorquez JZ, Bricq S, Acquitter C, Brunotte F, Walker PM, Lalande A. What are normal relaxation times of tissues at 3 T? *Magn Reson Imaging*. 2017;35:69-80. doi:10.1016/j.mri.2016.08.021

208. Rakow-Penner R, Daniel B, Yu H, Sawyer-Glover A, Glover GH. Relaxation times of breast tissue at 1.5T and 3T measured using IDEAL. *J Magn Reson Imaging*. 2006;23(1):87-91. doi:10.1002/jmri.20469

209. Mozes FE, Tunnicliffe EM, Pavlides M, Robson MD. Influence of fat on liver T1 measurements using modified Look–Locker inversion recovery (MOLLI) methods at 3T. *J Magn Reson Imaging*. 2016;44(1):105-111. doi:10.1002/jmri.25146

210. Reeder SB, Wen Z, Yu H, et al. Multicoil Dixon Chemical Species Separation with an Iterative Least-Squares Estimation Method. *Magn Reson Med*. 2004;51(1):35-45. doi:10.1002/mrm.10675

211. Han D, Kim M-O, Lee H, Hong T, Kim D-H. A Free-breathing water/fat separation and T1, T2 quantification method using dual TR FISP in abdomen. In: *Proc Intl Soc Mag Reson Med*. ; 2016:0575.

212. Ostenson J, Welch EB. Fat Signal Fraction Determination Using MR Fingerprinting. In: *Proc Intl Soc Mag Reson Med*. ; 2017:0134.

213. Cencici M, Biagi L, Kaggie J, Schulte RF, Rosetti MT, Buonincontri G. MR Fingerprinting in the knee with dictionary-based fat and water separation. In: *ISMRM Workshop on MRF*. ; 2017.

214. Nolte T, Truhn D, Gross-Weege N, et al. Undersampled Spiral Magnetic Resonance Fingerprinting with Water and Fat Blurring Correction. In: *Proceedings of the 26th Annual Meeting of ISMRM*. ; 2018:4215.

215. Koolstra K, Webb A, Koken P, Nehrke K, Börnert P. Water-Fat Separation in Spiral Magnetic Resonance Fingerprinting using Conjugate Phase Reconstruction. In: *Proceedings of the 26th Annual Meeting of ISMRM*. ; 2018:0681.

216. Cencini M, Biagi L, Kaggie JD, Schulte RF, Tosetti M, Buonincontri G. Magnetic resonance fingerprinting with dictionary-based fat and water separation (DBFW MRF): A multi-component approach. *Magn Reson Med*. 2019;81(5):3032-3045. doi:10.1002/mrm.27628

217. Wang D, Zwart NR, Pipe JG. Joint water-fat separation and deblurring for spiral imaging. *Magn Reson Med*. 2017;00:1-11. doi:10.1002/mrm.26950

218. Ostenson J, Robison RK, Zwart NR, Welch EB. Multi-frequency interpolation in spiral magnetic resonance fingerprinting for correction of off-resonance blurring. *Magn Reson Imaging*. 2017;41:63-72. doi:10.1016/j.mri.2017.07.004

219. Brodsky EK, Holmes JH, Yu H, Reeder SB. Generalized k-space decomposition with chemical shift correction for non-Cartesian water-fat imaging. *Magn Reson Med*. 2008;59(5):1151-1164. doi:10.1002/mrm.21580

220. Flassbeck S, Schmidt S, Breithaupt M, Bachert P, Ladd ME, Schmitter S. On the In fl uence of Intra-Voxel Dephasing in FISP-MRF with Variable Repetition Time. *Proc Intl Soc Mag Reson Med*. 2017:1492.

221. Uecker M, Tamir JI. BART: version 0.4.02 (Version v0.4.02). 2017. doi:http://doi.org/10.5281/zenodo.1066014

222. Jiang Y, Ma D, Keenan KE, Stupic KF, Gulani V, Griswold MA. Repeatability of magnetic resonance fingerprinting T 1 and T 2 estimates assessed using the ISMRM/NIST MRI system phantom. *Magn Reson Med*. 2017;78(4):1452-1457. doi:10.1002/mrm.26509

223. Yarnykh VL. Actual flip-angle imaging in the pulsed steady state: a method for rapid three-dimensional mapping of the transmitted radiofrequency field. *Magn Reson Med*. 2007;57(1):192-200. doi:10.1002/mrm.21120

224. Zhao B, Haldar JP, Liao C, et al. Optimal Experiment Design for Magnetic Resonance Fingerprinting: Cramér-Rao Bound Meets Spin Dynamics. *IEEE Trans Med Imaging*. 2019;38(3):844-861. doi:10.1109/TMI.2018.2873704

225. Crawford SB, Kosinski AS, Lin HM, Williamson JM, Barnhart HX. Computer programs for the concordance correlation coefficient. *Comput Methods Programs Biomed*. 2007;88(1):62-74. doi:10.1016/j.cmpb.2007.07.003

226. Li K, Zu Z, Xu J, et al. Optimized inversion recovery sequences for quantitative T1 and magnetization transfer imaging. *Magn Reson Med*. 2010;64(2):491-500. doi:10.1002/mrm.22440

227. Nehrke K, Börnert P. DREAM-a novel approach for robust, ultrafast, multislice B1 mapping. *Magn Reson Med*. 2012;68(5):1517-1526. doi:10.1002/mrm.24158

228. Weis J, Kullberg J, Ahlström H. Multiple breath-hold proton spectroscopy of human liver at 3T: Relaxation times and concentrations of glycogen, choline, and lipids. *J Magn Reson Imaging*. 2018;47(2):410-417. doi:10.1002/jmri.25734

229. Smits MM, van Geenen EJM. The clinical significance of pancreatic steatosis. *Nat Rev Gastroenterol Hepatol*. 2011;8(3):169-177. doi:10.1038/nrgastro.2011.4

230. Wong CX, Abed HS, Molaee P, et al. Pericardial fat is associated with atrial fibrillation severity and ablation outcome. *J Am Coll Cardiol*. 2011;57(17):1745-1751. doi:10.1016/j.jacc.2010.11.045

231. McGivney D, Deshmane A, Jiang Y, et al. Bayesian estimation of multicomponent relaxation parameters in magnetic resonance fingerprinting. *Magn Reson Med*. 2018;80(1):159-170. doi:10.1002/mrm.27017

232. Doneva M, Amthor T, Koken P, Sommer K, Börnert P. Matrix completion-based reconstruction for undersampled magnetic resonance fingerprinting data. *Magn Reson Imaging*. 2017;41:41-52. doi:10.1016/j.mri.2017.02.007

233. Zhao B, Setsompop K, Adalsteinsson E, et al. Improved magnetic resonance fingerprinting reconstruction with low-rank and subspace modeling. *Magn Reson Med*. 2018;79(2):933-942. doi:10.1002/mrm.26701

234. Sacolick LI, Wiesinger F, Hancu I, Vogel MW. B1 mapping by Bloch-Siegert shift. *Magn Reson Med*. 2010;63(5):1315-1322. doi:10.1002/mrm.22357

235. Buonincontri G, Schulte RF, Cosottini M, Tosetti M. Spiral MR fingerprinting at 7 T with simultaneous B1 estimation. *Magn Reson Imaging*. 2017;41:1-6.

doi:10.1016/j.mri.2017.04.003

236. Malik SJ, Sbrizzi A, Hoogduin JM, Hajnal J V. Equivalence of EPG and Isochromat-Based Simulation of MR Signals. In: *Proc Intl Soc Mag Reson Med*. ; 2016:3196.

237. Lebel RM, Wilman AH. Transverse relaxometry with stimulated echo compensation. *Magn Reson Med*. 2010;64(4):1005-1014. doi:10.1002/mrm.22487

238. Malik SJ, Padormo F, Price AN, Hajnal J V. Spatially resolved extended phase graphs: Modeling and design of multipulse sequences with parallel transmission. *Magn Reson Med*. 2012;68(5):1481-1494. doi:10.1002/mrm.24153

239. Guzek B, Körzdörfer G, Mathias N, Pfeuffer J. Influence of Off-Resonance on FISP Magnetic Resonance Fingerprinting (FISP-MRF). In: *Proceedings of the Joint Annual Meeting ISMRM-ESMRMB, Paris, France*. ; 2018:4264.

240. Körzdörfer G, Guzek B, Jiang Y, et al. Description of the off-resonance dependency in slice-selective FISP MRF. In: *Proceedings of the Joint Annual Meeting ISMRM-ESMRMB, Paris, France*. ; 2018:4232. http://indexsmart.mirasmart.com/ISMRM2018/PDFfiles/4232.html.

241. Bain AD, Anand CK, Nie Z. Exact solution to the Bloch equations and application to the Hahn echo. *J Magn Reson*. 2010;206(2):227-240. doi:10.1016/j.jmr.2010.07.012

242. Ostenson J, Damon BM, Welch EB. MR fingerprinting with simultaneous T1, T2, and fat signal fraction estimation with integrated B0 correction reduces bias in water T1 and T2 estimates. *Magn Reson Imaging*. 2019;60:7-19. doi:10.1016/j.mri.2019.03.017

243. Jankiewicz M, Gore JC, Grissom WA. Improved encoding pulses for Bloch-Siegert B 1 + mapping. *J Magn Reson*. 2013;226:79-87. doi:10.1016/j.jmr.2012.11.004

244. Wang D, Ostenson J, Smith DS. snapMRF: GPU-accelerated magnetic resonance fingerprinting dictionary generation and matching using extended phase graphs. *Magn Reson Imaging*. November 2019. doi:10.1016/j.mri.2019.11.015

245. Mcgivney D, Deshmane A, Jiang Y, et al. Bayesian Estimation of Multicomponent Relaxation Parameters in Magnetic Resonance Fingerprinting. 2018;170:159-170. doi:10.1002/mrm.27017

246. Nagtegaal M, Koken P, Amthor T, Doneva M. Fast multi-component analysis using a joint sparsity constraint for MR fingerprinting. *Magn Reson Med*. 2019;(July):mrm.27947. doi:10.1002/mrm.27947

247. Kobayashi Y, Terada Y. Diffusion-weighting Caused by Spoiler Gradients in the Fast Imaging with Steady-state Precession Sequence May Lead to Inaccurate T_2 Measurements in MR Fingerprinting. *Magn Reson Med Sci*. 2018:1-9. doi:10.2463/mrms.tn.2018-0027

248. Bland JM, Altman DG. Statistics Notes: Measurement error. *BMJ*. 1996;313(7059):744. doi:10.1136/bmj.313.7059.744

249. de Bazelaire CMJ, Duhamel GD, Rofsky NM, Alsop DC. MR Imaging Relaxation Times of Abdominal and Pelvic Tissues Measured in Vivo at 3.0 T: Preliminary Results. *Radiology*. 2004;230(3):652-659. doi:10.1148/radiol.2303021331

250. Banerjee R, Pavlides M, Tunnicliffe EM, et al. Multiparametric magnetic resonance for the non-invasive diagnosis of liver disease. *J Hepatol*. 2014;60(1):69-77. doi:10.1016/j.jhep.2013.09.002

251. Hamilton G, Middleton MS, Hooker JC, et al. In vivo breath-hold 1H MRS simultaneous estimation of liver proton density fat fraction, and T1 and T2 of water and fat, with a multi-TR, multi-TE sequence. *J Magn Reson Imaging*. 2015;42(6):1538-1543. doi:10.1002/jmri.24946

252. Nolte T, Gross-Weege N, Doneva M, et al. Spiral blurring correction with water–fat separation for magnetic resonance fingerprinting in the breast. *Magn Reson Med*. 2019;(August):mrm.27994. doi:10.1002/mrm.27994

253. Jaubert O, Cruz G, Bustin A, et al. Water–fat Dixon cardiac magnetic resonance fingerprinting. *Magn Reson Med*. 2019;(October):mrm.28070.

doi:10.1002/mrm.28070

254.   Lima da Cruz G, Bustin A, Jaubert O, Schneider T, Botnar RM, Prieto C. Sparsity and locally low rank regularization for MR fingerprinting. *Magn Reson Med*. 2019;(December 2018):1-14. doi:10.1002/mrm.27665

255.   Leporq B, Lambert SA, Ronot M, Vilgrain V, Van Beers BE. Quantification of the triglyceride fatty acid composition with 3.0 T MRI. *NMR Biomed*. 2014;27(10):1211-1221. doi:10.1002/nbm.3175

256.   Virtanen KA, Lidell ME, Orava J, et al. Functional Brown Adipose Tissue in Healthy Adults. *N Engl J Med*. 2009;360(15):1518-1525. doi:10.1056/NEJMoa0808949

257.   Flassbeck S, Schmidt S, Bachert P, Ladd ME, Schmitter S. Flow MR fingerprinting. *Magn Reson Med*. 2019;81(4):2536-2550. doi:10.1002/mrm.27588

258.   Barth M, Breuer F, Koopmans PJ, Norris DG, Poser BA. Simultaneous multislice (SMS) imaging techniques. *Magn Reson Med*. 2016;75(1):63-81. doi:10.1002/mrm.25897

259.   Ye H, Cauley SF, Gagoski B, et al. Simultaneous multislice magnetic resonance fingerprinting (SMS-MRF) with direct-spiral slice-GRAPPA (ds-SG) reconstruction. *Magn Reson Med*. 2016;00(April). doi:10.1002/mrm.26271

260.   Ye H, Ma D, Jiang Y, et al. Accelerating magnetic resonance fingerprinting (MRF) using t-blipped simultaneous multislice (SMS) acquisition. *Magn Reson Med*. 2016;75(5):2078-2085. doi:10.1002/mrm.25799

261.   Christodoulou AG, Shaw JL, Nguyen C, et al. Magnetic resonance multitasking for motion-resolved quantitative cardiovascular imaging. *Nat Biomed Eng*. 2018;2(4):215-226. doi:10.1038/s41551-018-0217-y